Synthesis novel catalysts with low crystallinity for effective elimination of volatile organic compounds (VOCs)

by

Peifen Wang

Supervisor: Professor Dr Guoqing Guan

A Dissertation Presented to

the Graduate School of Science and Technology

of the Hirosaki University in partial fulfillment of the requirement

for the degree of Doctor of Engineering

Hirosaki University

2021

ABSTRACT

Volatile organic compounds (VOCs), classified as major contributors to hazardous pollution, are harmful to human health as well as atmosphere. Therefore, it is highly desired to control the emissions of VOCs. So far, various processes such as biodegradation, adsorption and absorption, plasma-catalysis, photocatalytic oxidation, wet scrubbing and catalytic oxidation have been developed and applied for the VOC elimination. Among them, catalytic oxidation is considered as the most effective alternative because it has no harmful byproducts and can be operated at relatively low temperatures. However, the development of high-performance catalysts for the total VOCs oxidation plays the key role in the removal efficiency with low energy consumption. Due to the high cost and sintering of noble metal, transition metal oxide catalysts with high activity and low cost is necessary for the large-scale applications. Generally, transition metal oxide catalysts are limited owing to their higher operation temperature compared to the supported noble-metal ones. However, the catalytic activity can be tuned by adjusting morphology, specific surface area, oxygen species and so on. Therefore, it is important to design transition metal oxide catalysts for further promoting the catalytic performance. As we all known, oxygen vacancy defect (OVD) engineering has been recognized as an effective strategy to prepare high-performance catalysts for VOCs oxidation since the generated oxygen-deficient sites could lead to an unbalanced electronic structure, resulting in rapid electron transfer in the catalysts and thereby reducing the reaction temperature. Herein, a series of new effective strategies to prepare the oxide catalysts with low crystallinity were designed and applied for increasing the concentration of OVDs. Furthermore, in order to further improve the catalysts activity, the relationships between the correlating physiochemical properties and performance were explored to investigate the reaction mechanism and oxidation pathways.

Firstly, a facile agar-gel method was successfully applied to prepare a series of homogenous Mn-Co mixed oxides for highly efficient catalysis of total toluene oxidation. The obtained Mn2Co1 mixed oxide exhibited a high catalytic activity with $T_{50\%}$ of 228 °C and $T_{100\%}$ of 238 °C as well as high tolerability even under 20 vol.% water vapor environments. It was found that the obtained optimum Mn2Co1 mixed oxide had high specific surface area, large amounts of Co^{3+}, Mn^{3+}, and Mn^{4+} species, abundant adsorbed oxygen species, rich lattice defects, high reducibility at low temperature, and excellent O_2 adsorption ability. Meanwhile, *in situ* DRIFTS spectra measurements confirmed the generated intermediates at different environments during the toluene oxidation and revealed that both adsorbed oxygen and lattice oxygen species could simultaneously participate in the toluene adsorption-oxidation process, especially the rate-controlling step should be the C=C breakage of aromatic ring. It is expected that the present agar-gel method with low cost and convenient operation could be widely applied for the designing of novel mixed metal oxides catalysts for VOCs oxidation. Here, the catalytic activity of Co doping Mn-based oxides is limited by their relatively low surface area. Therefore, we focus on changing how to further improve the surface area of catalysts to expose more activity site.

Secondly, in this study, a series of holmium (Ho)-doped octahedral molecular sieve (OMS-2) catalysts with abundant active oxygen species were successfully synthesized via a facile redox co-precipitation route for the oxidation of toluene. The introduction of trace Ho species during the OMS-2 synthesis process resulted in not only larger surface area and more amorphous phases formation but also abundant active oxygen species, especially oxygen vacancies in the final Ho-doped OMS-2 by the delamination of OMS-2. EPR and XPS analyses were applied to confirm the generated oxygen vacancies and the elemental valences related to the active oxygen species on the catalyst surface. As a result, the 0.5% Ho-OMS-2

showed much higher catalysis performance ($T_{100\%}$ = 228 °C even under 5 vol.% H_2O vapor) than the OMS-2 for the toluene oxidation. Meanwhile, *in situ* DRIFTS analyses demonstrated that the oxidation of toluene was greatly facilitated on the 0.5% Ho-OMS-2 owing to the abundant active oxygen species on the surface, and benzyl, benzyl alcohol, benzaldehyde, benzoate, maleic anhydride, and carbonates were the main intermediates during oxidation of toluene at relatively low temperatures. Compared with the reported Mn-based catalysts, the as-prepared 0.5% Ho-OMS-2 exhibited lower 100% conversion temperature based on the excellent physiochemical properties. Therefore, in order to further decrease the conversion temperature, other transition metal oxide catalysts should be applied.

Finally, a series of samarium (Sm) doped cerium oxide (x% Sm/CeO_2) catalysts were prepared by pyrolysis of Sm containing Ce-based metal organic framework (Sm/Ce-MOF) precursor and applied for catalytic oxidation of toluene. The obtained catalysts were characterized by SEM, TEM, XRD, BET, Raman, XPS, H_2-TPR, O_2-TPD, and their catalytic activities were evaluated by oxidation of toluene over them. It was found that doping of Sm increased the concentration of oxygen vacancy as well as the low temperature reducibility, thereby improved the catalytic performance. Moreover, among the prepared Sm doped CeO_2 catalysts, the 1% Sm/CeO_2 catalyst showed the best performance for the oxidation of toluene with conversions of 50% and 100% at temperatures of 194 and 222 °C respectively under a WHSV of 60,000 mL/(g·h). In addition, the 1% Sm/CeO_2 catalyst also exhibited excellent stability and high toleration to the moisture.

ACKNOWLEDGMENTS

Aomori, Japan

TABLE OF CONTENTS

LIST OF TABLES

ix

LIST OF FIGURES

Chapter 1 Introduction

1.1 General Introduction

Volatile organic compounds (VOCs) including formaldehyde, benzene, toluene, styrene and some complex organic solvents produced from industries and vehicles are recognizing as the culprit of air pollution resources since they have toxic nature, and can serve as the precursors of ozone and photochemical smog [1-3]. To date, various methods including adsorption [4], plasma-catalysis [5], biological degradation [6], photocatalytic oxidation [7-10] and catalytic oxidation [11, 12] have been studied for the controlling of the VOCs emissions. Among them, the catalytic oxidation is a highly efficient way with low cost, in which catalysts play the key role. The developed catalysts for the VOCs oxidation include noble-metal-based and transition-metal-oxide-based ones. No matter what kind of catalysts, the oxygen species existed on the surface, in the subsurface as well as in the bulk have significant effect on the catalysis performance since the activating of oxygen to the reactive oxygen species is always the rate-determining step in the VOCs oxidation.

Generally, oxygen species on the catalysts can be divided into two types: the lattice oxygen species (O_{latt}) and the surface adsorbed oxygen species (O_{ads}). It has been confirmed that the O_{ads} species, especially those generated by the surface oxygen vacancy defects (OVDs) such as O_2^-, O^- and OH groups, have poor coordination ability with metal species so that they have higher mobility than the O_{latt} species [13-15]. The OVDs on the catalysts can not only serve as the electron donor to effectively catch hold of gaseous oxygen, but also accelerate the oxygen activation for various reactions in many fields such as gas sensor [16], wet desulfurization [17, 18], methane reforming [19, 20], O_3

decomposition [21], photothermocatalytic oxidation [13] and especially VOCs combustion [22]. Generally, the localized electrons of OVDs could change the balanced electronic structure in the catalyst, causing specific element valences, surface-active oxygen species and redox properties, thereby leading to the improvement of catalytic activity. For example, δ-MnO$_2$ with abundant OVDs showed 50 ºC lower conversion temperature than β-MnO$_2$ for toluene oxidation [23]. For MnO$_x$ or MnO$_x$-based catalysts, the fold-coordinating of O 2p with Mn 3d orbits followed by the lacking of oxygen atom to maintain the electrical neutrality could generate the OVDs. For the δ-MnO$_2$, the breaking of Mn^{x+} array can cause the layer mismatching, leading to more hybridizations for the generation of more OVDs, which is beneficial for the oxygen vacancies emergence/annihilation cycle as follows:

OVDs emergence:

$$Mn^{4+} + O^{2-} \rightarrow Mn^{3+}/Mn^{4+} + 1/2\ O_2\ (g) + OVDs$$

$$C_7H_8 + Mn^{4+} + O_{ads}/O^{2-} \rightarrow H_2O + CO_2 + Mn^{3+}/Mn^{2+} + OVDs$$

OVDs annihilation:

$$Mn^{3+}/Mn^{2+} + OVDs + O_2\ (g) \rightarrow Mn^{4+} + O_2{}^{2-}{}_{ads} \rightarrow Mn^{4+} + O^{2-} + O_{ads}$$
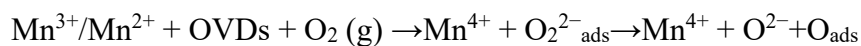
Herein, the Mn^{4+} species can be attacked by VOC molecules adsorbed on Mn^{3+} or Mn^{2+} sites, and the performance of toluene oxidation is highly dependent on the concentration of OVDs on the catalysts. On the other hand, for Co$_3$O$_4$-based catalysts, the hybridization between Co^{3+} and O 2f or O 3f orbit to form the OVDs still remains controversial. However, the emergence-annihilation cycling of Co^{3+}/Co^{2+} with OVDs can be expressed as [24, 25]:

$$Co^{3+} \leftrightarrow OVDs \leftrightarrow Co^{2+}$$

Herein, the OVDs can be formed by the removal of oxygen from the twofold-coordinate

oxygen (O 2f) site related to Co^{3+}, where the VOCs could be adsorbed on it and then the threefold-coordinate oxygen (O 3f) next to the Co^{3+} can be extracted to leave an oxygen vacancy for the refilling by an incoming O_2 molecule in the gas phase. Meanwhile, for the CeO_2-based catalysts, the complicated Ce 3d level including $3d_{5/2}$ and $3d_{3/2}$ could hybridize with oxygen orbit to form OVDs as following [26]:

$$4Ce^{4+} + O^{2-} \rightarrow 4Ce^{4+} + 2e^{-}/OVD + 0.5\ O_2 \rightarrow 2Ce^{4+} + 2Ce^{3+} + OVD + 0.5\ O_2$$
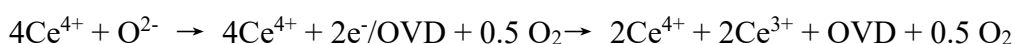
By increasing the OVDs amount in pure MnO_x, Co_3O_4, and CeO_2 based on the tuning of the flexible O–O bond or metal–O bond, total VOC oxidation temperature could be reduced about 50 ºC. To further improve the VOC oxidation performance, various rare earth species [27], Cu [28], and Fe [29] species can be incorporated into these oxide lattices, assisting the formation of more OVDs in them. In general, the OVDs can not only activate O_2 in the gas phase into the electrophilic active oxygen but also dramatically promote the reducibility of catalyst, leading to the deep VOCs oxidation [17]. However, it should be noted that the excessive density of OVDs on the catalysts could inversely hinder the activity improvement [30]. Thus, it is more important to generate appropriate number of OVDs by defect design engineering for the further promoting of the catalytic performance.

Herein, the importance of the OVDs on the catalysts was clarified based on the summary of the proposed VOCs oxidation mechanisms. Then, four approaches for the generation of OVDs, i.e., (i) synthesis and/or calcination temperature controlling; (ii) atom substitution (isovalent-substitution and aliovalent-substitution); (iii) surface modification (noble metal doping and transition metal doping); and (iv) *in-situ* surface treatment (chemical etching and surface reduction), were critically reviewed. Meanwhile, the recently reported novel catalysts with the controllable amounts of OVDs were

summarized. It is expected to provide a guidance for the design and fabrication of more efficient catalysts using OVD engineering for the VOCs oxidation.

1.2 Catalytic VOCs oxidation mechanisms
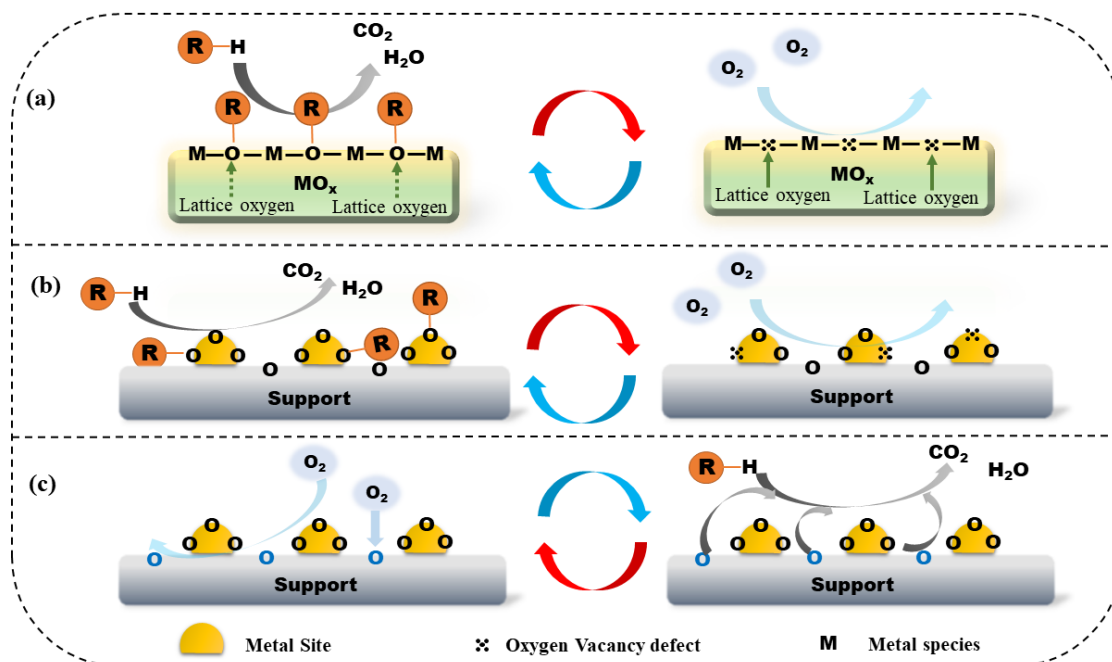
Fig 1.1 Schematic diagrams of (a) MVK mechanism; (b) L-H mechanism; (c) E-R mechanism.

Catalytic oxidations of various VOCs at low temperatures have been intensively investigated and the mechanisms were also well addressed. It is found that the reaction rates could be controlled by either the oxygen species or the VOC molecule type. The pioneering model proposed by Kroger and verified by Mars and van Krevelen to explore the catalytic VOCs oxidation mechanism is generally called as Mars-van Krevelen (MVK) model [31-34], in which the oxidation is considered to occur between the adsorbed organic molecule and the oxygen-rich site on the surface of the catalyst rather than the O_2 molecule in the gas phase. It assumed that two successive steps take place in a cyclic way, which is also known as the redox mechanism. As shown in Fig. 1.1a, in the first step, the adsorbed organic molecule interacts with the lattice oxygen, leading to the

reduction of metal oxide and the emergence of OVDs on the surface of catalyst. Subsequently, the reduced metal site can be re-oxidized by the O_2 in gas phase or the oxygen species transferred from the bulk to the surface [35]. In this MVK model, the rates of the two steps must be the same during the VOCs oxidation over the metal oxide based catalysts such as manganese oxide based catalysts [36, 37], cobalt oxide based catalysts [38], cerium oxide based catalysts [39], nickel oxide based catalysts [40] and tungsten oxide based catalysts [41].

According to the sites where the reaction occurs, the models can be further divided into Langmuir-Hinshelwood (L-H) model [42-44] and Eley-Rideal (E-R) model [45-47]. In the L-H model (Fig. 1.1b), the reaction is suggested to occur between the adsorbed VOC molecule and the adsorbed oxygen, in which the controlling step should be the rates of both VOC and oxygen species adsorbed on the active sites [48]. Furthermore, the L-H model can be divided into single-site L-H model and dual-site L-H model based on VOCs and oxygen adsorb on the same or different active sites. Figueiredo *et al.* [49] found that the methyl-isobutyl-ketone oxidation over Pt/zeolite catalysts was affected by the presence of o-xylene owing to the competitive adsorption, where the methyl-isobutyl-ketone was adsorbed on the metal active site before reacting with oxygen species, which followed the L-H mechanism. Meanwhile, for the E-R model as shown in Fig. 1.1c, the reaction is suggested to proceed between VOC molecule and O_2 molecule in the gas phase, which is similar to the L-H mechanism except the oxidization reaction occurring in the gas phase [50]. González-Velasco *et al.* [47] confirmed the positive correlation between kinetic data and the E-R mechanism in the trichloroethylene oxidation. Although both L-H model and E-R model are usually applied to explain the reaction mechanism of VOCs oxidation over the noble metal based catalysts, in some cases, the oxidation path over the

transition metal oxide based catalysts can be also explained by the L-H model or E-R model. For example, it was found that n-hexane oxidation over the pure Co oxide catalyst more followed the L-H model where that over the MnO_x and Co/MnO_x catalysts proceeded via MVK model [51]. Meanwhile, cyclohexane oxidation over the Co/activated carbon catalysts was found to be well fitted to the E-R model [52].

The validity for three mechanisms over various catalysts is also determined by the VOC type. The nonpolar VOC molecules such as benzene prefer to go through π-π interaction, π-complexation and electrostatic attraction on the surface of the catalysts. In contrast, the polar functionalities of VOCs derived from heteroatoms including halogen-, O-, S- or N-containing functional groups with lone pair of electrons could make them feasible to be involved in hydrogen bonding, polar-polar interaction, electron donor-acceptor interaction and acid-base interaction on the surface of the catalysts. Thus, the catalysis mechanism for the complete oxidation of VOCs diversifies based on the different properties of VOC molecules and catalysts. Especially, the generation of OVDs on the catalyst has a positive effect on adsorption of intermediates and/or O_2 in gas phase owing to the electronegativity of oxygen vacancies, thus leading to the improvement of catalytic activity [53-55]. As shown in Fig. 1.1a, the OVDs appear after the combination of VOC molecule with the oxygen-rich region in the MVK model, which played the key role in the replenishment and activation of surface adsorbed O_2 molecule, thus promoting the adsorption of VOC molecule more easily and efficiently [17]. Ko and Wan *et al.* [56, 57] found that *in situ* reduction of Pt nanoparticles decorated on the $NaInO_2$ can introduce the OVDs to provide more adsorbed oxygen species for the formaldehyde oxidation. As shown in Fig. 1.2a, it was found that the HCHO was easily adsorbed on the surface of catalyst via the OVDs as described in the L-H model, which was further oxidized as the

following order: formate → carbonate → CO_2 + H_2O. Meanwhile, it was also verified that the Pt/NaInO$_2$ catalyst with the properly relative concentration of OVDs could exhibit a highest catalytic performance based on the density functional theory (DFT) calculations. Herein, from the Hirshfeld charge distribution result, as described in Fig. 1.2b, it is well confirmed the relative concentration of OVDs originated from the interfacial lattice mismatch after the Pt loading, where the activated superoxide radicals ($O_2\cdot^-$) could be easily captured on the OVDs for further improvement of catalytic activity. Wang *et al.* [58] found that C3-C4 hydrocarbons oxidation over yttrium (Y) doping MnO$_x$ was dominated by the MVK model, and the Y doping resulted in more OVDs formation, which were beneficial for the VOC adsorption and oxidation. Especially, in this case, the oxygen in gas phase or in the bulk of catalyst could replenish the OVDs for the re-oxidizing of catalyst. Herein, the OVD is one of key factors to affect the migration of oxygen species at the interface between two phases, thereby promoting the catalytic activity [59]. In addition, it is considered that the OVDs should play an important role in the adsorbing and dissociating of O_2 molecule in the gas phase, by which the intensity of O-O and metal-O bonds of catalysts in the oxidation process could be directly affected owing to the unstable interstitial property and electronegativity of OVDs. Thus, it can be concluded that the increase in the number of OVDs could accelerate the replenishment of oxygen species for the improvement of the catalytic activity [60, 61].

To further confirm the contribution of OVDs, the DFT calculations are generally applied to understand the relationship between catalytic performance and OVDs [55, 62, 63]. During the DFT calculations, the oxygen vacancy formation energy (E_{O_v}) can be calculated using the following equation:

$$E_{O_v} = E_{surface-O_v} + \frac{1}{2}E_{O_2} - E_{surface}$$
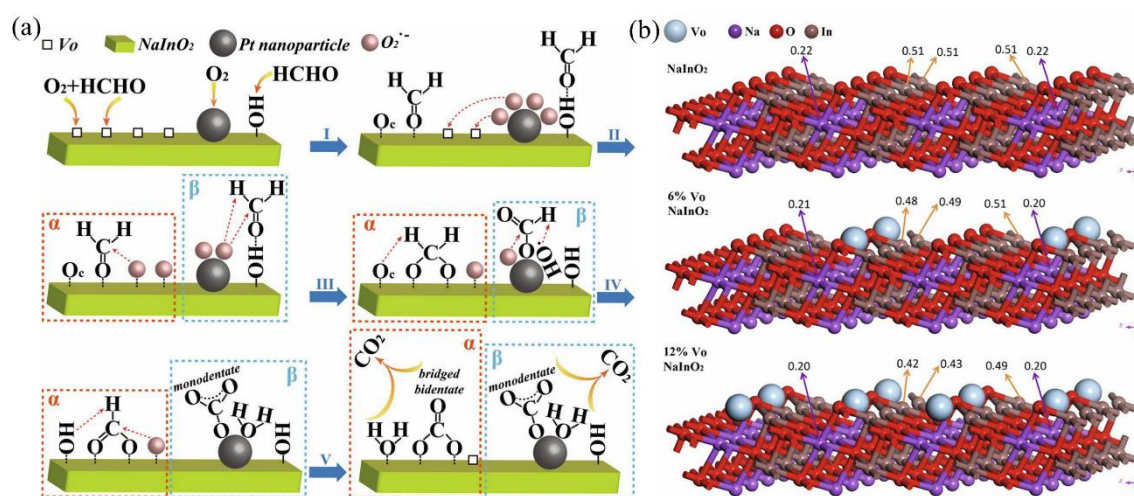
Fig 1.2. (a) The assistance mechanism of OVDs during ambient HCHO oxidation: offering much more active sites of $O_2 \cdot^-$ for the reaction; (b) DFT simulation of atomic Hirshfeld charges with and without OVDs [57]. Copyright 2020, Elsevier.

where E_{O_2}, $E_{surface-O_v}$, and $E_{surface}$ are the energy of a gas-phase O_2, energy of defective surface with an oxygen vacancy and the energy of perfect surface, respectively. Generally, one perfect and the other defective surfaces with optimized bulk lattice parameters are simultaneously proposed to calculate the oxygen vacancy formation energy. Here, the oxygen vacancy formation energy indicates the possibility of OVDs formation. For example, by using it, the order of $CuCoFe_2O_4$ (1.57 eV) < $CuFe_2O_4$ (2.42 eV) < $CoFe_2O_4$ (2.47 eV) on the oxygen vacancy formation energy of (311) facet of them was found, which indicated that the OVD should be more likely to be formed on the (311) facet of $CuCoFe_2O_4$ [54].

To sum up, O_2 is more easily adsorbed and activated on OVDs to form active oxygen species for VOC and its intermediates oxidation due to the reducing of dissociation energy barrier of C-H bonds in VOC molecule and the elongating of the distance of O-O bond [15, 62, 64]. Therefore, the strategies for generation of the OVDs on the catalysts should

be very important. To date, it was confirmed that the generation of abundant multi-phase interfaces could increase the number of OVDs on the exposed planes of catalysts for the VOC oxidation [54]. In the following sections, the progress on the research and development of the strategies for tuning of the OVDs on the VOCs oxidation catalysts was critically reviewed.

1.3 Strategies for tuning of the oxygen vacancy defects

Various defects could ubiquitously exist in different metal oxides. As stated above, among them, the OVDs can radically boost the catalytic activity owing to the improvement of the catalysis reducibility at low temperature. In recent years, the effect of OVDs on the catalytic VOCs oxidation have been paid great attentions. For example, the noble metal-based catalysts (e.g., Pt-, Pd-, Au- based catalysts), pure metal oxide catalysts (e.g., Mn-, Cu-, Co-, Ni- and Ce oxide-based catalysts), and mixed-component catalysts have been designed to achieve the desiring high-performance catalysts by tuning the concentration of OVDs. The OVD engineering used for designing the heterogeneous catalysts has identified that the changing of catalyst morphology and the growing of interface between different components could generate rich OVDs. To date, the strategies on the OVDs amount tuning involve four types: (i) temperature controlling, for example, altering the reaction temperature during the catalyst synthesis process and/or followed by altering the calcination temperature for the final catalyst preparation; (ii) atom substitution, taking Mn-based catalyst preparation as the example, co-substituting second or multifold metal elements such as Co, Fe, Ni, and Ce including isovalent and aliovalent substitution; (iii) surface elemental doping, using other metals or metal oxides to decorate the parent catalysts; (iv) *in-situ* surface treatment such as chemical etching to expose more crystal defects and surface reduction of metal oxide. During the catalyst preparation, it is

9

important to find an optimum way to generate suitable amount of OVDs. Tables 1.1-1.3 summarized the performances of various VOCs oxidations on the OVDs containing catalysts, which will be discussed in the following. Taking 90% toluene conversion temperature as the basis, Fig. 1.3 compares the corresponding activities over various catalysts prepared using the above four strategies based on the data shown in Table 1.1, and meanwhile, the characterization ways for OVDs are also mentioned. In the following sections, they are reviewed in details.
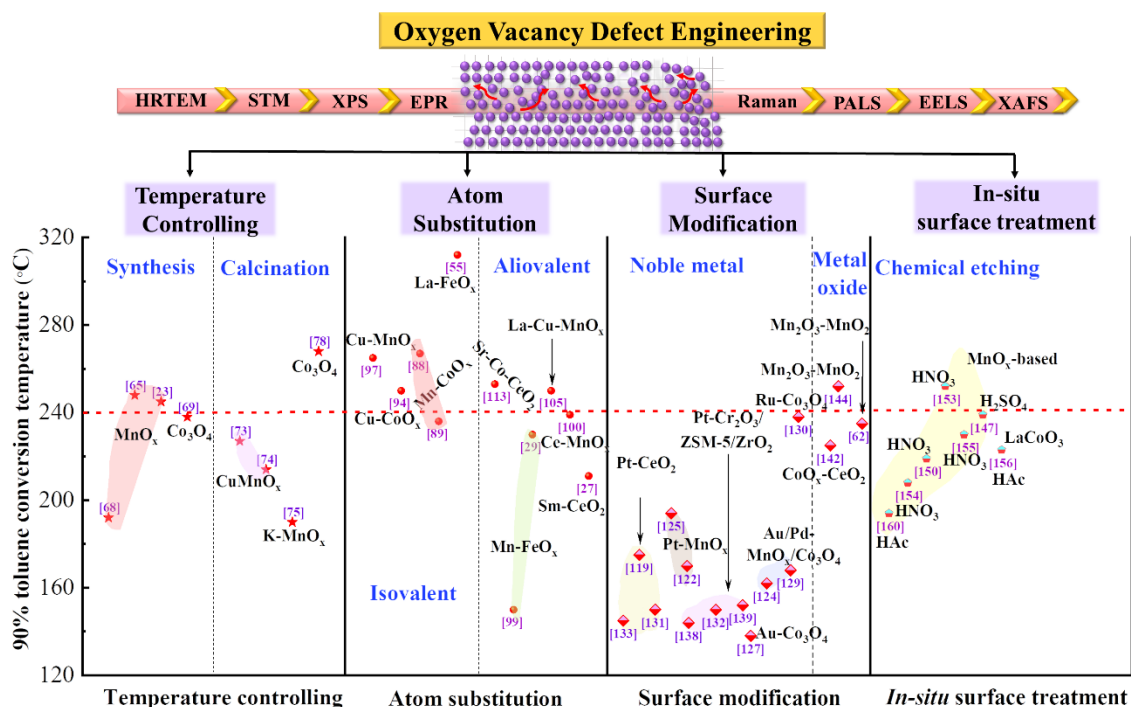
Fig 1.3. Summary of the corresponding activities over various catalysts prepared using the above four strategies based on the data shown in Table 1 with 90% toluene oxidation temperature and the characterization ways for OVDs.

Table 1.1 Survey of literature data on the catalytic activities for toluene oxidation

Catalysts	Method	S_{BET} (m^2 g^{-1})	Conc. (ppm)	Temperature (°C) [a]		T_x (°C) [b]	E_a (kJ/mol)	Ref.
				T_{50} (°C)	T_{90} (°C)			

10

Co-Ce oxide	Aliovalent-substitution	120	~266	225	241	$T_{100}=251$	/	[111]
$\alpha@\beta$-MnO$_2$	Reaction temperature	89	500	180	192	$T_{100}=210$	62.4	[68]
Layered Cu-Mn oxide	Isovalent-substitution	247	500	187	207	$T_{100}=240$	138	[28]
Cu-MnO$_2$	Isovalent-substitution	208	500	200	215	$T_{100}=220$	43.6	[30]
CoCeO$_x$	Aliovalent-substitution	71.4	500	212	227	$T_{100}=250$	/	[25]
La$_{0.9}$Ca$_{0.1}$CoO$_3$/MgO	Aliovalent-substitution	24.3	500	215	230	$T_{100}=250$	34	[112]
Mn-Co oxides	Isovalent-substitution	47	500	226	240	$T_{100}=340$	/	[87]
MnO$_x$	Reaction temperature	/	500	235	248	$T_{100}=262$	/	[65]
CuO-MnO$_x$	Calcination temperature	37.2	600	217	227	$T_{100}=230$	/	[73]
K-OMS-2-500 (MnO$_x$)	Calcination temperature	52.8	~750	175	190	$T_{100}=200$	/	[75]
Cu$_1$Co$_2$Fe$_1$O$_x$	Isovalent-substitution	128	800	224	238	$T_{100}=242$	36.6	[54]
CuHoCeO$_x$	Aliovalent-substitution	93.8	900	206	224	$T_{99}=250$	95.2	[110]
0.82 wt%Pt@M-Cr$_2$O$_3$	Noble modification	39.4	1000	140	144	$T_{100}=145$	78.6	[138]
0.24 wt% Pt/CeO$_2$-rod	Noble modification	98.7	1000	132	145	$T_{100}=160$	56.2	[133]
6.5 wt% Au-Co$_3$O$_4$	Noble modification	91	1000	109	138	$T_{100}=170$	45	[127]
1.9 nm Pt/ZSM-5	Noble modification	371	1000	146	150	$T_{98}=155$	/	[132]
5Mn1Fe binary oxides	Aliovalent-substitution	180.7	1000	140	150	$T_{100}=160$	/	[99]
0.19 wt% Pt/CeO$_2$-rod	Noble modification	102.6	1000	138	150	$T_{99}=200$	77.1	[131]
0.71 wt% Pt/ZrO$_2$	Noble modification	122.9	1000	147	152	$T_{100}=160$	/	[139]
3.8 wt% AuPd$_{1.92}$/Mn$_2$O$_3$	Noble modification	35.2	1000	146	162	$T_{100}=180$	26	[124]
1.99 wt%Au$_{0.99}$Pd$_1$/Co$_3$O$_4$	Noble modification	33.1	1000	164	168	$T_{99}=180$	33	[129]
0.39 wt% Pt/α-MnO$_2$	Noble modification	71.0	1000	156	170	$T_{100}=190$	46.73	[122]

0.5 wt% Pt-CeO$_2$	Noble modification	105	1000	160	175	T$_{99}$ = 180	92.5	[119]
2.3 wt% Pt/Mn$_2$O$_3$	Noble modification	33.7	1000	165	194	T$_{100}$ = 218	41	[125]
γ-MnO$_2$/SmMnO$_3$	HNO$_3$-etching	48.6	1000	187	208	T$_{100}$ = 220	55.0	[154]
Nanorods Cu/Mn oxides	Calcination temperature	45.9	1000	205	214	T$_{100}$ = 220	/	[74]
1 wt% Sm-CeO$_2$	Aliovalent-substitution	129	1000	194	211	T$_{100}$ = 222	/	[27]
Mesoporous γ-MnO$_2$	HNO$_3$-etching	123.2	1000	215	219	T$_{100}$ = 230	68	[150]
LaCoO$_3$ perovskite	HAc-etching	5.1	1000	206	223	T$_{100}$ = 270	/	[156]
1.0 wt% CoO$_x$-CeO$_2$	Oxide modification	89	1000	215	225	T$_{100}$ = 240	/	[142]
MnO$_2$/LaMnO$_3$ perovskites	HNO$_3$-etching	134.6	1000	225	230	T$_{100}$ = 240	38.6	[155]
Mn$_{3-x}$Fe$_x$O$_4$ spinel	Aliovalent-substitution	84.8	1000	210	230	T$_{100}$ = 250	70	[29]
Mn$_{0.3}$Zr$_{0.7}$O$_2$	Oxide modification	178.7	1000	231	235	T$_{100}$ = 250	87.2	[62]
MnCoO$_x$	Isovalent-substitution	85.4	1000	228	236	T$_{100}$ = 238	/	[89]
1 wt% Ru/Co$_3$O$_4$	Noble modification	80	1000	230	238	T$_{100}$ = 240	/	[130]
3D-Co$_3$O$_4$ nanoflower	Reaction temperature	84.6	1000	229	238	T$_{100}$ = 243	71.6	[69]
3MnO$_x$-1CeO$_y$	Aliovalent-substitution	140.2	1000	226	239	T$_{100}$ = 250	52.4	[100]
Acid-treated Mn$_2$O$_3$	H$_2$SO$_4$-etching	9.9	1000	231	239	T$_{100}$ = 250	161.8	[147]
δ-MnO$_2$	Reaction temperature	29.7	1000	225	245	T$_{100}$ = 290	55.0	[23]
Cu-Co mixed oxide	Isovalent-substitution	21.69	1000	243	250	T$_{100}$ = 290	/	[94]
La-CuMn oxides	Aliovalent-substitution	164.2	1000	220	250	T$_{95}$ = 400	/	[105]
γ-MnO$_2$-like	HNO$_3$-etching	245.7	1000	242	252	T$_{100}$ = 260	49	[153]
Mn$_2$O$_3$@MnO$_2$	Oxide modification	41.3	1000	235	252	T$_{99}$ = 295	/	[144]
Sr-Co/CeO$_2$	Aliovalent-substitution	181	1000	237	253	T$_{100}$ = 330	/	[113]
CuO-MnO$_2$	Isovalent-substitution	17.3	1000	243	265	T$_{100}$ = 290	/	[97]
Mn$_{1.5}$Co$_{1.5}$O$_4$ on Ni foam	Isovalent-substitution	14.2	1000	263	267	T$_{100}$ = 270	115.31	[88]
Hierarchical Co$_3$O$_4$	Calcination temperature	48.9	1000	264	268	T$_{100}$ = 270	/	[78]
Perovskite LaFeO$_3$	Isovalent-substitution	4.66	1000	286.5	312.1	T$_{100}$ = 320	101.1	[55]

oxides

Catalysts	Method	S_{BET} (m² g⁻¹)	Conc. (ppm)	T_{50}	T_{90}	T_x (°C)	E_a (kJ/mol)	Ref.
MnOx	HAc-etching	/	1000	188	194	$T_{99} = 195$	62.4	[160]
	KOH-etching			205	210	$T_{99} = 215$	68.0	
Cu₁Mn₂Ce₄ oxides	Aliovalent-substitution	45.3	1200	210	215	$T_{100} = 230$	/	[108]
3.5 wt% Pt/Co₃O₄	Noble modification	/	2000	148	150	$T_{100} = 152$	/	[126]
3.7 wt% Au/CeO₂	Noble modification	/	2000	240	250	$T_{100} = 340$	/	[135]
Rosette-like CeCoOx	Reaction temperature	45.1	3000	130	168	$T_{100} = 190$	33.1	[70]

Table 1.2 Survey of literature data on the catalytic activities for benzene oxidation.

Catalysts	Method	S_{BET} (m² g⁻¹)	Conc. (ppm)	Temperature (°C) [a]		T_x (°C) [b]	E_a (kJ/mol)	Ref.
				T_{50} (°C)	T_{90} (°C)			
CoₓNiAlO oxides	Aliovalent-substitution	172.7	100	208	227	$T_{100} = 260$	39.0	[192]
LiCoO₂ perovskite	HNO₃-etching	28	370 - 430	220	250	$T_{99} = 300$	/	[165]
Layered Cu-Mn oxide	Isovalent-substitution	247	500	218	240	$T_{100} = 250$	131	[28]
Pt/CaCO₃	Noble modification	3.4	1000	165	178	$T_{100} = 205$	/	[141]
2.0 wt% Pd/CeO₂	Noble modification	106	1000	160	180	$T_{100} = 200$	/	[134]
6.5 wt% Au-Co₃O₄	Noble modification	91	1000	162	189	$T_{100} = 200$	55	[127]
Coral-like CoMnOx	Calcination temperature	99	1000	175	195	$T_{100} = 210$	40.3	[83]
1.0 wt% Au-CeO₂	Noble modification	35.42	1000	200	210	$T_{100} = 220$	/	[136]
3MnOx-1CeOy	Aliovalent-substitution	128.4	1000	194	210	$T_{100} = 230$	66.5	[100]
Cu-Co mixed oxide	Isovalent-substitution	127.2	1000	250	290	$T_{99} = 325$	/	[95]
Mn-Co mixed oxide	Isovalent-substitution	101	1000	206	238	$T_{99} = 350$	/	[96]
Ce-Mn oxides	Isovalent-substitution	~52.6	1000	220	245	$T_{100} = 280$	66	[98]
CoₓMn₁₋ₓCeOδ	Aliovalent-substitution	68.47	1000	235	247	$T_{100} = 275$	/	[109]

oxides

Nanosheet Co-Mn oxides	Calcination temperature	139.3	1500	170	195	$T_{100}=240$	/	[84]
K/Ag-OMS-2 (MnO$_x$)	Aliovalent-substitution	133.2	1500	180	225	$T_{99}=300$	/	[101]
Ce-OMS-2 (MnO$_x$)	Aliovalent-substitution	322.1	2000	169	210	$T_{99}=260$	/	[104]

Table 1.3 Survey of literature data on the catalytic activities for the other VOC oxidation.

VOCs	Catalysts	Method	S_{BET} (m^2 g^{-1})	Conc. (ppm)	Temperature (°C) [a]		T_x (°C) [b]	E_a (kJ/mol)	Ref.
					T_{50} (°C)	T_{90} (°C)			
Methane	2 wt% Pt/K-OMS	Noble modification	/	0.4 vol%	325	375	$T_{100}=450$	/	[123]
Formaldehyde	Nanofiber Pt/TiO$_2$	Calcination temperature	9	~250 ppm	T_{100} = Room temperature			/	[80]
Formaldehyde	δ-MnO$_2$	Reaction temperature	108.4	170	58	75	$T_{100}=100$	/	[67]
Formaldehyde	Porous ε-MnO$_2$	HNO$_3$-etching	181	100	99	150	$T_{100}=190$	/	[151]
Formaldehyde	MnO$_x$−CeO$_2$	H$_2$SO$_4$-etching	130	400	$T_{67}=100$			/	[148]
Propylene	3.7 wt% Au/CeO$_2$	Noble modification	/	6000	170	200	$T_{99}=325$	/	[135]
Acetone	Spinel CuCo$_2$O$_4$	Isovalent-substitution	19	1000	157	190	$T_{100}=220$	60.2	[93]
Acetone	Layer CoAlO-200	Calcination temperature	187	1000	189	200	$T_{100}=238$	/	[85]
2-Propanol	Mesoporous Co$_3$O$_4$	Calcination temperature	83	6.4 vol%	149	157	$T_{100}=162$	69.7	[72]

14

VOC	Catalyst	Method							Ref.
Propene	Perovskite LaNiO$_3$	Calcination temperature	11.8	0.3 vol.%	225	250	T$_{100}$ = 300	/	[86]
Propane	MnNi$_{0.2}$O$_x$	Isovalent-substitution	111	2000	215	242	T$_{100}$ = 275	67	[90]
Propane	Cu-Mn mixed oxide	Isovalent-substitution	21.7	400 ppm	295	325	T$_{100}$ = 375	/	[91]
Propane	2 wt% Pt/K-OMS	Noble modification	/	0.1 vol%	270	290	T$_{100}$ = 350	/	[123]
O-xylene	Layered Cu-Mn oxide	Isovalent-substitution	247	500	213	227	T$_{100}$ = 235	198	[28]
O-xylene	3MnO$_x$-1CeO$_y$	Aliovalent-substitution	128.4	1000	251	268	T$_{100}$ = 275	59.0	[100]
O-xylene	Cu-OMS-2	Aliovalent-substitution	164.4	500	175	185	T$_{100}$ = 190	/	[103]
O-xylene	K-CeO$_2$	Aliovalent-substitution	120	200	175	195	T$_{100}$ = 210	/	[106]
O-xylene	6.5 wt% Au-Co$_3$O$_4$	Noble modification	91	1000	128	162	T$_{100}$ = 180	47	[127]
O-xylene	1.0 wt% Pd/CoO	Noble modification	65.1	1000	159	173	T$_{99}$ = 180	74.1	[128]
O-xylene	Nanocubes CeO$_2$	Calcination temperature	83	500	225	250	T$_{99}$ = 270	/	[71]
Ethyl acetate	Cs-OMS-2	Aliovalent-substitution	~55	1000	180	195	T$_{100}$ = 210	/	[102]
Ethyl acetate	MnO$_x$-CeO$_2$-s	Oxide modification	155.9	500	188	205	T$_{99}$ = 210	/	[14]
Ethyl acetate	15 wt% CuO-CeO$_2$	Oxide modification	45	1000	235	240	T$_{100}$ = 250	/	[143]
Chlorobenzene	3MnO$_x$-1CeO$_y$	Aliovalent-substitution	128.4	1000	314	355	T$_{100}$ = 350	147.2	[100]
Chlorobenzene	LaMnO$_3$-	HF-etching	45.1	1000	160	200	T$_{100}$ =	/	[158]

	CeO$_2$ perovskite						220		
Dimethyl ether	OMS-2	Surface reduction	89.8	1000	163	230	T$_{100}$ = 260	57.7	[117]
Dimethyl ether	MnO$_2$	acid-etching	128.2	700	175	182	T$_{100}$ = 200	/	[159]
Dichloromethane	La$_3$Mn$_2$O$_7$ perovskite	H$_3$PO$_4$-etching	/	0.1 vol%	355	410	T$_{99}$ = 450	/	[157]

a Partially data units are unified for the purpose of comparison.

b x = Maximum removal efficiency.

1.3.1 Temperature controlling

Temperature controlling at various preparation method is a common strategy to introduce and/or tune the concentration of OVDs since the crystalline state greatly depends on the temperature. For example, by controlling the synthesis temperature, it is possible to obtain catalysts with different crystallographic structures like 1D, 2D, and 3D, resulting in the exposure of different places, thereby generating different degrees of OVDs efficiently. While, by controlling the calcination temperatures in the post-processing, the phase transition could occur, resulting in different interface states to tune the concentration of OVD on the interface.

1.3.1.1 Synthesis temperature

Typically, the hydrothermal synthesis is a cost-effective way for the preparation of various VOC oxidation catalysts at different temperatures. Generally, the degree of crystallization is depended on the hydrothermal synthesis temperature, which could also affect the formation of OVDs, resulting in different performances [65]. For instance, in the early studies, α-, β-, γ- and δ-MnO$_2$ powders were synthesized hydrothermally at different synthesis temperatures by the redox reactions between of MnO$_4^-$ and/or Mn^{2+} in

16

a temperature range of 120-180 °C [66]. Subsequently, the α- and δ-MnO$_2$ were prepared via the redox reactions between Mn^{2+} and MnO$_4^-$ at 160 and 240 °C respectively, while, the β-, γ-MnO$_2$ were prepared via the redox reactions between Mn^{2+} and S$_2$O$_8^{2-}$ at 140 and 90 °C respectively [67]. It was found that the order for the 90% HCHO conversion temperature was δ-MnO$_2$ (75 °C) < α-MnO$_2$ (120 °C) < γ-MnO$_2$ (145 °C) < β-MnO$_2$ (173 °C). Herein, the δ-MnO$_2$ with 2D layer tunnel structure possessed abundant OVDs with higher catalytic activity. Moreover, it was found that the different types of tunnel structures in Mn-based catalyst could have different numbers of OVDs. However, the generation of OVDs in the tunnel structure is still not fully understood. In order to further investigate the location of OVDs in MnO$_x$, the α-MnO$_2$ consisting of 2×2 and 1×1 tunnel structures and β-MnO$_2$ composed of only 1×1 tunnel structure were designed to fabricate a core-shell α@β-MnO$_2$ catalysts for toluene oxidation by Qu *et al*. [68]. It was confirmed that the α@β-MnO$_2$ catalysts under 180 °C possessed the richest OVDs owing to the existence of mixed phase interfaces between α-MnO$_2$ and β-MnO$_2$, which were verified by HRTEM (Figs. 1.4a-c), Raman and XPS analyses. Fig. 1.4d illustrates the generation of the OVDs on the special two-phase structure, which was confirmed to improve the reducibility at low temperature (Fig. 1.4e), resulting in 90% toluene conversion temperature was reduced from 245 °C (β-MnO$_2$) to 192 °C (α@β-MnO$_2$) (Fig. 1.4f). Recently, by the *in-situ* DRIFTS analysis, it is verified that the rich adsorbed oxygen on the OVDs induced the rapid dehydrogenation of methyl, which followed the MVK model and facilitated the toluene decomposition at low temperatures [23].

Similarly, by changing the synthesis temperature, 1D-Co$_3$O$_4$, 2D-Co$_3$O$_4$, and 3D-Co$_3$O$_4$ catalysts were successfully prepared using the template-free hydrothermal way at 100 °C, 100 °C, and 180 °C, respectively [69]. It was found that the 3D-Co$_3$O$_4$ with a
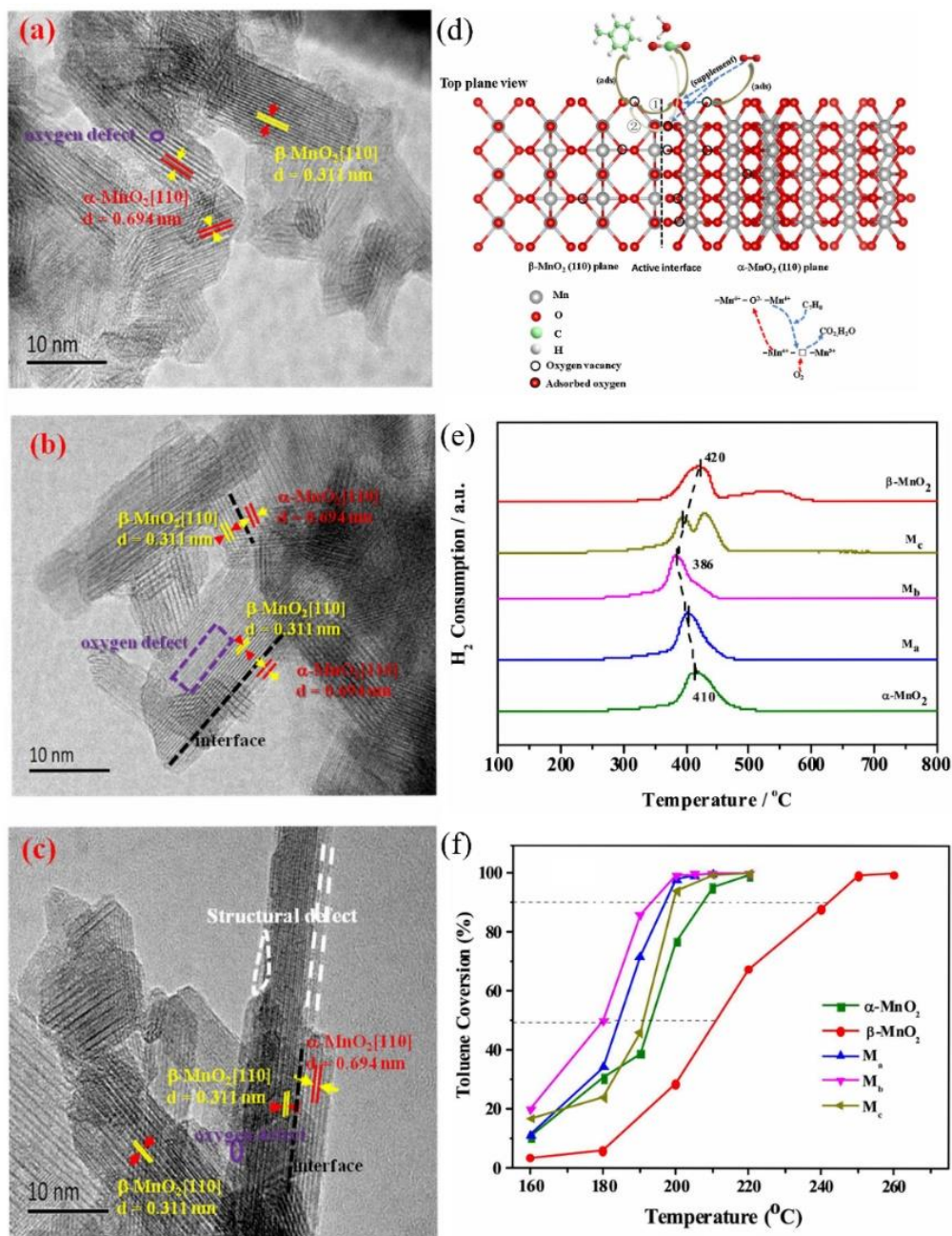
Fig 1.4. (a-c) HRTEM images of α@β-MnO$_2$ catalysts, M$_a$ (a), M$_b$ (b), M$_c$ (c); (d) Reaction scheme of toluene oxidation over α@β-MnO$_2$ catalysts; (e) H$_2$-TPR profiles of five samples; (f) Activity profiles of the five samples for toluene oxidation as a function of temperature. The sample of reaction temperature at 150 °C, 180 °C, 200 °C were denoted as M$_a$, M$_b$ and M$_c$, respectively. [68] Copyright 2020, Elsevier.

nanoflower structure had the highest activity with $T_{90\%}$ of 238 °C for toluene oxidation due to the exposure of more (111) facets with OVDs. Combining with Ce species, the rosette-like $CeCoO_x$ catalysts were prepared under different hydrothermal temperatures of 25, 100 and 200 °C, respectively, and the concentrations of OVDs possessed the same sequence with their performances for the toluene oxidation: $CeCoO_x$-200 ($T_{90\%}$ = 175 °C) > $CeCoO_x$-25 ($T_{90\%}$ = 275 °C) > $CeCoO_x$-100 ($T_{90\%}$ = 310 °C). It is worth noting that the effect of Ce species was ignored here since the CeO_2 phase emerged on all of $CeCoO_x$ samples but the synthesis temperature dominated the final catalytic activity [70].

As discussed above, the changing of synthesis temperature can result in different amounts of OVDs by the transformation of crystal phase for optimizing of corresponding activity. Thus, it is possible to tune the OVDs in various metal oxide catalysts via adjusting the synthesis temperature. However, the nature of chemical element is regarded as a key factor in catalyst preparation, which limits the wide application of controlling synthesis temperature. At present, only Mn-based and Co-based oxides catalysts were successfully designed, while, a small minority of mixed metal oxide catalysts were selected using changing the synthesis temperature to tune the concentration of OVDs.

1.3.1.2 Calcination temperature

Comparing with the adjusting of synthesis temperature, it is more convenient to control the calcination temperature for tuning the OVDs concentration since the crystallization of catalysts could be carefully tuned to create different phases from amorphous phase to various crystalline phases. For example, as the pure CeO_2 was annealed at 350, 450, 550 and 650 °C, it was found that more OVDs were formed on the surface of CeO_2-550 °C, which exhibited the lowest 90% o-xylene conversion temperature of 250 °C [71]. A series of mesoporous Co_3O_4 catalysts calcinated at 150, 250, 350 and 450 °C were compared by

the catalytic oxidation of 2-propanol over them. As shown in Figs. 1.5a and b, the relative crystallinity increased with the increased in the calcination temperature, but the 90% conversion temperature was in the order of Co_3O_4-350 (157 °C) < Co_3O_4-250 (175 °C) < Co_3O_4-450 (195 °C) < Co_3O_4-100 (220 °C) [72]. It is found that the appropriate crystallinity exists for the improvement of catalytic activity since the optimal concentration of OVDs could be obtained by the partial generation of amorphous phases. However, the excessive amorphous phase in the catalysts such as Co_3O_4-100 and Co_3O_4-250 inversely hindered the activity improvement.

For binary or trinary metal mixed catalysts, the effects of calcination temperature on the performance also cannot be ignored due to the formation of different multi-phase interfaces. As shown in Fig. 1.5c, the crystallinity sequence of Cu/MnO_x (CM) calcinated at different temperatures was CM-800 > CM-700 > CM-600 > CM-500 > CM-400 ≈ CM-300 based on XRD analysis. It was found that the Cu/MnO_x calcinated at 500 °C showed the highest catalytic activity ($T_{100\%}$ of 230 °C) for the toluene oxidation (Fig. 1.5d). Herein, the OVDs could be more generated on the amorphous region or the interface between the amorphous and crystalline phases [73]. Meanwhile, the morphology of $CuMnO_x$ catalysts was found to have great effect on the VOCs oxidation. For instance, the Cu/MnO_x calcinated at 500 °C by *in-situ* pyrolysis of Cu/Mn precursors had a nanorod morphology, which achieved the total toluene conversion at 220 °C [74]. In addition, $Cu_1Co_2Fe_1O_x$ catalysts prepared under various calcinated temperatures were found to have different amounts of OVD sites due to the generation of different multi-phase interfaces, which also resulted in different performances [54]. As shown in Figs. 1.5e and f, the catalyst calcined at 400 °C with low crystallinity was mainly composed of Co_3O_4, Fe_3O_4 and CuO phases with rich phase interfaces so that more OVDs were generated, thereby achieving

20

a highest catalytic activity for toluene oxidation with an $T_{90\%}$ of 238 °C. With the increase in the calcination temperature, the $CoFe_2O_4$ and $CuFe_2O_4$ with spinel structure were formed, which led to the concentration of OVDs decreased. Based on the above results, the oxidation mechanism of OVDs was proposed based on the DRIFTS results (Fig. 1.5g), in which the benzene ring of toluene was considered to be quickly oxidized with the assistance of surface active oxygen and OVDs since O_2 in the feed could be easily captured on the OVD sites to replenish the consumption of active oxygen on the surface of catalysts with the MVK mechanism [73].

Tuning of the catalyst performance by adjusting the calcination temperature has been also applied for the pure metal oxide catalysts such as manganese oxide catalysts [75-77], cobalt oxide catalysts [76, 78] and ceria oxide catalysts [79], supported catalysts such as Pt/TiO_2 (noble metal) [80], CuO/Fe_2O_3 [81] and Fe_2O_3/Al_2O_3 [82] (metal oxides), mixed catalysts such as Sm/CeO_2 [79], $CoMnO_x$ [83, 84], $CoAlO_x$ [85], and perovskite-like $LaNiO_3$ catalysts [86]. In general, the annealing temperature could greatly affect the crystalline composition of catalysts, leading to the changing of morphology, surface area, reducibility, and the concentration of OVDs on the surface of catalysts. It is found that the temperatures ranged from 350 to 500 °C are considered more suitable for the formation of the optimal ratio of crystalline and amorphous phases. It is worth noting that the metal oxide catalyst with proper crystallinity always exhibit higher activity when compared to those catalysts with too high or too low crystallinity since the properly proportioned amorphous structure could be conducive to the improvement of the mobility of oxygen species and the increase in the number of OVDs.
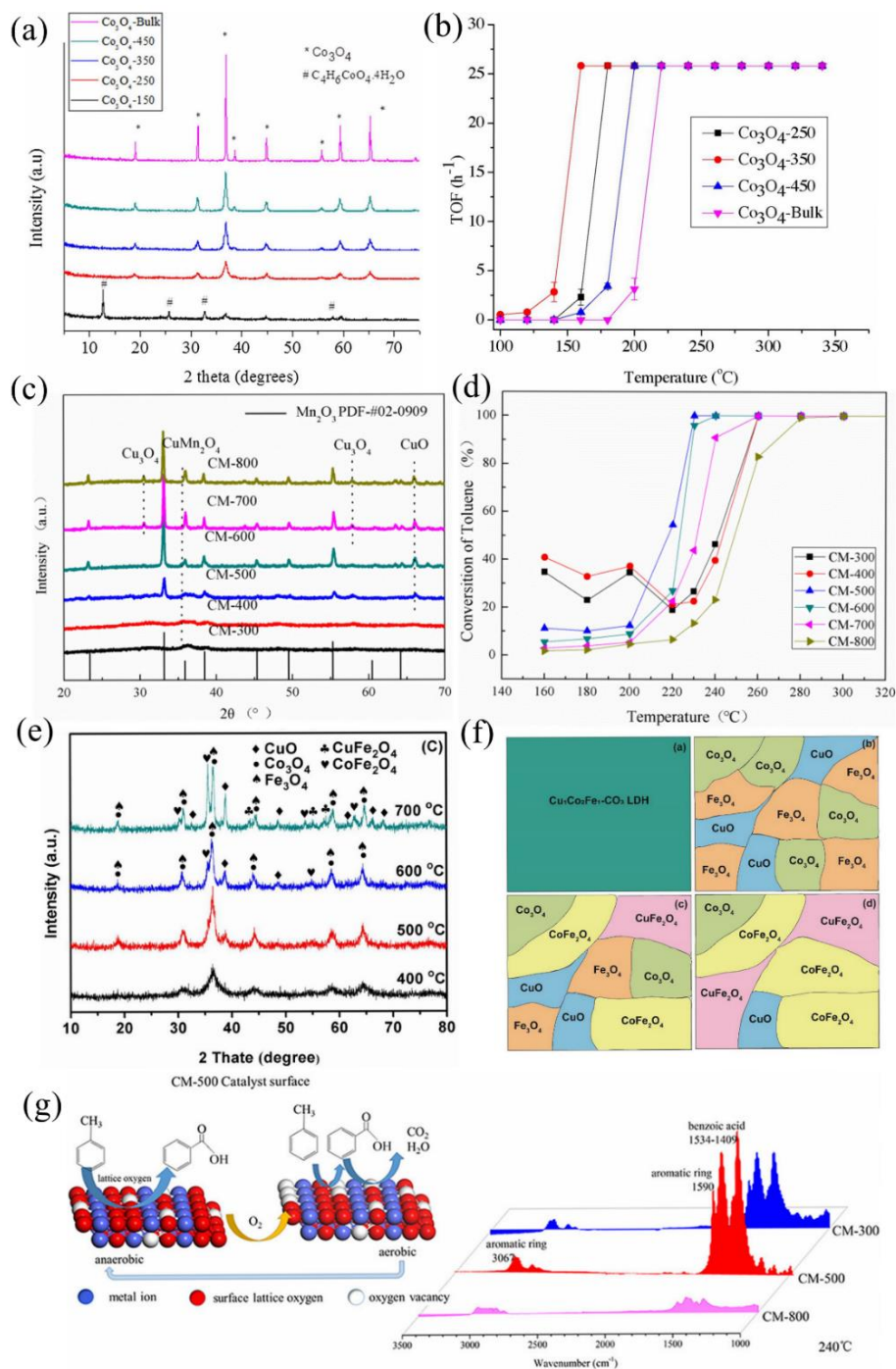
Fig 1.5. (a) XRD patterns of various Co_3O_4 catalysts, (b) TOF conversion of 6.4 % 2-propanol in air over the Co_3O_4-based catalysts with a WHSV of 60 L g^{-1} h^{-1}. TOF = moles of 2 propanol converted per hour/moles of catalyst [72]. Copyright 2020, Elsevier; (c) XRD patterns of CuO-MnOₓ catalysts, (d) Conversion of toluene over the CuO-MnOₓ

catalysts [73]. Copyright 2019, Elsevier; (e) XRD patterns of $Cu_1Co_2Fe_1O_x$ catalysts; (f) Schematic illustration of the phase change of mixed oxides and interfaces of $Cu_1Co_2Fe_1O_x$ catalyst obtained at different calcination temperatures, (g_a) fresh $Cu_1Co_2Fe_1$-CO_3 LDH, (g_b) $Cu_1Co_2Fe_1O_x$ calcined at 400 °C, (g_c) $Cu_1Co_2Fe_1O_x$ calcined at 500 °C, and (g_d) $Cu_1Co_2Fe_1O_x$ calcined at 600 °C [54]. Copyright 2020, Elsevier; (g) Schematic diagrams of intermediate species on the surface of the catalyst based on the DRIFTS analysis [73]. Copyright 2019, Elsevier.

1.3.2 Atom substitution

Substitution of part of metal atom on single metal oxide catalysts by other metal species to reconstruct the crystal phases for the generation OVDs is one of the most feasible and effective methods to improve the catalytic performance. Recently, atom substitution was widely applied to tune the catalyst nanostructure and valence ion proportion for the enhancement of low-temperature reducibility, the increase of surface area, the improvement of lattice oxygen releasing ability, and especially the generation of more OVDs. There are two atom substitution ways, i.e., (i) replacing one of the metal atoms by another one in lattice and (ii) exchanging the atom in the interstitial sites of layered metal oxide. The atom substitution way could determine the interface state as well as the number of OVDs, thereby critically influencing the catalytic activity. It is found that either the iso- or alio-valent atom substitution could result in abundant multi-phase interfaces for OVDs in the catalysts.

1.3.2.1. Isovalent-substitution

The isovalent-substitution is a way to prepare the mixed transition metal oxide catalysts with chemically-similar elements. It is proved that this method is effective for the preparation of Mn-Co mixed oxide catalysts working at low temperatures. For example,

by using metal-organic frameworks (MOFs) as the porous precursors, Mn and Co species could be mixed at the atomic level, achieving large specific surface area, excellent thermal stability and the tunable activity [87]. Moreover, the OVDs amount could be tuned by adjusting surface elemental ratio of catalysts. It was found that Mn-Co mixed oxide with a Mn/Co molar ratio of 1 exhibited the best performance for the toluene oxidation ($T_{90\%}$ of 240 °C) since the highest valences of Mn^{4+} and Co^{3+} could be generated on the surface with the highest amount of active oxygen species. Xu *et al.* [88] interconnected the mixed Co-Mn oxide nanosheets on the surface of nickel foam via a hydrothermal process, and confirmed that the molar ratio of Mn and Co could influence the concentration of OVDs by a synergistic effect, achieving 90% of toluene oxidation at 267 °C. It is considered that OVDs could be generated during the preparation stage by the balancing of the electrophilic surface of catalyst, which also result in the adsorption of oxygen species for the performance improvement. However, by using this method, the obtained Mn-Co oxide catalyst still worked at a relatively high temperature for the toluene oxidation. In order to further decrease the VOC oxidation temperature, the interaction between Mn and Co were also investigated in our previous study [89], in which the doping of Co species (Co^{2+}) into the Mn-O lattice not only increased the amorphous phase and surface area, but also enhanced the $(Mn^{3+}+Mn^{4+})/Mn$ ratio and OVDs generation, thereby resulting in the toluene oxidation at a $T_{100\%}$ of 238 °C with excellent stability in more than 50 h. Meanwhile, doping the similar element as the Co, e.g., Cu and Ni in the periodic table, on the Mn-based oxides was also reported as a promising strategy to generate more OVDs for improving the catalytic activity. For example, Xie *et al.* [90] substituted a small amount of Mn atoms with Ni in the MnO_x catalysts by using a co-precipitation method, and found that more amorphous MnO_x phases were generated, causing more OVDs in the

24

MnNiO$_x$ catalysts. Among them, MnNi$_{0.2}$O$_x$ with the richest OVDs exhibited the highest activity with T$_{90\%}$ propene oxidation temperature at 242 °C, which was 52 °C lower than those cases using pure MnO$_x$. The isovalent-substitution method was also used to prepare the Cu-Mn mixed oxide catalyst for the VOCs oxidation [73, 91]. It was found that the existence of Cu^{2+} ↔ O^{2-} ↔ Mn^{4+} cycle effectively improved the number of OVDs on the surface of catalysts [28].

Co-based catalysts have also been applied to efficiently eliminate VOCs since the exposed crystal face could provide highly active sites and the changing of Co$_3$O$_4$ morphology could remarkably alter the activity [92]. The isovalent-substitution method can be also used to substitute the Co atom with various metal species involving Ni and Cu. For example, by using a solvothermal method for the isovalent-substitution, the obtained catalysts had a performance order for acetone oxidation of CuCo$_2$O$_4$ (T$_{90\%}$ of 183 ° C) > NiCo$_2$O$_4$ (T$_{90\%}$ of 193 ° C) > Co$_3$O$_4$ (T$_{90\%}$ of 202 ° C) [93]. Herein, it was found that the nature of substituted Cu species induced more structural distortion than Ni species for the increase of OVDs, thereby exhibiting superior catalytic activity. Although the doping of Cu into Co$_3$O$_4$ is more benefit for the formation of OVDs, the obtained Cu-Co based catalysts even with abundant OVDs sometimes exhibited unsatisfied performances, e.g., an T$_{90\%}$ of 250° C in the toluene oxidation [94] and an T$_{90\%}$ of 290° C in the benzene oxidation [95]. Meanwhile, comparing with the isovalent-substitution with Cu or Ni, the isovalent-substitution of Mn into Co$_3$O$_4$ showed a higher benzene oxidation performance, i.e., MnCo$_2$O$_4$ (T$_{90\%}$ of 238 °C) > NiCo$_2$O$_4$ (T$_{90\%}$ of 257 °C) > CuCo$_2$O$_4$ (T$_{90\%}$ of 272 °C) [96].

In recent years, various novel synthesis methods for the isovalent substitution including self-propagated flaming method for the preparation of mixed Cu-Mn oxide catalysts [97],

Pechini method (gel) for the preparation of mixed La-Fe oxide catalysts [55] and *in-situ* pyrolysis of mixed MOF precursors for the preparation of Sm-Ce oxide catalysts [27, 98] have been developed to increase the concentration of OVD. However, since the similar physicochemical properties of the mixed elements always have relatively weak interactions, the catalytic activity of the obtained mixed-isovalent metal oxide catalysts is sometimes not satisfactory. Thus, the other aliovalent-substitution is further considered for high-performance catalyst synthesis.

1.3.2.2. Aliovalent-substitution

Great efforts have been made to develop efficient catalysts with abundant OVDs using the aliovalent-substitution method, especially for the preparation of earth-abundant transition metal oxide catalysts for the low temperature VOC oxidation. For instance, it is proven that the pure MnO_x catalysts like α-, β-, γ- and δ-MnO_2, Mn_2O_3, Mn_3O_4 and OMS-2 are good for the catalytic oxidation of hydrocarbon [96]. As stated above, the mixed Cu-Mn oxide catalysts prepared by isovalent-substitution strategy could adsorb and oxidate hydrocarbons effectively by tunning the OVDs. However, it should be noted that the precursors of MnO_4^- and Cu^{2+} (equal to the aliovalent-substitution) rather than Mn^{2+} and Cu^{2+} (equal to the isovalent-substitution) during the catalyst synthesis could play an important role for the high performance. Herein, the K^+ from $KMnO_4$ in interstitial sites could be exchanged with the Cu^{2+}, leading to the generation of OVDs as illustrated in Fig. 1.6a [30]. As such, the Mn-Cu oxides with abundant OVDs exhibited the higher catalytic activity (Fig. 1.6b), and by controlling the Cu species content, the concentration of OVDs (relating to Mn^{3+}) was effectively tuned (Fig. 1.6c). Remarkably, the Cu-Mn oxide catalyst using the precursors of MnO_4^- and Cu^{2+} resulted in lower toluene oxidation temperature ($T_{50\%}$ =200 °C and $T_{100\%}$ =220 °C) than the Cu-Mn oxide catalyst prepared

26

by using Mn^{2+} and Cu^{2+} precursors ($T_{50\%}$ = 295 °C and $T_{100\%}$ = 350 °C) [91]. Therefore, the strong oxidization ability of MnO_4^- promoted the reducibility of catalysts. Meanwhile, the special morphology of obtained Cu-Mn oxide catalysts provided special phase interface, which also influenced the catalytic performance. The effect of morphologies including layered, rod, and particle structure of Cu-Mn oxide catalysts on the catalytic activity for the benzene, toluene and o-xylene oxidation was studied by Guo *et al.* [28]. It is found that by controlling the molar ratio of MnO_4^-, Mn^{2+}, and Cu^+, Cu-Mn oxide catalysts with the different morphologies as well as different concentrations of OVDs can be obtained. The layered Cu-Mn oxide exhibited the best catalytic activity ($T_{90\%}$ =240 °C for benzene; $T_{90\%}$ = 207 °C for toluene; $T_{90\%}$ = 227 °C for o-xylene) since it contained the highest OVDs. Herein, the characterization results indicated that the interaction in the $Cu^{2+} \leftrightarrow O^{2-} \leftrightarrow Mn^{4+}$ on the phase interface between Cu and Mn species was facilitated, which promoted the generation of abundant OVDs, thereby greatly improving the reducibility at low temperatures.

Similarly, for the Fe-Mn oxide catalysts prepared by the aliovalent-substitution strategy, e.g., $Mn_{3-x}Fe_xO_4$ by using $Fe(NO_3)_3$ and $Mn(CH_3COO)_2$ precursors, it achieved a $T_{100\%}$ for the toluene oxidation at 250 °C [29]. In comparison, for the Fe-Mn oxide catalysts prepared using $Fe(NO_3)_3$ and $KMnO_4$ as the precursors, the 100% toluene oxidation was achieved at 160 ˚C under the same condition [99]. Based on the XRD analysis (Fig. 1.7a), in this case, the substitution Mn atom in the MnO_2 lattice with Fe led to the decrease in the crystallinity, which should be benefit for the generation of OVDs on the amorphous region and/or the interface of crystal and amorphous phases. Herein, the MnO_4^- as the source of Mn species instead of Mn^{2+} effectively improve the generation of OVDs. While, by using the aliovalent-substitution strategy, the substitution of Mn

27

atom in the MnO_2 with Ce also promoted the 90% toluene conversion from 267 ˚C (MnO_2) to 239 ˚C (3Mn1Ce) owing to the excellent oxygen-storage/mobility ability of Ce species and the abundant OVDs on the surface of catalyst [100]. As shown in Figs. 1.7b and c, the 3Mn1Ce possessed lower crystallinity and more OVDs than the pure MnO_2 and CeO_2, and as such, the existence of amorphous phase can also promote the reducibility of catalysts, thereby resulting in the efficient VOCs oxidation.
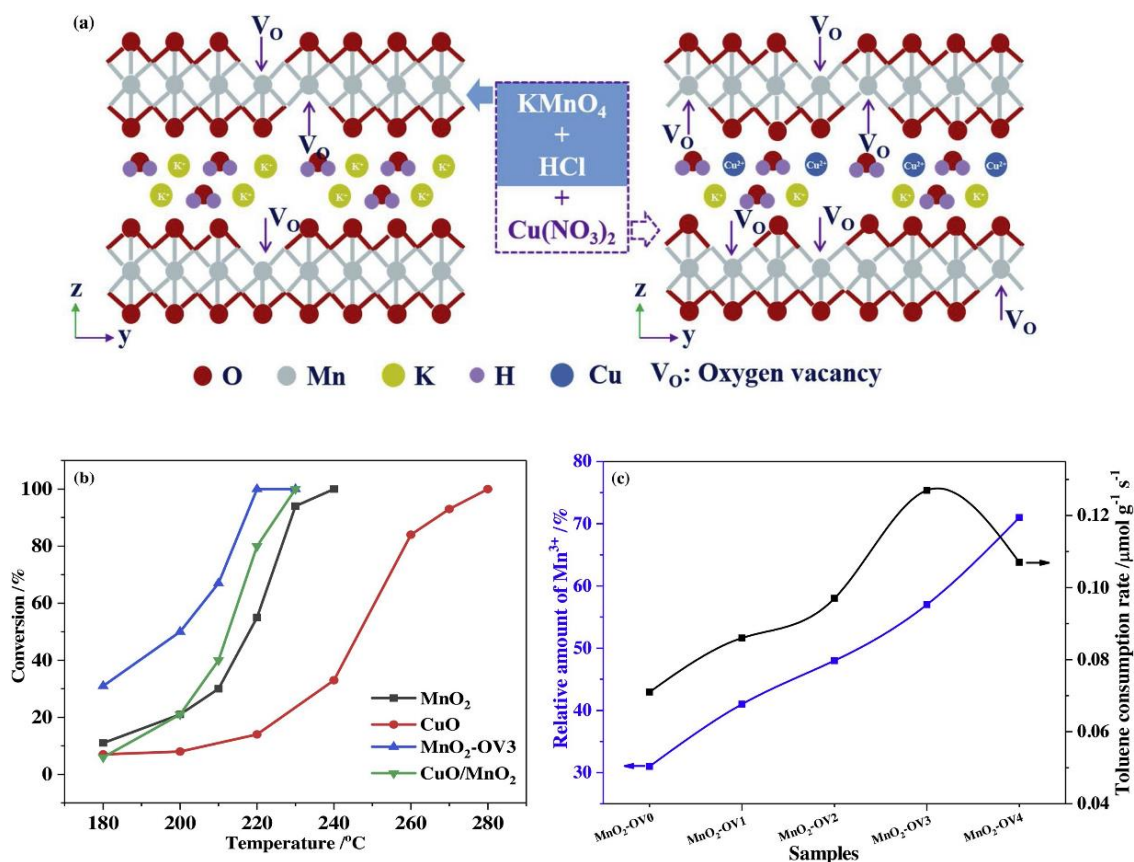
Fig 1.6. (a) Schematic explanation of doping mechanism over birnessite-type MnO_2 catalyst, (b) Activity profile of the MnO_2-OVD, MnO_2, CuO and CuO/MnO_2 catalysts, and (c) Relationship of OVD concentration and toluene consumption rate over all catalysts [30]. Copyright 2020, Elsevier.

Cryptomelane-type MnO_x (i.e., octahedral molecular sieve, OMS-2) prepared by the redox reaction between MnO_4^- and Mn^{2+} also showed relatively lower hydrocarbon

oxidation temperature owing to its unique 1D tunnel structure, mixed valences (Mn^{2+}, Mn^{3+}, and Mn^{4+}), easy mobility of lattice oxygen and rich acidic sites. Herein, by using the aliovalent-substitution strategy, the ion exchange ability of K^+ in the tunnel with a size of 0.46 nm × 0.46 nm in the OMS-2 could modulate the concentration of OVDs. Those metal ions (e.g., +1, +2 and even +3 valence metal species) can enter the inside of tunnel structure to exchange with the K^+ so that the tunnel becomes distorted, thereby changing the concentration and distribution of OVDs. Ma *et al*. [101] examined the catalytic oxidation of benzene over a series of Ag^+ incorporated OMS-2, and found that the best catalysts achieved the 90% conversion at 230 ˚C (70 ˚C lower than OMS-2). Herein, the incorporation of Ag^+ into the K-OMS-2 (Mn/Ag=40:1) can not only significantly improve the reducibility of catalysts, but also decrease the crystalline size to generate more OVDs, resulting in excellent performance and tolerance. Meanwhile, compared with the case by Li substitution, it was found that the substitution by Cs with larger size in OMS-2 not only preserved the chemical composition and textural properties but also improved the number of OVDs [102]. As a result, Cs-OMS-2 had the higher activity for ethyl acetate oxidation ($T_{90\%}$ of 195 °C, 10 °C and 20 °C lower than those of Li-OMS-2 and OMS-2, respectively). In order to further investigate the difference between +1 and +2 ion substitutions, the Ag (+1) and Cu (+2) incorporated OMS-2 catalysts were used for the o-xylene oxidation. As a result, 100% conversion was achieved at 190 ˚C over the Ag-OMS-2 and 200 ˚C over Cu-OMS-2, respectively [103]. As shown in Fig. 1.7d, the XRD results showed that the peak intensity was in order of Ag-OMS-2 < Cu-OMS-2 < OMS-2, indicating that the incorporation of Ag^+ and Cu^{2+} decreased the crystallinity of catalysts for the generating of OVDs. The introduction of Ag^+ did not cause any observable changes in the porosity and surface area of OMS-2 whereas Cu^{2+}

substitution increased the surface area and pore volume (Fig. 1.7e). Combination of density functional theory (DFT) calculations, it was confirmed that the introduction of aliovalent-ions caused dramatical decrement of OVDs formation energy (E_{ov}). For example, when two Ce^{4+} ions were incorporated into the tunnel structure of OMS-2, a lower oxygen vacancy E_{ov} of 2.23 eV than that of OMS-2 (2.32 eV) was obtained due to more OVDs generated to maintain the charge balance of Ce species, and therefore favoring the 90% benzene oxidation at 210 °C [104]. While, the doped of low content of La species (4 wt%) also resulted in the decrease the crystallinity of mixed La-Cu-Mn oxide catalysts, which showed higher activity ($T_{90\%}$ of 255 °C) than the La-free Cu-Mn catalyst ($T_{90\%}$ of 274 °C) for the toluene oxidation [105].

Ce-based catalysts were also widely used for VOCs oxidation. For the pure CeO_2 catalyst, a broad temperature region with conversions lower than 100% usually appears for the VOC oxidation. To reduce the $T_{100\%}$, by using the aliovalent-substitution method, various metals including alkali metals, transition metal and rare-earth metal have been considered to substitute Ce atoms on the CeO_2, and the enhancement effect is generally attributed to the formation of more OVDs. For examples, Wang et $al.$ [106] prepared K-CeO_2 catalysts by in-$situ$ pyrolysis of K-Ce-MOF precursor to achieve K species embedding in the lattice of CeO_2 for the o-xylene oxidation, and found that the mismatching led to the generation of defect sites, particularly OVDs. As a result, o-xylene could be 100% oxidated at 210 ˚C. As illustrated in Figs. 1.8a and b, Cu species can be also doped into Ce-MOF to achieve the atom-level mixing in the final product by in-$situ$ pyrolysis of bimetallic Cu-Ce-MOF precursor. The abundant OVDs generated owing to Cu^{2+} and Ce^{4+} resulted in a noticeable promotion in the toluene oxidation ($T_{90\%}$ =186 ˚C for the $CeCuO_x$ $vs.$ 275 ˚C for the pure CeO_2) [107]. Based on the fact that the substitution

of second cation in the CeO_2 would improve the catalytic activity, the ternary oxide was further designed for the VOC oxidation. For example, Cu-Mn-Ce ternary oxide catalysts were synthesized for the combining of the advantages of Mn, Ce, and Cu species. It is found more OVDs can be created on the interfaces of different species, which can improve the oxygen mobility and reducibility at low temperature, resulting a $T_{100\%}$ of 230 °C for the toluene oxidation [108]. Meanwhile, the similar ternary Co-Mn-Ce oxides were also synthesized for benzene oxidation, in which the incorporation of Co into Mn-Ce solid solution resulted in a high amount of Ce^{3+} with charge imbalance. As a result, abundant OVDs as the unsaturated structure appeared on catalyst, which exhibited a $T_{100\%}$ of 275 ˚C [109]. A series of rare earth elements (e.g., Y, Eu, Ho, Sm) were also selected to generate OVDs in the mixed Cu-Ce oxide based catalysts by using the aliovalent-substitution. It was found that the catalytic activity of toluene oxidation was in the order of $CuHoCeO_x$ ($T_{90\%}$=224 ˚C) < $CuEuCeO_x$ ($T_{90\%}$ = 228 ˚C) < $CuYCeO_x$ ($T_{90\%}$ = 230 ˚C) < $CuSmCeO_x$ ($T_{90\%}$ = 246 ˚C) < $CuCeO_x$ ($T_{90\%}$ = 249 ˚C) [110]. Herein, the substitution with the Ho species could change the π-bonding of CeO_2 to weaken the Ce-O bonds, leading to the generation of more OVDs with an enhanced oxygen storage capacity.

For the Co-based catalysts, the aliovalent-substitution have been also applied to increase the number of OVDs for catalytic oxidation of hydrocarbons [111]. For example, to substitute the inactive Co^{2+} on the surface of Co oxides with Ce, $Ce\text{-}Co_3O_4$ oxides with rich OVDs were synthesized by Yeung *et al.* [25]. As shown in Figs. 1.8c, d and e, the mixing of Ce and Co atoms under atomic level was also realized by using the MOF precursors. It was found that the substitution of Ce into Co_3O_4 greatly increased the number of OVDs with a decrease in the crystallinity, which achieved a 90% toluene conversion at 227 ˚C, ca. 81 ˚C lower than that of the mixed Co_3O_4 and CeO_2. More

OVDs could be also generated by decreasing the crystallinity of Co_3O_4-based catalysts by modification with other alkaline or alkaline earth metals during the aliovalent-substitution process [112]. The rare earth metal such as strontium (Sr) was also applied to modify the Ce-Co mixed oxide for the toluene oxidation. It was found that the Sr doping could generate more OVDs and as a result, the 90% toluene conversion temperature was reduced to 253 °C from 270 °C [113]. However, comparing with the CeO_2- and MnO_x-based catalysts, the Co_3O_4-based catalysts always exhibited relatively higher conversion temperature since the low efficiency of Co species for the generating of the OVDs. Therefore, how to improve the efficiency of OVDs generation on the Co_3O_4-based catalysts is still an important issue in the future studies.
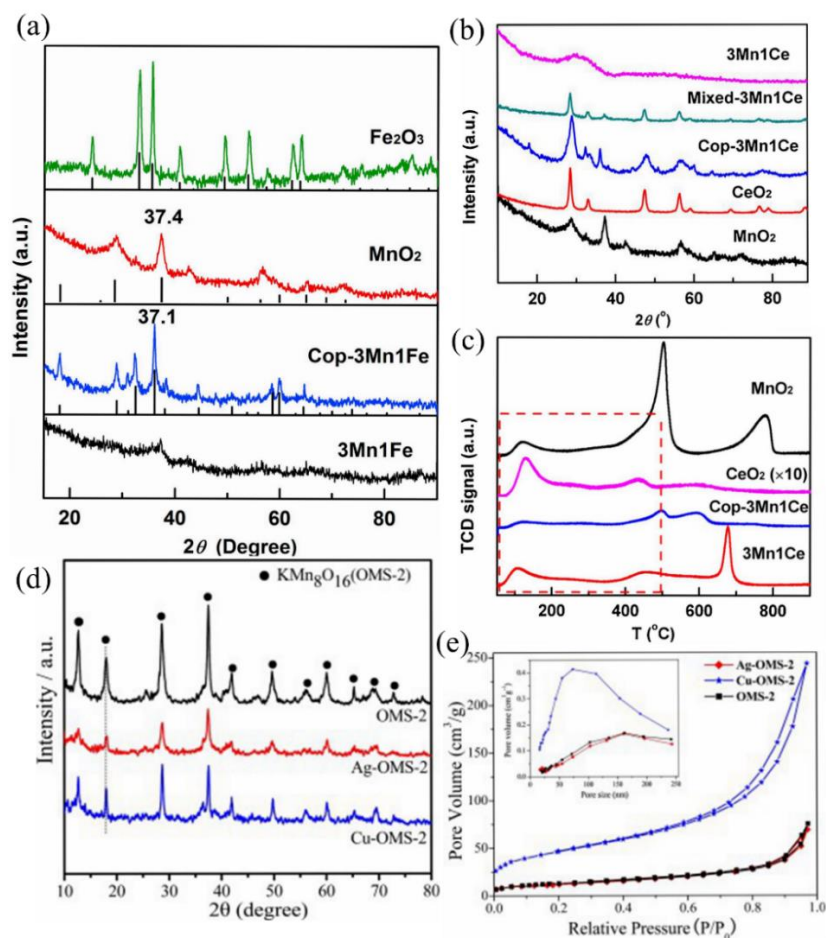
Fig 1.7. (a) XRD patterns of the Mn-Fe oxide catalysts [99]. Copyright 2017, Elsevier;

(b) XRD patterns of the Mn-Fe oxide catalysts, (c) O_2-TPD at the temperature range of 50-900 °C [100]. Copyright 2018, Elsevier; (d) X-ray diffraction patterns and (e) N_2 adsorption-desorption isotherms and pore size distribution (inset) of the catalysts [103].
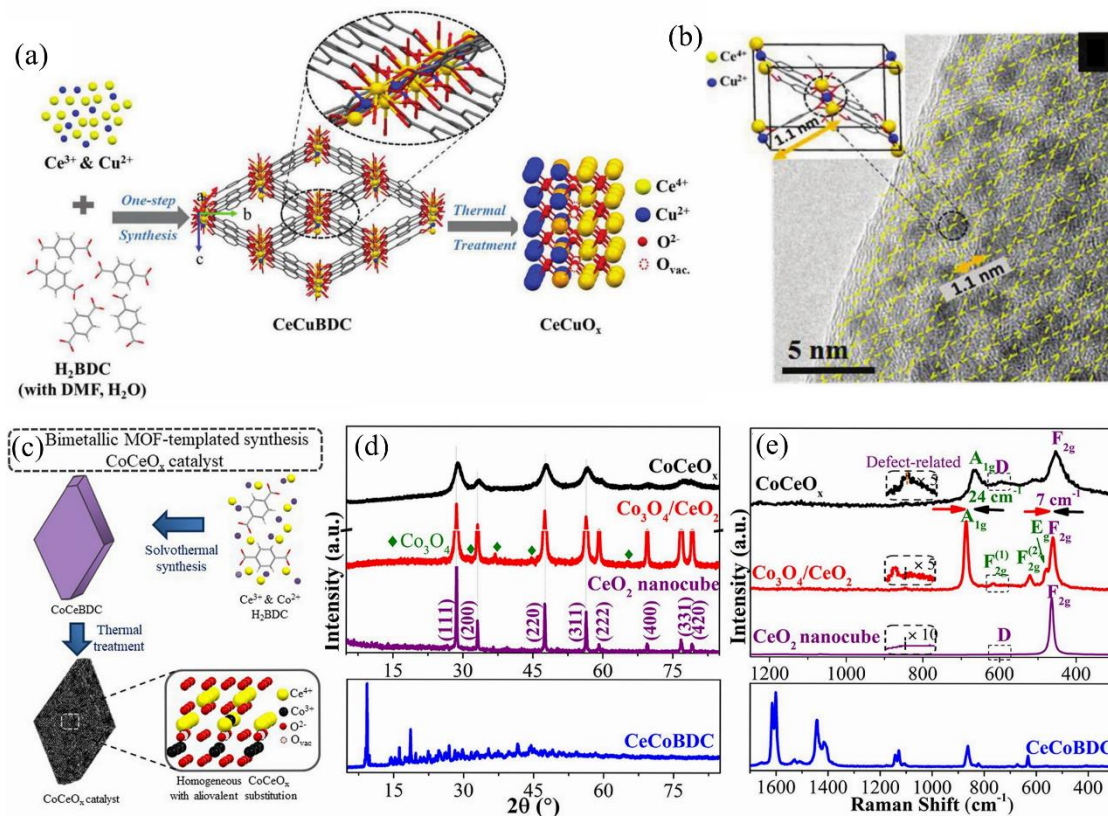
Fig 1.8. (a) Schematic diagram of the synthesis procedure of bimetallic MOF-derived $CeCuO_x$ catalyst, (b) HRTEM images of CeCuBDC MOF and (inset) schematic drawing of the unit cell [107]. Copyright 2020, Wiley; (c) Preparation procedure of CoCeBDC bimetallic MOF and its conversion to $CoCeO_x$ catalyst, (d) XRD patterns, (e) Micro-Raman spectra of CoCeBDC MOF, $CoCeO_x$, Co_3O_4/CeO_2 and CeO_2 nanocube catalysts [25]. Copyright 2020, Elsevier.

As stated above, the isovalent-substitution and the aliovalent-substitution have been extensively applied for the improving of OVDs amounts in the MnO_x-, CeO_2-, and Co_3O_4-based catalysts since the strength of metal-oxygen bond can be adjusted by the cation

substitution. The Ni, Cu, Fe, alkaline and alkaline earth metals as well as rare earth metals are commonly applied to substitute the inactive species in those catalysts for the VOCs oxidation, by which the crystallinity of the catalysts could be weakened, the reducibility strengthened, the active oxygen and OVDs increased. In contrast, the modification of metal oxide catalysts with anion-substitution was rarely reported for the VOCs oxidation. It seems to be more beneficial for the preparation of effective catalysts for the oxidation of small molecules like CO [114] and HCHO [115]. Liu *et al.* [116] gave a comprehensive review on the oxygen-site anion substitution for the metal oxide catalysts, and emphasized the effect of substituted anions on the concentration of OVDs and application. Hence, the know-how of anion-substituted metal oxide catalysts could be useful for the design and fabrication of novel catalysts for VOC oxidation with rich OVDs in the future.

1.3.3 Surface modification

Surface modification by doping of noble metal or metal oxide on the surface of catalyst is another effective way to increase the concentration of OVDs on the parent catalysts. Herein, the catalytic activity of surface modified catalysts highly depends on the nature of modifying species, the precursor type of modifying species, the parent catalyst properties, the modifying process and so on. In general, the parent catalysts with large surface area should be beneficial for the surface modification and the modifying species should have small size for the good dispersion. However, the performance of such catalysts could be negatively affected by the sintering of modifying species.

1.3.3.1 Noble metal doping

In spite of the high cost, easy to sintering and irreversible deactivation, a series of noble metal modified catalysts with high dispersion are recognized as the ideal candidates for VOCs oxidation due to their excellently catalytic performance at low temperatures. The

noble metal is usually doped either on the transition metal oxides such as MnO_x-, Co_3O_4-, and CeO_2-based catalysts with high activity for the VOCs oxidation or those materials such as Al_2O_3, Cr_2O_3, ZrO_2, TiO_2 and $CaCO_3$ with low or no activity for the VOCs oxidation. The former ones with various morphologies commonly show good catalytic activity for the VOC oxidation even without noble metal doping, however, their performances could be limited by the relatively low specific surface area (lower than 100 m^2/g) [92, 117, 118]. In contrast, the latter ones generally have large surface area (e.g., $S_{Al_2O_3}$= 214 m^2/g [119]; S_{TiO_2}= 126 m^2/g [120]; S_{ZrO_2}= 193 m^2/g [121]) and excellent thermal stability, but their performances are always lower than the former ones.

Pt nanoparticles can be applied to decorate the VOC oxidation catalysts. For example, when α-, β-, γ-, and hollow (H-) MnO_2 were decorated by Pt nanoparticles and applied for the toluene oxidation, it was found that only a little amount of Pt loading (0.39 wt% Pt) on them, the $T_{90\%}$ could be reduced to lower than 200 °C with an order of Pt/α-MnO_2 (170 °C) < Pt/H-MnO_2 (180 °C) < Pt/β-MnO_2 (185 °C) < Pt/γ-MnO_2 (190 °C) [122]. Herein, the difference in the modifying metal, i.e., Pt, and the various parent MnO_2 was observed due to the weakening of the lattice oxygen species after the doping of Pt, which was consider to play an important role in tailoring the Pt-MnO_2 property with the generation of more Mn^{4+}, O_{ads} and OVDs in the catalysts. However, the effect of K^+ on the MnO_2 structure was always ignored although all these kinds of MnO_2 were prepared using $KMnO_4$. To consider this issue, Kotarba *et al.* [123] prepared a series of noble metals (i.e., Ag, Au, and Pt) modified MnO_x in the presence of different alkali cations (Li, Na, K, or Rb), and found that K^+ played more promising role for intercalating into MnO_x since the introduction of K^+ needed the lowest ionization energy with the most thermal stability. As a result, the Pt doped K-MnO_x exhibited a $T_{90\%}$ of ~350 °C for propane

oxidation. Dai *et al.* [124] doped Au-, Pd-, and Au-Pd alloy on Mn_2O_3 respectively and applied for the toluene combustion, and found that the Au-Pd alloy doped Mn_2O_3 ($3.8AuPd_{1.92}/Mn_2O_3$) exhibited the most excellent performance with a $T_{90\%}$ of 162 °C. Herein, the strong electron-donating ability of alloy Au-Pd nanoparticles and the strong interaction between the Au-Pd alloy and Mn_2O_3 was considered to promote the generation of OVDs obviously, thereby resulting in easier activation of molecular oxygen. However, 60 h durability test indicated that this catalyst was unstable due to the adsorption H_2O and CO_2 and nanoparticle sintering. In order to improve the catalytic stability, Dai *et al.* [125] prepared Pt-embedded Mn_2O_3 with an *in-situ* metal-embedding method, in which the Pt nanoparticle was partially embedded into Mn_2O_3 framework to further improve the metal-support interaction via the cycling conversion of $Pt^0 + Mn^{3+} \rightleftharpoons Pt^{\delta+} + Mn^{2+}$, thereby increasing the concentration of OVDs. As a result, the catalyst achieved a $T_{90\%}$ of 190 °C with excellent stability.

Noble metal can be also doped on Co_3O_4 to prepare VOCs oxidation catalyst with high performance. Herein, it should be noted that the physicochemical properties of noble metal doped Co_3O_4 catalysts are strongly determined by the synthesis route. For example, the Pt/Co_3O_4 catalysts with a Pt loading amount of 3.5 wt% prepared by using a galvanic displacement method exhibited a lowest $T_{90\%}$ of 150 °C for toluene oxidation, which is superior to the same catalysts prepared by a nanoparticle loading method ($T_{90\%} = 207$ °C) and by an incipient-wetness impregnation way ($T_{90\%} = 228$ °C) [126]. As shown in Fig. 1.9a, the Pt/Co_3O_4 catalysts prepared by *in situ* growth of Pt nanoparticle on Co_3O_4 not only increased the oxygen-deficient sites (OVDs) but also improved the stability of Pt species, leading to outstanding activity and stability (100 h durability test without catalytic activity loss). Similarly, Au can be also doped on Co_3O_4 to prepare high-

performance VOC oxidation catalysts. It was found that the strong metal-support interaction between Au^0 and Co^{3+} via the cycle of $Au^0 + Co^{3+} \rightleftharpoons Au^{\delta+} + Co^{2+}$ could greatly increase the number of OVDs in the catalysts. For example, when Au was doped on Co_3O_4 (6.5 wt% Au/Co_3O_4) showed the $T_{90\%}$ values of 138, 162 and 189 °C for the catalytic oxidations of toluene, o-xylene and benzene, respectively [127]. Besides, the highly active and stable Co_3O_4-based catalysts, such as Pd/CoO [128], alloy $Au-Pd/Co_3O_4$ [129], and Ru/Co_3O_4 [130] also exhibited high performances for the VOC oxidation. It is also found that the strong noble metal-Co_3O_4 interaction can effectively tune the concentration of OVDs in the catalysts, thereby improving the catalytic activity for the VOC combustion.

As stated above, CeO_2 has outstanding oxygen storage capacity, low-temperature reducibility, and abundant oxygen species, which is always considered for the application in the VOC oxidation. Especially, its morphology can be controllably tuned. Noble metal could be doped on CeO_2 catalysts with different morphologies. For example, Pt nanoparticles have been immobilized on CeO_2 particles with different shapes, i.e., nanorods (CeO_2-r), nanoparticles (CeO_2-p), and nanocubes (CeO_2-c), respectively [131], and found that the Pt/CeO_2-r showed a lower $T_{90\%}$ of 150 °C than the Pt/CeO_2-p ($T_{90\%} =$ 175 °C) and the Pt/CeO_2-c ($T_{90\%} = 190$ °C) for toluene oxidation since the Pt doped on CeO_2 nanorods with (110) plane exposed a highest concentration of OVDs (Fig. 1.9b), following the order of crystalline Pt/CeO_2-r < Pt/CeO_2-p < Pt/CeO_2-c (Fig. 1.9c). Meanwhile, it is reported that the size and distribution of Pt nanoparticles on the CeO_2 catalysts could greatly affect the catalytic activity for VOCs oxidation [132, 133]. Other noble metals could be also doped on CeO_2 for VOCs oxidation. For example, a Pd/CeO_2 catalyst with a three-dimensionally ordered mesoporous (3DOM) structure showed

excellent performance for benzene oxidation with a $T_{90\%}$ as low as 160 °C. Herein, it was observed that the Pd^0 species on the surface of CeO_2 as the catalytic sites had no deactivation even after 150 h on-stream reaction at 190 °C [134]. Moreover, after measuring the catalytic activities with different Pd doping amounts in parallel, it is considered that the Pd loading amount should be lower than 1.0 wt% in order to balance the cost and efficiency. Aboukaïs *et al.* [135] prepared 3.5 wt% Au/CeO_2 with two different methods, i.e., impregnation and deposition-precipitation methods, for propylene and toluene oxidation, and found that the deposition-precipitation method was more suitable for the Au loading and as a result, $T_{propylene\ 90\%}$ of 200 °C and $T_{toluene\ 90\%}$ of 250 °C were achieved. Considering the existence of narrow f-band in CeO_2 and its ability for the OVDs generation, Au nanoparticles doped CeO_2 should be a good VOC oxidation catalyst [136]. In addition, during the Au/CeO_2 catalyst preparation, it should consider some important issues such as poor thermal stability caused by the structure collapse due to oxidation-reduction process [137].

Compared with MnO_x, Co_3O_4 and CeO_2 with relatively high activity for VOCs oxidation, some metal oxides such as Al_2O_3, ZrO_2 and Cr_2O_3 are hardly to be oxidized/reduced, thereby the number of OVDs are comparatively low on them. Although VOC molecules are difficult to be oxidized by oxygen species on the Al_2O_3, the toluene oxidation over 0.5 wt% Pt loaded Al_2O_3 still achieved an $T_{90\%}$ as low as 178 °C, near the value based on 0.5 wt% Pt/CeO_2 ($T_{90\%}$ of 175 °C) but even lower than that based on 0.5 wt% Pt/Co_3O_4 ($T_{90\%}$ of 190 °C) [119]. Therefore, the large surface area of Al_2O_3 should play an important role for the well dispersion of Pt nanoparticles, and the interfaces between Pt and Al_2O_3 could provide abundant OVDs for the VOCs oxidation due to the strong Pt-Al_2O_3 interactions. To increase the surface area and promote the dispersion of

noble metal nanoparticles, various MOFs were used as the precursor to prepare the catalysts for the VOC oxidation. For example, Chen *et al*. [138] prepared mesoporous Cr_2O_3 from Cr-MOF precursor and further modified it by Pt nanoparticles, in which the Pt nanoparticles with an average size of 2.3 nm were immobilized in the porous MOF structure, providing many advantages such as controlling Pt nanoparticle size in the limited tunnel space, avoiding them agglomeration, achieving high dispersity with high surface area. As a result, an $T_{90\%}$ as low as 144 °C for the toluene oxidation was achieved. Besides, the Pd/ZrO_2 [139], Pd-Al-doped TiO_2 [140], and Pt/$CaCO_3$ [141] have been also prepared for the VOCs oxidation. However, it should be noted that the performances of such catalysts are determined by the utilization efficiency of noble metal. That is, the nature, dispersity and particle size of the loaded noble metal mainly determine the final catalytic performance. In addition, considering the cost and efficiency for VOC oxidation, the noble metal loading amount should as low as possible.
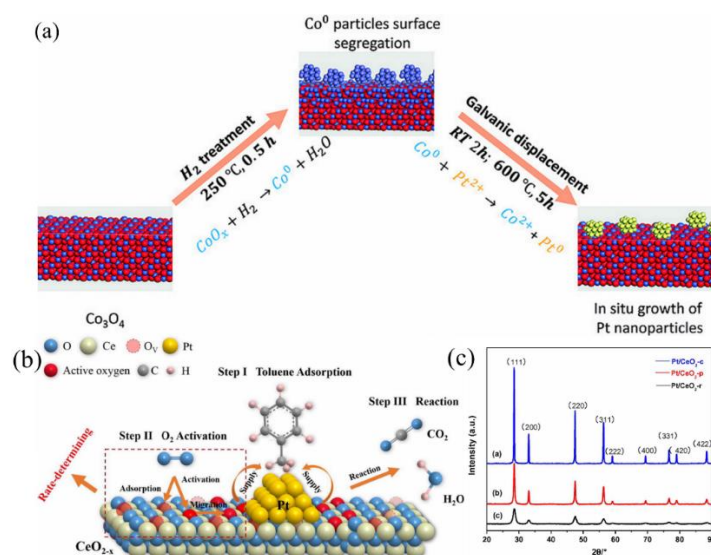
Fig 1.9. (a) Synthetic process based on galvanic displacement reaction [126]. Copyright 2019, Wiley; (b) Reaction mechanism of toluene oxidation over Pt/CeO_2 catalysts. (c) XRD patterns of various Pt/CeO_2 catalysts with well-defined facets [131]. Copyright

2016, Elsevier.

1.3.3.2 Transition metal oxide doping

Besides surface modification by the noble metal, transition metal oxides modification is also an effective strategy to decrease the VOCs oxidation temperature. In this case, the inherent synergistic effect between the doped metal oxide and the parent metal oxide should be beneficial for the generation of more OVDs, thereby improving the catalytic activity at low temperatures.

As stated above, CeO_2 with various morphologies is widely used as one of VOCs oxidation catalysts. Other transition metal oxides could be selected to dope it and improve the performance. For example, when 1 wt% of CoO_x was doped on CeO_2 nanoparticles (CoCe-P), nanocubes (CoCe-C) and nanorods (CoCe-R) separately, it was found that CoO_x can be highly dispersed on the exposed (111) plane of CeO_2-P, which dramatically improved the catalytic activity, achieving an $T_{90\%}$ of 230 °C for toluene oxidation, lower than those of CoCe-R ($T_{90\%}$ of 260 °C) and CoCe-C ($T_{90\%}$ of 320 °C) [142]. Herein, more OVDs were generated on CoCe-P owning to the stronger interaction of Ce and Co species on the (111) plane interface. Meanwhile, the modification of MnO_x on the surface of CeO_2 by an impregnation method was also applied to tune the concentration of OVDs for the enhancement of activity for the ethyl acetate oxidation [14]. As shown in Fig. 1.10a, the peak intensities of CeO_2-s and MnO_x-CeO_2-s (s stand for CeO_2 prepared by the pyrolysis of Ce-MOF precursor) were obviously broadened and weaken in contrast to those of CeO_2-h and MnO_x-CeO_2-h (h stand for CeO_2 prepared by the hydrothermal method). As a result, the activity of catalysts with low crystallinity was higher than those catalysts with high crystallinity with an $T_{90\%}$ of 200 °C (MnO_x-CeO_2-s) and an $T_{90\%}$ of 275 °C (CeO_2-s) (Fig. 1.10b). It was considered that the formation of more amorphous phase could more

significantly distorted the lattice structure and more easily generate OVDs, thereby promoting the catalytic activity. In this case, a L-H mechanism was proposed as depicted in Fig. 1.10c, in which the OVDs were considered to play a critical role in conversion of the interstitial intermediates during the oxidation process. However, it should be noted that not all interfaces are effective for creating the OVDs. For example, Konsolakis et al. [143] prepared a series of 15 wt% CuO modified $Ce_{1-x}Sm_{\chi}O_{\delta}$ mixed oxides with different amount Sm species for ethyl acetate oxidation, and found that 15 wt% CuO decorated CeO_2 catalyst (without Sm species) had the highest activity ($T_{100\%}$ of 250 °C) among all catalysts due to no occupying of Sm on the oxygen sites.

Li et al. [144] synthesized $Mn_2O_3@MnO_2$ catalysts with heterostructure interfaces, and found that the interface-related rebuilding effect in the process of $H^+/KMnO_4$ treatment resulted in the generation of abundant OVDs (Fig. 1.10d), achieving $T_{90\%}$ for toluene oxidation at 250 °C (30 °C lower than that using Mn_2O_3).
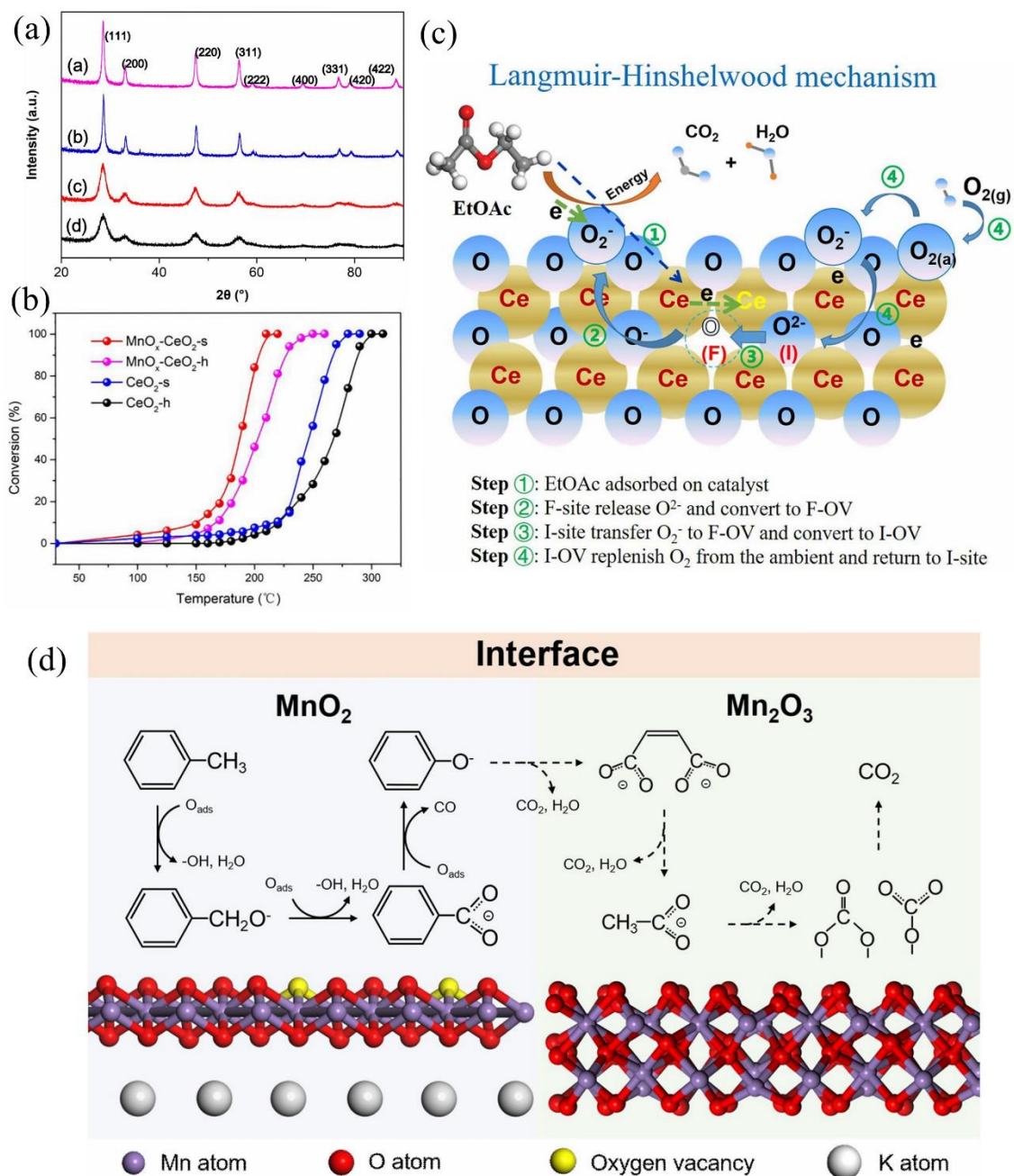
Fig 1.10. (a) XRD patterns of (a_a) CeO₂-h, (a_b) MnOₓ-CeO₂-h, (a_c) CeO₂-s, and (a_d) MnOₓ-CeO₂-s, (b) Conversion of ethyl acetate over all catalysts (60,000 mL g⁻¹ h⁻¹), (c) Supposed L-H mechanism for ethyl acetate catalytic oxidation reaction on cerium-based catalysts [14]. Copyright 2019, Elsevier; (d) Probable toluene oxidation mechanism at the MnO₂-Mn₂O₃ interface of T-0.5 [144]. Copyright 2020, Elsevier.

42

1.3.4 *In-situ* surface treatment

In-situ surface treatment such as acid etching and surface reduction have been also applied to prepare oxygen-deficient metal oxide catalysts for VOCs oxidation.

1.3.4.1 Chemical etching

Chemical etching is generally performed by controlling the concentration of acidic or alkaline solution and/or etching time. It can improve the number of OVDs but it should have no perceptible effect on the textural properties of parent catalysts. This method has been successfully applied for the treatment of the MnO_x-based catalysts to achieve the disproportionation of Mn^{3+} species in acidic media for creating more OVDs [145, 146]. For instance, the Mn_2O_3 catalysts leached by low concentration H_2SO_4 achieved an $T_{90\%}$ of 235 °C, 13 °C lower than the parent one [147]. It is considered that the acid etching can induce the exposure of the various defective surfaces such as corners, vertexes, edges and steps with high energy to form the OVDs. For the mixed MnO_x-CeO_2 catalysts with a Mn content above 50%, its catalytic activity could be highly improved via the acid-etching, inversely, the acid treatment had no effect on the performance when the MnO_x-CeO_2 catalysts with a Mn content below 50% [148].Thus, the efficiency of acid-etching is not so effective in some cases. Meanwhile, the acid-treated catalysts always showed lower crystallinity than the non-treated ones, and the disproportionation reaction of Mn^{3+} could more easily occur to generate the OVDs [149]. As illustrated in Figs. 1.11a and b, when the meso-γ-MnO_2 catalysts were treated by HNO_3, $T_{90\%}$ values of 219 and 237 °C for the toluene and o-xylene oxidations were achieved respectively. It was found that the crystallinity was reduced with the prolonging of acid treatment time [150]. Similarly, γ-MnO_2, $LaMnO_x$ perovskite, $SmMnO_x$ perovskite catalysts had ever been treated by HNO_3 to control the crystalline phases for VOCs removal [151-154]. By using different acids

(HNO$_3$ [155], H$_2$SO$_4$ [147], HAc [156], H$_3$PO$_4$ [157], and HF [158]) with the varying of concentration and etching time, the MnO$_x$-based catalysts were found to have different surfaces with varying crystalline phases as well as OVDs. Recently, Sun *et al*. [159] compared the catalytic activities of MnO$_2$ catalysts treated by HNO$_3$, H$_2$SO$_4$ and HAc for the dimethyl ether combustion, respectively, and found that the catalytic activities followed the order of MnO$_2$-HAc (T$_{90\%}$ of 175 °C) < MnO$_2$-HNO$_3$ (T$_{90\%}$ of 185 °C) < MnO$_2$-H$_2$SO$_4$ (T$_{90\%}$ of 200 °C) < MnO$_2$-without acid etching (T$_{90\%}$ of 235 °C), indicating that the weaker acid treatment could enhance the reducibility more effectively than the stronger acid since the weak acid could induce more Brönsted acid sites on the surface of catalysts [160, 161]. On the other hand, MnO$_x$ treated by alkali (KOH) always showed the worse catalytic activity since the acidity (Brönsted acid sites and Lewis acid sites) on the surface was decreased obviously [162]. In general, the alkaline solution can be used to etch the surface of the parent catalysts for easier loading of metal, but it is difficult to improve the number of OVDs on MnO$_x$ [162-164]. For the Co$_3$O$_4$-based catalysts, it seems that the acid etching cannot significantly enhance the catalytic activity [165]. To date, it can be concluded that the chemical etching is more suitable for the MnO$_x$-based catalysts treatment to increase the number of OVDs.
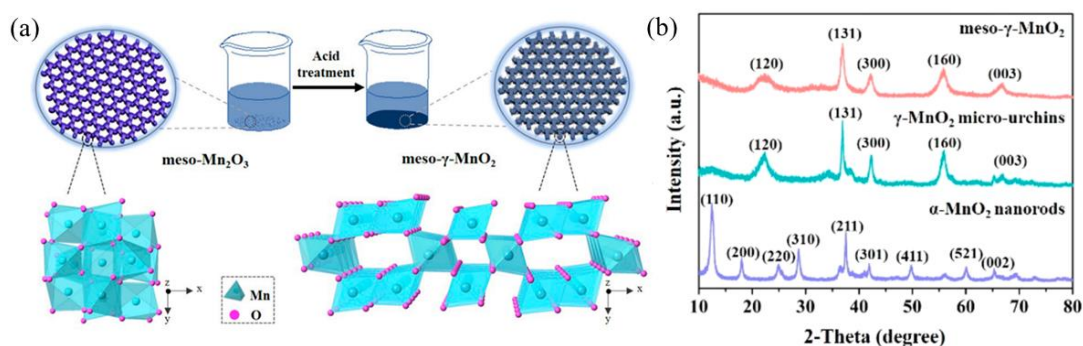
Fig 1.11. (a) Schematic illustration of transformation process from meso-Mn$_2$O$_3$ into meso-γ-MnO$_2$, (b) Wide-angle XRD patterns of the MnO$_2$ products [150]. Copyright

2019, ACS.

1.3.4.2 Surface reduction

Surface reduction has been also investigated to reduce partial atoms on the surface of oxide catalysts for creating the oxygen-deficient structure. For example, Yu *et al.* [117] reduced OMS-2 by NaBH$_4$ with different time (i.e., 0, 0.25, 0.5, 1 and 2 h), and found that the 0.5 h-treated OMS-2 exhibited the best performance of dimethyl ether combustion (T$_{90\%}$ of 230 °C) since it had the highest OVDs among all pretreated catalysts. To date, various approaches including hydrogen reduction [166-168], active metal reduction [169-171], chemical reductants [117, 172], electrochemical reduction [126, 173], high energy particle bombardment [174, 175], calcination-vacuum activation [176, 177], and arc-melting procedure [178, 179] have been applied to reduce partial atoms on the catalyst surface for creating the oxygen-deficient oxides. It should be noted that the generation of OVDs using these methods for the treatment of VOCs oxidation catalysts is rarely discussed. It is possible that the surface reduction cannot be endowed with high quality OVDs for the adsorption and oxidation of VOC molecules. However, it is still worth for further exploration in the future study.

As reviewed above, various catalyst preparation strategies have been developed to generate abundant OVDs efficiently for the improving of VOCs oxidation activity. Among those strategies, the temperature controlling and atom substitution methods represent the most promising methods for the generation of suitable OVDs amount. Compared to the temperature controlling method, the atom substitution method is more effective to significantly decrease VOC conversion temperature for the VOC oxidation over the prepared catalysts since it has the capability of precisely tailoring/introducing of OVDs under an atomic scale, affecting the intrinsic properties of catalysts. Meanwhile,

although the surface modification method could result in abundant oxygen-deficiencies on the catalysts, the durability of the catalysts is still needed to be more improved since the uniformly distributed nanoparticles on surface are easily sintered, leading to the decreasing of the number of OVDs. Thus, how to resist the agglomeration of nanoparticles is still full of challenges. For the *in-situ* surface treatment method, the treatment time is typically correlated with the amounts of OVDs. In fact, two or more above catalysts preparation strategies can be applied together for tuning the concentration of OVDs to achieve the desired activity for the VOCs oxidation.

For the various metal oxide based catalysts, no matter which method was used, the OVDs seems to be easily generated on the MnO_x-based catalysts, illustrating that the Mn species is endowed with high quality of OVDs for the VOC adsorption and oxidation. However, it should be noted that Mn-based catalysts can be only extensively applied for hydrocarbons or oxygenated VOCs oxidation, and they are always deactivated by S-containing halocarbons in the system due to the formation of manganese sulfate [180].

1.4 Characterization ways to detect the existence of oxygen vacancy defects

The OVDs have been confirmed to have positive effect on the catalytic activity. To more understand the formation and function of OVDs, the identified and powerful analysis technique is extremely necessary, which could promote further researches on the catalysis mechanism relating to the OVDs. To date, the formation and relative amount of OVDs can be characterized using different existing techniques including high-resolution transmission electron microscopy (HRTEM), Scanning tunneling microscopy (STM), X-ray photoelectron spectroscopy (XPS), Raman, Electron paramagnetic resonance (EPR), Positron annihilation lifetime spectroscopy (PALS), X-ray Absorption Fine Structure (XAFS), and electron energy-loss spectroscopy (EELS).

1.4.1 HRTEM analysis

Defects always cause the appearance of modulated dark stripes on the HRTEM image. HRTEM analysis should be one way to detect the existence of the OVDs-related nanostructures on the catalysts for discussion of underlying catalysis mechanism corresponding to OVDs. As shown in Figs. 1.4a-c, various nanostructures relating to the defects can be observed on mixed phase interfacial structure in the HRTEM images of the different MnO_x catalysts [68]. In our recent work, the defect structure was also observed on the HRTEM images of Co-doped MnO_x catalysts with low crystallinity (Fig. 1.12a) [89]. To date, HRTEM have been also applied to verify the existence of OVDs in other metal oxides such as $MnCo_2O_4$ [181], TiO_2 [182], $BiFeO_3$ [183], and MoO_3 [184].
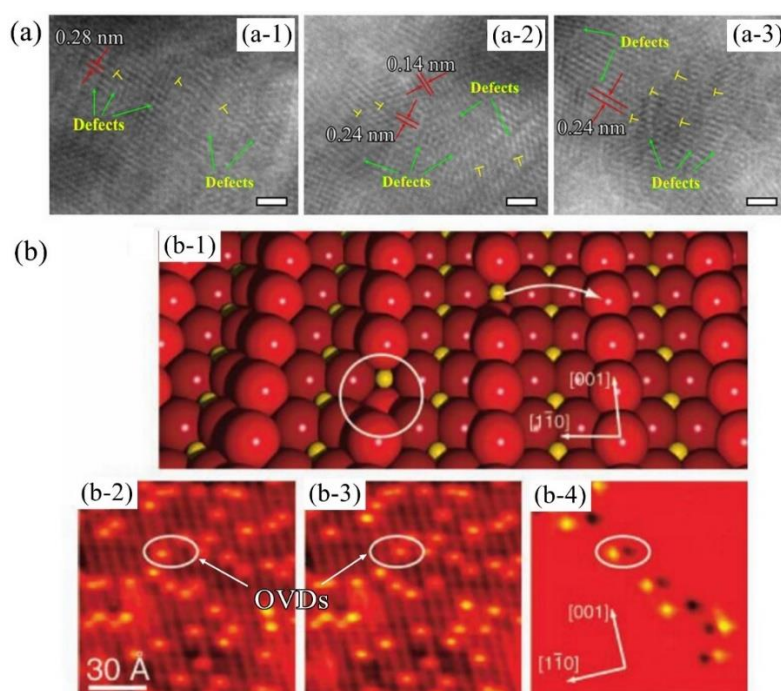
Fig 1.12. (a) HRTEM images of the Mn_xCo_y mixed oxide catalyst with abundant OVDs [89]. Copyright 2021, Elsevier; (b-1) Ball model of the TiO_2 (110) surface, (b-2 and b-3) Two consecutive STM images, (b-4) Difference STM image. A bridging O vacancy is marked by a circle and dark depressions indicate the vacancy positions [189]. Copyright

2003, Science.

1.4.2 STM analysis

The more detail information of electronic structure around the OVDs can be detected by using STM technique [185]. When we use this technique for the study of OVDs, the following points should be taken into considerations: (i) Only the local area of the catalysts can be observed; (2) Only the sample with a very thin thickness allowing the beam electrons transmitting can be analyzed; (3) Only the environment with extremely clean, stable, excellent vibration isolation, and sophisticated electronics is allowed [186]. As shown in Fig. 1.12b, the short and bright points centered on dark rows with the interface connected with neighboring bright rows indicated the OVDs in TiO_2 (110) [187-189]. Shaikhutdinov et $al.$ [190] also used STEM to study the OVDs derived from the growth of Ru on the surface of CeO_2.

1.4.3 XPS analysis

XPS is a general way to examine the composition oxidation degree on the superficial layer of as-synthesized catalysts, which can be used to qualify the degree of the OVDs. For example, the ratio of Ce^{3+} can be applied to estimate the concentration of OVDs on the catalyst surface since the transformation of Ce^{4+} to Ce^{3+} will cause the consumption of lattice oxygen to form the OVDs [14]. The presence of the OVD can be also confirmed via the monitoring of Co^{2+} species [191]. Qu et $al.$ [30] considered that the amount of Mn^{3+} species should be related to the amount of OVDs and a higher density of Mn^{3+} species implied a higher concentration of OVDs as described in Fig. 1.13a. Furthermore, the $quasi$-in $situ$ XPS was also conducted to characterize the changes of surface compositions. It was found that the surface Mn^{3+} species (OVDs) was monotonous during the oxidation reaction, implying that the dynamic balance of $Mn^{2+} \leftrightarrow Mn^{3+} \leftrightarrow Mn^{4+}$ could

be achieved and Mn^{4+} can be reduced to Mn^{3+} during the toluene oxidation [17].

For the Mn-Co mixed oxides, the OVDs were affirmed by the O 1s XPS spectra (Fig. 1.13b), in which the peak at 529.8 eV indexed to the lattice oxygen, the peak at 531.2 eV indicated the surface adsorbed oxygen species with low coordination such as OVDs, and the peak at 533.5 eV related to the oxygen species in the adsorbed H_2O, respectively, suggesting that the OVDs were stabilized on the adsorbed oxygen species [89]. In addition, the O 1s XPS spectrum was also used to prove the existence of OVDs in other deficient metal oxides such as $Cu_yCo_{3-y}Fe_1O_x$ [54], Co_xNiAlO [192], $CoCeO_x$ [25] and $Pd-Al/TiO_2$ [140].

1.4.4 Raman spectrum analysis

Raman spectrum can be used to verify the molecular vibration and rotations based on their native fingerprint vibrational information, and the change of vibrational level could cause the Raman peak shifting or disappearing [193]. Generally, the existence of OVDs in the catalyst sample could affect the vibrational mode, making the broader, weaker, and/or more down-shifting peak [194]. For the MnO_x-based catalysts, Li *et al.* [195] reported that the Mn-O stretching vibration should be related to the OVDs. As shown in Fig. 1.13c, the intensity of Raman peak at around 655 cm^{-1} was in the order of OMS-180 > OMS-90 > OMS-70 whereas the density of OVDs followed OMS-70 > OMS-90 > OMS-180. Herein, the much broader, weaker, and more down-shift peak should be related to the higher concentration of OVDs on the catalysts.

Compared with the visible Raman, the UV Raman has more advantages in the probing of defect sites. For example, in the UV Raman spectrum, the ratio of integral intensity (A_{600}/A_{465}) was considered to reflect the relative concentration of OVDs [61]. Furthermore, *in situ* UV Raman spectrum was used to further observe the evolution of

OVD (Figs. 1.13d and e). Herein, although the peak at 600 cm^{-1} was considered to be the MO8-type defect structure related to the defects derived from the moving of the lattice oxygen into the interstitial oxygen, the assignment was still controversial. To date, the Raman spectrum have been applied to the detection of OVDs in various defective metal oxides such as Bi_2WO_6 [196], BiO_{2-x} [197], BiOI [198], Eu/CeO_2 [199], MnO_x [200], especially, the down-shift of Raman peak is always related to the existence of OVDs.

1.4.5 EPR analysis

EPR is an effective and straightforward tool to detect and characterize the OVDs based on the electron transfer since the adsorbed O_2 on the surface is always reduced on the OVDs to form the O_2^- species. Furthermore, the EPR analysis could give the finger printing information of OVDs regardless of the sample is liquid or solid states under specific frequency, which depends on the following equation [201, 202]:

$$h\nu = g\beta B$$

where h is the Planck's constant, ν is the frequency, g is a constant, β is the Bohr magneton and B is applied magnetic field. The g value is around 2, which is the diagnostic data for OVDs. In the EPR spectrum, the symmetrical signal is attributed to unpaired electrons at the OVD sites, and the signal intensity can reflect the concentration of OVDs [13, 17, 28]. As shown in Fig. 1.13f, the MnO_x-ET exhibited a strongest signal at g = 2.004, manifesting that there were more OVDs in the lattice of MnO_x-ET [17]. However, EPR technique cannot confirm that the defects are in the bulk or on the surface of catalysts.

1.4.6 PALS analysis

PALS is a nondestructive measurement method to test the OVDs with low concentrations in the nano-scale due to the inherent ability of the positron to get trapped in low electron density [203]. In the PALS analysis, the annihilation time is recorded after

the injecting of one electron into the sample via γ ray and as such, the relative concentration of OVDs can be detected according to the positron lifetime. To date, the PALS analysis has been applied for the determination of OVDs concentration in various oxygen defective materials such as TiO_2 [204, 205], ZnO [206], Eu^{3+}, Nb^{5+}, Co^{3+} doped CeO_2 [207], MoS_2 [208], and BiO_{2-x} [209].

1.4.7 EELS analysis

From the EELS spectrum, the electronic property and the unoccupied density of states on the sample can be understood, which could be used to investigate the relative concentration of OVDs [210-212]. A comprehensive investigation on the relationship between the OVD and the Mn valence distribution in different MnO_x was performed by Peng *et al.* [23]. It was found that the intensity of O K-edge was originated from the hybridization of M 3d and O 2p levels (Figs. 1.13g and h). Herein, the weaker intensity of peak indicated the fuller filling of Mn 3d orbits and more lacking of O species in the Mn coordination shell, which could be explained by the presence of OVDs.

1.4.8 XAFS analysis

XAFS spectroscopy has been used to characterize the atomic and electronic structures in various materials regardless of solid, liquid or even gaseous samples [213, 214]. It offers a power technique to investigate the existence of OVDs. In general, the peak intensity and the distance of the neighboring coordination atoms are applied to reveal the concentration of defects. Jiang *et al.*[215] applied the XAFS technology and found that the disorder and dislocation of WO_3 lattice should be caused the absence of oxygen atoms on the specific position. Meanwhile, it was considered that the similar Mn K-edge profiles of $CaMnO_3$ and S-doped $CaMnO_3$ indicated no obvious change of framework after doping of S, nevertheless, the edge shift evidenced that the oxygen atoms around Mn

atom were reduced and the OVDs were formed (Fig. 13k) [216].
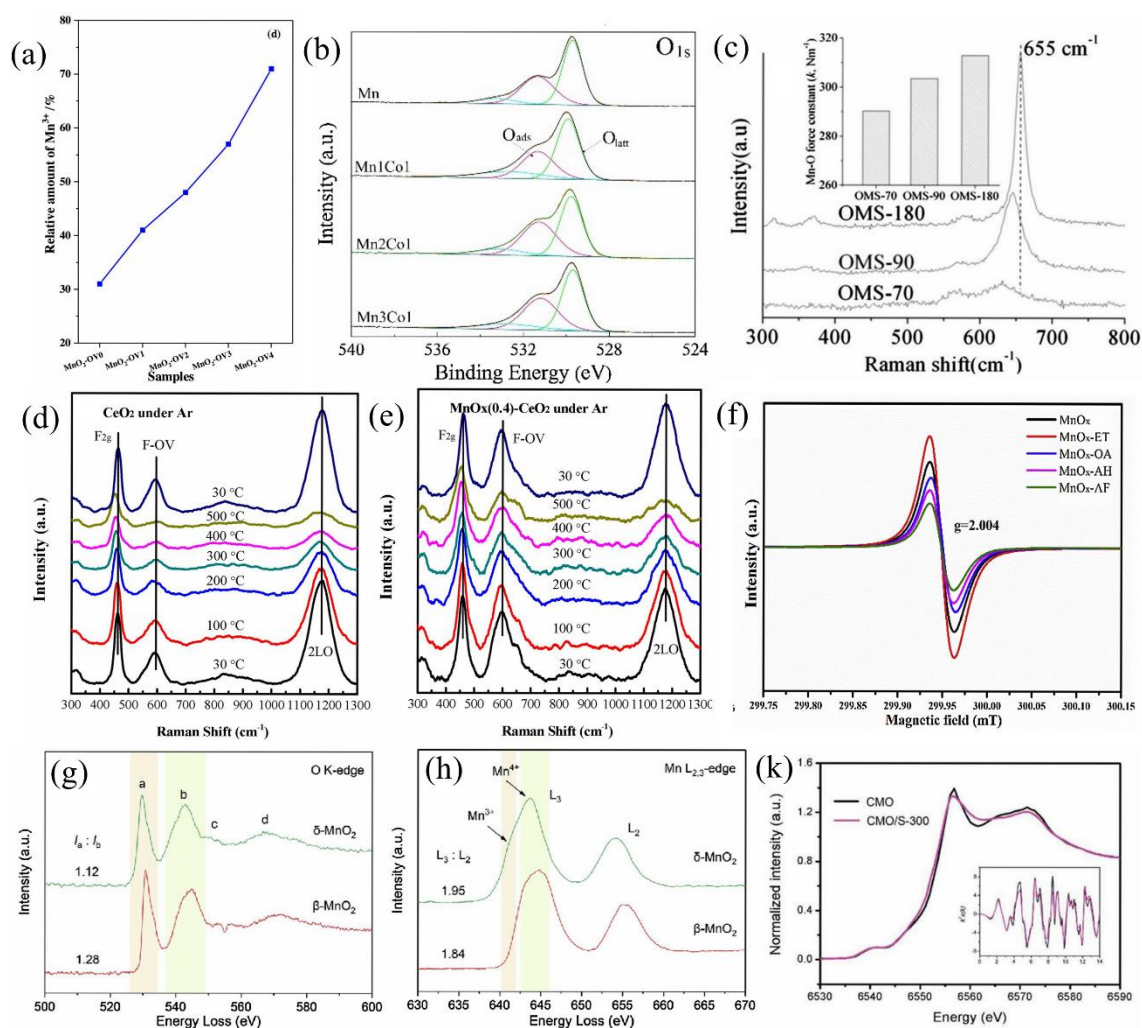
Fig 1.13. (a) XPS spectra of samples for relative amount of Mn^{3+} [30]. Copyright 2020, Elsevier; (b) XPS spectra of O 1s for the Mn-based catalysts [89]. Copyright 2021, Elsevier; (c) Raman spectra of MnO$_x$ [195]. Copyright 2020, ACS; (d-e) In situ UV Raman spectra of samples [61]. Copyright 2018, Elsevier; (f) EPR profiles of samples [17]. Copyright 2020, Elsevier; (g-h) O K-edge spectra in EELS core loss region and Mn L$_{2,3}$-edge spectra in EELS core loss region [23]. Copyright 2020, Elsevier; (k) Mn K-edge XANES curves, Mn K-edge EXAFS oscillation function (inset) [216]. Copyright 2018, Wiley.

1.4.9 Other analysis

Many other techniques such as thermogravimetric analysis (TG) [217, 218], oxygen temperature programed desorption (O_2-TPD) [112, 219] and hydrogen temperature-programmed reduction (H_2-TPR) [92, 220] have been also applied to identify the existence of OVDs. However, it is difficult to determine the concentration of OVDs by using these methods since the obtained signal includes the information of not only OVDs, but also the adsorbed oxygen species such as H_2O molecule and -OH at the specific temperature region.

1.5 Objective of this study

As reviewed above, development of high quality OVDs in catalysts is the crucial factor to increase the efficiency of VOC oxidation. Compared with the supported noble metal catalysts, the transition metal oxide catalysts have attracted extensive attentions due to their low cost, abundant resources, high stability, and good flexibility for OVDs engineering. The transition metal oxides developed in this study have low crystallinity, which can provide large surface area and abundant active oxygen species, especially OVDs, thereby resulting in excellent performance at relatively low temperature for VOC oxidation even in the presence of water vapor. Meanwhile, the energy consumption for the preparation of such catalysts is also significantly lower than those reported catalysts due to synthesis at room temperature and calcination at low temperature (350 ºC). In order to further improve the catalysts activity, the relationship between the correlating physiochemical properties and performance is explored to investigate the reaction mechanism and oxidation pathways over catalysts with amorphous phase. It is expected that the application of such catalysts with low crystallinity could open up new possibilities in catalyst production for the VOC complete oxidation. Especially, we devote to design the facile strategies for developing environmentally-friendly catalysts with

minimum chemical reagent and processing steps but maximizing the catalytic activity.

1.6 Scope of this dissertation

Chapter 1 reviews the importance and the development progress of the OVDs on the various catalysts for VOC oxidation, especially four approaches for the generation of OVDs are summarized.

Chapter 2 describes a facile agar-gel method to prepare a series of homogenous Mn-Co mixed oxides. Characterizations by XRF, XRD, N_2 adsorption-desorption, SEM, TEM, H_2-TPR, O_2-TPD, XPS measurements with density functional theory (DFT) calculations indicated that the obtained optimum Mn-Co mixed oxide had high specific surface area, large amounts of Co^{3+}, Mn^{3+}, and Mn^{4+} species, abundant OVDs, high reducibility at low temperature, and excellent O_2 adsorption ability. *In situ* DRIFTS spectra measurements confirmed the generated intermediates at different environments during the toluene oxidation and revealed that both adsorbed oxygen and lattice oxygen species could simultaneously participate in the toluene adsorption-oxidation process, especially the rate-controlling step should be the $C = C$ breakage of aromatic ring.

Chapter 3 presents the facile redox co-precipitation route for holmium (Ho)-doped octahedral molecular sieve (OMS-2) catalysts with abundant active oxygen species. The introduction of trace Ho species during the OMS-2 synthesis process resulted in not only larger surface area and more amorphous phases formation but also abundant active oxygen species, especially OVDs between amorphous and crystal phases in the final Ho-doped OMS-2 by the delamination of OMS-2. *In situ* DRIFTS analyses demonstrated that the oxidation of toluene was greatly facilitated on the 0.5% Ho-OMS-2 owing to the abundant active oxygen species on the surface, and benzyl, benzyl alcohol, benzaldehyde,

benzoate, maleic anhydride, and carbonates were the main intermediates during oxidation of toluene at relatively low temperatures.

Chapter 4 introduces a series of samarium (Sm) doped cerium oxide (x% Sm/CeO$_2$) catalysts by pyrolysis of Sm containing Ce-based metal organic framework (Sm/Ce-MOF) precursor. The obtained catalysts were characterized by SEM, TEM, XRD, BET, Raman, XPS, H$_2$-TPR, O$_2$-TPD, and their catalytic activities were evaluated by oxidation of toluene over them. The doping of Sm increased the concentration of oxygen vacancy as well as the low temperature reducibility, thereby improved the catalytic performance.

Chapter 5 gives the general conclusions of this research and discusses on the challenges and prospects for the future work.

References

[1]   H. Huang, Y. Xu, Q. Feng, D.Y.C. Leung, Catalysis Science & Technology 5 (2015) 2649-2669.

[2]   C. Yang, G. Miao, Y. Pi, Q. Xia, J. Wu, Z. Li, J. Xiao, Chemical Engineering Journal 370 (2019) 1128-1153.

[3]   L.F. Liotta, H. Wu, G. Pantaleo, A.M. Venezia, Catalysis Science & Technology 3 (2013) 3085.

[4]   L. Li, S. Liu, J. Liu, Journal of hazardous materials 192 (2011) 683-690.

[5]   F. Thevenet, L. Sivachandiran, O. Guaitella, C. Barakat, A. Rousseau, Journal of Physics D: Applied Physics 47 (2014) 224011.

[6]   L. Malhautier, G. Quijano, M. Avezac, J. Rocher, J.L. Fanlo, Chemical Engineering Journal 247 (2014) 199-204.

[7]   V. Héquet, C. Raillard, O. Debono, F. Thévenet, N. Locoge, L. Le Coq, Applied Catalysis B: Environmental 226 (2018) 473-486.

[8]   C. Jiang, H. Wang, Y. Wang, C. Xue, Z. Yang, C. Yu, H. Ji, Journal of hazardous materials 390 (2020) 122182.

[9]   A. Wang, Z. Zheng, H. Wang, Y. Chen, C. Luo, D. Liang, B. Hu, R. Qiu, K. Yan, Applied Catalysis B: Environmental 277 (2020) 119171.

[10]   X. Liang, P. Wang, Y. Gao, H. Huang, F. Tong, Q. Zhang, Z. Wang, Y. Liu, Z. Zheng, Y. Dai, B. Huang, Applied Catalysis B: Environmental 260 (2020) 118151.

[11]   C. Zhang, C. Wang, W. Zhan, Y. Guo, Y. Guo, G. Lu, A. Baylet, A. Giroir-Fendler, Applied Catalysis B: Environmental 129 (2013) 509-516.

[12]   Y. Wang, Y. Xue, C. Zhao, D. Zhao, F. Liu, K. Wang, D.D. Dionysiou, Chemical Engineering Journal 300 (2016) 300-305.

[13]   J. Kong, Z. Xiang, G. Li, T. An, Applied Catalysis B: Environmental 269 (2020) 118755.

[14]   Y. Jiang, J. Gao, Q. Zhang, Z. Liu, M. Fu, J. Wu, Y. Hu, D. Ye, Chemical Engineering Journal 371 (2019) 78-87.

[15]   J. Deng, W. Song, L. Chen, L. Wang, M. Jing, Y. Ren, Z. Zhao, J. Liu, Chemical Engineering Journal 355 (2019) 540-550.

[16]   X. Wang, T. Wang, G. Si, Y. Li, S. Zhang, X. Deng, X. Xu, Sensors and Actuators B: Chemical 302 (2020) 127165.

[17]   S. Mo, Q. Zhang, J. Li, Y. Sun, Q. Ren, S. Zou, Q. Zhang, J. Lu, M. Fu, D. Mo, J. Wu, H. Huang, D. Ye, Applied Catalysis B: Environmental 264 (2020) 118464.

[18]   L. Xing, J. Liu, T. Qi, L. Wang, Z. Wang, S. Zhang, Applied Catalysis B: Environmental 275 (2020) 119143.

[19]   A.I. Paksoy, B.S. Caglayan, A.E. Aksoylu, International Journal of Hydrogen Energy 45 (2020) 12822-12834.

[20]   M. Zhang, J. Zhang, Z. Zhou, S. Chen, T. Zhang, F. Song, Q. Zhang, N. Tsubaki, Y. Tan, Y. Han, Applied Catalysis B: Environmental 264 (2020) 118522.

[21]   H. Deng, S. Kang, J. Ma, L. Wang, C. Zhang, H. He, Environ Sci Technol 53 (2019) 10871-10879.

[22]   X. Zhang, Z.a. Ma, Z. Song, H. Zhao, W. Liu, M. Zhao, J. Zhao, The Journal of Physical Chemistry C 123 (2019) 17255-17264.

[23]   W. Yang, Z.a. Su, Z. Xu, W. Yang, Y. Peng, J. Li, Applied Catalysis B: Environmental 260 (2020) 118150.

[24]   X. Xie, Y. Li, Z.Q. Liu, M. Haruta, W. Shen, Nature 458 (2009) 746-749.

[25]   Y. Li, W. Han, R. Wang, L.-T. Weng, A. Serrano-Lotina, M.A. Bañares, Q. Wang,

K.L. Yeung, Applied Catalysis B: Environmental 275 (2020) 119121.

[26]   X. Liu, K. Zhou, L. Wang, B. Wang, Y. Li, Journal of the American Chemical Society 131 (2009) 3140-3141.

[27]   P. Wang, J. Wang, J. Shi, X. Du, X. Hao, B. Tang, A. Abudula, G. Guan, Molecular Catalysis 492 (2020) 111027.

[28]   Y. Wang, D. Yang, S. Li, L. Zhang, G. Zheng, L. Guo, Chemical Engineering Journal 357 (2019) 258-268.

[29]   L. Liu, J. Sun, J. Ding, Y. Zhang, T. Sun, J. Jia, Inorganic chemistry 58 (2019) 13241-13249.

[30]   C. Dong, Z. Qu, X. Jiang, Y. Ren, Journal of hazardous materials 391 (2020) 122181.

[31]   S. Balasubramanian, D. Viswanath, Industrial & Engineering Chemistry Fundamentals 14 (1975) 158-165.

[32]   R.K. Grasselli, Topics in Catalysis 21 (2002) 79-88.

[33]   N. Burgos, M.a. Paulis, M.M. Antxustegi, M. Montes, Applied Catalysis B: Environmental 38 (2002) 251-258.

[34]   P. Mars, D.W. Van Krevelen, Chemical Engineering Science 3 (1954) 41-59.

[35]   K.S. Song, D. Klvana, J. Kirchnerova, Applied Catalysis A: General 213 (2001) 113–121.

[36]   J.-J. Li, E.-Q. Yu, S.-C. Cai, X. Chen, J. Chen, H.-P. Jia, Y.-J. Xu, Applied Catalysis B: Environmental 240 (2019) 141-152.

[37]   J.M. Gatica, J. Castiglioni, C. de los Santos, M.P. Yeste, G. Cifredo, M. Torres, H. Vidal, Catalysis Today 296 (2017) 84-94.

[38]   P.M. Kouotou, G.-F. Pan, J.-J. Weng, S.-B. Fan, Z.-Y. Tian, Journal of Industrial

and Engineering Chemistry 35 (2016) 253-261.

[39]   Q. Wang, K.L. Yeung, M.A. Bañares, Catalysis Today   (2019).

[40]   M. Stoyanova, P. Konova, P. Nikolov, A. Naydenov, S. Christoskova, D. Mehandjiev, Chemical Engineering Journal 122 (2006) 41-46.

[41]   M. Alvarez-Merino, M. Ribeiro, J. Silva, F. Carrasco-Marin, F. Maldonado-Hodar, Environmental science & technology 38 (2004) 4664-4670.

[42]   V.V. Kaichev, A.Y. Gladky, I.P. Prosvirin, A.A. Saraev, M. Hävecker, A. Knop-Gericke, R. Schlögl, V.I. Bukhtiyarov, Surface Science 609 (2013) 113-118.

[43]   T.F. Garetto, C. Apesteguıa, Applied Catalysis B: Environmental 32 (2001) 83-94.

[44]   T.-K. Tseng, H. Chu, Science of the total environment 275 (2001) 83-93.

[45]   A. Aranzabal, J. Ayastuy-Arizti, J. González-Marcos, J. González-Velasco, Industrial & engineering chemistry research 42 (2003) 6007-6011.

[46]   I. Banu, C.M. Manta, G. Bercaru, G. Bozga, Chemical Engineering Research and Design 102 (2015) 399-406.

[47]   A. Aranzabal, Journal of Catalysis 214 (2003) 130-135.

[48]   K. Everaert, J. Baeyens, Journal of hazardous materials 109 (2004) 113-139.

[49]   J. Tsou, P. Magnoux, M. Guisnet, J.J.M. Órfão, J.L. Figueiredo, Applied Catalysis B: Environmental 57 (2005) 117-123.

[50]   S. Behar, N.-A. Gómez-Mendoza, M.-Á. Gómez-García, D. Świerczyński, F. Quignard, N. Tanchoux, Applied Catalysis A: General 504 (2014) 203-210.

[51]   S. Todorova, A. Naydenov, H. Kolev, J.P. Holgado, G. Ivanov, G. Kadinov, A. Caballero, Applied Catalysis A: General 413-414 (2012) 43-51.

[52]   M. Zabihi, F. Khorasheh, J. Shayegan, Reaction Kinetics, Mechanisms and

Catalysis 114 (2015) 611-628.

[53]   J. Yang, S. Hu, Y. Fang, S. Hoang, L. Li, W. Yang, Z. Liang, J. Wu, J. Hu, W. Xiao, C. Pan, Z. Luo, J. Ding, L. Zhang, Y. Guo, ACS Catalysis 9 (2019) 9751-9763.

[54]   Z. Li, Q. Yan, Q. Jiang, Y. Gao, T. Xue, R. Li, Y. Liu, Q. Wang, Applied Catalysis B: Environmental 269 (2020) 118827.

[55]   M. Wu, S. Chen, W. Xiang, Chemical Engineering Journal 387 (2020) 124101.

[56]   F. Liu, J. Shen, D. Xu, W. Zhou, S. Zhang, L. Wan, Chemical Engineering Journal 334 (2018) 2283-2292.

[57]   F. Liu, X. Liu, J. Shen, A. Bahi, S. Zhang, L. Wan, F. Ko, Chemical Engineering Journal 395 (2020) 125131.

[58]   T. Zhang, X. Lang, A. Dong, X. Wan, S. Gao, L. Wang, L. Wang, W. Wang, ACS Catalysis 10 (2020) 7269-7282.

[59]   Z. Wang, G. Shen, J. Li, H. Liu, Q. Wang, Y. Chen, Applied Catalysis B: Environmental 138-139 (2013) 253-259.

[60]   P. Wu, S. Dai, G. Chen, S. Zhao, Z. Xu, M. Fu, P. Chen, Q. Chen, X. Jin, Y. Qiu, S. Yang, D. Ye, Applied Catalysis B: Environmental 268 (2020) 118418.

[61]   X. Lin, S. Li, H. He, Z. Wu, J. Wu, L. Chen, D. Ye, M. Fu, Applied Catalysis B: Environmental 223 (2018) 91-102.

[62]   X. Yang, X. Yu, M. Jing, W. Song, J. Liu, M. Ge, ACS applied materials & interfaces 11 (2019) 730-739.

[63]   M. Jing, W. Song, L. Chen, S. Ma, J. Deng, H. Zheng, Y. Li, J. Liu, Z. Zhao, The Journal of Physical Chemistry C 122 (2018) 438-448.

[64]   R. Panta, V. Ruangpornvisuti, International Journal of Hydrogen Energy 42 (2017) 19106-19113.

[65]   X. Zhang, H. Zhao, Z. Song, J. Zhao, Z.a. Ma, M. Zhao, Y. Xing, P. Zhang, N. Tsubaki, Transition Metal Chemistry 44 (2019) 663-670.

[66]   X. Wang, Y. Li, Chemistry–A European Journal 9 (2003) 300-306.

[67]   J. Zhang, Y. Li, L. Wang, C. Zhang, H. He, Catalysis Science & Technology 5 (2015) 2305-2313.

[68]   N. Huang, Z. Qu, C. Dong, Y. Qin, X. Duan, Applied Catalysis A: General 560 (2018) 195-205.

[69]   Q. Ren, Z. Feng, S. Mo, C. Huang, S. Li, W. Zhang, L. Chen, M. Fu, J. Wu, D. Ye, Catalysis Today 332 (2019) 160-167.

[70]   W. Han, H. Zhao, F. Dong, Z. Tang, Nanoscale 10 (2018) 21307-21319.

[71]   L. Wang, Y. Yu, H. He, Y. Zhang, X. Qin, B. Wang, Scientific reports 7 (2017) 12845.

[72]   S. Dissanayake, N. Wasalathanthri, A. Shirazi Amin, J. He, S. Poges, D. Rathnayake, S.L. Suib, Applied Catalysis A: General 590 (2020) 117366.

[73]   G. Wei, Q. Zhang, D. Zhang, J. Wang, T. Tang, H. Wang, X. Liu, Z. Song, P. Ning, Applied Surface Science 497 (2019) 143777.

[74]   J. Hu, W.B. Li, R.F. Liu, Catalysis Today 314 (2018) 147-153.

[75]   C. Kaewbuddee, P. Kidkhunthod, N. Chanlek, R. Khunphonoi, K. Wantala, Sains Malaysiana 48 (2019) 1447-1457.

[76]   W.-X. Tang, H.-D. Liu, X.-F. Wu, Y.-F. Chen, Ozone: Science & Engineering 36 (2014) 502-512.

[77]   J. Wang, H. Zhao, J. Song, T. Zhu, W. Xu, Catalysts 9 (2019) 726.

[78]   Q. Zhang, S. Mo, B. Chen, W. Zhang, C. Huang, D. Ye, Molecular Catalysis 454 (2018) 12-20.

[79]   N. Sutradhar, A. Sinhamahapatra, S. Pahari, M. Jayachandran, B. Subramanian, H.C. Bajaj, A.B. Panda, The Journal of Physical Chemistry C 115 (2011) 7628-7637.

[80]   F. Xu, Y. Le, B. Cheng, C. Jiang, Applied Surface Science 426 (2017) 333-341.

[81]   A.E.-A.A. Said, M.M.M. Abd El-Wahab, M.N. Goda, Applied Surface Science 390 (2016) 649-665.

[82]   I.H. Kim, H.O. Seo, E.J. Park, S.W. Han, Y.D. Kim, Scientific reports 7 (2017) 40497.

[83]   Q. Li, T. Odoom-Wubah, Y. Zhou, R. Mulka, Y. Zheng, J. Huang, D. Sun, Q. Li, Industrial & Engineering Chemistry Research 58 (2019) 2882-2890.

[84]   X. Zhang, Y. Junhui, Y. Jing, C. Ting, X. Bei, L. Zhe, Z. Kunfeng, Y. Ling, H. Dannong, Applied Catalysis A: General 566 (2018) 104-112.

[85]   Q. Zhao, Y. Ge, K. Fu, N. Ji, C. Song, Q. Liu, Chemosphere 204 (2018) 257-266.

[86]   K. Rida, M.A. Peña, E. Sastre, A. Martinez-Arias, Journal of Rare Earths 30 (2012) 210-216.

[87]   Y. Luo, Y. Zheng, J. Zuo, X. Feng, X. Wang, T. Zhang, K. Zhang, L. Jiang, Journal of hazardous materials 349 (2018) 119-127.

[88]   X. Jiang, W. Xu, S. Lai, X. Chen, RSC Advances 9 (2019) 6533-6541.

[89]   P. Wang, J. Wang, X. An, J. Shi, W. Shangguan, X. Hao, G. Xu, B. Tang, A. Abudula, G. Guan, Applied Catalysis B: Environmental 282 (2020) 119560.

[90]   Y. Xie, Y. Guo, Y. Guo, L. Wang, W. Zhan, Y. Wang, X. Gong, G. Lu, RSC Advances 6 (2016) 50228-50237.

[91]   M. Morales, B. Barbero, L. Cadus, Applied Catalysis B: Environmental 67 (2006) 229-236.

[92]   W. Zhang, J. Díez-Ramírez, P. Anguita, C. Descorme, J.L. Valverde, A. Giroir-

Fendler, Applied Catalysis B: Environmental 273 (2020) 118894.

[93]   C. Zhang, J. Wang, S. Yang, H. Liang, Y. Men, Journal of colloid and interface science 539 (2019) 65-75.

[94]   J. Zeng, H. Xie, G. Zhang, X. Cheng, G. Zhou, Y. Jiang, Ceramics International 46 (2020) 21542-21550.

[95]   S. Li, H. Wang, W. Li, X. Wu, W. Tang, Y. Chen, Applied Catalysis B: Environmental 166-167 (2015) 260-269.

[96]   X. Wang, W. Zhao, X. Wu, T. Zhang, Y. Liu, K. Zhang, Y. Xiao, L. Jiang, Applied Surface Science 426 (2017) 1198-1205.

[97]   L. Li, J. Luo, Y. Liu, F. Jing, D. Su, W. Chu, ACS applied materials & interfaces 9 (2017) 21798-21808.

[98]   B. Chen, X. Yang, X. Zeng, Z. Huang, J. Xiao, J. Wang, G. Zhan, Chemical Engineering Journal 397 (2020) 125424.

[99]   J. Chen, X. Chen, W. Xu, Z. Xu, J. Chen, H. Jia, J. Chen, Chemical Engineering Journal 330 (2017) 281-293.

[100]   J. Chen, X. Chen, X. Chen, W. Xu, Z. Xu, H. Jia, J. Chen, Applied Catalysis B: Environmental 224 (2018) 825-835.

[101]   H. Deng, S. Kang, J. Ma, C. Zhang, H. He, Applied Catalysis B: Environmental 239 (2018) 214-222.

[102]   V.P. Santos, O.S.G.P. Soares, J.J.W. Bakker, M.F.R. Pereira, J.J.M. Órfão, J. Gascon, F. Kapteijn, J.L. Figueiredo, Journal of Catalysis 293 (2012) 165-174.

[103]   Y. Wu, S. Yuan, R. Feng, Z. Ma, Y. Gao, S. Xing, Molecular Catalysis 442 (2017) 164-172.

[104]   Y. Liu, J. Hou, Materials Research Bulletin 118 (2019) 110497.

[105]   J. Pan, W. Du, Y. Liu, Y. Cheng, S. Yuan, Journal of Rare Earths 37 (2019) 602-608.

[106]   H. Wang, M. Liu, S. Guo, Y. Wang, X. Han, Y. Bai, Molecular Catalysis 436 (2017) 120-127.

[107]   Q. Wang, Z. Li, M.A. Banares, L.T. Weng, Q. Gu, J. Price, W. Han, K.L. Yeung, Small 15 (2019) 1903525.

[108]   H. Lu, X. Kong, H. Huang, Y. Zhou, Y. Chen, Journal of environmental sciences 32 (2015) 102-107.

[109]   L. Deng, Y. Ding, B. Duan, Y. Chen, P. Li, S. Zhu, S. Shen, Molecular Catalysis 446 (2018) 72-80.

[110]   Z. Jiang, C. Chen, M. Ma, Z. Guo, Y. Yu, C. He, Catalysis Science & Technology 8 (2018) 5933-5942.

[111]   S.A.C. Carabineiro, X. Chen, M. Konsolakis, A.C. Psarras, P.B. Tavares, J.J.M. Órfão, M.F.R. Pereira, J.L. Figueiredo, Catalysis Today 244 (2015) 161-171.

[112]   J. Zhang, D. Tan, Q. Meng, X. Weng, Z. Wu, Applied Catalysis B: Environmental 172-173 (2015) 18-26.

[113]   X. Feng, J. Guo, X. Wen, M. Xu, Y. Chu, S. Yuan, Applied Surface Science 445 (2018) 145-153.

[114]   C. Yin, Y. Liu, Q. Xia, S. Kang, X. Li, Y. Wang, L. Cui, Journal of colloid and interface science 553 (2019) 427-435.

[115]   T. He, X. Zeng, S. Rong, Journal of Materials Chemistry A 8 (2020) 8383-8396.

[116]   Y. Liu, W. Wang, X. Xu, J.-P. Marcel Veder, Z. Shao, Journal of Materials Chemistry A 7 (2019) 7280-7300.

[117]   M. Sun, W. Li, B. Zhang, G. Cheng, B. Lan, F. Ye, Y. Zheng, X. Cheng, L. Yu,

Chemical Engineering Journal 331 (2018) 626-635.

[118]   X. Chen, X. Chen, E. Yu, S. Cai, H. Jia, J. Chen, P. Liang, Chemical Engineering Journal 344 (2018) 469-479.

[119]   Q. Zhang, S. Mo, J. Li, Y. Sun, M. Zhang, P. Chen, M. Fu, J. Wu, L. Chen, D. Ye, Catalysis Science & Technology 9 (2019) 4538-4551.

[120]   Y. Shu, J. Ji, Y. Xu, J. Deng, H. Huang, M. He, D.Y.C. Leung, M. Wu, S. Liu, S. Liu, G. Liu, R. Xie, Q. Feng, Y. Zhan, R. Fang, X. Ye, Applied Catalysis B: Environmental 220 (2018) 78-87.

[121]   M. Wang, D. Chen, N. Li, Q. Xu, H. Li, J. He, J. Lu, ACS applied materials & interfaces 12 (2020) 13781-13789.

[122]   S. Mo, Q. Zhang, M. Zhang, Q. Zhang, J. Li, M. Fu, J. Wu, P. Chen, D. Ye, Nanoscale Horizons 4 (2019) 1425-1433.

[123]   T. Jakubek, C. Hudy, P. Indyka, E. Nowicka, S. Golunski, A. Kotarba, Catalysis Communications 132 (2019) 105807.

[124]   S. Xie, J. Deng, Y. Liu, Z. Zhang, H. Yang, Y. Jiang, H. Arandiyan, H. Dai, C.T. Au, Applied Catalysis A: General 507 (2015) 82-90.

[125]   W. Pei, Y. Liu, J. Deng, K. Zhang, Z. Hou, X. Zhao, H. Dai, Applied Catalysis B: Environmental 256 (2019) 117814.

[126]   X. Hu, Z. Zhang, Y. Zhang, L. Sun, H. Tian, X. Yang, European Journal of Inorganic Chemistry 2019 (2019) 2933-2939.

[127]   Y. Liu, H. Dai, J. Deng, S. Xie, H. Yang, W. Tan, W. Han, Y. Jiang, G. Guo, Journal of Catalysis 309 (2014) 408-418.

[128]   S. Xie, Y. Liu, J. Deng, J. Yang, X. Zhao, Z. Han, K. Zhang, Y. Wang, H. Arandiyan, H. Dai, Catalysis Science & Technology 8 (2018) 806-816.

[129]   S. Xie, J. Deng, S. Zang, H. Yang, G. Guo, H. Arandiyan, H. Dai, Journal of Catalysis 322 (2015) 38-48.

[130]   X. Liu, J. Wang, J. Zeng, X. Wang, T. Zhu, RSC Advances 5 (2015) 52066-52071.

[131]   R. Peng, X. Sun, S. Li, L. Chen, M. Fu, J. Wu, D. Ye, Chemical Engineering Journal 306 (2016) 1234-1246.

[132]   C. Chen, F. Chen, L. Zhang, S. Pan, C. Bian, X. Zheng, X. Meng, F.-S. Xiao, Chemical communications 51 (2015) 5936-5938.

[133]   R. Peng, S. Li, X. Sun, Q. Ren, L. Chen, M. Fu, J. Wu, D. Ye, Applied Catalysis B: Environmental 220 (2018) 462-470.

[134]   Y. Guo, Y. Gao, X. Li, G. Zhuang, K. Wang, Y. Zheng, D. Sun, J. Huang, Q. Li, Chemical Engineering Journal 362 (2019) 41-52.

[135]   A. Aboukaïs, M. Skaf, S. Hany, R. Cousin, S. Aouad, M. Labaki, E. Abi-Aad, Materials Chemistry and Physics 177 (2016) 570-576.

[136]   J. Dai, Y. Guo, L. Xu, G. Zhuang, Y. Zheng, D. Sun, J. Huang, Q. Li, Molecular Catalysis 486 (2020) 110849.

[137]   M.A. Carreon, V.V. Guliants, European Journal of Inorganic Chemistry 2005 (2005) 1189-1189.

[138]   X. Chen, X. Chen, S. Cai, J. Chen, W. Xu, H. Jia, J. Chen, Chemical Engineering Journal 334 (2018) 768-779.

[139]   X. Yang, X. Ma, X. Yu, M. Ge, Applied Catalysis B: Environmental 263 (2020) 118355.

[140]   J. Zhu, W. Mu, L. Su, X. Li, Y. Guo, S. Zhang, Z. Li, Journal of Solid State Chemistry 248 (2017) 142-149.

[141]   Y. Guo, Y. Sun, D.-P. Yang, J. Dai, Z. Liu, Y. Chen, J. Huang, Q. Li, ACS applied

materials & interfaces 12 (2019) 2469-2480.

[142]   F. Hu, Y. Peng, J. Chen, S. Liu, H. Song, J. Li, Applied Catalysis B: Environmental 240 (2019) 329-336.

[143]   M. Konsolakis, S.A. Carabineiro, P.B. Tavares, J.L. Figueiredo, Journal of hazardous materials 261 (2013) 512-521.

[144]   W. Yang, Y. Peng, Y. Wang, Y. Wang, H. Liu, Z.a. Su, W. Yang, J. Chen, W. Si, J. Li, Applied Catalysis B: Environmental 278 (2020) 119279.

[145]   J.-H. Lee, R. Black, G. Popov, E. Pomerantseva, F. Nan, G.A. Botton, L.F. Nazar, Energy & Environmental Science 5 (2012) 9558.

[146]   J.K. Ngala, S. Alia, A. Dobley, V.M.B. Crisostomo, S.L. Suib, Chemistry of materials 19 (2007) 229-234.

[147]   X. Yang, X. Yu, M. Lin, X. Ma, M. Ge, Catalysis Today 327 (2019) 254-261.

[148]   J. Quiroz, J.-M. Giraudon, A. Gervasini, C. Dujardin, C. Lancelot, M. Trentesaux, J.-F. Lamonier, ACS Catalysis 5 (2015) 2260-2269.

[149]   S. Sui, P. Zhang, H. Zhang, R. Cao, Chinese Journal of Catalysis 40 (2019) 1525-1533.

[150]   X. Zeng, G. Cheng, Q. Liu, W. Yu, R. Yang, H. Wu, Y. Li, M. Sun, C. Zhang, L. Yu, Industrial & Engineering Chemistry Research 58 (2019) 13926-13934.

[151]   Y. Xu, J. Dhainaut, G. Rochard, J.-P. Dacquin, A.-S. Mamede, J.-M. Giraudon, J.-F. Lamonier, H. Zhang, S. Royer, Chemical Engineering Journal 388 (2020) 124146.

[152]   W. Si, Y. Wang, S. Zhao, F. Hu, J. Li, Environ Sci Technol 50 (2016) 4572-4578.

[153]   W. Si, Y. Wang, Y. Peng, X. Li, K. Li, J. Li, Chemical communications 51 (2015) 14977-14980.

[154]   L. Liu, J. Li, H. Zhang, L. Li, P. Zhou, X. Meng, M. Guo, J. Jia, T. Sun, Journal

of hazardous materials 362 (2019) 178-186.

[155]   S. Wang, Q. Liu, Z. Zhao, C. Fan, X. Chen, G. Xu, M. Wu, J. Chen, J. Li, Industrial & Engineering Chemistry Research 59 (2020) 6556-6564.

[156]   Q. Yang, D. Wang, C. Wang, X. Li, K. Li, Y. Peng, J. Li, Catalysis Science & Technology 8 (2018) 3166-3173.

[157]   X. Weng, Q. Meng, J. Liu, W. Jiang, S. Pattisson, Z. Wu, Environ Sci Technol 53 (2019) 884-893.

[158]   W.L. Wang, Q. Meng, Y. Xue, X. Weng, P. Sun, Z. Wu, Journal of Catalysis 366 (2018) 213-222.

[159]   Y. Jiang, G. Cheng, R. Yang, H. Liu, M. Sun, L. Yu, Z. Hao, Journal of Solid State Chemistry 272 (2019) 173-181.

[160]   M. Sun, B. Zhang, H. Liu, B. He, F. Ye, L. Yu, C. Sun, H. Wen, RSC Advances 7 (2017) 3958-3965.

[161]   R. Kumar, S. Sithambaram, S.L. Suib, Journal of Catalysis 262 (2009) 304-313.

[162]   X. Yu, S. Liu, G. Lin, Y. Yang, S. Zhang, H. Zhao, C. Zheng, X. Gao, Applied Surface Science 496 (2019) 143617.

[163]   B. Solsona, T. García, R. Sanchis, M.D. Soriano, M. Moreno, E. Rodríguez-Castellón, S. Agouram, A. Dejoz, J.M. López Nieto, Chemical Engineering Journal 290 (2016) 273-281.

[164]   L. Nie, J. Yu, X. Li, B. Cheng, G. Liu, M. Jaroniec, Environ Sci Technol 47 (2013) 2777-2783.

[165]   T. Dai, H. Zhou, Y. Liu, R. Cao, J. Zhan, L. Liu, B.W.L. Jang, ACS Sustainable Chemistry & Engineering 7 (2019) 5072-5081.

[166]   S. Chen, L. Li, W. Hu, X. Huang, Q. Li, Y. Xu, Y. Zuo, G. Li, ACS applied

materials & interfaces 7 (2015) 22999-23007.

[167]   N. Wang, J. Yue, L. Chen, Y. Qian, J. Yang, ACS applied materials & interfaces 7 (2015) 10348-10355.

[168]   Q. Xu, H. Jiang, H. Zhang, H. Jiang, C. Li, Electrochimica Acta 259 (2018) 962-967.

[169]   G. Ou, Y. Xu, B. Wen, R. Lin, B. Ge, Y. Tang, Y. Liang, C. Yang, K. Huang, D. Zu, R. Yu, W. Chen, J. Li, H. Wu, L.M. Liu, Y. Li, Nature communications 9 (2018) 1302.

[170]   Z. Zhao, H. Tan, H. Zhao, Y. Lv, L.J. Zhou, Y. Song, Z. Sun, Chemical communications 50 (2014) 2755-2757.

[171]   A. Sinhamahapatra, J.P. Jeon, J. Kang, B. Han, J.S. Yu, Scientific reports 6 (2016) 27218.

[172]   H. Chen, M. Yang, S. Tao, G. Chen, Applied Catalysis B: Environmental 209 (2017) 648-656.

[173]   S. Lee, G. Nam, J. Sun, J.S. Lee, H.W. Lee, W. Chen, J. Cho, Y. Cui, Angewandte Chemie 55 (2016) 8599-8604.

[174]   L. Xu, Q. Jiang, Z. Xiao, X. Li, J. Huo, S. Wang, L. Dai, Angewandte Chemie 55 (2016) 5277-5281.

[175]   N. Liu, V. Haublein, X. Zhou, U. Venkatesan, M. Hartmann, M. Mackovic, T. Nakajima, E. Spiecker, A. Osvet, L. Frey, P. Schmuki, Nano letters 15 (2015) 6815-6820.

[176]   Y. Zhou, Y. Liu, P. Liu, W. Zhang, M. Xing, J. Zhang, Applied Catalysis B: Environmental 170-171 (2015) 66-73.

[177]   Z.H. Wei, T.S. Zhao, X.B. Zhu, P. Tan, Journal of Power Sources 306 (2016) 724-732.

[178]   G. Ou, D. Li, W. Pan, Q. Zhang, B. Xu, L. Gu, C. Nan, H. Wu, Advanced

materials 27 (2015) 2589-2594.

[179]   H. Wei, X. Ma, L. Gu, J. Li, W. Si, G. Ou, W. Yu, C. Zhao, J. Li, M. Song, Z. Peng, H. Wu, Nano Research 9 (2016) 3839-3847.

[180]   R. Wang, J. Li, Environmental science & technology 44 (2010) 4282-4287.

[181]   T.Y. Ma, Y. Zheng, S. Dai, M. Jaroniec, S.Z. Qiao, J. Mater. Chem. A 2 (2014) 8676-8682.

[182]   H.Y. Jeong, J.Y. Lee, S.-Y. Choi, Applied Physics Letters 97 (2010) 042109.

[183]   D. Chen, F. Niu, L. Qin, S. Wang, N. Zhang, Y. Huang, Solar Energy Materials and Solar Cells 171 (2017) 24-32.

[184]   S. Zhang, G. Wang, J. Jin, L. Zhang, Z. Wen, J. Yang, Nano Energy 36 (2017) 186-196.

[185]   M. Ziatdinov, O. Dyck, X. Li, B.G. Sumpter, S. Jesse, R.K. Vasudevan, S.V. Kalinin, Science advances 5 (2019) eaaw8989.

[186]   P. Sutter, Springer Handbook of Microscopy, Springer, 2019, pp. 2-2.

[187]   U. Diebold, J. Lehman, T. Mahmoud, M. Kuhn, G. Leonardelli, W. Hebenstreit, M. Schmid, P. Varga, Surface science 411 (1998) 137-153.

[188]   M. Aizawa, Y. Morikawa, Y. Namai, H. Morikawa, Y. Iwasawa, The Journal of Physical Chemistry B 109 (2005) 18831-18838.

[189]   R. Schaub, E. Wahlström, A. Rønnau, E. Lægsgaard, I. Stensgaard, F. Besenbacher, Science 299 (2003) 377-379.

[190]   J.L. Lu, H.J. Gao, S. Shaikhutdinov, H.J. Freund, Surface Science 600 (2006) 5004-5010.

[191]   E. Genty, J. Brunet, C. Poupin, S. Ojala, S. Siffert, R. Cousin, Applied Catalysis B: Environmental 247 (2019) 163-172.

[192]   S. Li, S. Mo, J. Li, H. Liu, Y. Chen, RSC Advances 6 (2016) 56874-56884.

[193]   P. Larkin, Infrared and Raman spectroscopy: principles and spectral interpretation, Elsevier, 2017.

[194]   M. Moskovits, Journal of Raman Spectroscopy 36 (2005) 485-496.

[195]   J. Hou, Y. Li, L. Liu, L. Ren, X. Zhao, Journal of Materials Chemistry A 1 (2013) 6736.

[196]   X.Y. Kong, Y.Y. Choo, S.P. Chai, A.K. Soh, A.R. Mohamed, Chemical communications 52 (2016) 14242-14245.

[197]   J. Li, X. Wu, W. Pan, G. Zhang, H. Chen, Angewandte Chemie 57 (2018) 491-495.

[198]   Y. Huang, H. Li, W. Fan, F. Zhao, W. Qiu, H. Ji, Y. Tong, ACS applied materials & interfaces 8 (2016) 27859-27867.

[199]   Y. Huang, B. Long, M. Tang, Z. Rui, M.-S. Balogun, Y. Tong, H. Ji, Applied Catalysis B: Environmental 181 (2016) 779-787.

[200]   W. Yang, Y. Zhu, F. You, L. Yan, Y. Ma, C. Lu, P. Gao, Q. Hao, W. Li, Applied Catalysis B: Environmental 233 (2018) 184-193.

[201]   K. Ye, K. Li, Y. Lu, Z. Guo, N. Ni, H. Liu, Y. Huang, H. Ji, P. Wang, TrAC Trends in Analytical Chemistry 116 (2019) 102-108.

[202]   A. Antuzevics, M. Kemere, G. Krieke, R. Ignatans, Optical Materials 72 (2017) 749-755.

[203]   R. Siegel, Annual Review of Materials Science 10 (1980) 393-425.

[204]   X. Jiang, Y. Zhang, J. Jiang, Y. Rong, Y. Wang, Y. Wu, C. Pan, The Journal of Physical Chemistry C 116 (2012) 22619-22624.

[205]   J. Li, M. Zhang, Z. Guan, Q. Li, C. He, J. Yang, Applied Catalysis B:

Environmental 206 (2017) 300-307.

[206]   Z. Geng, X. Kong, W. Chen, H. Su, Y. Liu, F. Cai, G. Wang, J. Zeng, Angewandte Chemie 130 (2018) 6162-6167.

[207]   K. Sudarshan, V. Tiwari, P. Utpalla, S.K. Gupta, Inorganic Chemistry Frontiers 6 (2019) 2167-2177.

[208]   Z. Luo, Y. Ouyang, H. Zhang, M. Xiao, J. Ge, Z. Jiang, J. Wang, D. Tang, X. Cao, C. Liu, W. Xing, Nature communications 9 (2018) 2120.

[209]   J. Li, X. Wu, W. Pan, G. Zhang, H. Chen, Angewandte Chemie International Edition 57 (2018) 491-495.

[210]   S. STEINSVIK, R. BUGGE, J. GjØNnes, J. TAFTØ, T. Norby, Journal of Physics and Chemistry of Solids 58 (1997) 969-976.

[211]   E.D. Hanson, L. Lajaunie, S. Hao, B.D. Myers, F. Shi, A.A. Murthy, C. Wolverton, R. Arenal, V.P. Dravid, Advanced Functional Materials 27 (2017) 1605380.

[212]   A.M. D'Angelo, A.C.Y. Liu, A.L. Chaffee, The Journal of Physical Chemistry C 120 (2016) 14382-14389.

[213]   Z. Sun, Q. Liu, T. Yao, W. Yan, S. Wei, Science China Materials 58 (2015) 313-341.

[214]   V.R. Mastelaro, E.D. Zanotto, Materials 11 (2018) 204.

[215]   N. Zhang, X. Li, H. Ye, S. Chen, H. Ju, D. Liu, Y. Lin, W. Ye, C. Wang, Q. Xu, J. Zhu, L. Song, J. Jiang, Y. Xiong, J Am Chem Soc 138 (2016) 8928-8935.

[216]   S. Peng, X. Han, L. Li, S. Chou, D. Ji, H. Huang, Y. Du, J. Liu, S. Ramakrishna, Advanced Energy Materials 8 (2018) 1800612.

[217]   Z. Li, K. Sibudjing, ChemCatChem 10 (2018) 2994-3001.

[218]   A.M. D'Angelo, A.L. Chaffee, ACS omega 2 (2017) 2544-2551.

[219]   V.P. Santos, M.F.R. Pereira, J.J.M. Órfão, J.L. Figueiredo, Applied Catalysis B: Environmental 99 (2010) 353-363.

[220]   Z. Cui, W. Wang, C. Zhao, C. Chen, M. Han, G. Wang, Y. Zhang, H. Zhang, H. Zhao, ACS applied materials & interfaces 10 (2018) 31394-31403.

Chapter 2 Generation of abundant defects in Mn-Co mixed oxides by a facile agar-gel method for highly efficient catalysis of total toluene oxidation

2.1 Introduction

Volatile organic compounds (VOCs) are harmful to the atmosphere environment and human health [1, 2]. Among VOCs, toluene with toxic, mutagenic and malodorous characteristics, is always used as a model VOC to evaluate the performances of potential VOC removal technologies [3, 4]. So far, various processes such as biodegradation [5], adsorption and absorption [6], plasma-catalysis [7], photocatalytic oxidation [1], wet scrubbing [8], and catalytic oxidation [9, 10] have been developed and applied for the toluene removal. Especially, the catalytic oxidation is considered as a most economical way due to its high removal efficiency, low energy consumption, and almost no harmful byproducts [9, 10]. However, development of high-performance catalysts for the total VOCs oxidation plays the key role in the removal efficiency. To date, the developed catalysts mainly include the supported noble metals (e.g., Pt, Au, Pd, and Ag) and transition metal oxides [3]. The former ones commonly demonstrate excellent activities at low temperatures [11, 12], however, their widely practical applications are limited owing to the rare resource and high cost [13, 14]. In contrast, the latter ones have abundant resources and low cost, but the performances are always lower the former ones. Nowadays, various methods have been developed to tune the catalytic performance so that transition metal oxide based catalysts can achieve high activity as well as stability comparable to the noble metal based ones [15-17].

Among various transition metal oxide based catalysts for the total toluene oxidation,

manganese oxide exhibits excellent catalytic performance due to the mixed valences of Mn (Mn^{2+}, Mn^{3+} and Mn^{4+}), open tunnel structure, high mobility of lattice oxygen, and abundant oxygen species on the surface [18, 19]. Meanwhile, cobalt oxide with modified morphology and more exposed crystalline planes also shows high catalytic performance [4]. Moreover, it is found that combining of manganese with cobalt and/or other metal oxides to create Mn containing mixed oxide catalyst by using a suitable method could achieve higher activity for the total toluene oxidation than either single MnO_x or single CoO_x due to the synergistic effect. Zhan *et al.* [20] prepared various bimetal M-Mn_2O_3 (M = Zn, Co, Ce) mixed oxide catalysts with highly dispersed active sites and designable compositions and found that the ratio of different valences of Mn species in the mixed oxides could be adjusted by mixing with different metal species. They confirmed that the presence of more Mn^{2+} species is not benefit for the oxidation reaction. Xu *et al.* [21] loaded Co-Mn mixed oxides on Ni foam support by hydrothermal method for the total toluene oxidation and certified that high concentrations of Mn^{3+} and Co^{3+} species with rich oxygen vacancy defects existed on the surface, which played the key role in the improving of catalytic activity. Meanwhile, Luo *et al.* [22] synthesized the Mn-Co mixed oxides by pyrolysis of the metal organic framework (MOF) precursors, and found that the optimum one with excellent catalytic performance for the total toluene oxidation contained more Mn^{4+} rather than Mn^{3+} with the Co^{3+} species and abundant oxygen vacancy defects on the surface. It seems that the generation of more Mn^{3+} as well as Mn^{4+} species on the surface of Mn-based catalysts could result in higher catalytic activity for the total VOCs oxidation. In addition, the formation of abundant multi-phase interfaces by metal doping can enhance the catalytic activity for the total toluene oxidation since more oxygen vacancies could be generated on the catalyst surface [23, 24]. Thus,

generation of abundant defects with the appropriate oxygen vacancy defects in the Mn-Co mixed oxides is necessity for the promoting of catalyst performance.

Many traditional strategies such as coprecipitation method [2, 25], sol-gel method [26, 27], and electrodeposition method [28] have been proposed to increase the surface defects of various mixed metal oxides for the total VOCs oxidation. Recently, some templating strategies were also applied to improve the catalyst performance of transition metal oxide catalysts. For instance, Liu $et\ al$. [29] used a carboxy-modified colloidal crystal templating method to prepare $M_xCo_{3-x}O_4$ (M = Zn and Ni) mixed oxide catalysts and observed that the carboxy-group (-COOH) in the precursor had great influence on the activity of final catalysts. Fu $et\ al$. [30] applied citric acid (including -COOH and -OH group) gel method to synthesize various MnO_x-CeO_2 mixed oxides, and found that more oxygen vacancy defects were formed on the surface of catalysts. In our previous study, a regenerated cellulose template was used to synthesize Co_3O_4 catalysts with rich scattered defects and disorder phases, and it is found that the template played an important role in the formation of surface defects, thereby improving the catalytic performance [31]. Inspired by these templating methods, herein, we developed an agar-gel synthesis method to prepare novel Mn-Co mixed oxide catalysts with controllable structure and optimum amount of oxygen vacancy defects for the total toluene oxidation. The obtained catalysts were characterized by XRF, XRD, BET, SEM, TEM, H_2-TPR, O_2-TPD, XPS analyses with density functional theory (DFT) calculations. The catalysis stability was tested in the absence and presence of water vapor. Furthermore, to understand the rate-controlling step as well as the structure-activity relationship, the key intermediates during the adsorption-oxidation of toluene over the catalysts were identified by $in\ situ$ DRIFTS analysis. It is expected to provide a facile but effective way to coordinate the metal species

homogeneously with controllable structure and optimum amount of oxygen vacancy defects in the obtained catalysts for the total toluene oxidation.

2.2 Experimental and measurements

2.2.1 Preparation of Mn_xCo_y mixed oxides by agar-gel method

Mn-Co mixed oxides were prepared by an agar-gel method for the first time. Briefly, 1 g of agar powder (Wako, Japan) and 2.91 g of cobalt nitrate hydrate ($Co(NO_3)_2 \cdot 6H_2O$, Wako, Japan) were dissolved in 100 mL of distilled water and then the calculated amount (0-8.61g) of manganese nitrate hydrate ($Mn(NO_3)_2 \cdot 6H_2O$, Wako, Japan) was added into the above solution based on the molar ratio of Mn : Co (0, 1, 2, and 3). Thereafter, the mixture solution was heated to 80 °C and magnetically stirred until the solution became transparent, then the solution was naturally cooled down to room temperature. The transparent solution was covered with a parafilm and aged at least 72 h. Finally, the as-synthesized gel was calcined at 350 °C for 2.5 h with a heating rate of 5 °C/min to obtain the final powder catalysts, which are labelled as Co, Mn1Co1, Mn2Co1, and Mn3Co1, respectively (Mn-based catalysts). For comparison, 1 g of agar powder and 2.87 g of $Mn(NO_3)_2 \cdot 6H_2O$ were dissolved in 100 mL of distilled water and the calculated amount of $Co(NO_3)_2 \cdot 6H_2O$ in the range of 0-8.73 g was also introduced into the solution based on the molar ratio of Co : Mn (0, 2, and 3), and then followed the same steps as the above to obtain the final powder catalysts, which are labelled as Mn, Mn1Co2, and Mn1Co3 respectively (Co-based catalysts).

2.2.2 Catalyst characterization

The average chemical contents in the catalysts were determined by using X-ray fluorescence (XRF) analysis (Energy Dispersive X-ray spectrometer, EDX-800HS,

Shimadzu). Morphology was observed by a Hitachi SU8010 SEM at 15 kV. TEM image was collected by a JEM-2100 transmission electron microscope (JEOL) with an operating voltage of 200 kV. XRD pattern was obtained by a Rigaku SmartLab X-Ray diffractometer using a Cu-Kα (λ=1.5405 Å) radiation source. Raman spectrum was measured using a JASCO NRS-5100 Raman spectrometer at 532 nm. The Brunauer-Emmett-Teller (BET) surface area was measured on an ASAP 2020 Plus Phys sorption instrument (Micromeritics, ASAP 2020, US) at the liquid N_2 temperature (-196 °C). The surface chemical composition and elemental valence states of catalysts were acquired by an X-ray photoelectron spectrometer (XPS) with a VG Scientific ESCALab250i-XL unit equipped with an Al Kα radiation source.

Hydrogen temperature programmed reduction analysis (H_2-TPR) was performed on a BELCAT catalyst analyzer equipped with a thermal conductivity detector (TCD). In brief, 50 mg of catalyst was pretreated at 300 °C in a He atmosphere with a flow rate of 50 cm^3/min for 30 min at first and then, cooled down to 30 °C at the same condition. H_2-TPR analysis was performed in a 5% H_2/Ar flow (50 cm^3/min) from 30 to 900 °C with a heating rate of 10 °C/min. Oxygen temperature programmed desorption (O_2-TPD) was tested on the same instrument. In brief, 50 mg of catalyst was pretreated under a O_2 atmosphere (30 cm^3/min) at 120 °C for 60 min and cooled down to 30 °C at the same condition. Then, the pretreated catalyst was heated from 30 to 900 °C in a He flow (30 cm^3/min) with a heating rate of 10 °C/min [2].

All of the operando diffuse reflectance infrared FT spectroscopy (DRIFTS) studies were carried out through a Frontier FTIR spectrometer (PerkinElmer) equipped with a DRIFTS cell and a highly sensitive MCT detector cooled by liquid N_2 in the range of 650-4000 cm^{-1} with 32 scans. Firstly, the powder sample was pre-treated in pure N_2 (100

cm^3/min) at 300 °C for 30 min to remove the adsorbed gas, and then the temperature was cooled down to 236 °C to collect the background in N$_2$ atmosphere. Subsequently, the reactant gas (1000 ppm toluene/N$_2$) with a flow rate of 100 cm^3/min was continuously introduced into the *in situ* reaction chamber at 236 °C, and the DRIFTS spectrum (4000–650 cm^{-1}) was collected for 50 min. Thereafter, N$_2$ purging was performed for about 1 h to remove the physical absorbed toluene. Then, air was introduced into the cell and simultaneously the spectrum was started to record. After removing the reactant gas from the cell using pure N$_2$ gas, a mixture of toluene/air/5 vol.% water vapor was introduced into the system and simultaneously the DRIFTS spectrum (4000–650 cm^{-1}) was collected.

2.2.3 Catalytic performance test

Catalytic toluene oxidation was performed in a tubular fixed bed reactor (i.d. = 8.0 mm), in which about 50 mg of catalysts (40-60 mesh) were mixed with quartz sand (SiO$_2$, 40 mesh). Before activity test, the reactor system was pretreated in a N$_2$ flow at 100 ºC with a ramp rate of 10 ºC/min for 60 min in order to avoid the possibility of over-estimation of toluene oxidation conversion. Subsequently, the activities from 100 ºC to 300 ºC with a temperature ramp of 10 ºC/min were investigated under a gas mixture contained 1000 ppm toluene in 20 vol.% O$_2$ with a total gas flow rate of 50 cm^3/min (N$_2$ as balance gas), corresponding to a weight hourly space velocity (WHSV) of 60,000 cm^3/(g h). Herein, a thermocouple was inserted into the center of catalyst bed for monitoring the actual reaction temperature and it is found that the actual temperature was about 12 °C higher than the setting temperature. To investigate the effect of WHSV, the amounts of catalysts were adjusted to the demands of WHSVs = 30,000 and 120,000 cm^3/(g h). Moreover, the effect of water steam on the catalytic toluene oxidation over the catalyst with the best performance in this study was studied by introducing 5, 10 and 20

vol.% water vapors separately into the reaction system.

Inlet and outlet gases were analyzed by on-line gas chromatographs (GC) equipped with a flame ionization detector (FID, GC-2014, Shimadzu) and a thermal conductivity detector (TCD, GC-8A, Shimadzu). Concentration of CO_2 in the outlet gas was measured by using an FT-IR gas analyzer (Horiba, FG-120). Toluene conversion ($X_{toluene}$) and CO_2 selectivity (Y_{CO_2}) were calculated respectively by the following two equations:

$$X_{toluene} = \frac{C_{Inlet} - C_{Outlet}}{C_{Inlet}} \times 100\%$$

$$Y_{CO_2} = \frac{C_{CO_2}}{7(C_{Inlet} - C_{Outlet})} \times 100\%$$

where, C_{Outlet} and C_{Inlet} represent the outlet and inlet concentrations of toluene, respectively, and C_{CO_2} represents the outlet CO_2 concentration.

3.2.4 Computational method

The O_2 adsorption energy on the (211) facet was calculated based on the Cambridge Serial Total Energy Package (CASTEP) implemented in Materials Studio using the ultrasoft pseudopotential method. The ideal Mn_3O_4 and $CoMn_2O_4$ (Co-doped Mn_3O_4) were geometrically optimized based on the minimizing of the total energy at first. Then, the electron-exchange correlation functions of generalized gradient approximation (GGA) and Perdew-Burke-Ernzerhof (PBE) were used for all calculations. The plane-wave cut-off was chosen to be 340 eV to ensure the acceptable precision, and 3×3×3 k-point grids were used in the geometry optimization of the bulk structure whereas Gamma k-point was selected for slab models. The convergence criterion was within 1.0×10^{-5} eV per atom for the total energy with an internal stress less than 0.05 GPa.

The adsorption energy (E_{ad}) of O_2 was calculated according to the following formula:

$$E_{ad} = E_{slab+O_2} - \{E_{empty\ slab} + E_{O_2}\}$$

where E_{slab+O_2}, $E_{empty\ slab}$, and E_{O_2} are the DFT total energy of O_2 adsorbed on the slab (Mn_3O_4 (211) facet or $CoMn_2O_4$ (211) facet), empty slab, and O_2 molecule after the structure optimization, respectively.

2.3 Result and discussion

The average element contents of Mn_xCo_y mixed oxide catalysts in bulk confirmed by XRF analysis are summarized in Tables 2.1. The atomic ratios of Mn to Co (Mn/Co) were 2.91, 1.93, 0.99, 0.49 and 0.33 for Mn3Co1, Mn2Co1, Mn1Co1, Mn1Co2 and Mn1Co3, respectively, which decreased with the increase in the doping amount of Co species. It is noteworthy that the measured Mn/Co ratios well matched the corresponding theoretical values (3, 2, 1, 0.5, 0.33) in Mn_xCo_y mixed oxide catalysts. To describe conveniently, the theoretical doping amount in Mn_xCo_y mixed oxide catalysts was used in the following context. In addition, the Mn-based catalysts were mainly discussed in the main context since one of the Mn-based catalysts, i.e., Mn2Co1, exhibited the best catalysis performance.

Table 2.1 Elemental contents based on XRF analysis, BET surface areas, and surface molar ratios based on XPS spectra of the Mn_xCo_y mixed oxides (Mn-based catalysts).

Sample	Element content (at. %) [a]			BET [b]	D [c]	V [d]	Surface molar ratio [e]			
	Mn	Co	Mn/Co	(m²/g)	(nm)	(cm³/g)	Mn^{4+}/Mn^{2+}	Mn^{3+}/Mn^{2+}	Co^{3+}/Co^{2+}	O_{ads}/O_{latt}
Mn	100	/	/	35.5	10.05	0.11	0.87	2.36	/	0.72
Mn1Co1	49.8	50.2	0.99	21.9	10.63	0.096	2.68	3.42	0.88	0.64
Mn2Co1	65.9	34.1	1.93	85.4	5.81	0.17	3.14	4.43	1.00	0.87
Mn3Co1	74.4	25.6	2.91	53.6	7.09	0.12	2.83	4.01	0.87	0.83

[a] Element content determined by XRF analysis.

[b] BET specific surface area.

Average pore diameter calculated from the desorption branch of the isotherm using the BJH method.

[d] Total pore volume measured at $P/P_0=0.99$.

[e] Calculated based on XPS spectra

2.3.1 SEM, TEM and XRD characterization

SEM images of the Mn_xCo_y mixed oxide catalysts with different Mn/Co molar ratios are shown in Fig. 2.1. Interestingly, for the single Mn or Co oxide, an overall coral-like network structure was formed, but for the Mn_xCo_y mixed oxides, three-dimensional porous structure with random pore size distribution was obviously observed. This morphology may be caused by the strong interaction between Mn and Co species, which hinder the separately aggregations of either MnO_x or CoO_x crystals [32].
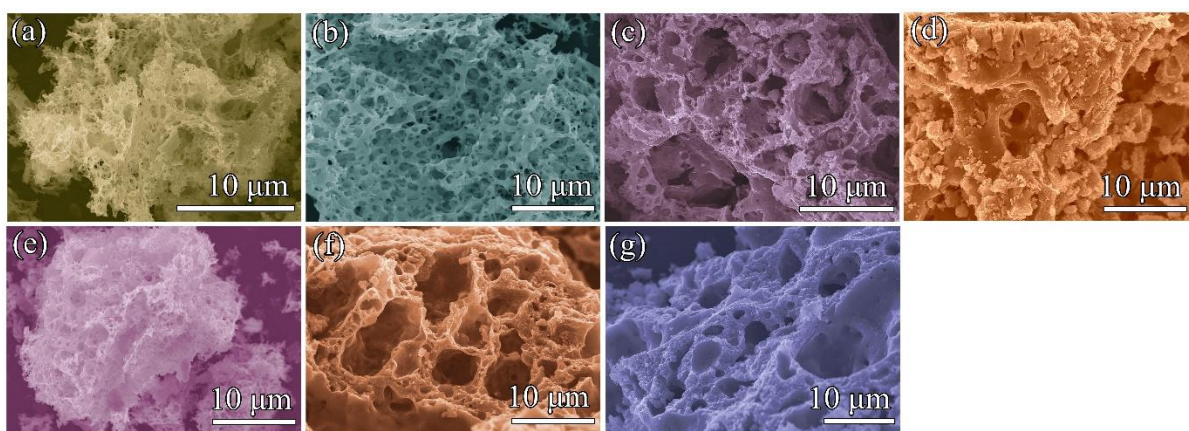
Fig 2.1. SEM images of (a) Mn, (b) Mn1Co1, (c) Mn2Co1, (d) Mn3Co1, (e) Co, (f) Mn1Co2, and (g) Mn1Co3 mixed oxide catalysts.

The nanostructures of single MnO_x and the Mn2Co1 mixed oxide catalysts with the best catalytic performance were further elucidated by TEM analyses in Figs. 2.2 and 2.3 respectively. The nanostructure of catalysts was formed by assembling of the nanoparticles. The distinct lattice fringes of the Mn oxide with the interplanar spacings of 0.20, 0.24, 0.28, and 0.49 nm corresponded to the (220), (211), (103) and (101) planes

of the Mn_4O_3 phase, respectively, and the Mn_3O_4 particle sizes were relatively uniform (Fig. 2.2). The distinct lattice fringes of Mn2Co1 mixed oxide with the interplanar spacings of 0.14, 0.20, 0.24, 0.27 nm indicated the presences of (400), (220), (211), and (103) planes of the $CoMn_2O_4$, respectively (Fig. 2.3). Compared with the lattice fringes of the single Mn oxide, those of the Mn2Co1 mixed oxide were not obvious but still observed as shown in Fig. 2.3a, indicating its much lower crystallinity, which are consistent with the XRD results in Fig. 2.3c. Thus, the doping of Co species decreased the crystallinity of mixed oxide and resulted in the formation of more amorphous phases [22, 32]. In this case, as shown in Figs. 2.1 and 2.3b, it is very difficult to measure the particle size based on SEM or TEM images. Especially, abundant defects and edge dislocations were confirmed by the TEM image. As observed in Fig. 2.3(a-1), there were distinct lattice fringes. However, as shown in Figs. 2.3(a-2) to (a-4), the crystalline fringes along the crooked edge were discontinuous, which could provide abundant defect structures. Fig. 2.3(a-5) illustrate the possible defect structures derived by the edge dislocation with the additional active edge sites. It is well-known that crystal defects existed ubiquitously in metal oxides can radically boost the catalytic performance, and especially the oxygen vacancy defects on the catalysts could have great effect on the reducibility of heterogeneous catalysts, leading to excellent catalytic activity for VOC oxidation at low temperature. The crystal defects include interface and edge dislocations, crystalline deformation and so on, and the oxygen vacancy defects usually appears along with these defects. In general, the oxygen vacancy defects should be benefit for the promoting of the replenishment and reconstruction of oxygen species, and enhance the cycling of the emergence-annihilation of oxygen vacancy defects during the VOC oxidation process at low temperature [21, 22]. Therefore, a large number of defects on

the basal surface could generate abundant oxygen vacancies, creating additional reaction sites to improve the catalytic activity [31]. Such defects were considered to be derived from agar-gel aging process, which should be benefit for the total toluene oxidation at low temperatures.
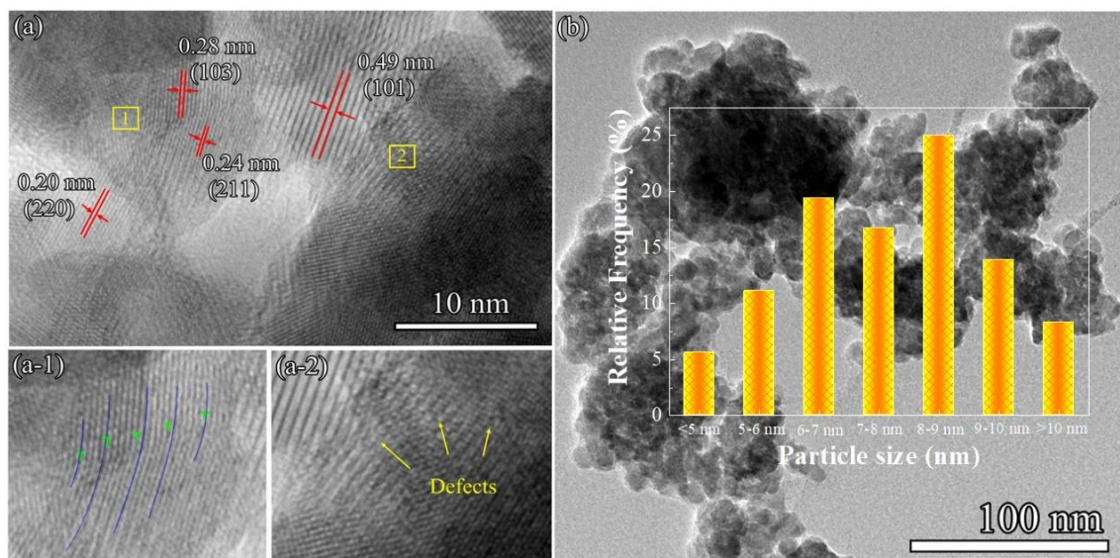
Fig 2.2. TEM images of single Mn oxide catalyst; (a), (a-1), (a-2) and (b) are different magnification areas. The edge dislocations are marked by green "T". The distribution of Mn particle size in (b).
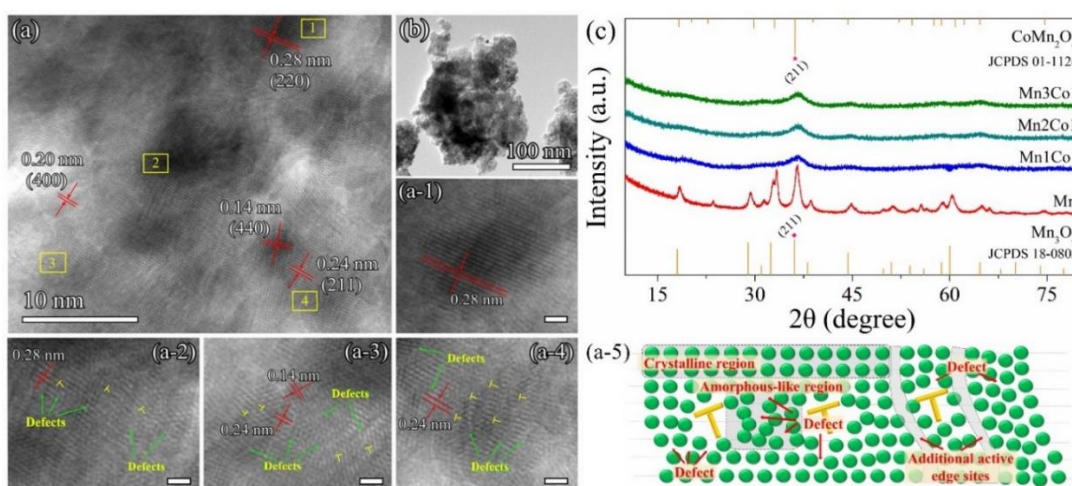
Fig 2.3. TEM images of the Mn2Co1 mixed oxide catalyst (a, b); (a-1), (a-2), (a-3) and (a-4) are different magnification areas in Fig. 1a. (a-5) Schematic illustration of defect

structure derived from edge dislocation with additional active edge sites generation. The edge dislocations are marked by yellow "T". The defects are indicated in Figs a-2 to a-4. Scale bar is 2 nm. XRD patterns of the as-prepared Mn_xCo_y mixed oxides (Mn-based catalysts) (c).

Fig. 2.3c show XRD patterns of the Mn_xCo_y mixed oxide catalysts. For the single Mn oxide, all diffraction peaks can be ascribed to those of Mn_3O_4 (JCPDS 18-0803) (Fig. 2.3c), which is consistent with the TEM observation results (Fig. 2.2). In contrast, for the Mn_xCo_y mixed oxides, the broad characteristic XRD peaks indicated the formation of $CoMn_2O_4$-like phase (JCPDS 01-1126), which is also consistent with the TEM analysis results (Fig. 2.3a). Herein, the main diffraction peaks corresponding to the $CoMn_2O_4$ phase were 18.3, 20.3, 29.9, 33.1, 36.2, 44.4, 54.2, 60.9, 64.7°. With the decrease in the percentage of Co species in mixed oxide catalyst, the intensity of diffraction peak got weaker and weaker, indicating that the incorporation of cobalt species lowered the crystallinity of Mn_3O_4 oxides with the formation of more amorphous-like structure. Meanwhile, the main (211) facet was observed clearly but slightly right-shifted, which should be resulted from the contraction of the unit cell due to the incorporation of cobalt into the Mn_3O_4 framework. The existence of the mixed crystalline and amorphous phases could lead to rich defect structures, thereby improving the intrinsic catalytic activity. For example, Aguilera *et al*. and Zhang *et al.* [2, 25] also reported that the coupling of Mn and Co species could result in the generation of amorphous phases with the enhancement of redox properties, leading to superior VOC oxidation activity. Herein, the similar effectiveness could be also expected for the catalytic total toluene oxidation. In addition, as shown in Fig. 2.3c, no typical broad peaks of amorphous carbon in the 2θ range of 20-30° and 40-45° were detected, demonstrating that the agar in Mn_xCo_y mixed catalysts was

85

completely removed in the annealing process and a portion of the carbon maybe remained as the carbide state in the catalysts [33].

2.3.2 Raman analysis

Fig. 2.4 shows Raman spectra of the prepared Mn_xCo_y mixed oxide catalysts. For the Mn-based ones, with the increase in the Co amount, the most intensive peak at 645 cm^{-1} belonging to the symmetric stretching of Mn (III, IV) decreased, and even disappeared in the case of the Mn/Co molar ratio of 1:1 whereas the weak peak at 355 cm^{-1} (out-of-plane bending modes) disappeared soon after the doping of Co species, indicating the strong interaction between Mn and Co species, which could weaken the Mn−O bond. These results are consistent with the XRD analysis results [32]. Meanwhile, three weak Raman peaks at the 190, 473, 515 cm^{-1} and a strong peak at 670 cm^{-1} were observed for the single Co oxide, where the strong Raman peak at 670 cm^{-1} was attributed to the Co_3O_4. With the addition of Mn species in the Co-based catalysts, even the strongest peaks became much broader, weaker and even shifted to some extent or disappeared, also suggesting the strong interaction between Mn and Co species [22]. As such, the mobility of oxygen species could be enhanced so that abundant oxygen vacancy defects could be more easily generated around the weakened Mn−O or Co−O bond, and the cycling of the emergence-annihilation of oxygen vacancy defects could be easily realized during the oxidation process, thereby improving the catalysis performance.
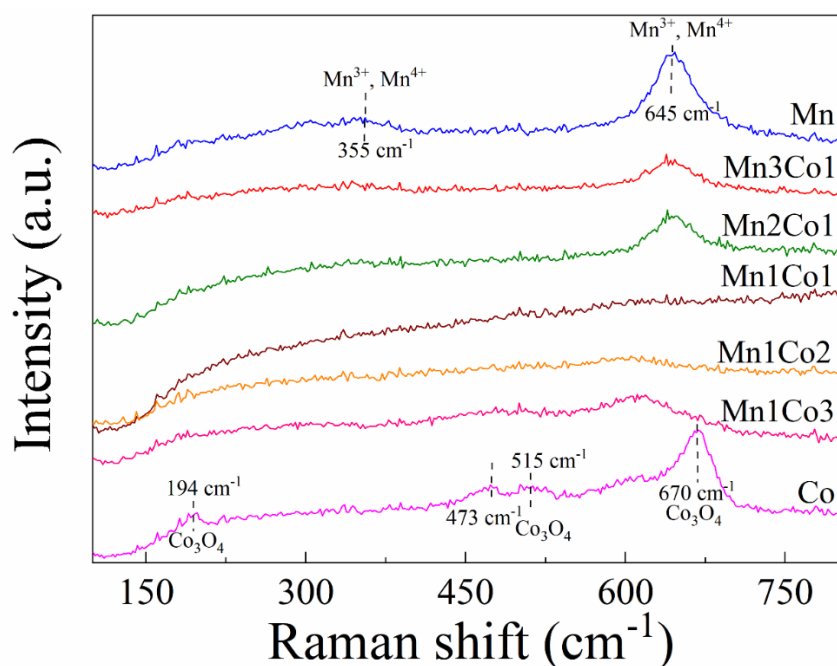
Fig 2.4. Raman spectra of the prepared Mn_xCo_y mixed oxide catalysts.

2.3.3 N_2 adsorption-desorption measurements

Fig. 2.5 show nitrogen adsorption-desorption isotherms of the Mn_xCo_y mixed oxide catalysts, respectively. One can see that all these catalysts had a type IV N_2 isotherm but with distinct H3-shaped hysteresis loops [34] at 0.4-1.0, 0.7-1.0, 0.45-1.0, 0.43-1.0 for the single Mn, Mn1Co1, Mn2Co1, and Mn3Co1 mixed oxide catalysts respectively, which should be resulted from the aggregation of nano-particles to form slit-like mesoporous pores (as indicated in the TEM images). Tables 2.1 summarize the corresponding BET surface areas of the Mn_xCo_y mixed oxide catalysts, respectively. One can see that the Mn2Co1 mixed oxide catalyst had the highest BET surface area and too large fractions of either Mn or Co were not beneficial for the improvement of surface area since they cannot result in good three-dimensional mesoporous structure. As such, the optimal Mo/Co ratio to achieve the best performances existed for Mn-based catalysts by using the agar-gel method. Hence, it can be concluded that the addition of Co species had

obvious influence on the pore structure of the Mn_xCo_y mixed oxide catalysts due to the strong interaction between Mn and Co species.
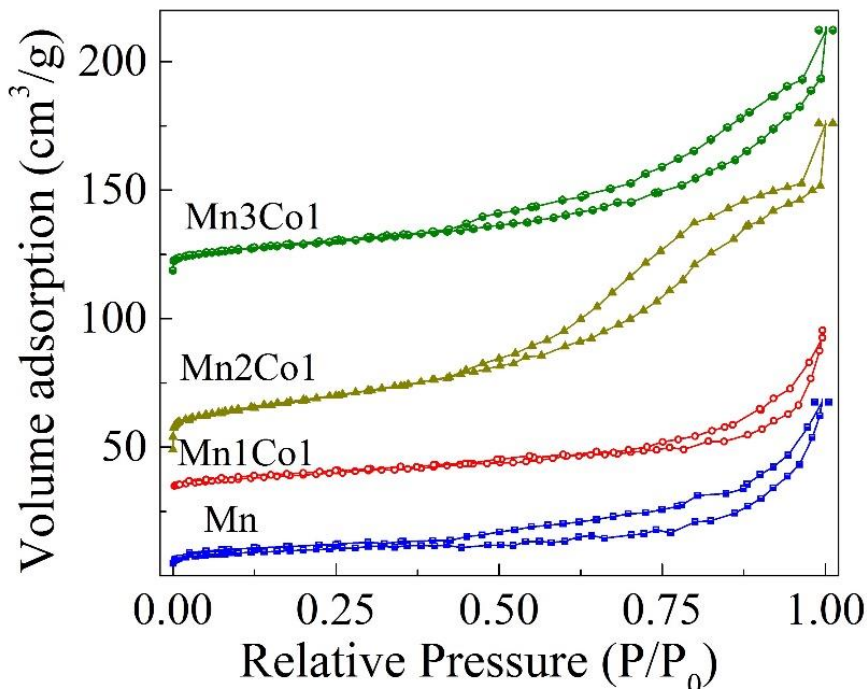
Fig 2.5. Nitrogen adsorption-desorption isotherms of the Mn_xCo_y mixed oxides (Mn-based catalysts).

2.3.4 O_2-TPD and H_2-TPR analyses

O_2-TPD analysis was applied for studying oxygen species and oxygen desorption behavior of the Mn_xCo_y mixed oxides and the results are shown in Fig. 2.6a and Table 2.2. Obviously, three O_2 desorption peaks in the temperatures centered at 223°C (α-species, O_2, O_2^- and O_2^{2-} adsorbed on O-vacancies), 414 °C (β-species, oxygen atoms bound to Mn(III)) and 561 °C (γ-species, oxygen atoms bound to Mn(IV)) were observed in the Mn oxide, which are consistence with the reported results [35]. For the Mn2Co1 and Mn3Co1 mixed oxide catalysts, the O_2 desorption peaks also appeared in the similar ranges of 150-300, 300-467, and 467-685 °C °C, respectively, but the corresponding peaks shifted to lower temperatures and became obviously stronger, indicating that the

oxygen desorption ability for the Mn2Co1 and Mn3Co1 mixed oxides was significantly enhanced via the doping of Co species into the MnO_x lattice by the agar-gel method, which should be benefit for the deep toluene oxidation at a lower temperature [36]. In comparison, only two peaks at a higher temperature range of 320-770 °C were observed for the Mn1Co1 mixed oxide, indicating no existence of O_2, O_2^- and O_2^{2-} species on it, which could lead to a low efficiency in the total toluene oxidation. Such differences between the single Mn oxide and the Mn-based Mn_xCo_y mixed oxides should be related to the conversion of crystal phase, especially the appearance of amorphous $CoMn_2O_4$ phase in the mixed oxides after the Co-doping using the agar-gel method [2, 37].
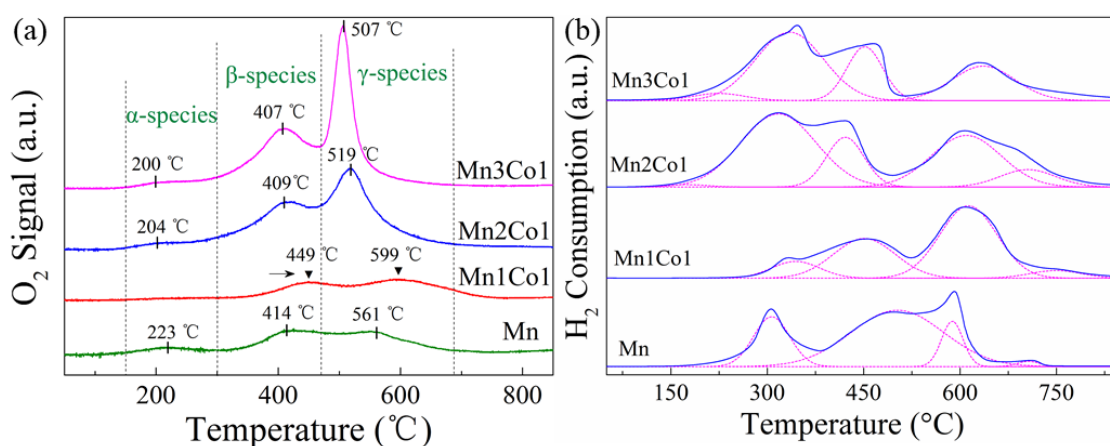
Fig 2.6. (a) O_2-TPD profiles and (b) H_2-TPR profiles of the Mn_xCo_y mixed oxides (Mn-based catalysts).

H2-TPR analysis was used for studying the reducibility of catalysts and the corresponding results are shown in Fig. 2.6b and Table 2.2. As shown in Fig. 2.6b, an obvious reduction peak at 306 °C, and other two large broad peaks at 491 and 591 °C were observed for the single Mn oxide catalyst, which corresponded to the reductions of $MnO_2 \rightarrow Mn_2O_3$, $Mn_2O_3 \rightarrow Mn_3O_4$, and $Mn_3O_4 \rightarrow MnO$, respectively [38, 39]. In comparison, for the Mn2Co1 and Mn3Co1 mixed oxides, two reduction peaks

89

corresponding to the reductions of $MnO_2 \rightarrow Mn_2O_3$ and $Mn_2O_3 \rightarrow Mn_3O_4$ at the similar peak positions became more obvious, implying that the Mn^{4+} and Mn^{3+} species should be the main species in these mixed oxides [38]. Thus, the incorporation of Co into MnO_x also promoted the reducibility of catalysts, which could enhance the total toluene oxidation at a lower temperature. Meanwhile, the peak area corresponding to the reduction of $Mn_3O_4 \rightarrow MnO$ in the high temperature region also became larger significantly, however, it should have a minimal effect on catalytic activity at the low operating temperature range in the toluene oxidation. In addition, for the Mn1Co1 mixed oxide, all the reduction peaks shifted to high temperature direction when comparing with the single Mn oxide, indicating its relatively poor reduction properties. Moreover, the peaks on the TPR at high temperature range (above 600 °C) in the Mn_xCo_y mixed oxide catalysts could be resulted from the reductions of the different local environment phases species, such as carbide, Co-Co, Mn-Co, and Mn-Mn [39], which also indicated the strong interaction between Co and Mn species in the Mn_xCo_y mixed oxide catalysts. As summarized in Table 2.2, the total amounts of O_2 consumptions were in the order of Mn3Co1> Mn2Co1 > Mn > Mn1Co1 whereas the total amounts of H_2 consumptions were in the order of Mn2Co1> Mn1Co1 > Mn3Co1> Mn. Thus, considering the oxygen species and reducibility, as confirmed in section 3.5, the Mn2Co1 mixed oxide had the best catalytic performance among all prepared catalysts for the total toluene oxidation.

2.3.5 XPS analysis

The surface atomic concentrations and valence states of elements on the catalysts were investigated by XPS analysis, and the results are shown in Fig. 2.6, and summarized in Tables 2.1. As shown in Fig. 2.6a, the Mn 2p spectra of the Mn_xCo_y mixed oxide catalysts can be decomposed into three main spin orbital lines with the binding energies at 640.5,

641.8 and 643.5 eV, which are assigned to the Mn^{2+}, Mn^{3+} and Mn^{4+} species, respectively [40]. The relatively high surface atomic ratios of Mn^{4+}/Mn^{2+} and Mn^{3+}/Mn^{2+} indicated the abundance Mn^{3+} and Mn^{4+} species on Mn2Co1 oxide, which are consistence with the H_2-TPR results. It should be noted that the Mn^{2+} amount on the Mn2Co1 oxide was lower than those on other Mn-based Mn_xCo_y mixed oxides but more Mn^{4+} and Mn^{3+} species were found on it, which could promote the redox property [41]. Meanwhile, the asymmetrical Co 2p XPS spectra featured at the binding energies of 780.9, 779.6 and 786.3 eV were assigned to Co^{3+} and Co^{2+} species (Fig. 2.6b) whereas the shake-up satellites were related to Co^{2+} species [42]. As summarized in Table 2.1, the surface molar ratio of Co^{3+}/Co^{2+} decreased in the sequence of Mn2Co1 > Mn3Co1≈Mn1Co1. Herein, more Co^{3+} species exposed on the surface of the Mn2Co1 oxide could also lead to excellent performance for the total toluene oxidation [22].

In Fig. 2.6c, the O 1s XPS spectrum of each Mn-based Mn_xCo_y mixed oxide catalyst can be divided into three peaks at the binding energies of 529.8, 531.2, and 533.5 eV, which are ascribed to the lattice oxygen (O_{latt}, O_2^{2-}), the surface adsorbed oxygen species with low coordination such as OH groups, oxygen vacancies (O_{ads}, O^{2-} or O^-), and the oxygen species in the adsorbed molecular water, respectively [43]. Generally, the surface adsorbed oxygen species, especially oxygen vacancy defects (O^{2-} or O^-), could contribute to a greater extent on the catalytic activity since they have higher mobility than the lattice oxygen [44]. As summarized in Table 2.1, the Mn2Co1 oxide had a highest ratio of O_{ads}/O_{latt} with the sequence of Mn2Co1 > Mn3Co1 > Mn > Mn1Co1, which is also consistence with the catalytic performances in the total toluene oxidation. Herein, it should be noted that the three surface molar ratios of O_{ads}/O_{latt}, Mn^{4+}/Mn^{2+}, and Co^{3+}/Co^{2+} on the Mn2Co1 mixed oxide catalyst were the highest ones among all the samples.

91

Table 2.2. Peak positions, O_2 consumptions in O_2-TPD and H_2 consumptions in H_2-TPR for the Mn-based Mn_xCo_y mixed oxide catalysts.

Catalyst	O_2-TPD (mmol/g)							H_2-TPR (mmol/g)						
	T (°C)	O_2-uptake	T (°C)	O_2-uptake	T (°C)	O_2-uptake	Total uptake	T (°C)	H_2-uptake	T (°C)	H_2-uptake	T (°C)	H_2-uptake	Total uptake
Mn	223	0.179	414	0.592	561	0.613	1.384	306	3.313	491	5.092	591	3.715	12.12
Mn1Co1	/	/	449	0.397	599	0.508	0.905	331	1.375	451	6.606	610	11.946	19.927
Mn2Co1	204	0.106	409	0.899	519	1.334	2.339	325	7.544	436	4.917	628	8.167	20.628
Mn3Co1	200	0.149	407	1.148	507	1.468	2.765	332	7.644	452	5.144	636	3.979	16.767

2.3.6 Catalytic performances

Toluene oxidations over all the prepared catalysts were performed under a WHSV = 60000 cm^3/(g h) at first, and the toluene conversions as a function of reaction temperature over the Mn-based catalysts and Co-based catalysts are shown in Fig. 2.8. As displayed in Fig. 2.8a, the toluene conversion increased with the rise in temperature, but the complete conversion temperatures had significant differences for different Mn_xCo_y mixed oxide catalysts. It is found that the Mn2Co1 mixed oxide catalyst exhibited the best performance in the total toluene oxidation to CO_2 and H_2O. As summarized in Table 2.3, the temperatures for converting half amount of toluene ($T_{50\%}$) and for converting completely ($T_{100\%}$) were in the order of Mn2Co1 (228 °C, 238 °C) < Mn3Co1 (243 °C, 254 °C) < Mn (253 °C, 270 °C) < Mn1Co1 (256 °C, 274 °C). Compared with the previously reported Mn-Co mixed oxide catalysts, the prepared Mn2Co1 mixed oxide catalyst in this study also showed a higher catalytic activity. Meanwhile, according to the temperature of mineralization as shown in Fig. 2.8b, the Mn2Co1 mixed oxide also

exhibited a better performance than those over other Mn-based catalysts. These results are well consistent with the characterizations as stated above. Herein, the intrinsic catalytic activity of the Mn-Co mixed oxide catalysts prepared by the ager-gel method for the toluene oxidation should be related to the oxygen vacancy defects on the catalysts. The strong interaction between Co and Mn species in Mn-Co mixed oxide could result in abundant the oxygen vacancy defects. Thus, the Mn2Co1 mixed oxide with the best catalytic performance for total toluene oxidation should be due to its appropriate molar ratio of Mn/Co, leading to higher surface molar ratios of O_{ads}/O_{latt}, Mn^{4+}/Mn^{2+}, Mn^{3+}/Mn^2 and Co^{3+}/Co^{2+} with more oxygen vacancies than other ones.

In addition, Fig. 2.8c compare the performances of Mn-based catalysts and Co-based catalysts in terms of $T_{50\%}$ and $T_{100\%}$ conversions along with the Mn/Co molar ratio. Interestingly, the plots of toluene conversion temperature *vs.* the Mn/Co molar ratio presented an inverted "M" shape with the increase of the Co ration. The Mn1Co1 mixed oxide catalyst exhibited a highest conversion temperature whereas the Mn2Co1 and Mn1Co2 mixed oxide catalysts showed the lowest conversion temperatures in the Mn-based and Co-based catalysts, respectively, which indicated that the optimal doping ratio existed for either Mn-bases or Co-based catalysts. In this study, Mn/Co of 2/1 (Mn2Co1 mixed oxide) and Mn/Co of 1/2 (Mn1Co2 mixed oxide) were the optimum balance ratio when the agar-gel method was used for the catalyst preparation.
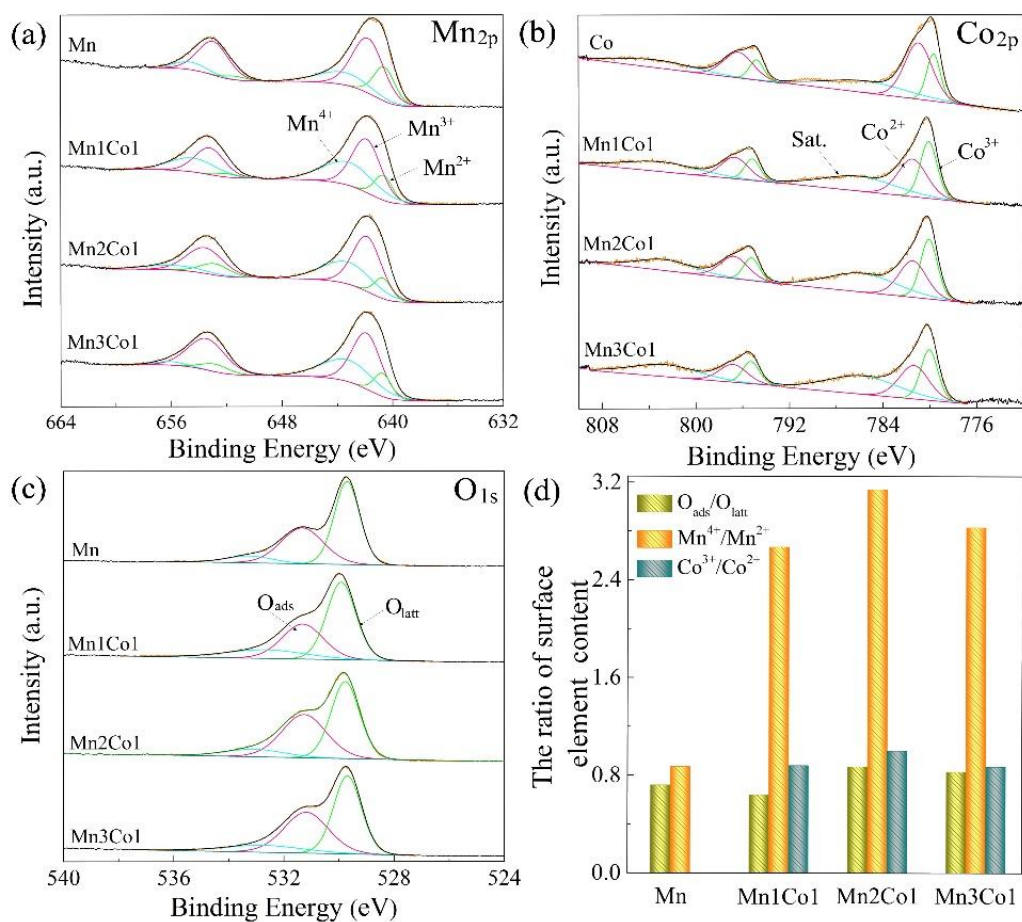
Fig 2.7. XPS spectra of (a) Mn 2p, (b) Co 2p, and (c) O 1s for the Mn-based catalysts, (d) Comparison of the surface molar ratios of O_{ads}/O_{latt}, Mn^{4+}/Mn^{2+}, and Co^{3+}/Co^{2+} on the surfaces of Mn-based catalysts.
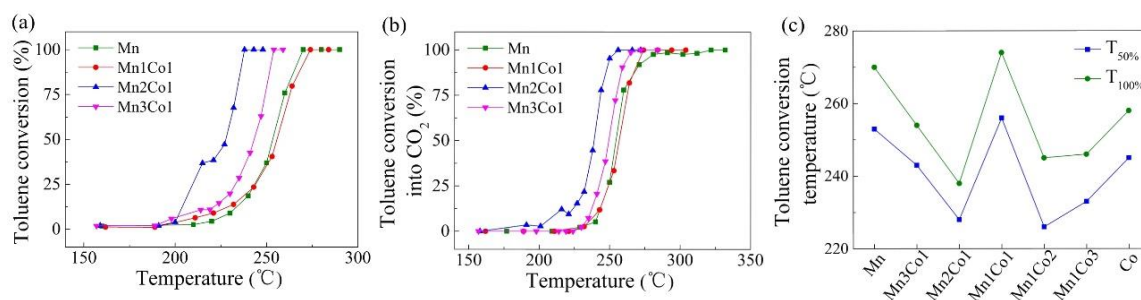
Fig 2.8. (a) Toluene conversions as a function of reaction temperature over the Mn-based catalysts; (b) CO_2 selectivity during the catalytic toluene oxidation; (c) Comparison between Mn-based catalysts and Co-based catalysts in terms of $T_{50\%}$ and $T_{100\%}$

94

conversions.

Table 2.3. Comparison of the performances of the Mn-Co mixed oxide catalysts reported in the literature with the present work.

Catalyst	Preparation Method	WHSV cm³/(g h)	Toluene conversion/°C			Stability time/h	Ref.
			$T_{50\%}$	$T_{90\%}$	$T_{100\%}$		
CoMn/AC oxide	Impregnation	66,000	244	246	263	11.7	[65]
Mn-Co oxides	Pyrolysis	96,000	226	240	300	25	[22]
Co1Mn1 BHNCs	Pyrolysis	60,000	232	248	300	35	[66]
Mn-Co (1:1)/CZ	Co-precipitation.	30,000	222	242	250	50	[67]
Co-Mn composite	Hydrothermal	30.000	263	267	270	30	[21]
Mn oxide	Agar-gel	60,000	253	266	270	/	
Mn1Co1 oxides	Agar-gel	60,000	256	270	274	/	This work
Mn2Co1 oxides	Agar-gel	60,000	228	236	238	50	
Mn3Co1 oxides	Agar-gel	60,000	243	252	254	/	

2.3.7 Effect of WHSV

WHSV is usually considered as a significant factor to affect the conversion in the catalytic VOCs oxidation [45]. Herein, the toluene conversions over the Mn2Co1 mixed oxide catalyst under different WHSVs of 30,000, 60,000 and 120,000 cm³/(g h) were investigated. As shown in Fig. 2.9a, the toluene conversion decreased gradually with the increase in the WHSV. When the WHSV was 60,000 cm³/(g h), $T_{50\%}$ (228 °C) and $T_{100\%}$ (238 °C) were obtained, which were only 13 and 6 °C higher than those under WHSV =30,000 cm³/(g h), but 16 and 20 °C lower than those under 120,000 cm³/(g h), respectively. As shown in Fig. 2.9b, the mineralization temperature under the WHSV of

60,000 cm^3/(g h) was higher than that of total toluene conversion. Meanwhile, the WHSVs of 30,000 and 120,000 cm^3/(g h) exhibited the mineralization temperatures similar to those of toluene conversion. It indicated that the WHSV had obvious effect on the toluene oxidation performance at a low reaction temperature. However, compared with the case where the WHSV=120,000 cm^3/(g h), the performance of catalytic toluene oxidation had a little difference when comparing with those in the cases of WHSVs =30,000 and 60,000 cm^3/(g h). Thus, to reduce the cost and maintain efficiency for the catalytic total toluene oxidation, the WHSV of 60,000 cm^3/(g h) was selected as the optimum one for the further study.
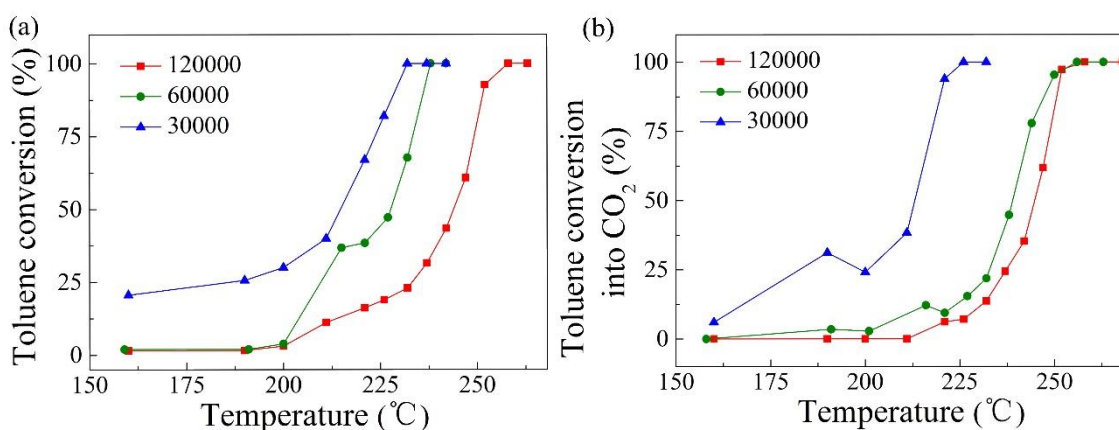
Fig 2.9. Effect of WHSV on the catalytic performance of Mn2Co1 mixed oxide catalyst (a) Toluene conversion; (b) Selectivity towards CO_2.

2.3.8 Stability test

To investigate the catalytic stability and durability, long-term activity of the Mn2Co1 mixed oxide catalyst was evaluated in the absence of water vapor under different temperatures at first. As shown in Fig. 2.10a, the complete oxidation of toluene maintained unchanged during the long-term test at a temperature of 252 °C, indicating that the catalyst was very stable at this temperature. After decreasing of the reaction temperature to 247 °C, the toluene conversion over the Mn2Co1 mixed oxide catalyst was

96

reduced to ca. 30% but also maintained long-term durability at this condition.

In order to further examine the effect of water vapor on the performance of the Mn2Co1 mixed oxide catalyst, 5, 10, and 20 vol% of water vapors were separately introduced into the reaction system with the air at a WHSV of 60,000 cm^3/(g h). As shown in Fig. 2.10b, the toluene conversion remained at 100% during the introducing of 5, 10 and 20 vol% H_2O at 252 °C in 50 h test period. At 247 °C, the conversion of toluene still maintained a stable value of ca. 30% in the presence of 5 vol% of water vapor. It is noteworthy that the further increasing of water vapor content to 10 and even 20 vol% resulted in the increase of conversion from ca. 30 % to ca. 40 %, which was higher at the same reaction temperature, indicating that the catalytic performance was improved after the addition of moderate amounts of water vapor. Herein, since abundant hydroxyl-modified sites existed on the Mn-Co mixed oxide catalysts, the introduction of H_2O vapor into the reaction system could activate those hydroperoxyl-like groups on the catalysts, which should be benefit to the activation O-O bond and enhancement of the O_2 replenishment during the oxidation process, thereby improving the performance [32]. In addition, more H_2O vapor introducing could more easily take away the generated intermediates from the surface of catalyst, which is also beneficial to expose the active sites for the deep oxidation. To further understand the improvement effect, *in situ* DRIFTS study was performed as shown in the following section 2.3.9. Moreover, after water vapor introduction was interrupted, the toluene conversion was recovered back to ca. 29%. In addition, the morphology of Mn2Co1 mixed oxide catalyst after the long-term stability test was observed, and as shown in Fig. 2.11, the 3D porous structure was also maintained, further indicating that the Mn2Co1 mixed oxide catalyst had good tolerance to the water vapor and retained excellent catalytic performance in the simulated real exhausting gas condition.
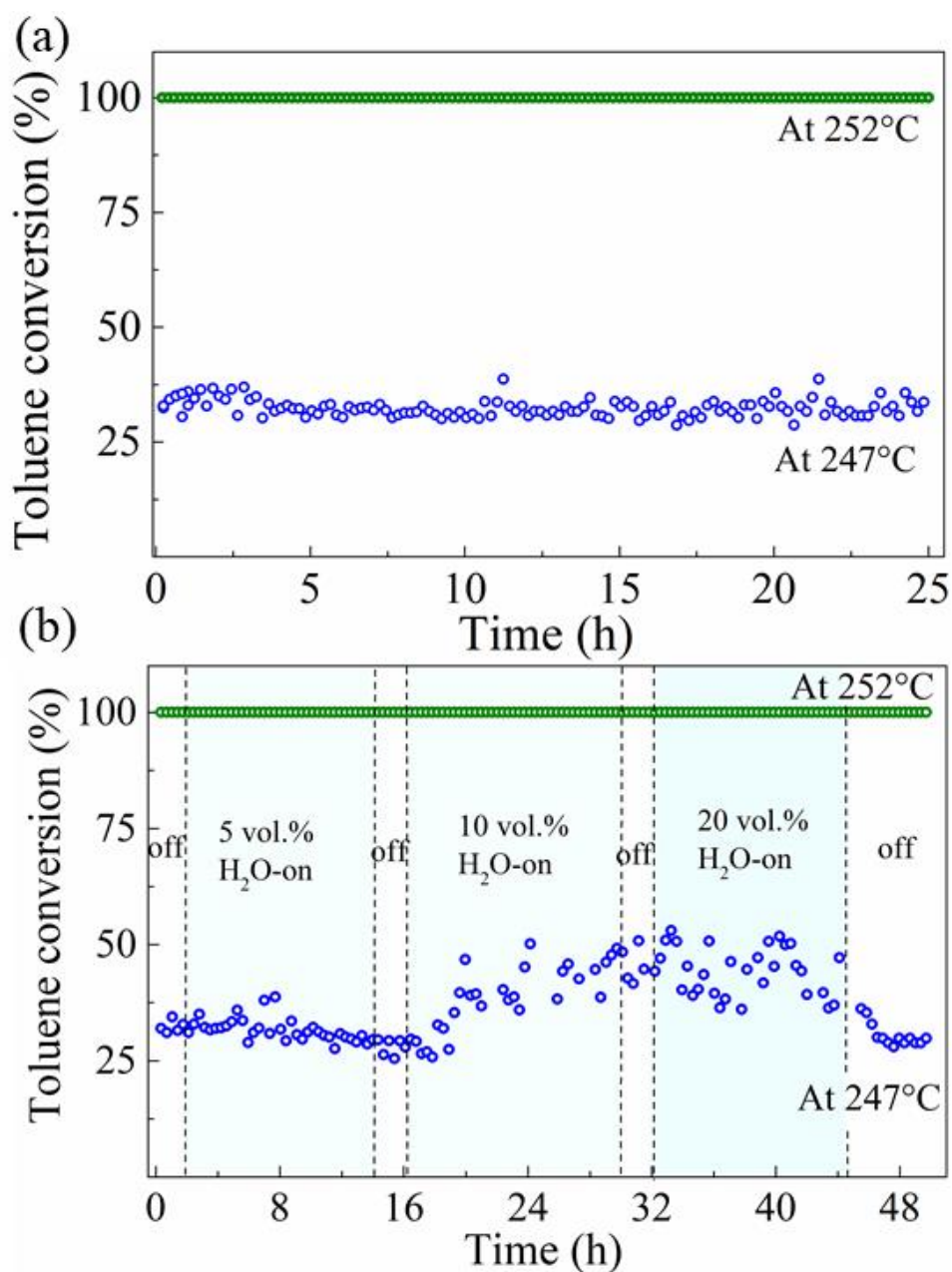
Fig 2.10. (a) Reaction stability test for the toluene oxidation over the Mn2Co1 mixed oxide catalyst; (b) Effect of water vapor on the catalytic stability and durability for the Mn2Co1 mixed oxide catalyst at 247 and 252 °C respectively with a WHSV of 60,000 cm^3/(g h).
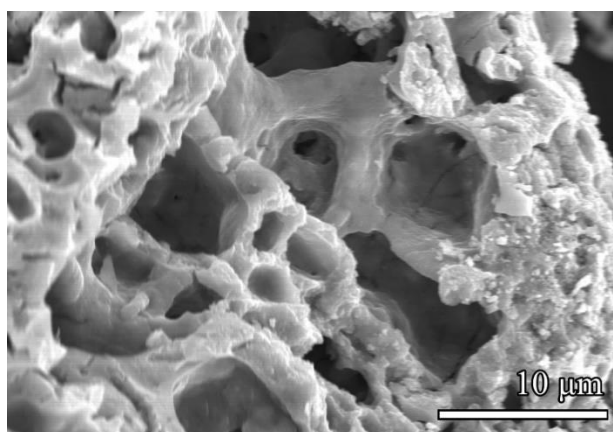
Fig 2.11. SEM image of Mn2Co1 mixed oxide catalyst after long-term stability test.

2.3.9 *In situ* DRIFTS analysis

The Mars-van Krevelen (MVK) mechanism is becoming widely accepted especially for the VOCs oxidation over the transition metal oxide catalysts. To understand the relationship between the surface adsorbed species and catalytic reaction process of toluene oxidations over the single Mn oxide and Mn2Co1 mixed oxide catalysts, *in situ* DRIFTS analysis was performed. As shown in Fig. 2.12, the peak at 1302 cm^{-1} is attributed to C-H in-plane bending vibration of toluene aromatic ring [46, 47], the peaks at 1072 and 1087 cm^{-1} belong to the CO− stretching vibrations of alkoxide, symbolizing the formation of benzyl alcohol [48], the peak at 1212 cm^{-1} corresponds to the CO− stretching vibration of phenolate species [47], the peak at 1302 cm^{-1} is assigned to CH$_2$ deformation vibration of benzyl [49], the peaks at around 1388 and 1551 cm^{-1} belong to the symmetric and antisymmetric carboxylate C=O stretching vibration of benzoate, respectively, and the peak at 1388 cm^{-1} may be also assigned to monodentate carbonates [50-52]. Herein, the bridging structure of carboxylate species can be confirmed by the distance ($\Delta\upsilon$) between asymmetric and symmetric carboxylate C=O stretching vibrations [53]. Meanwhile, the peaks at 1452, 1496 and 1603 cm^{-1} are attributed to skeletal C=C stretching vibration of the aromatic ring [51, 52, 54], the bands at 1725, 1795, 1863 and

1944 cm^{-1} are associated with the symmetric and asymmetric C=O stretching vibrations of maleic anhydride [48, 49], the peaks at 2749 and 2888 cm^{-1} can be assigned to C=O stretching vibrations of carbonyl, suggesting the formation of benzaldehyde species [55], the bands at approximately 2936 and 3038 cm^{-1} are ascribed to the symmetric and asymmetric CH- stretching vibrations of benzyl, respectively [56, 57], and the peak at 3086 cm^{-1} corresponds to the phenylic C-H stretching vibration of -CH$_3$ group [46, 47]. Furthermore, the final product of CO$_2$ indicated by the peaks at around 2324 and 2361 cm^{-1} were also observed obviously at the all *in situ* DRIFTS spectra and the intensities were gradually intensified with the prolonging of detecting time [32, 58]. In addition, the peak at around 3236 cm^{-1} is assigned to O-H, suggesting the formation of water as the important final product in the catalytic toluene oxidation.

Fig. 2.12a displays a typical set of time-dependent DRIFTS spectrum during a toluene oxidation process over the Mn oxide catalyst at 236 °C in N$_2$ atmosphere. It is observed that two weak peaks appeared at 1551 and 1388 cm^{-1} at the first 2 min period, and the related position on the $\Delta\upsilon$ (about 163 cm^{-1}) of asymmetric and symmetric C=O stretching vibration was very close to the free ion values, suggesting that the carboxylate species with a bridging structure were coupled with Mn valence ions on the surface of catalyst and the adsorbed toluene could interact with the oxygen species on the catalyst surface to produce benzoate with a rapid speed. However, many functional groups of intermediates were difficult to be observed at the first 5 min period besides the aromatic ring. With extending of reaction time, the species adsorbed on the catalyst surface increased significantly and accumulated to a maximum till 50 min. In this process, the peak at 1212 cm^{-1} appeared after 10 min, indicating that the CO- of phenolate species could be accumulated in the O$_2$-free environment. With further extending of time, four peaks at

1725, 1795, 1863, and 1944 cm^{-1} were detected, which also enhanced with the extending time, indicating that the related intermediates could react with lattice oxygen in the bulk to form anhydride even after exhausting the adsorbed oxygen species on the surface or subsurface of catalyst. In contrast, for the Mn2Co1 mixed oxide catalyst (Fig. 2.12c), all characteristic peaks appeared at the first 2 min period in the time-dependent DRIFTS spectra and their intensities increased significantly with extending of time, indicating that the Mn2Co1 mixed oxide catalyst accelerated the toluene oxidation rate more greatly than the pure Mn oxide catalyst. Moreover, it should be noted that there was no peak of carboxylate group at around 1550 cm^{-1} appeared, instead, the characteristic peak at 1388 cm^{-1} of carbonates monotonously increased, confirming that the oxygen-free atmosphere prevented the decomposition of carbonates preferentially to CO_2 and H_2O. Significantly, the weak peak at 1212 cm^{-1} was hardly observed, indicating that the formation of phenolate species was not enhanced with time in the toluene oxidation process. Thus, the benzoate should be preferentially decomposed to carbonates, or the transformation between phenolate and maleic anhydride could be interrupted rapidly on the surface of the Mn2Co1 mixed oxide catalyst. In addition, two higher peaks at around 2360 and 3236 cm^{-1} than those shown in the Fig. 2.12a belong to CO_2 and crystal water species respectively, demonstrating the mobility of oxygen species was greatly improved on the surface of the Co-doped Mn-based catalyst to enhance the formation of the final product when compared with the single Mn oxide catalyst. As stated above, the amorphous-like structure in the Mn2Co1 mixed oxide catalyst could produce abundant surface oxygen species, which can enhance the oxidation of the intermediates into CO_2 species. These results indicated that toluene can be rapidly adsorbed and activated on the surface of Mn2Co1 mixed oxide catalyst, which is conducive to the catalytic toluene oxidation even

under oxygen-free conditions due to the improvement of the migration rate of lattice oxygen as well as the oxygen storage capacity as confirmed by the O_2-TPD analysis.

Furthermore, in order to study the effect of O_2 in the gas phase on the toluene oxidation over the single Mn oxide and Mn2Co1 mixed oxide catalysts, air was introduced into the system at 236 °C for *in situ* DRIFTS analysis on the toluene adsorption and oxidation processes. As shown in Figs. 2.12b and d, all characteristic peaks of various intermediates appeared at the first 2 min period and their intensities gradually enhanced with the time increasing, indicating that the presence of O_2 accelerated the toluene oxidation rate. The relatively lower intensities of IR bands corresponding to anhydride were observed in Figs. 2.12b and d, indicating the presence of less maleic anhydride species under the air atmosphere since the consumable adsorbed oxygen species on the surface or subsurface of catalyst can be replenished and reconstructed rapidly by O_2 in the gas phase via the oxygen vacancy defects. Importantly, small differences were observed when compared with *in situ* DRIFTS spectra obtained in the N_2 atmosphere. For the single Mn oxide catalyst as shown in Fig. 2.12b, the intensity of peak at 1555 cm^{-1} assigning to benzoate obviously increased with the time due to the oxidation of the benzaldehyde to benzoate, manifesting that benzaldehyde was quickly transformed to benzoate in the presence of rich gaseous oxygen. Meanwhile, a weak band at 1212 cm^{-1} corresponding to phenolate was observed, implying that C=C could not be quickly broken to maleic anhydride or carbonates. In comparison, for the Mn2Co1 mixed oxide catalyst as shown in Fig. 2.12d, no increases in the characteristic peaks of benzoate, monodentate, and phenolate at around 1550, 1380, and 1212 cm^{-1} respectively with the time were observed, confirming that the Co-doped Mn-based catalyst can effectively promote the toluene oxidation. Therefore, it can be verified that the C=C breakage of the aromatic ring

could be the rate-controlling step in the catalytic toluene oxidation over the Mn-based catalysts. Herein, the oxygen vacancies caused by the abundant crystal defects could promote the C=C breakage of aromatic ring, which further accelerate the reaction efficiency [59].

Furthermore, the bond length for O_2 adsorbed on the surface of catalyst after migrating from gas phase to the oxygen vacancy defect site was investigated based on DFT calculations. In Fig. 2.13, the bond length was defined as the distance between the O atom and metal atom, which was represented by the dotted lines, and showed that the oxygen molecule was adsorbed on the model surface. Herein, 2.137 Å and 1.875 Å were the distances of two different Mn atoms on the Mn_3O_4 (211) plane in the single Mn oxide to O atom whereas 2.008 Å and 1.868 Å were the distances of Mn-O and Co-O on the $CoMn_2O_4$ (211) plane in the Mn_xCo_y mixed oxide, respectively. The shorter distances indicated that the oxygen adsorption ability was promoted by the doping of Co species on the Mn oxide. Moreover, the adsorption energy of O_2 adsorbed on the $CoMn_2O_4$ (211) plane was -4.2726 eV, which was also higher than that on the Mn_3O_4 (211) plane model, also demonstrating that the doping of Co species on the Mn oxide enhanced the O_2 adsorption ability on the (211) facet, which should be benefit for the replenishing and reconstructing of the surface adsorbed oxygen though O_2 in the gas phase for intermediate oxidation via abundant defect sites generated on amorphous region.

To further investigate the effect of water vapor on the formation of intermediates, 5 vol.% H_2O was introduced with 1000 ppm toluene/air atmosphere at 236 °C based on durability test over the Mn2Co1 mixed oxide catalyst under the condition with water vapor. As shown in Fig. 2.12e, all intensities of bands were higher than those recorded in the cases without water vapor, indicating that the presence of water vapor could activate

O-O bond, which should be benefit for the toluene adsorption on the surface of catalyst [32, 60]. Here, the intensities of the bands at ca. 2324 and 2361 cm^{-1} ascribed to the adsorbed CO_2, suggesting that the accumulation of CO_2 occurred on the surface of Mn-Co mixed catalyst. Meanwhile, the bands also attributed to the continuous increasing of carbonate species. As such, the competition between accumulation and desorption of CO_2 should exist on the active sites. However, in the water vapor environment, it should be noted that the characteristic band at 1402 cm^{-1} disappeared quickly at the first 2 min period, manifesting that the carbonates were quickly and preferentially transformed to CO_2 and H_2O, leading to the regeneration of active sites, which is beneficial to the catalyst stability. The durability test as shown Fig. 2.10b also confirmed that the introduction of water vapor enhanced the catalytic activity of toluene oxidation over the Mn2Co1 mixed oxide catalyst.

Based on the above DRIFTS spectra analyses, Table 2.4 summaries the important intermediates, and Fig. 2.12f illustrates the proposed mechanism for toluene oxidation on the surface of Mn-based catalysts. As shown in Fig. 2.12f, toluene molecule attracted on the surface of catalyst could be oxidized as the following order: benzyl $\rightarrow$ benzyl alcohol $\rightarrow$ benzaldehyde $\rightarrow$ benzoate. Then, the benzoate could be decomposed into either the short-chain carbonates by breaking C=C bond or phenolate by breaking C=O bond, and further oxidized to maleic anhydride and finally to CO_2 and H_2O. Herein, the fast C=C breaking of aromatic ring in benzoate could be the rate-controlling step. In addition, it should be noted that the typical time-dependent DRIFTS spectra exposed to the three environments of N_2, air and water vapor were similar, suggesting that both lattice oxygen and adsorbed oxygen in the Mn2Co1 mixed oxide catalyst could participate in the toluene oxidation since the rich defect sites in the catalyst could enhance the mobility of lattice

oxygen species, thereby improving the activation. Meanwhile, the consumable oxygen species would be replenished and reconstructed rapidly in the presence of gas-phase oxygen molecules via the oxygen vacancy defects.
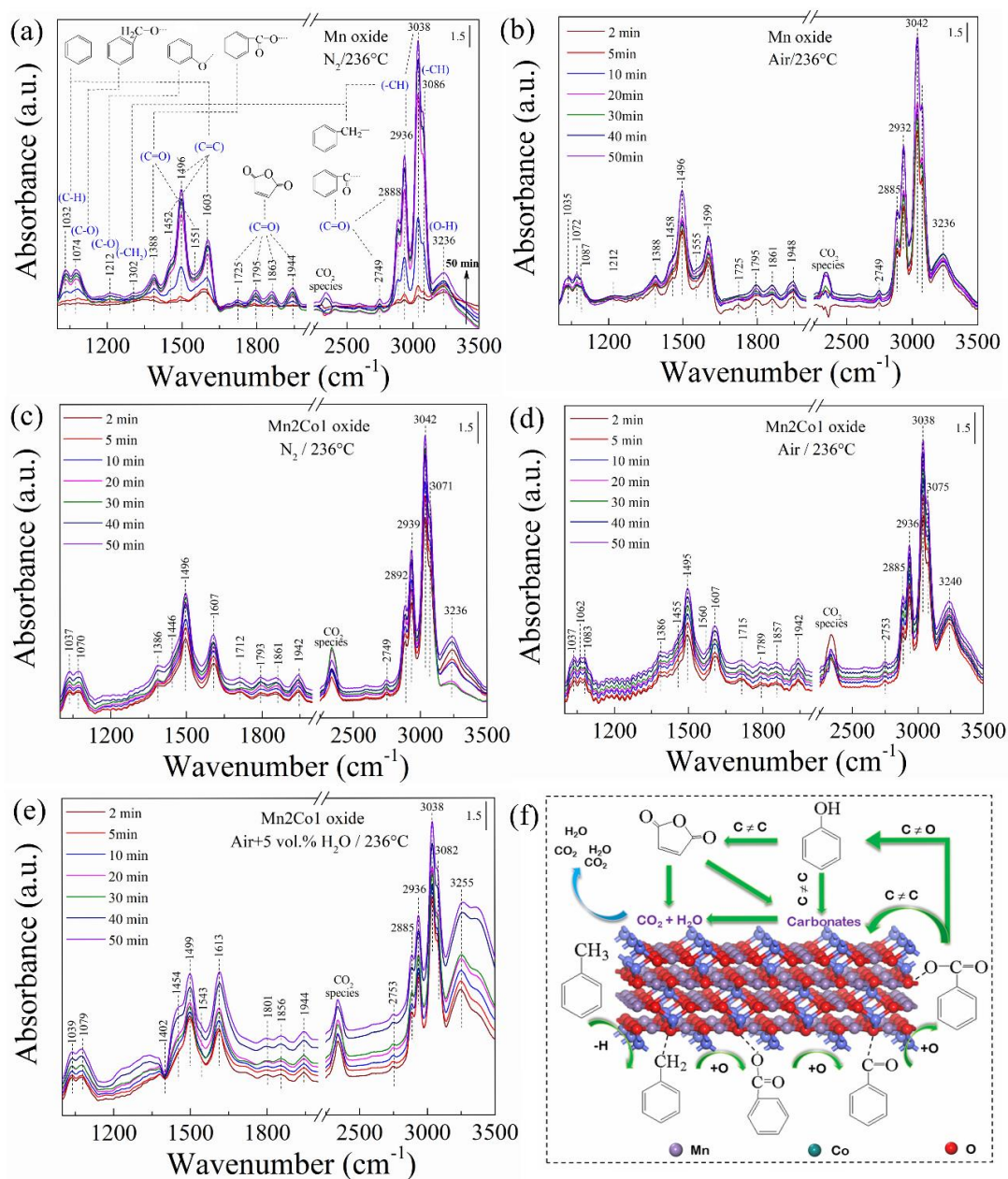
Fig 2.12. *In situ* DRIFTS spectra of toluene oxidation as a function of time exposed to (a) 1000 ppm toluene/N_2 atmosphere and (b) 1000 ppm toluene/air atmosphere over Mn oxide catalyst; (c) 1000 ppm toluene/N_2 atmosphere, (d) 1000 ppm toluene/air

atmosphere, and (e) 1000 ppm toluene/air atmosphere with 5 vol.% water vapor over Mn2Co1 mixed oxide catalyst; (f) Proposed mechanism for toluene oxidation over Mn-based catalysts.
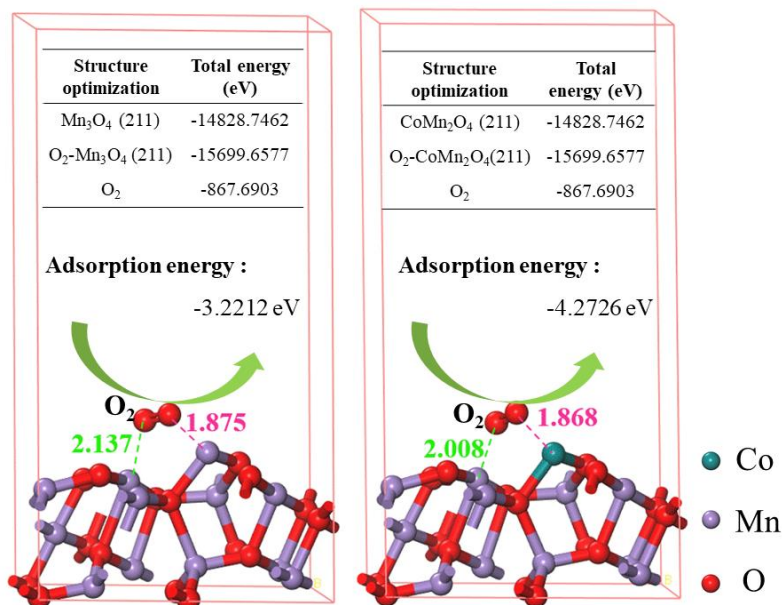
Fig 2.13. The models illustrating O_2 adsorbed on the surfaces of Mn_3O_4 (211) and $CoMn_2O_4$ (211), respectively.

Table 2.4. Assignment of IR bands appearing in the process of toluene oxidation over the Mn oxide catalyst and Mn2Co1 mixed oxide catalyst at 236 °C.

Position (cm^{-1})	Assignment	Corresponding species
1032	C-H in-plane bending vibration	Aromatic ring
1072, 1087	CO- stretching vibrations of alkoxide species	Benzyl alcohol
1212	CO- stretching vibration	Phenolate
1302	-CH$_2$ deformation vibration	Benzyl
1388, 1551	Symmetric and asymmetric C=O stretching vibrations of carboxylate group	Benzoate
1452, 1496, 1603	Skeletal C=C stretching vibrations	Aromatic ring
1725, 1795, 1863, 1944	Symmetric and asymmetric C=O stretching vibrations of cyclic anhydrides	Maleic anhydride
2749, 2888	C=O stretching vibrations of carbonyl	Benzaldehyde
2936, 3038	Symmetric and asymmetric CH- stretching	Benzyl

106

	vibrations of CH_2 group	
3086	Phenylic C-H stretching vibration	Aromatic ring
3236	O-H stretching vibrations	Crystal water

2.3.10 Effect of agar in the process of catalyst preparation

As discussed above, it is found that abundant adsorbed oxygen species are formed in the Mn2Co1 mixed oxide catalyst due to the rich defects, which should be originally derived from the agar structure. Agar is generally consisted of the polydisperse linear polymers of D-galactose and 3,6-anhydro-L-galactose with few variations in the repetitive units (Fig. 2.14) [61], resulting in at least two conformations, i.e., ordered and helical conformations [62]. Furthermore, the structural change is mainly resulted from a series of reactions regarding to the hydrolysis and oxidation [61, 63, 64]. As shown in Fig. 2.14, the aggregation of agar could occur primarily via intermolecular and intramolecular hydrogen bonds or Vander Waals forces. After the introduction of Mn^{2+} and Co^{2+} ions, the ionic bonds between the agar and metal ions will be formed. Subsequently, the agar gelation takes place with the generation of agarose, in which the divalent cations are wrapped in the structure of agar [62]. The combining effect of both agar conformations and chemical reactions should be taken into consideration in the agar-gel aging process. The helical conformation could result in the molecule rotation at random, where the rotational strength always depends on the configuration of the polymer chains attached with nearby metal ions like Mn^{2+} and Co^{2+} [62]. For example, a fraction of the Co^{2+} and Mn^{2+} ions attached to the helical conformation section could lead to the crystalline deformation, leading to the formation of edge dislocations and amorphous-like region in the final catalyst structure (as shown in Figs. 2.3a-2 to 1a-4). Meanwhile, Mn^{2+} and Co^{2+} connected with the ordered conformation section of agar could lead to the formation of crystalline region (Fig. 2.3a-1). Simultaneously, as shown in Fig. 2.14, the

polymer chains become shorter owing to the hydrolysis reaction and the generation of exfoliated small molecules, which could cause abundant defects and edge dislocation structures and more catalytic sites will be exposed. The intermolecular oxidation could make the hydroxyl groups connected to the primary carbon atoms, resulting in the formation of carboxyl functional groups and the generation of a large amount of free H^+ ions in the agar gel. According to the report by Yang *et. al* [48], the Mn-based catalyst can be treated by acid (H^+) to generate a relatively high amount of surface Mn^{4+} ions and probably lead to the formation of oxygen vacancy defects though the disproportionation of Mn^{3+}, which could further contribute to better oxygen mobility and lower temperature reducibility. Similarly, herein, it can be considered that the oxidation of hydroxyl groups promotes the H^+ ion generation, which can serve as leaching species to provide high concentration of oxygen vacancy defects in the final oxide catalysts. As such, the high concentration of defects is conducive to the formation of adsorbed oxygen species on the surface or subsurface of catalysts.

2.4 Conclusions

The Mn_xCo_y mixed oxide catalysts with defect-rich structures were successfully synthesized using the agar-gel method. It is demonstrated that the molar ratio of Mn/Co greatly affected the phase structure and textural properties of the as-prepared catalysts. Among the Mn_xCo_y mixed oxide catalysts, the Mn2Co1 mixed oxide catalyst exhibited a highest catalytic performance with $T_{50\%}$ of 228 °C and $T_{100\%}$ of 238 °C for the toluene oxidation. According to the characterizations of the Mn2Co1 mixed oxide catalyst, it is considered that the enhanced catalytic performance was contributed to the higher surface area, higher contents of Mn^{4+}, Mn^{3+} and Co^{3+} species with more oxygen vacancies and better reducibility. The high stability and renewability of Mn2Co1 mixed oxide catalyst

were also confirmed by the activity and endurability tests with 5, 10, and 20 vol% of water vapors. Furthermore, *in situ* DRIFTS analysis revealed that both adsorbed oxygen and lattice oxygen species could simultaneously participate in the toluene adsorption-oxidation process, especially the rate-controlling step should be the C = C breakage of aromatic ring. It is expected that the present agar-gel method with low cost and convenient operation can be widely applied for the designing of novel mixed metal oxides catalysts for VOCs oxidation.

Fig 2.14. Schematic diagram of the synthesis of Mn_xCo_y mixed oxide catalysts using the agar-gel method.

References

[1]   V. Héquet, C. Raillard, O. Debono, F. Thévenet, N. Locoge, L. Le Coq, Applied Catalysis B: Environmental 226 (2018) 473-486.

[2]   Q. Zhang, X. Liu, W. Fan, Y. Wang, Applied Catalysis B: Environmental 102 (2011) 207-214.

[3]   H. Huang, Y. Xu, Q. Feng, D.Y.C. Leung, Catalysis Science & Technology 5 (2015) 2649-2669.

[4]   L.F. Liotta, H. Wu, G. Pantaleo, A.M. Venezia, Catalysis Science & Technology 3 (2013) 3085.

[5]   L. Malhautier, G. Quijano, M. Avezac, J. Rocher, J.L. Fanlo, Chemical Engineering Journal 247 (2014) 199-204.

[6]   L. Li, S. Liu, J. Liu, Journal of Hazardous Materials 192 (2011) 683-690.

[7]   F. Thevenet, L. Sivachandiran, O. Guaitella, C. Barakat, A. Rousseau, Journal of Physics D: Applied Physics 47 (2014) 224011.

[8]   C.J. Hennigan, M.M.H. El-Sayed, A. Hodzic, Atmospheric Environment 188 (2018) 12-17.

[9]   C. Zhang, C. Wang, W. Zhan, Y. Guo, Y. Guo, G. Lu, A. Baylet, A. Giroir-Fendler, Applied Catalysis B: Environmental 129 (2013) 509-516.

[10]   Y. Wang, Y. Xue, C. Zhao, D. Zhao, F. Liu, K. Wang, D.D. Dionysiou, Chemical Engineering Journal 300 (2016) 300-305.

[11]   G. Spezzati, A.D. Benavidez, A.T. DeLaRiva, Y. Su, J.P. Hofmann, S. Asahina, E.J. Olivier, J.H. Neethling, J.T. Miller, A.K. Datye, E.J.M. Hensen, Applied Catalysis B: Environmental 243 (2019) 36-46.

[12]   S. Xie, Y. Liu, J. Deng, X. Zhao, J. Yang, K. Zhang, Z. Han, H. Arandiyan, H.

Dai, Applied Catalysis B: Environmental 206 (2017) 221-232.

[13]   H. Deng, S. Kang, J. Ma, C. Zhang, H. He, Applied Catalysis B: Environmental 239 (2018) 214-222.

[14]   K. Everaert, J. Baeyens, Journal of Hazardous Materials 109 (2004) 113-139.

[15]   W.B. Li, J.X. Wang, H. Gong, Catalysis Today 148 (2009) 81-87.

[16]   M. Romero-Sáez, D. Divakar, A. Aranzabal, J.R. González-Velasco, J.A. González-Marcos, Applied Catalysis B: Environmental 180 (2016) 210-218.

[17]   Z. Ren, Z. Wu, W. Song, W. Xiao, Y. Guo, J. Ding, S.L. Suib, P.-X. Gao, Applied Catalysis B: Environmental 180 (2016) 150-160.

[18]   L. Lamaita, M.A. Peluso, J.E. Sambeth, H. Thomas, G. Mineli, P. Porta, Catalysis Today 107-108 (2005) 133-138.

[19]   L. Lamaita, M.A. Peluso, J.E. Sambeth, H.J. Thomas, Applied Catalysis B: Environmental 61 (2005) 114-119.

[20]   B. Chen, X. Yang, X. Zeng, Z. Huang, J. Xiao, J. Wang, G. Zhan, Chemical Engineering Journal 397 (2020) 125424.

[21]   X. Jiang, W. Xu, S. Lai, X. Chen, RSC Advances 9 (2019) 6533-6541.

[22]   Y. Luo, Y. Zheng, J. Zuo, X. Feng, X. Wang, T. Zhang, K. Zhang, L. Jiang, Journal of Hazardous Materials 349 (2018) 119-127.

[23]   Z. Li, Q. Yan, Q. Jiang, Y. Gao, T. Xue, R. Li, Y. Liu, Q. Wang, Applied Catalysis B: Environmental 269 (2020) 118827.

[24]   C. Dong, Z. Qu, X. Jiang, Y. Ren, Journal of Hazardous Materials 391 (2020) 122181.

[25]   D.A. Aguilera, A. Perez, R. Molina, S. Moreno, Applied Catalysis B: Environmental 104 (2011) 144-150.

[26]   X. Li, J. Zheng, S. Liu, T. Zhu, Journal of Colloid and Interface Science 555 (2019) 667-675.

[27]   D.P. Debecker, V. Hulea, P.H. Mutin, Applied Catalysis A: General 451 (2013) 192-206.

[28]   J. Wang, A. Yoshida, P. Wang, T. Yu, Z. Wang, X. Hao, A. Abudula, G. Guan, Applied Catalysis B: Environmental 271 (2020) 118941.

[29]   M. Zhao, J. Deng, J. Liu, Y. Li, J. Liu, Z. Duan, J. Xiong, Z. Zhao, Y. Wei, W. Song, Y. Sun, ACS Catalysis 9 (2019) 7548-7567.

[30]   X. Lin, S. Li, H. He, Z. Wu, J. Wu, L. Chen, D. Ye, M. Fu, Applied Catalysis B: Environmental 223 (2018) 91-102.

[31]   X. Li, X. Su, Y. Pei, J. Liu, X. Zheng, K. Tang, G. Guan, X. Hao, Journal of Materials Chemistry A 7 (2019) 10745-10750.

[32]   L. Zhao, Z. Zhang, Y. Li, X. Leng, T. Zhang, F. Yuan, X. Niu, Y. Zhu, Applied Catalysis B: Environmental 245 (2019) 502-512.

[33]   A.A. Voevodin, S.V. Prasad, J.S. Zabinski, Journal of Applied Physics 82 (1997) 855-858.

[34]   L. Yu, R. Peng, L. Chen, M. Fu, J. Wu, D. Ye, Chemical Engineering Journal 334 (2018) 2480-2487.

[35]   Y.G. Yin, W.Q. Xu, R. Deguzman, S.L. Suib, C.L. O'Young, Inorganic Chemistry 33 (1994) 4384-4389.

[36]   X. Xie, Y. Li, Z.Q. Liu, M. Haruta, W. Shen, Nature 458 (2009) 746-749.

[37]   L. Xue, C. Zhang, H. He, Y. Teraoka, Applied Catalysis B: Environmental 75 (2007) 167-174.

[38]   W. Gac, Applied Catalysis B: Environmental 75 (2007) 107-117.

[39]   S. Todorova, H. Kolev, J.P. Holgado, G. Kadinov, C. Bonev, R. Pereñíguez, A. Caballero, Applied Catalysis B: Environmental 94 (2010) 46-54.

[40]   Z. Sihaib, F. Puleo, J.M. Garcia-Vargas, L. Retailleau, C. Descorme, L.F. Liotta, J.L. Valverde, S. Gil, A. Giroir-Fendler, Applied Catalysis B: Environmental 209 (2017) 689-700.

[41]   Z. Ye, J.M. Giraudon, N. Nuns, P. Simon, N. De Geyter, R. Morent, J.F. Lamonier, Applied Catalysis B: Environmental 223 (2018) 154-166.

[42]   H. Yi, Z. Yang, X. Tang, S. Zhao, F. Gao, J. Wang, Y. Huang, Y. Ma, C. Chu, Q. Li, J. Xu, Chemical Engineering Journal 333 (2018) 554-563.

[43]   V.P. Santos, M.F.R. Pereira, J.J.M. Órfão, J.L. Figueiredo, Applied Catalysis B: Environmental 99 (2010) 353-363.

[44]   M.A. Peluso, L.A. Gambaro, E. Pronsato, D. Gazzoli, H.J. Thomas, J.E. Sambeth, Catalysis Today 133-135 (2008) 487-492.

[45]   J. Chen, X. Chen, X. Chen, W. Xu, Z. Xu, H. Jia, J. Chen, Applied Catalysis B: Environmental 224 (2018) 825-835.

[46]   H. Sun, Z. Liu, S. Chen, X. Quan, Chemical Engineering Journal 270 (2015) 58-65.

[47]   Q. Zhang, S. Mo, J. Li, Y. Sun, M. Zhang, P. Chen, M. Fu, J. Wu, L. Chen, D. Ye, Catalysis Science & Technology 9 (2019) 4538-4551.

[48]   X. Yang, X. Yu, M. Lin, X. Ma, M. Ge, Catalysis Today 327 (2019) 254-261.

[49]   J. Li, H. Na, X. Zeng, T. Zhu, Z. Liu, Applied Surface Science 311 (2014) 690-696.

[50]   A. Lu, H. Sun, N. Zhang, L. Che, S. Shan, J. Luo, J. Zheng, L. Yang, D.-L. Peng, C.-J. Zhong, B. Chen, ACS Catalysis 9 (2019) 7431-7442.

[51]   S. Mo, Q. Zhang, Y. Sun, M. Zhang, J. Li, Q. Ren, M. Fu, J. Wu, L. Chen, D. Ye, Journal of Materials Chemistry A 7 (2019) 16197-16210.

[52]   C. Zhang, C. Wang, H. Huang, K. Zeng, Z. Wang, H.-p. Jia, X. Li, Applied Surface Science 486 (2019) 108-120.

[53]   X. Chemical Engineering JournalChen, X. Chen, E. Yu, S. Cai, H. Jia, J. Chen, P. Liang, Chemical Engineering Journal 344 (2018) 469-479.

[54]   M.D. Hernández-Alonso, I. Tejedor-Tejedor, J.M. Coronado, M.A. Anderson, Applied Catalysis B: Environmental 101 (2011) 283-293.

[55]   X. Du, X.G. Hao, Z.D. Wang, G.Q. Guan, Journal of Materials Chemistry A 4 (2016) 6236-6258.

[56]   M. Wang, F. Zhang, X. Zhu, Z. Qi, B. Hong, J. Ding, J. Bao, S. Sun, C. Gao, Langmuir 31 (2015) 1730-1736.

[57]   J.-J. Li, E.-Q. Yu, S.-C. Cai, X. Chen, J. Chen, H.-P. Jia, Y.-J. Xu, Applied Catalysis B: Environmental 240 (2019) 141-152.

[58]   S. Mo, Q. Zhang, J. Li, Y. Sun, Q. Ren, S. Zou, Q. Zhang, J. Lu, M. Fu, D. Mo, J. Wu, H. Huang, D. Ye, Applied Catalysis B: Environmental 264 (2020) 118464.

[59]   X. Dong, W. Cui, H. Wang, J. Li, Y. Sun, H. Wang, Y. Zhang, H. Huang, F. Dong, Science Bulletin 64 (2019) 669-678.

[60]   A. Bongiorno, U. Landman, Physical Review Letters 95 (2005) 106102.

[61]   B. Mao, A. Bentaleb, F. Louerat, T. Divoux, P. Snabre, Food Hydrocolloids 64 (2017) 59-69.

[62]   A.H. Clark, Food Polymers Gels & Colloids 83 (1991) 322-338.

[63]   R. Armisén, F. Gaiatas, Handbook of Hydrocolloids (2009) 82-107.

[64]   J. Zhao, Z. Chen, R. Zou, X. Zhang, Food Hydrocolloids 77 (2018) 421-426.

114

[65]   G. Zhou, X. He, S. Liu, H. Xie, M. Fu, Journal of Industrial and Engineering Chemistry 21 (2015) 932-941.

[66]   Z. Weitao, Z. Yang-Yu, W. Xiangwei, Z. Yingying, W. Xiuyun, A. Chak-Tong, J. Lilong, Catalysis Science & Technology 8 (2018) 4494-4502.

[67]   J. Feng, Z.-Y. Hou, X.-Y. Zhou, H.-L. Zhang, T.-Q. Cheng, T. Lin, Y.-Q. Chen, Chemical Papers 72 (2017) 161-172.

Chapter 3 Holmium-assisting delaminated octahedral molecular sieve catalysts with abundant active oxygen species for total toluene oxidation

3.1 Introduction

Nowadays, significantly increasing of various pollutants especially the harmful volatile organic compounds (VOCs) has caused great environmental deterioration and human health threat [1, 2]. For VOCs removal, various technologies such as photocatalysis [3], self-precipitation [4], vacuum adsorption [5], wet scrubbing [6] and catalytic combustion [7, 8] have been studied and some of them have been successfully applied in the practical process. In particular, the catalytic oxidation of VOCs at low temperature is considered as the most effective way with less energy consumption and low cost [7, 8]. However, developing of catalysts with high-performance is the crucial step for applications. Two categories of catalysts, i.e., the supported noble metal catalysts (e.g., Pt, Au and Pd based catalysts) [8-11] and transition metal oxide based catalysts (e.g., MnO_x, Co_3O_4 and CeO_2 based catalysts) [7, 12, 13], are widely studied. Compared with the supported noble metal ones, the transition metal oxide based catalysts have attracted extensive attentions due to their low cost and comparably high stability and good oxygen storage capacity.

Cryptomelane-type manganese oxide octahedral molecular sieve (*OMS-2*) with a tunnel size of 0.46 nm × 0.46 nm and K^+ ions in the tunnel for charge balancing is made from the edge-sharing double MnO_6 octahedral chains, in which some chains are corner-shared to result the formation of one dimensional tunnel [14, 15]. Owing to its unique

116

porous structure, mixed valences (Mn^{2+}, Mn^{3+}, and Mn^{4+}), easy mobility of lattice oxygen and rich acidic sites, it is confirmed that the *OMS-2 has high performance for* the catalytic oxidation of hydrocarbons [16-20]. Especially, the nanostructure and oxygen distribution on the OMS-2 play important roles on the catalytic reactions on the surface of OMS-2, which always follows the Mars-van Krevelen (MVK) mechanism, i.e., the reaction occurs between the absorbed VOC molecules and the lattice oxygen on the OMS-2. Thus, the VOC oxidation over OMS-2 relies on the oxygen-rich sites on the surface of OMS-2 rather than O_2 molecule in the gas phase [21, 22]. Based on this mechanism, a feasible strategy to promote the OMS-2 catalytic activity should be the increase of surface oxygen vacancies on it, which could be effectively replenished by gaseous oxygen or lattice oxygen moving from the bulk [23]. Li *et al*. [24] constructed OMS-2 nanorods and tuned the oxygen vacancy defect content via controlling the synthesis temperature. They observed that the increase in the oxygen vacancy defect content considerably enhanced the lattice oxygen reactivity during the deep toluene oxidation process. To increase the oxygen vacancies and active interfaces, Yu *et al.*[25] synthesized the OMS-2 with $NaBH_4$ reduction. They also found that the concentration of surface oxygen vacancies had strong relationship with the molar ratio of adsorbed oxygen (O_{ads}) and lattice oxygen (O_{latt}), which directly related to catalytic activity. Hence, various existing oxygen species on the catalysts could affect the VOC oxidation efficiency, and suitably tune the relative amounts among lattice oxygen, adsorbed oxygen, and oxygen vacancies in the design of highly efficient OMS-2 based catalysts is necessary.

To date, various strategies for the modulating of oxygen vacancy concentration in OMS-2, including chemical etching (ion-exchange of K^+ in the channel) [26], atom substitution (multiple substitution of various ions into OMS-2 structure) [19, 27] and

117

surface modification (increasing surface area) [28], have been proposed. The obtained OMS-2 catalysts always have good crystallinity. However, the relative perfect crystallinity of OMS-2 always provides limited surface oxygen number and reduced interfaces, especially less oxygen vacancies, thereby resulting in relatively low VOC oxidation performance [24]. To solve this issue, it is possible to introduce some amorphous-like phases on the OMS-2, which could increase the surface area, enhance the lattice oxygen mobility, and lead to rich unsaturated coordination, thereby providing abundant surface oxygen, oxygen vacancies, and interfaces as the active sites for the VOC oxidation [12, 29, 30]. However, it should be also noted that excessive amorphous OMS-2 phase could vice versa weaken the oxidation capability owing to the competitive water adsorption on the surface in the treatment of practical VOCs emission with steam [25, 30]. Therefore, modulating the ratio of crystallinity and amorphous in OMS-2 based catalysts should be also necessary for obtaining highly stable OMS-2 for the VOC oxidation.

Herein, the ratio of crystallinity and amorphous phase in OMS-2 was tuned by doping holmium (Ho) with different amounts (x% Ho-OMS-2) via a facile redox co-precipitation method using $KMnO_4$, $Mn(CH_3COO)_2$, and $Ho(NO_3)_3$ as the precursors and applied for the catalytic oxidation of toluene. Scanning electron microscopy (SEM), Transmission electron microscopy (TEM), Energy dispersive X-ray spectrometry (EDX), X-ray diffraction (XRD), Raman, N_2-physisorption, Hydrogen temperature-programmed reduction (H_2-TPR), Oxygen temperature-programmed desorption (O_2-TPD), Electron paramagnetic resonance (EPR) and X-ray photoelectron spectroscopy (XPS) were applied to explore the relationships between the correlating physiochemical properties and the catalysis performance. Furthermore, *in situ* DRIFT analyses were carried out to

understand the possible toluene oxidation pathways over the x% Ho-OMS-2 catalysts.

3.2 Experimental

3.2.1 Preparation of catalysts

OMS-2 and x% Ho-OMS-2 were prepared with a redox co-precipitation way [31, 32] by using potassium permanganate ($KMnO_4$, Wako, Japan), manganous acetate ($Mn(CH_3COO)_2 \cdot 4H_2O$, Wako, Japan), and holmium nitrate ($Ho(NO_3)_3 \cdot 5H_2O$, Wako, Japan) as the precursors. Briefly, 1.475 g $KMnO_4$ and the calculated amount of $Ho(NO_3)_3 \cdot 5H_2O$ (i.e., 0, 0.0148, 0.0735, 0.221 or 0.443 g) was dissolved in 350 mL of deionized (DI) water as (I) solution to maintain x% = 0, 0.1, 0.5, 1 and 3 wt%, respectively. 3.063 g of $Mn(CH_3COO)_2 \cdot 4H_2O$ was dissolved in 350 mL of DI water to obtain (II) solution. Then, a liquid feeding pump was used to feed the (I) solution into the (II) solution with 10 mL/min under strenuous stirring at ambient temperature. The obtained mixed solution was aged for 3 h. Finally, the suspension was centrifugated and washed for three times using DI water, dried at 60 °C for 24 h and calcined at 350 °C in air for 3h (heating rate = 5 °C/min). The obtained sample was denoted based on the doping weight percentages of Ho as follows: 0.1% Ho-OMS-2, 0.5% Ho-OMS-2, 1% Ho-OMS-2, and 3% Ho-OMS-2. Meanwhile, the pure OMS-2 was prepared for a reference.

3.2.2 Catalyst characterizations

Morphology of the sample was obtained on SEM machine (Hitachi SU8010, Japan) with an applied voltage of 15 kV. Nanostructure was observed on a TEM system (JEM-2100, Japan) at 200 kV. The distribution of holmium, manganese, potassium and oxygen elements on the surface of the sample was characterized by the EDX mapping. Crystalline structure was analyzed by a XRD instrument (Rigaku Smartlab, Japan) with a Cu-Kα

radiation (λ=1.5418 Å) in a 2θ range of 10-90° and the scanning rate was set at 10 °/min. Raman analysis was conducted on a Laser Raman spectrometer (JASCO NRS-5100) at 532 nm. Nitrogen adsorption-desorption isotherm was performed at 77.3 K on a Nova 4200 equipment (Quantachrome Inc., USA) after the sample was evacuated at 300 °C for 12 h. EPR measurement was carried out at room temperature on a Bruker A300 spectrometer (Bruker, Germany) operating at the center field of 3520 G with a sweep width of 100 G, a microwave frequency of 9.77 GHz, a modulation frequency of 100 kHz and a power supply of 12.72 mW. The g value was determined by the frequency and magnetic field values. XPS spectrum was obtained by an XPS analysis system (VG Thermo ESCALab220i-XL, VG Scientific, UK).

H_2-TPR and O_2-TPD were tested on a BELCAT instrument (BEL Japan, Inc.). The detailed procedures of H_2-TPR and O_2-TPD were described in the Supplementary Material. *In situ* diffuse reflection infrared Fourier transform spectroscopy (*in situ* DRIFTs) was carried out on a PerkinElmer with a highly sensitive MCT detector and the detailed procedures were also described in the Supplementary Material.

3.2.3 Catalyst activity test

Catalytic activity of toluene oxidation over the as-obtained OMS-2 and x% Ho-OMS-2 catalysts were evaluated in a quartz fixed-bed reactor, and a thermocouple was placed in the centre of catalyst bed to monitor the real reaction temperature. The toluene concentration of 1000 ppm was mixed with O_2 (20 vol.%) and N_2 (the balance gas) for the simulated VOC gas in this study. The catalysts were pressed and crashed to 40-60 mesh, and approximately 50 mg of them were used and the whole gas flow velocity was 50 cm^3/min. Three weight hourly space velocities (WHSV), i.e., 30,000, 60,000, and 100,000 cm^3/(g h), were used in this study. Typically, the WHSV of 60,000 cm^3/(g h) was

applied. Water resistance performances of x% Ho-OMS-2 were investigated by using the simulated VOC gas mixture with 5, 10, and 20 vol.% of H_2O vapors respectively. The products were in-situ determined by a connected online gas chromatograph (Shimadzu-2014) equipped with a flame ion detector (FID) and a Horiba FG-120 infrared spectrum analysis instrument.

$X_{toluene}$ (Toluene conversion) and Y_{CO_2} (CO2 selectivity) were obtained by eqs. (1) and (2) respectively:

$$X_{toluene} = \frac{C_{Inlet} - C_{Outlet}}{C_{Inlet}} \times 100\% \qquad (1)$$

$$Y_{CO_2} = \frac{C_{CO_2}}{7(C_{Inlet} - C_{Outlet})} \times 100\% \qquad (2)$$

where C_{Outlet} and C_{Inlet} are toluene concentrations at the outlet and inlet of the reactor, respectively, and C_{CO_2} is CO2 concentration at the outlet.

3.3. Results and discussion

Based on the STEM elemental mapping results (Table 3.1), it is obvious that the Ho/Mn ratio increased gradually with the increase in the initially added Ho amount from 0.1 to 3 wt.% in the precursor solutions (In this work, the theoretical doping amount of Ho species was used in order to describe conveniently), nevertheless, the contents of K species remained almost the same until the doping amount of 3 wt.%. It should be noted that the concentration of oxygen species on the 0.5% Ho-OMS-2 was higher than those on other x% Ho-OMS-2, indicating that more oxygen enriched on the superficial layer, which should be resulted from the complexation-assisting effect Ho^{3+} species for the changing of the crystal growth orientations of OMS-2 with a fine tailoring function. This result was in accordance with the XPS result. As the representative of x% Ho-OMS-2 catalysts, the completely overlapping of color images in the elemental mapping of 0.5% Ho-OMS-2

(Fig. 3.1) demonstrated that the Mn, O, K, and Ho species were homogeneously dispersed on the catalysts.

Table 3.1. Elemental compositions based on STEM analysis, BET surface areas and elemental valences based on XPS analysis for the OMS-2 and x% Ho-OMS-2.

Catalysts	STEM element mapping (at. %)					BET surface area^a (m²/g)	D^b (nm)	Mn^{4+} (%)	Mn^{3+} (%)	O_{ads}/O_{latt} (%)
	O	K	Mn	Ho	Ho/Mn					
OMS-2	14.83	0.16	85.01	/	/	116.6	12.3	37.6	52.9	44.8
0.1% Ho-OMS-2	13.48	0.14	85.48	0.9	0.01	291.8	3.4	29.8	61.8	49.5
0.5% Ho-OMS-2	17.9	0.1	80.15	1.85	0.02	285.5	3.4	30.7	64.1	52.1
1% Ho-OMS-2	16.88	0.1	80.31	2.71	0.03	244.8	3.4	31.2	62.9	50.4
3% Ho-OMS-2	4.58	0	85.64	9.78	0.11	231.2	3.4	24	69.4	49
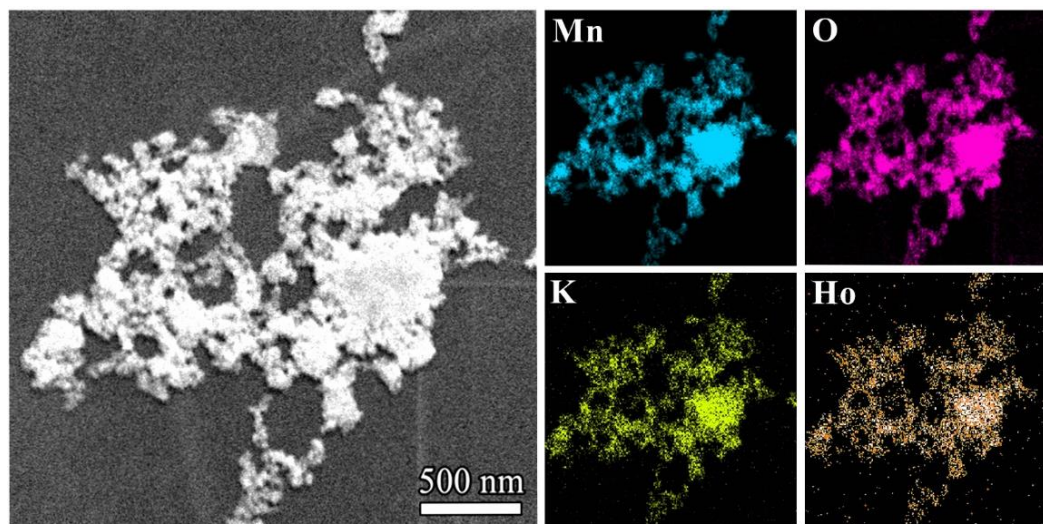
Fig 3.1. STEM elemental mapping of 0.5% Ho-OMS-2 catalyst.

3.3.1 SEM and TEM images

Fig. 3.2 shows the morphologies of the OMS-2 and x% Ho-OMS-2, in which no obvious differences were observed for all samples. Fig. 3.3 shows TEM and HRTEM

images of the OMS-2 and the representative Ho doped OMS-2 catalyst of 0.5% Ho-OMS-2. In the low magnifications (Figs. 3.3a and 3.3c), no obvious differences were found for both samples and the exact particle sizes were hardly confirmed. In the enlarged magnifications, for the OMS-2 (Fig. 3.3b), the distinct lattice fringes with 0.18, 0.22, 0.24, and 0.31 nm distances ascribed well to (411), (204), (211), and (301) facets of OMS-2 crystal, respectively, which were agreement with the XRD analysis results (Fig. 3.4) [31]. Moreover, the edge dislocation was confirmed on the HRTEM image (Fig. 3.3b-1), which is generally beneficial for the generation of additional active edge sites and defects. Meanwhile, for the 0.5% Ho-OMS-2 (Fig. 3.3d), the distinct lattice fringes with 0.18, 0.22, and 0.24 nm distances were also observed obviously. Especially, more (211) planes corresponding to the lattice fringe of 0.24 nm were found but the (301) plane disappeared, which was also consistence with the XRD analysis results (Fig. 3.4). It is worth noting that more amorphous phases were obviously observed on the HRTEM images of the 0.5% Ho-OMS-2 (Figs. 3.3d-1 and 3.3d-2), indicating that the Ho doping resulted in the generation of more amorphous structure. As a result, the defects derived from the edge dislocation were also found in Fig. 3.3d-1 although they were not so obvious. Moreover, in this case, the interfaces between the crystalline and amorphous phases in the catalyst were generated, which could provide additional active sites and promote the intermediate adsorption/desorption for catalytic oxidation of toluene at low temperatures [22]. Additionally, the interplanar d-spacing in the 0.5% Ho-OMS-2 had no change when compared with those in the OMS-2 besides the appearance of more (211) planes, indicating that the Ho species should hardly enter the lattice of Mn-O to form the Ho–O bond [33]. Therefore, the doping of trace Ho species caused the formation of the mixed crystal/amorphous structure, which could expose more oxygen species and interfaces for

the toluene adsorption and oxidation as discussed in the following.
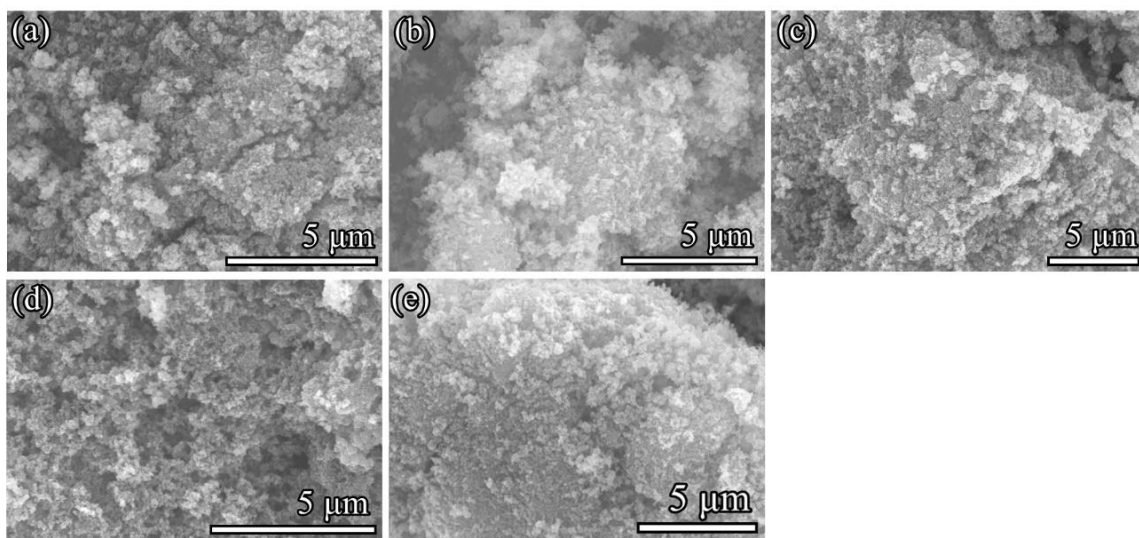
Fig 3.2. SEM images of (a) OMS-2; (b) 0.1% Ho-OMS-2; (c) 0.5% Ho-OMS-2; (d) 1% Ho-OMS-2; and (f) 3% Ho-OMS-2.
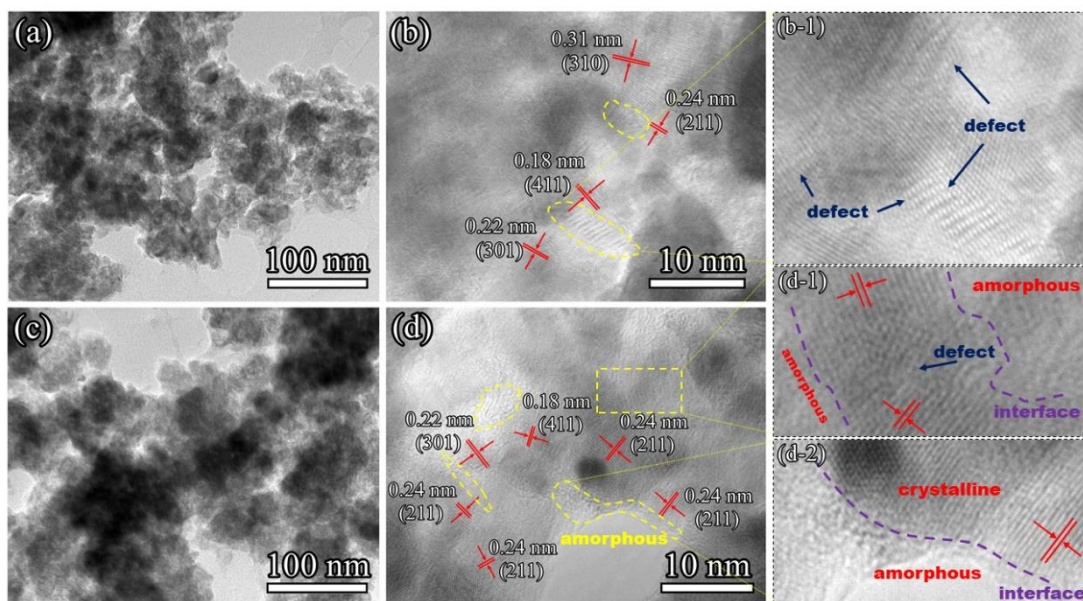
Fig 3.3. TEM and HRTEM images of OMS-2 (a) and (b); 0.5% Ho-OMS-2 (c) and (d). (b-1), (d-1) and (d-2) are different magnification areas in Figs. 2b and 2d, respectively.

3.3.2 XRD and Raman characterizations

XRD spectra of all samples are shown in Fig. 3.4. The typical diffraction peaks at 13.2°,

29.1°, 37.7°, 41.9° and 50.1° corresponded to the cryptomelane $K_{2-x}Mn_8O_{16}$ with a I2/m(12) space group (JCPDS Card No. 44-1386) [32, 34], indicating the formation of manganese oxide with OMS-2 structure. In contrast, only one weak peak at 37.9° corresponding to the (211) plane of OMS-2 was observed for the x% Ho-OMS-2 with Ho doping amounts even less than 0.1 wt%, confirming that the doping of Ho species decreased the crystallinity of OMS-2, which led to the generation of more amorphous structure. As stated above, it is benefit for the formation of more defects, especially the formation of the oxygen vacancies owing to the surface unsaturated coordination, and provide abundant active sites for deep VOC oxidation. It is reported that K^+ ions serve as the hard template for maintaining the layer structure of cryptomelane-type manganese oxides with a tunnel size of 0.46 nm × 0.46 nm [35]. While, the radius of Ho^{3+} (0.104 nm) is much larger than those of Mn^{2+} (0.066 nm), Mn^{3+} (0.064 nm) and Mn^{4+} (0.060 nm) [33, 36, 37], and thus Ho^{3+} should be hardly incorporated into the OMS-2 lattice, however, it could enter the interlayers as the K^+, causing the delamination of OMS-2 to single layers (Fig. 3.5) due to the exchange repulsion between K^+ and Ho^{3+} species, and the Coulomb repulsion between Mn^{x+} and Ho^{3+} species within the limited tunnel spacing. Thus, the delaminated OMS-2 showed higher surface area [38-40]. Moreover, as illustrated in Fig. 3.5, for the OMS-2, only A-1 and D-2 of (211) plane can provide active sites for the reaction. In comparison, after the delamination with the assistance of Ho species, all the A-1/A-2, B-1/B-2, C-1/C-2, and D-1/D-2 can be exposed, providing more active sites. Meanwhile, the strong interaction between Ho and Mn during the redox reaction in the preparation of x% Ho-OMS-2 also led to the formation of more low-crystallinity phase. Herein, the amorphous phase in the x% Ho-OMS-2 could be also derived from the strong interaction of Ho and Mn species within the cryptomelane matrix, especially the

125

regulating effect on the octahedral chains in their crystal growth directions [41]. In addition, no diffraction peaks belonging to the Ho_2O_3 and $HoMnO_x$ perovskite crystalline structure were showed in the XRD patterns of x% Ho-OMS-2, possibly due to the low content of Ho doping and/or high dispersion of the Ho oxide on the OMS-2.
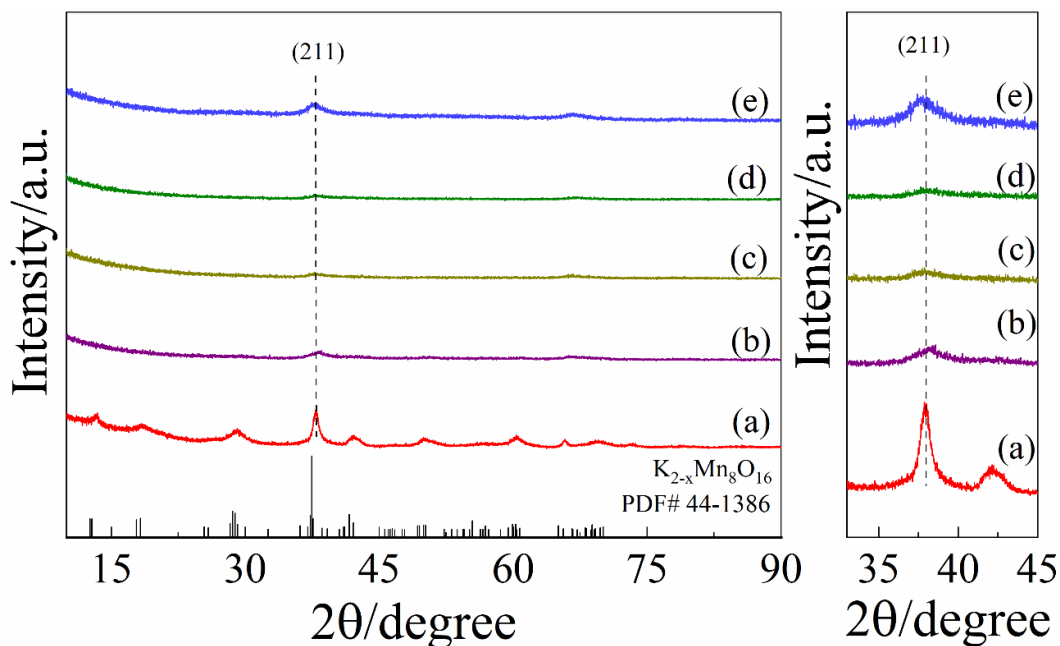
Fig 3.4. XRD patterns of (a) OMS-2; (b) 0.1% Ho-OMS-2; (c) 0.5% Ho-OMS-2; (d) 1% Ho-OMS-2; and (e) 3% Ho-OMS-2, and the enlarged parts in the 2θ range from 33 to 45°.
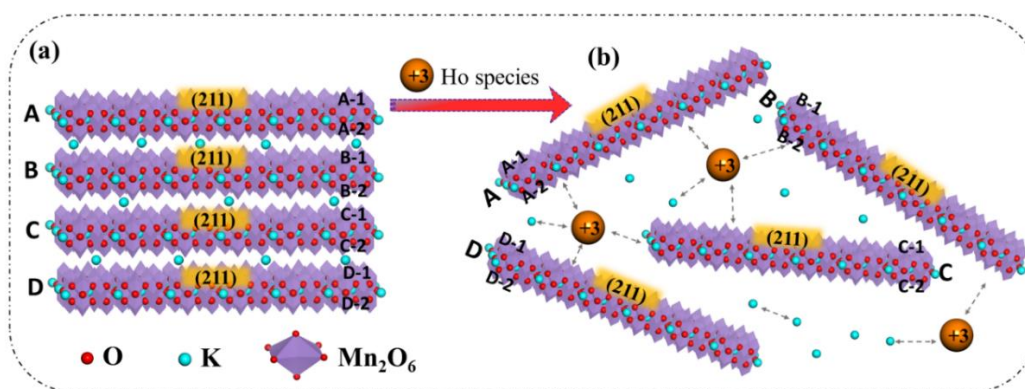
Fig 3.5. Schematic illustration of the delamination of OMS-2 from OMS-2 (a) to x% Ho-OMS-2 (b) with the assistance of Ho species.

The local structure of catalysts was further investigated by Raman spectroscopy and

the corresponding results are depicted in Fig. 3.6. One can see that only one strong peak located at 640 cm^{-1} assigning to symmetric stretching vibrations of Mn^{3+} and Mn^{4+} species corresponding to the MnO$_6$ group was found whereas the peaks at around 180 and 580 cm^{-1} related to Mn-O-Mn were hardly observed, demonstrating the weak interaction of Mn-O bond, which could further lead to the generation of more crystal defects [22, 24]. Besides, with the doping of Ho species, even in the case of 3 wt% Ho-OMS-2, the similar one-peak curve as that of OMS-2 was obtained, also indicating that the Ho species was difficult to incorporate into the lattice of OMS-2 and only caused the delamination of OMS-2, which is lined with the XRD analysis results (Fig. 3.4).
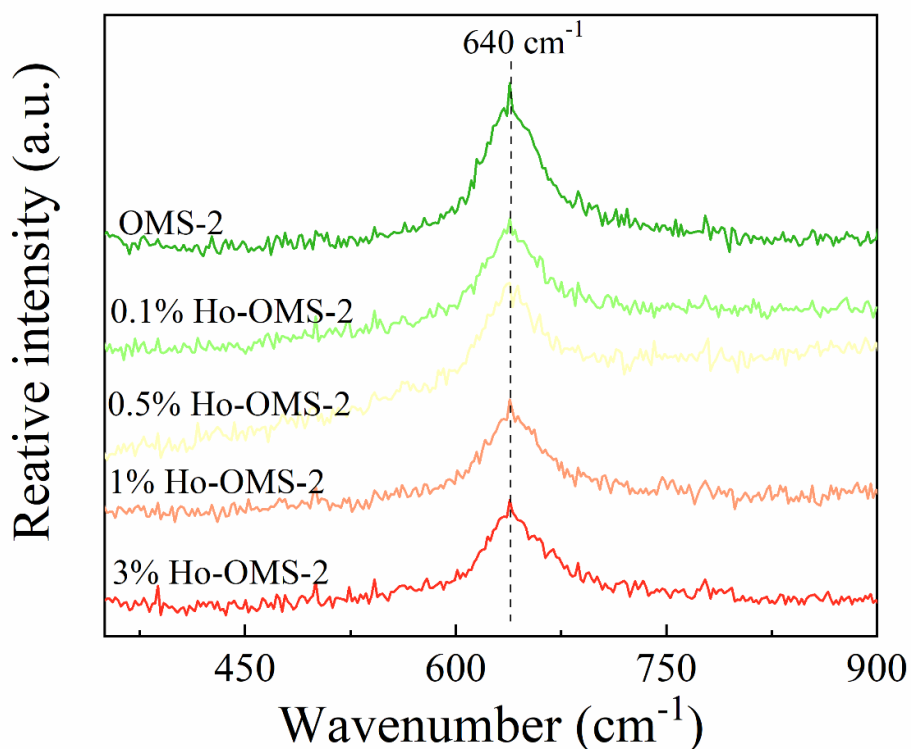
Fig 3.6. Raman spectra of OMS-2 and x% Ho%-OMS-2.

3.3.3 BET analysis

N$_2$ adsorption-desorption isotherms and the corresponding BJH pore size distributions of OMS-2 and x% Ho-OMS-2 are displayed in Fig. 3.7. The obtained BET specific

surface areas, average pore volumes and average pore diameters were also listed in Table 1. One can see that all catalysts had the type IV isotherms with the distinct H3 type hysteresis loop, indicating that these catalysts possessed the similar mesoporous structure [42, 43]. Additionally, the specific BET surface areas of x% Ho-OMS-2 were much higher than that of OMS-2 with smaller average pore sizes. It should be due to the delamination of OMS-2 in the existence of Ho species and the formation of amorphous phases, also manifesting the strong interaction between Mn and Ho species. It is worth noting that the specific BET surface areas decreased with doping more Ho species, possibly due to more Ho species covered on the surface of OMS-2.
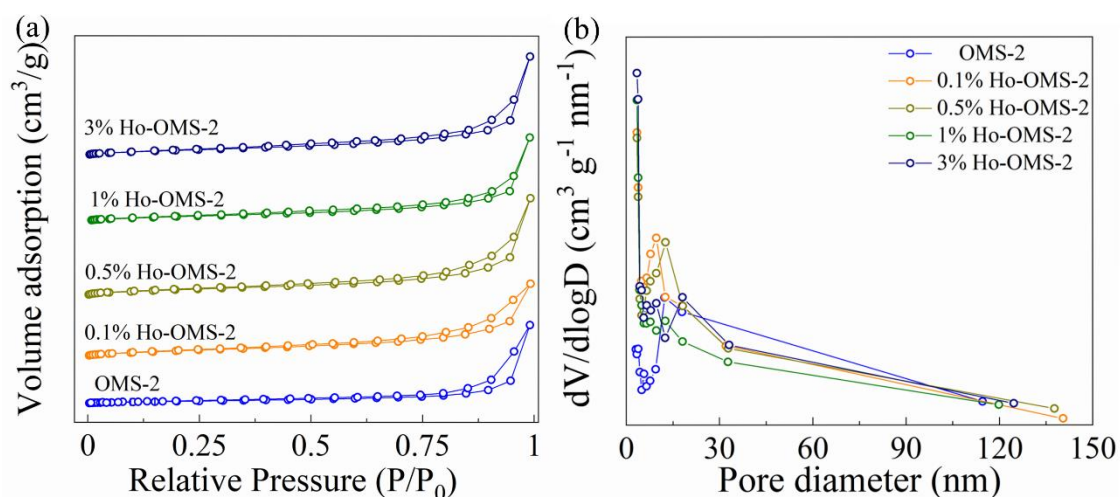
Fig 3.7. (a) N_2 adsorption-desorption isotherms and (b) the pore size distributions calculated from the desorption branch of the isotherm using the BJH method.

3.3.4 Reducibility and oxygen vacancy analyses

Fig. 3.8a shows the H_2-TPR profiles of the obtained catalysts and Table 3.2 summarized the related results. For all catalysts, two strong reduction peaks ($Mn^{4+} \rightarrow Mn^{3+} \rightarrow Mn^{2+}$) and a weak reduction peak corresponding to the surface oxygen species appeared in temperatures ranged from 100 to 200 °C. In Fig. 3.8a, the first reduction peak was associated with the reduction of oxygen vacancies. One can see that more oxygen

vacancies were formed after the doping of Ho species into OMS-2, especially for 0.5% Ho-OMS-2, which should be beneficial for the improvement of catalytic activity at low temperature [44]. The second and third peaks with strong intensity represented the reductions of MnO_2/Mn_2O_3 into Mn_3O_4 and Mn_3O_4 into MnO, respectively [30, 45]. One can see that the reduction temperatures of x% Ho-OMS-2 were higher than that of OMS-2, however, the H_2 consumptions for the x% Ho-OMS-2 were significantly higher than that for the OMS-2. It revealed that more Mn^{4+} and Mn^{3+} species existed in the x% Ho-OMS-2 and the Mn^{4+}/Mn^{3+} amount increased with the increase in the amount of Ho species, which could result in more oxygen vacancies generation for the effective redox cycle. Moreover, it should be noted that the 0.5% Ho-OMS-2 showed the lowest reduction temperature for Mn^{4+} and Mn^{3+} species, indicating that it had the most excellent low-temperature reducibility among all x% Ho-OMS-2. As indicated in the following section, it also exhibited the highest toluene oxidation activity.
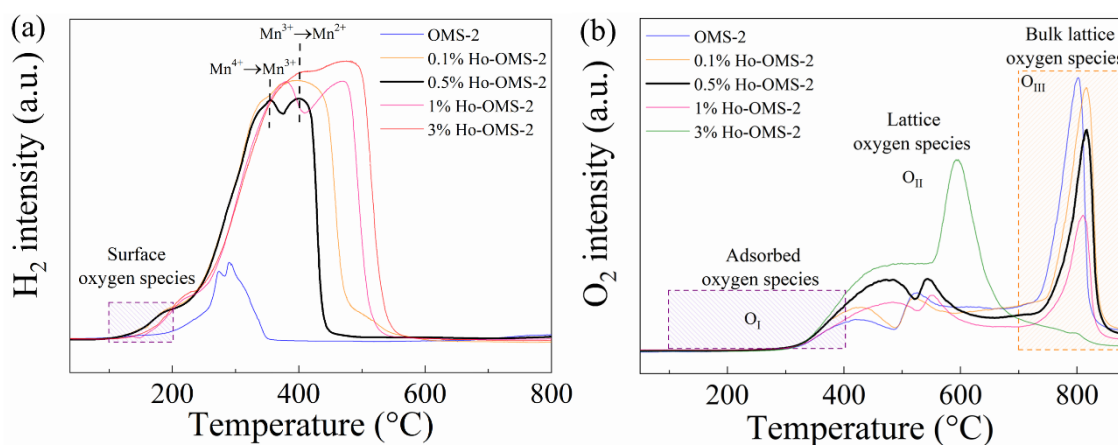
Fig 3.8. (a) H_2-TPR and (b) O_2-TPD profiles of OMS-2 and x% Ho-OMS-2.

Table 3.2 H_2 and O_2 consumption amounts based on H_2-TPR and O_2-TPD analyses respectively for the OMS-2 and x% Ho-OMS-2.

Catalyst	H_2 consumption amount (mmol/g)	O_2 consumption amount (mmol/g)

	H₂-uptake (T<280°C)	Total H₂-uptake	O₂-uptake (T<400°C)	O₂-uptake (400°C<T<700 °C)	O₂-uptake (T>700°C)	Total O₂-uptake
OMS-2	1.83	3.66	0.51	1.06	2.92	4.49
0.1% Ho-OMS-2	2.05	29.84	0.69	0.98	3.02	4.69
0.5% Ho-OMS-2	2.3	20.146	1.32	0.92	2.16	4.4
1% Ho-OMS-2	1.63	36.86	0.99	0.78	1.4	3.17
3% Ho-OMS-2	1.56	31.96	2.13	2.68	0	4.81

Fig. 3.8b shows O_2-TPD spectra of OMS-2 and x% Ho-OMS-2, in which three typical temperature regions corresponding to the oxygen states can be classified: low temperature (< 400 °C, denoted as O_I region), medium temperature (400-700 °C, denoted as O_{II} region), and high temperature (> 700 °C, denoted as O_{III} region). Herein, the amount of desorbed O_2 was calculated by integrating the peak area of O_2-TPD profile [42, 46]. The peak in the O_I region is ascribed to the release of physical adsorbed oxygen, including chemisorbed oxygen molecules, surface lattice oxygen (O_{latt}) and oxygen vacancies [47]. As shown in Fig. 3.8b, the O_2 consumption in O_I region increased after the Ho doping, which should be due to the exposure of more active oxygen species on the catalyst surface by the Ho doping. It can also effectively promote the utilization of bulk oxygen species. The desorption peak in the O_{II} region belonged to the evolution of sub-surface O_{latt} due to the unsaturated Mn-O bonds breakage, and the desorption peak in the O_{III} region corresponded to the evolution of bulk O_{latt} [48, 49]. It is obvious that the amounts of adsorbed oxygen and sub-surface O_{latt} species increased whereas the amount of bulk O_{latt} species decreased with the doping of Ho species into OMS-2. As such, the oxygen mobility capacity should be increased. Meanwhile, it should be noted that the O_{III} desorption peak of 3% Ho-OMS-2 disappeared, indicating that excessive Ho doping was not conducive to the formation of the O_{latt} species in the bulk, which could impede the

cycle of $O_{surface} \leftrightarrow O_{sub\text{-}surface} \leftrightarrow O_{bulk}$ and decrease the structural stability of catalysts, thereby reducing the catalytic performance.

To understand the oxygen vacancies more quantitatively and directly, EPR analysis at room temperature was also performed [33, 50]. As displayed in Fig. 3.9, symmetrical EPR spectrum peaks with a g factor = 2.003 were obtained for all catalysts, which can be used to quantitatively compare the concentrations of oxygen vacancies based on the change in the signal intensity [51]. It is obvious that the number of oxygen vacancies increased with the increase in the Ho doping amount, illustrating a certain positive role of Ho species in generation of oxygen vacancies. However, as shown in the following catalytic performance tests, the activity was not increased with the same trend, and excessive doping of Ho resulted in the decrease of activity. It indicated that the excessive density of oxygen vacancies on the x% Ho-OMS-2 could inversely hinder the activity improvement. In addition, as indicated in the following section, XPS analysis results also showed the similar tendency for the oxygen vacancies based on the detected of Mn^{3+} amounts, which is the representative of oxygen vacancies in XPS analysis. However, it should be noted that only the information of the surface layers of samples can be detected by XPS. In comparison, the EPR analysis reflected the average state of oxygen vacancies in the entire catalyst.
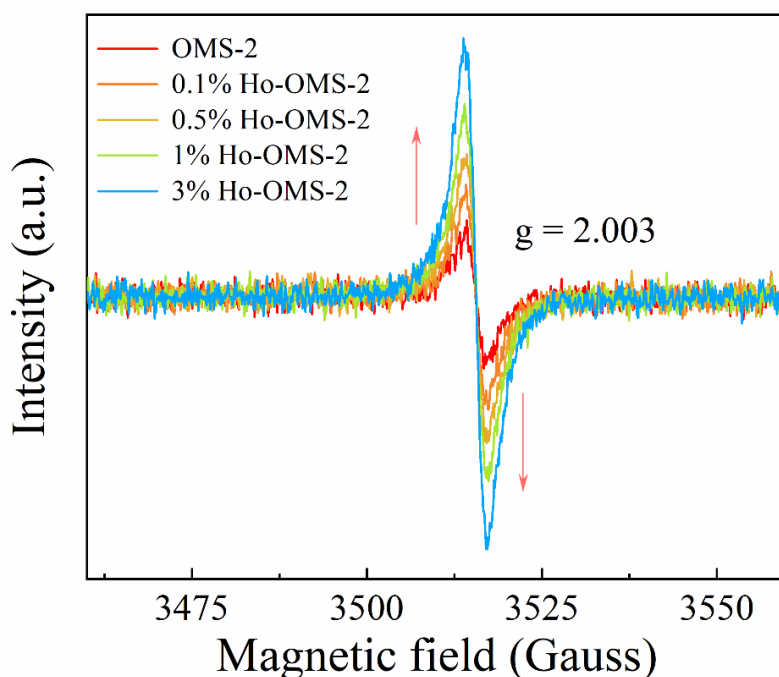
Fig 3.9. Electron paramagnetic resonance (EPR) spectra of OMS-2 and x% Ho-OMS-2 at room temperature.

3.3.5 Surface composition and chemical state analysis

Fig. 3.10 shows XPS analysis results for all the catalysts and Table 1 listed the various elemental molar ratios. Herein, the Mn 2p spectrum can be divided into three main components centered at 643.3, 641.8 and 640.5 eV, ascribing to Mn^{4+}, Mn^{3+} and Mn^{2+}, respectively (Fig. 3.10a) [21, 22]. As summarized in Fig. 3.10d, the sequence of Mn^{4+} percentage on the surface followed the order of OMS-2 > 1% Ho-OMS-2 > 0.5% Ho-OMS-2 > 0.1% Ho-OMS-2 > 3% Ho-OMS-2. Meanwhile, the surface Mn^{3+} percentage decreased gradually with an order of 3% Ho-OMS-2 > 0.5% Ho-OMS-2 > 1% Ho-OMS-2 > 0.1% Ho-OMS-2 > OMS-2. In general, the number of Mn^{3+} species has strong relationship with the oxygen vacancy defect amount owing to the reaction cycling of -Mn^{4+}-O^{2-}-Mn^{4+}- $\rightarrow$ -Mn^{3+}-oxygen vacancy-Mn^{3+}- + 1/2 O_2 [52], which is one key factor to affect the activation and generation of oxidized intermediates on the catalysts since the

132

oxygen-deficient sites with unbalanced electronic structure can help to rapidly replenish the oxygen species, thereby enhancing the oxygen migration rate and improving the oxygen storage capacity. However, the controversy results on the effect of Mn^{3+} and Mn^{4+} to the VOC oxidation also existed in the reported literatures. For example, Zhang *et al.* [53] found that the binding capacity of Mn-O was weakened by the improving of Mn^{3+} species content, thereby leading to a high activity for the total oxidation of toluene. In contrast, Song *et al.* [54] pointed out that the increasing of Mn^{4+} rather than Mn^{3+} concentration was important for the deep oxidation of VOCs. In this study, it is obvious that the proportion of Mn^{4+} and Mn^{3+} in the 0.5% Ho-OMS-2 was in a relatively more balanced manner than other samples, which led to the maximum ratio of O_{ads}/O_{latt} among all the prepared catalysts. Combined with the above characterizations and the catalytic activity, it is obvious that the excessive oxygen vacancies density could inversely hinder the activity improvement, suggesting that the O_{ads} species concentration of x% Ho-OMS-2 could be finely tailored by the doping amount of Ho species, which plays the decisive role in the catalysis performance.

As seen in Fig. 3.10c, the asymmetrical O 1s spectra of OMS-2 and x% Ho-OMS-2 can be fitted into three distinct components with binding energy peaks at 529-529.6 eV, 531.1 eV, and 532.2-532.9 eV, which corresponded to the lattice oxygen (O_{latt}), adsorbed oxygen (O_{ads}, such as O_2^-, O_2^{2-}, O^- or oxygen vacancy defects), and adsorbed H_2O molecule, respectively [22]. The molar ratio of O_{ads}/O_{latt} changed obviously after the Ho doping, and the 0.5% Ho-OMS-2 exhibited the largest value, which is consistent with the catalytic performance in section of 3.6. Herein, the largest O_{ads}/O_{latt} molar ratio was observed for the 0.5% Ho-OMS-2 should be due to the optimum Ho doping amount caused by the interaction equilibrium between Ho species and Mn species, leading to rich

active sites on the delaminated OMS-2. Based on the MVK oxidation mechanism, more oxygen vacancy defects can promote the catalytic efficiency by accelerating the converting speed between gaseous O_2 and the electrophilic reactive oxygen species on the catalyst surface [21, 52]. Since both O_{ads} species and oxygen vacancies are beneficial for the oxidation reaction, 0.5% Ho-OMS-2 should have the highest activity in the toluene oxidation at low temperatures as described in following section.
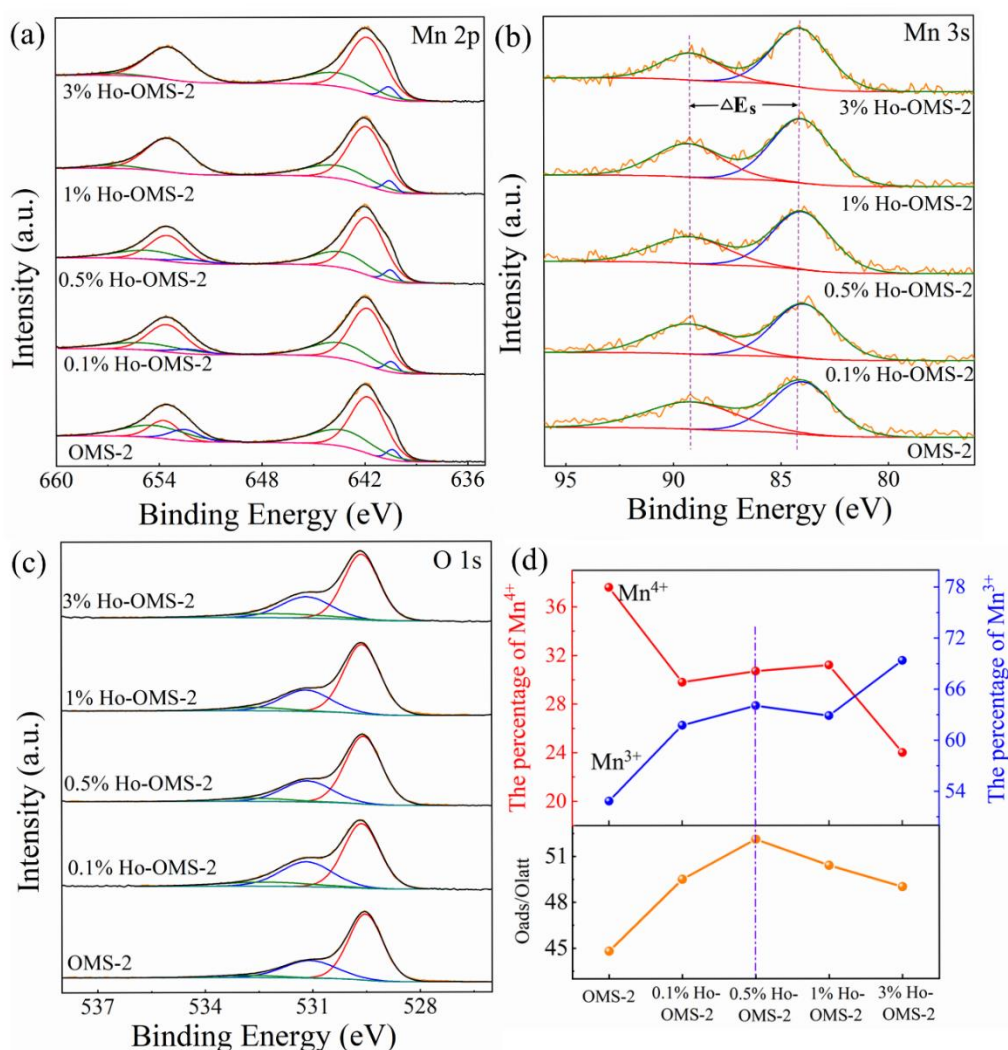
Fig 3.10. (a) Mn 2p spectra, (b) Mn 3s spectra, (c) O 1s spectra profiles of OMS-2 and x% Ho-OMS-2, (d) The relation of surface Mn^{4+}/Mn, Mn^{3+}/Mn, and O_{ads}/O_{latt} of OMS-2 and x% Ho-OMS-2.

3.3.6 Catalytic performance

The performances of the OMS-2 and x% Ho-OMS-2 catalysts for the toluene oxidation were evaluated. As shown in Fig. 3.11a, $T_{50\%}$ values were 220, 223, 226, 234, and 251 °C over the 0.1% Ho-OMS-2, 0.5% Ho-OMS-2, 1% Ho-OMS-2, 3% Ho-OMS-2 and OMS-2 whereas those corresponding $T_{100\%}$ values were 238, 232, 237, 248, and 268 °C, respectively. Herein, the 0.5% Ho-OMS-2 exhibited the highest activity for the complete oxidation of toluene, which is consistence with its largest O_{ads}/O_{latt} molar ratio among the obtained x% Ho-OMS-2 catalysts. It is worth noting that a small amount of Ho doping into OMS-2 promoted the catalytic activity but excessive Ho doping decreased the activity, revealing that the optimal ratio of Mn/Ho is existed for the preparation of x% Ho-OMS-2 catalysts. Moreover, as shown in Table 3.3, the as-prepared 0.5% Ho-OMS-2 exhibited lower 100% conversion temperature when compared with the reported MnO_x-based catalysts. Meanwhile, as depicted in Fig. 3.11b, the 0.5% Ho-OMS-2 exhibited the best activity in toluene mineralization.

To evaluate the catalytic performance with H_2O vapor, 5% of H_2O vapor in the feed was introduced. Interestingly, as shown in the Fig. 3.11c, the $T_{100\%}$ values were reduced for ca. 5-10 °C after the introduction of water vapor. It is reported that the hydroperoxyl-like species could be generated on the surface of catalysts in the presence of H_2O molecules, which is beneficial to the activating of O-O bond on the catalysts, thereby enhancing the toluene oxidation. Meanwhile, it is observed that the generated intermediates of toluene oxidation were easily taken away via the introduction of more H_2O molecules so that more the active sites are exposed for the deep toluene oxidation [22, 33]. In addition, as shown in Fig. 3.11d, except 0.1% Ho-OMS-2, all other x% Ho-OMS-2 catalysts mineralized the toluene in time at $T_{100\%}$, exhibiting excellent deep

oxidation performance. Especially, the 0.5% Ho-OMS-2 also showed the highest catalytic activity for toluene oxidation even in the presence of water vapor.
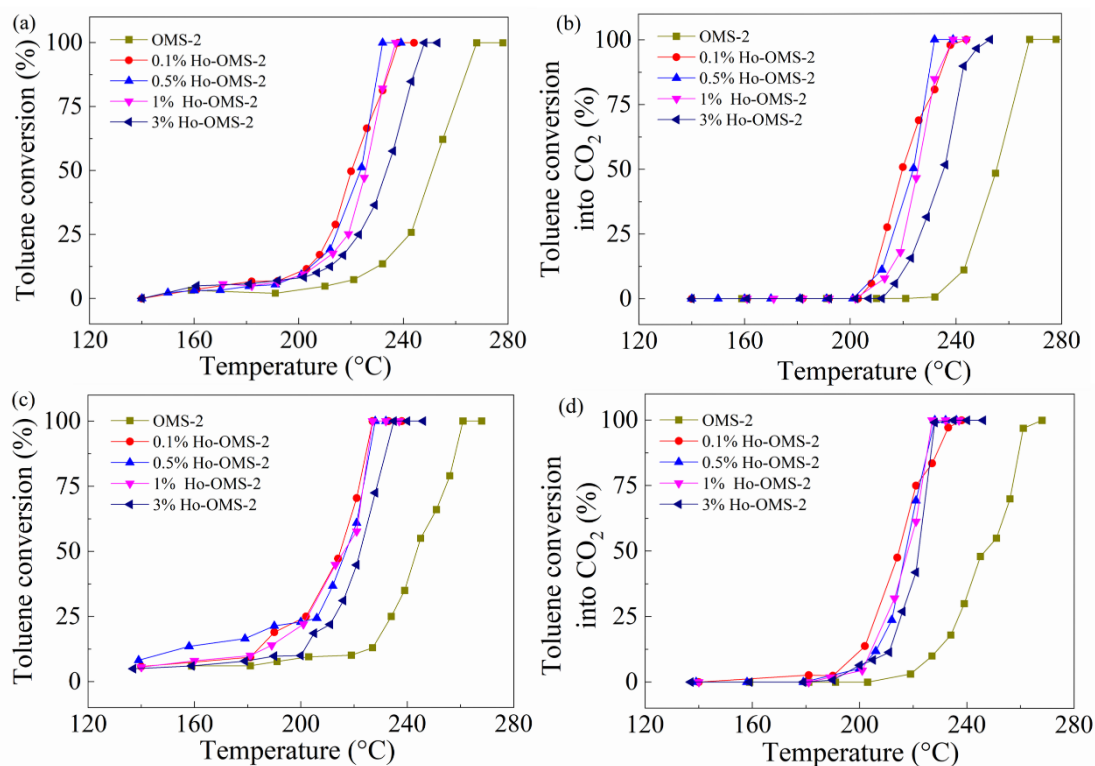
Fig 3.11. (a) Toluene conversions vs. reaction temperature over OMS-2 and x% Ho-OMS-2 without H_2O; (b) CO_2 selectivity in the toluene oxidation without H_2O; (c) Toluene conversions as a function of reaction temperature over OMS-2 and x% Ho-OMS-2 with 5 vol.% H_2O vapor; (d) CO_2 selectivity in the toluene oxidation with 5 vol.% H_2O vapor. (Herein, $[C_7H_8]$ is 1000 ppm, $[O_2]$ is 20% with N_2 balance, and WHSV is 60,000 $cm^3/(g\ h)$).

3.3.7 Effect of WHSV and stability test

The effect of WHSV on the oxidation of toluene over 0.5% Ho-OMS-2 was investigated by changing the catalyst amount in the reactor. As shown in Fig. 3.12a and Table 3.3, $T_{100\%}$ at WHSV = 60,000 $cm^3/(g\ h)$ was 232 °C, which was 13 and 19 °C lower than those at WHSVs = 30,000 and 100,000 $cm^3/(g\ h)$, respectively. Furthermore, as

shown in Fig. 3.12b, the timely 100% toluene mineralization was realized in the cases of WHSVs = 60,000 and 30,000 cm^3/(g h) whereas the mineralization temperature was ca. 5 °C higher than the $T_{100\%}$ at WHSV = 100,000 cm^3/(g h). Therefore, the WHSV value of 60,000 cm^3/(g h) was used as the optimum in this study in order to balance the efficiency and cost for the toluene oxidation.
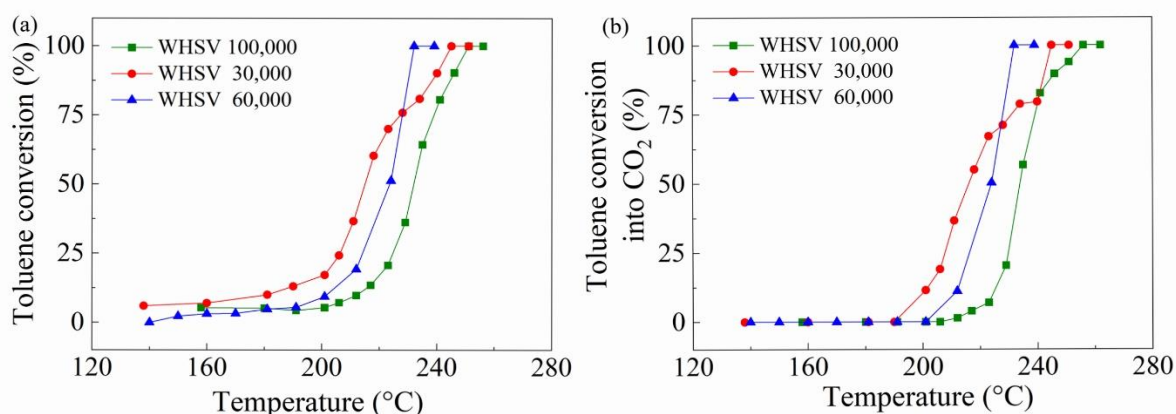
Fig 3.12. Effect of WHSV on toluene oxidation over 0.5% Ho-OMS-2(a) and CO_2 selectivity in toluene oxidation (b).

The catalytic performance stability test for 0.5% Ho-OMS-2 in the absence of H_2O vapor was tested with WHSV=60,000 cm^3/(g h) at 232 °C, 229 °C and 223 °C respectively. As shown in Fig. 3.13a, 100% of the toluene conversion was remained almost unchanged for 35 h at 232 °C, meanwhile, ca. 62% and ca. 40% of toluene conversion at 229 °C and 223 °C respectively were also maintained. In addition, the toluene oxidations over the 0.5% Ho-OMS-2 for three successive runs are shown in Fig. 3.14. One can see that $T_{100\%}$ values were 232, 234 and 232 °C for the 1st, 2nd and 3rd runs, respectively, also illustrating the excellent stability of Ho-doped OMS-2 structure owing to no significant difference in the three successive tests.
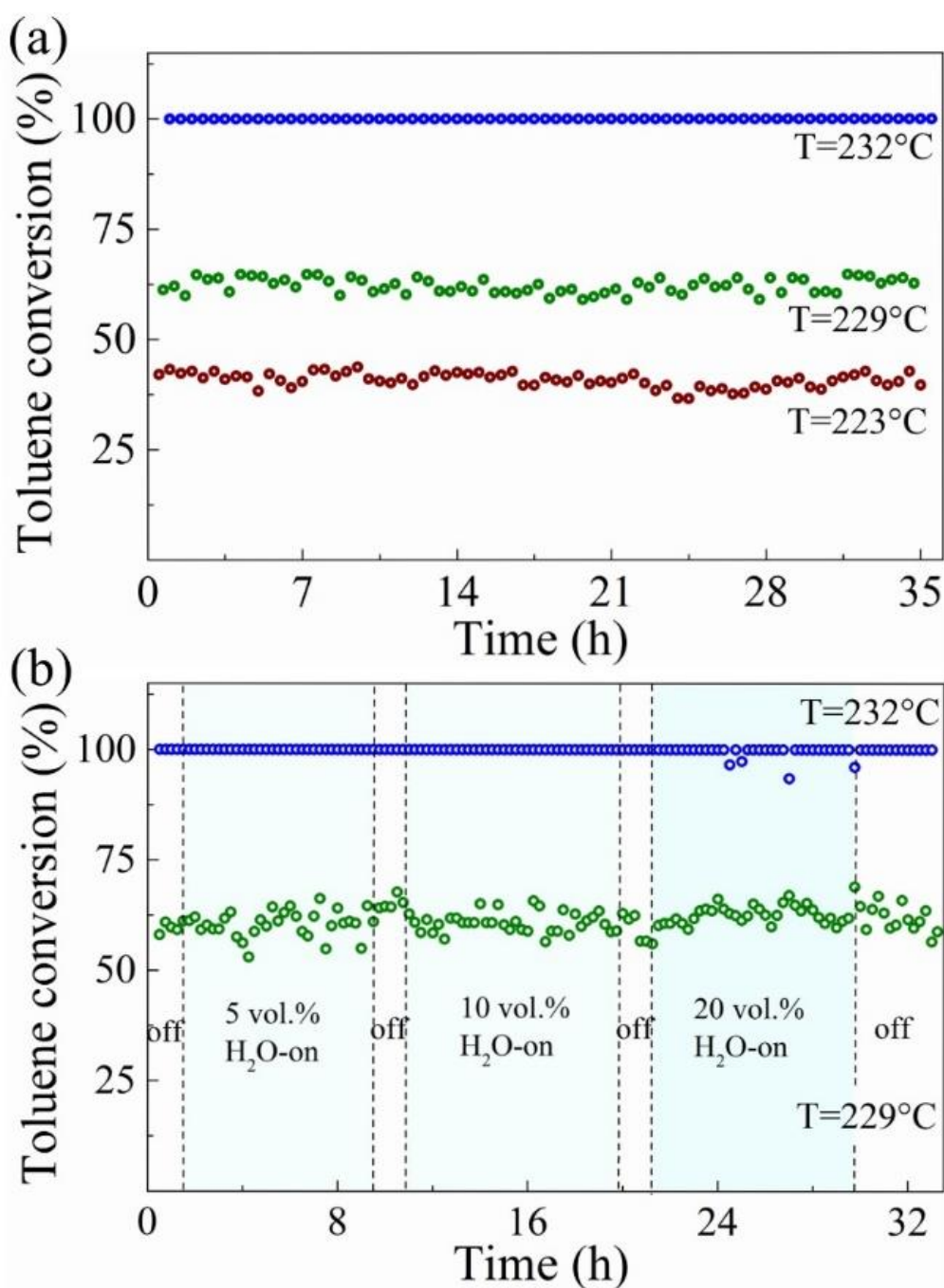
Fig 3.13. (a) Stability testing for the 0.5% Ho-OMS-2 at different temperatures without H_2O vapor for the toluene oxidation at WHSV=60,000 $cm^3/(g\ h)$; (b) The influence of H_2O vapor (5, 10, and 20 vol%) on the activity over the 0.5% Ho-OMS-2 at different temperatures with a WHSV of 60,000 $cm^3/(g\ h)$.

138
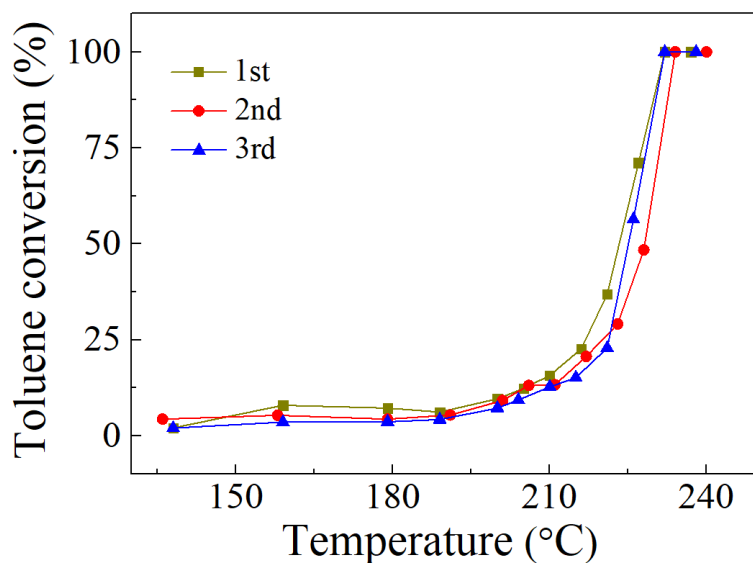
Fig 3.14. Catalytic performances of 0.5% Ho-OMS-2 with repeated runs.

In order to further estimate the moisture tolerance of catalysts in the practical application, the effect of H_2O vapor on the 0.5% Ho-OMS-2 performance was also investigated in the presence of H_2O vapor with a concentration range from 5 vol% to 20 vol% in the feed. As shown in Fig. 3.13b, the total toluene oxidation at 232 °C was also remained when 5 vol%, 10 vol%, or 20 vol% of H_2O vapor was fed to the stream during 33 h of consecutive test, revealing that the H_2O vapor had no effect on toluene oxidation stability. Meanwhile, ca. 60% of conversion at 229 °C was fluctuated to some extent within 33 h when 5 vol.%, 10 vol.% or 20 vol.% of H_2O vapor was introduced to the stream, but the catalytic activity can be considered stable. Moreover, it should be noted that the toluene conversion increased to some extent after the introduction H_2O vapor, which is consistent with the result of the catalytic performances shown in Fig. 3.11c. In addition, as soon as the H_2O vapor was stopped, the conversion at 232 or 229 °C was also perfectly recovered to the state as the case without H_2O vapor. Meanwhile, the morphology of 0.5% Ho-OMS-2 after the long-term stability test maintained the original three-dimensional structure (Fig. 3.15). These results indicated that the 0.5% Ho-OMS-2

had excellent water vapor tolerance, which is suitable for the practical application.
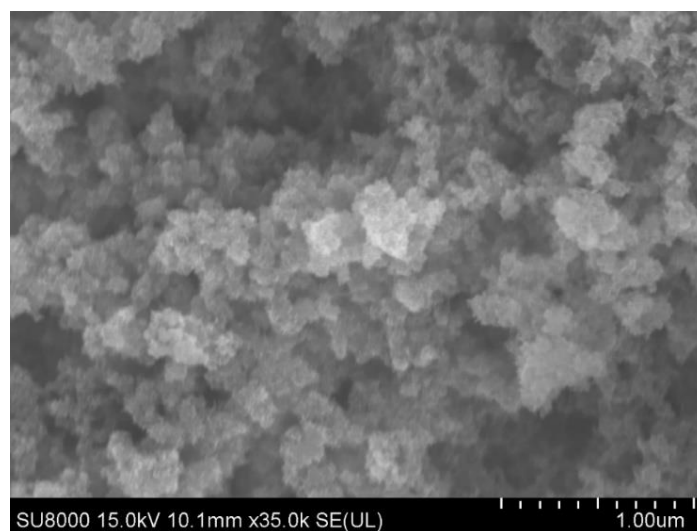
Fig 3.15. SEM image of 0.5% Ho-OMS-2 after the long-term stability test.

Table 3.3. Comparison of the catalytic performances of various reported OMS-2 based catalysts with the present work.

Catalysts	WHSV cm^3/(g h)	Toluene conversion/^{o}C						Preparation Method	Ref.
		$T_{50\%}$	$T_{50\%}$-H$_2$O	$T_{90\%}$	$T_{90\%}$-H$_2$O	$T_{100\%}$	$T_{100\%}$-H$_2$O		
OMS-2		251 [a]	245 [a]	265 [a]	258 [a]	268 [a]	261 [a]		
0.1% Ho-OMS-2	60,000	220 [a]	215 [a]	235 [a]	226 [a]	238 [a]	227 [a]		
0.5% Ho-OMS-2	100,000	232 [a]	/	246 [a]	/	251 [a]	/	Redox co-precipitation	This work
	60,000	223 [a]	217 [a]	230 [a]	226 [a]	232 [a]	228 [a]		
	30,000	215 [a]	/	240 [a]	/	245 [a]	/		
1% Ho-OMS-2	60,000	226 [a]	217 [a]	235 [a]	226 [a]	237 [a]	227 [a]		
3% Ho-OMS-2		234 [a]	223 [a]	245 [a]	233 [a]	248 [a]	235 [a]		
x% Ag/OMS-2	360,000	250 [b]		260 [b]		∼390 [b]		Pre-incorporation	[8]
Cu/OMS-2	30,000	∼218 [b]		∼305 [b]		350 [b]		Coprecipitation	[12]
OMS-2	20,000	∼210 [b]		∼225 [b]		240 [b]		Hydrothermal	[23]

| OMS-2-70°C, | 48,000 | 190 [b] | 200 [b] | 300 [b] | Hydrothermal | [24] |

3.3.8. *In situ* **DRIFTS study**

To further investigate the generated intermediates during the toluene oxidation over the OMS-2 and 0.5% Ho-OMS-2 catalysts, *in situ* DRIFTS was employed to monitor the oxidation process with a series of time-related DRIFTS spectra under various environments (Fig. 3.16). The peak located at 3073 cm^{-1} is the phenylic C–H aromatic peak [23, 55]; the peaks at 3040 and 2938 cm^{-1} are assigned to the asymmetric and symmetric CH– stretching vibrations of benzyl [56]; the ones at 2752 and 2886 cm^{-1} correspond to C=O stretching vibrations of carbonyl (benzaldehyde) [22]; the peaks at 1948, 1857 and 1794 cm^{-1} are the signals of maleic anhydride species associated to the symmetric and asymmetric C=O stretching vibrations [48, 57]; the absorption ones at 1610, 1499, and 1450 cm^{-1} are the typical aromatic ring skeleton stretching vibrations; the one at 1034 cm^{-1} is ascribed to the in-plane C–H bending vibration (aromatic ring) [47, 58, 59]; the peaks at 1385 and 1543 cm^{-1} separately correspond to the carboxylate C=O stretching vibration of benzoate symmetrically and antisymmetrically; and the peak located at 1385 cm^{-1} is related to monodentate carbonates [47, 60]. Meanwhile, the adsorption peak at 1080 cm^{-1} is attributed to the CO-stretching vibrations of benzyl alcohol [48]; the peaks at approximately 2300-2400 cm^{-1} are attributed to the carbon dioxide, and the peak at ~3243 cm^{-1} is from the oxhydryl (O-H), demonstrating that the generation of the products of CO_2 and H_2O [21]. As shown in Fig. 3.16, all peaks related to the different intermediates were generated at the first 2 min; meanwhile, the intensities of these peaks gradually increased with the increasing of adsorption time, suggesting the

toluene molecules could be rapidly adsorbed and oxidized on the surfaces of OMS-2 and 0.5% Ho-OMS-2. Herein, it is worth noting that the value of the related position ($\Delta\upsilon$) between symmetric (1385 cm^{-1}) and antisymmetric (1543 cm^{-1}) carboxylate C=O stretching vibration was 158 cm^{-1}, which is very similar to the free ion value, indicating the formation of a bridging structure due to the carboxylate species derived from the toluene coupling with Mn on the surface of OMS-2 and 0.5% Ho-OMS-2 [21, 22].

The *in situ* DRIFTS measurements in the N_2, air, or air with H_2O vapor (5 vol.%) atmospheres were also performed. As shown in Fig. 3.16, the intermediates species were almost the same in these cases, illustrating that the similar oxidation pathway occurred even under different environments. Under the N_2 atmosphere, since either lattice oxygen in bulk or surface adsorbed oxygen could take part in the oxidation of toluene due to the lattice oxygen migration from bulk to surface of the catalyst, the oxidation of toluene was still proceeded even after 50 min reaction. Meanwhile, it should be noted that the peak intensities of the DRIFTS spectra under different environments were different owing to the difference of the reaction rates. For example, in the case using OMS-2, as shown in Figs. 3.16a and b, the characteristic peaks of the intermediates such as maleic anhydride (1794, 1857, and 1945 cm^{-1}), benzyl (2938 and 3040 cm^{-1}) and benzyl alcohol (1080 cm^{-1}) showed stronger intensities under the N_2 atmosphere than those in the air atmosphere, demonstrating the accumulation of intermediates in the N_2 environment. In comparison, since the consumed oxygen species on the catalysts could be rapidly replenished and reconstructed via O_2 in air atmosphere, a faster response on the DRIFTS spectrum could be achieved for the toluene oxidation under the air atmosphere. Meanwhile, the peaks appeared in the range of 2300-2400 cm^{-1} assigned to CO_2 species were obviously increased under the air atmosphere (Fig. 3.16b) whereas these peaks were

noticeably decreased after 10 min reaction under the N_2 atmosphere (Fig. 3.16a). Furthermore, higher peak intensities were found after the introduction of H_2O vapor (5 vol.%) into the system when compared with those in N_2 and air atmospheres (Fig. 3.16c), manifesting that the H_2O molecule would hinder the transfer of O_2 to the active sites owing to the competitive adsorption H_2O molecule especially on those amorphous area on the catalysts. Herein, comparing with the spectra in the case using OMS-2, all characteristic peak intensities on the spectra in the case using 0.5% Ho-OMS-2 were obviously lower (Figs. 3.16c-f), indicating that those intermediates were more easily oxidized over the 0.5% Ho-OMS-2 since more labile and active oxygen species on the Ho-OMS-2 can be provided for the toluene oxidation, which are also consistent with the catalytic performance as shown in Fig. 3.11. Therefore, these time-dependent DRIFTS spectra also demonstrated that the doping of Ho species on OMS-2 increased the density of oxygen vacancies and O_{ads} species as described in XPS analysis, which is benefit for the oxygen-vacancies-oxygen cycle especially via more abundant defects provided by the generated amorphous phase. Meanwhile, the presence of H_2O molecules in the feed could activate O-O bond on the catalysts to provide more active oxygen species and/or help to take away more generated intermediates so that more the active sites for the oxidation of toluene, which is in accordance with the results of performance and durability tests as described in sections of 3.3.6 and 3.3.7. In addition, the peaks at 2300-2400 cm^{-1} corresponding to CO_2 species and the weak peak at the around 3243 cm^{-1} belonging to crystal water were hard to be detected, implying that the final products of CO_2 and H_2O have been quickly removed from the surface of the catalysts. Besides, the signal at around 2088 cm^{-1} attributed to CO species was also not observed, indicating the high selectivity toward CO_2 of such catalysts.

Combined with the above DRIFTS spectrum analyses, the performance test and catalyst characterization results, the important intermediates were summarized in Table. 3.4, and a mechanism for toluene oxidation over the present catalysts was proposed as illustrated in Fig. 3.17. Firstly, the toluene adsorbed on the 0.5% Ho-OMS-2 may follow the pathways of oxidation: toluene (C_6H_5–CH_3) $\rightarrow$ benzyl (C_6H_5–CH_2–) $\rightarrow$ benzyl alcohol (C_6H_5–CH_2–OH) $\rightarrow$ benzaldehyde (C_6H_5–CHO) $\rightarrow$ benzoate (C_6H_5–$COOH$). Subsequently, the breaking C=C bond of benzoate causes the ring opening to the short-chain carbonates; meanwhile, the benzoate also can result in the formation of the phenolate via the breaking C=O bond. Finally, as we all known, the carbonates can be preferentially decomposed into CO_2 and H_2O whereas the phenolate can be decomposed into the maleic anhydride and ultimately mineralized to final product (CO_2 and H_2O) [22]. As such, the higher concentration of active oxygen species on the 0.5% Ho-OMS-2 than that on the OMS-2 played key role in the toluene oxidation since the consumable oxygen species such as O_{ads} could be more quickly replenished via richer oxygen vacancy defects as described above.
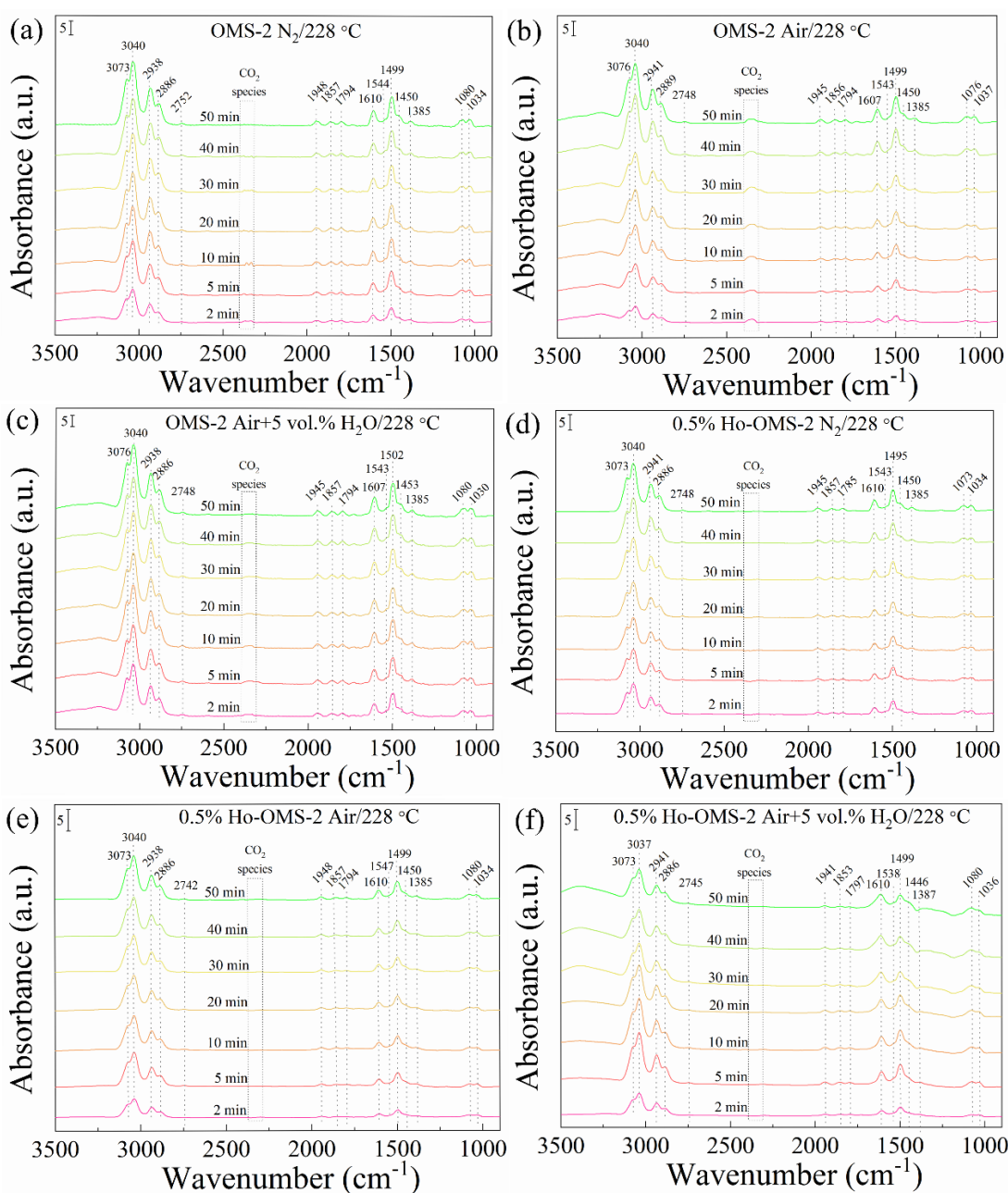
Fig 3.16. *In situ* DRIFTS spectra during toluene oxidation exposed to (a) 1000 ppm toluene/N_2 environment, (b) 1000 ppm toluene/air environment, and (c) 1000 ppm toluene/air environment with H_2O vapor (5 vol.%) in the cases using OMS-2; and (c) 1000 ppm toluene/N_2 environment, (d) 1000 ppm toluene/air environment, and (e) 1000 ppm toluene/air environment with H_2O vapor (5 vol.%) in the cases using 0.5% Ho-OMS-2.

Table 3.4 Assignment of IR peaks appearing in the process of toluene oxidation over OMS-2 and 0.5% Ho-OMS-2 at 228 °C based on the *in situ* DRIFTS analyses.

Position (cm^{-1})	Assignment	Corresponding species
1034	C-H in-plane bending vibration	Aromatic ring
1080	CO- stretching vibrations of alkoxide species	Benzyl alcohol
1385, 1543	C=O stretching vibrations of carboxylate group	Benzoate
1450, 1499, 1610	Skeletal C=C stretching vibrations	Aromatic ring
1794, 1857, 1948	C=O stretching vibrations of cyclic anhydrides	Maleic anhydride
2752, 2886	C=O stretching vibrations of carbonyl	Benzaldehyde
2938, 3040	CH- stretching vibrations	Benzyl
3073	Phenylic C-H stretching vibration	Aromatic ring
3236	O-H stretching vibrations	Crystal water
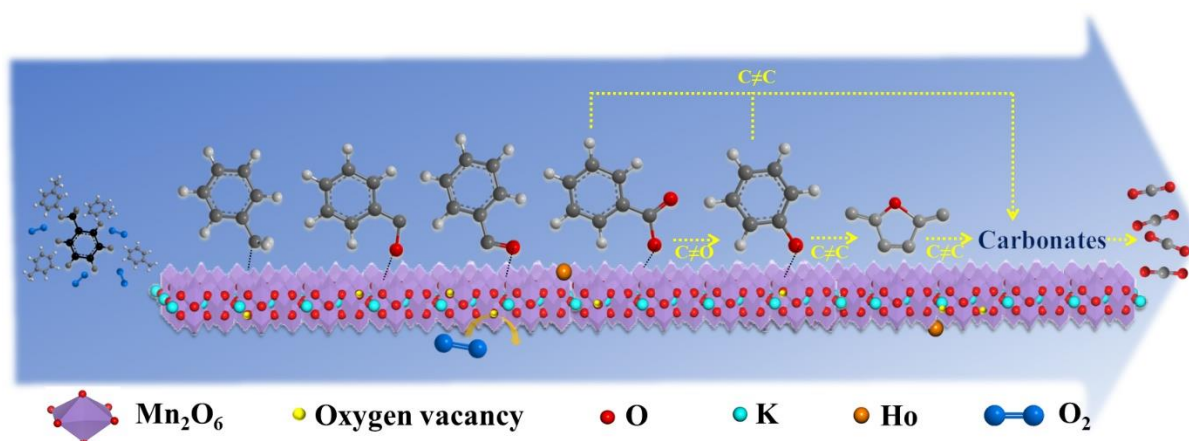
Fig 3.17. Proposed toluene oxidation mechanism over x% Ho-OMS-2.

3.4. Conclusions

In summary, a novel Ho-doped OMS-2 catalyst with abundant active oxygen species was successfully prepared via a facile redox co-precipitation route. It is found that the addition of Ho species in the OMS-2 catalyst preparation stage can effectively tune the oxygen vacancy defects on the final Ho-doped OMS-2 catalyst via adjusting the Ho doping amount, and the trace Ho doping not only regulated the surface oxygen species, but also changed the textural properties of OMS-2 including crystal structure, specific surface area, low-temperature reducibility, oxygen storage capacity and surface elemental

composition. As a result, the 0.5% Ho-OMS-2 exhibited the highest molar ratio of O_{ads}/O_{latt} with the highest performance for toluene oxidation among the prepared x% Ho-OMS-2, and its $T_{50\%}$, $T_{90\%}$ and $T_{100\%}$ values in the case with H_2O vapor (5 vol%) achieved at 217, 226, 228 °C, respectively. Comparing with the OMS-2, the active oxygen species on the Ho-doped OMS-2 were more easily released for promoting the adsorption and oxidation of toluene as well as intermediates. *In situ* DRIFTS study confirmed that either the adsorbed oxygen species on the surface or lattice oxygen in the bulk of catalysts could take part in the adsorption and oxidation reaction simultaneously, where the benzyl, benzyl alcohol, benzaldehyde, benzoate, maleic anhydride, and carbonates should be the main intermediates during toluene adsorption-oxidation process at relatively low temperatures.

References

[1] H. Huang, Y. Xu, Q. Feng, D.Y. Leung, Catalysis Science & Technology 5 (2015) 2649-2669.

[2] C. Yang, G. Miao, Y. Pi, Q. Xia, J. Wu, Z. Li, J. Xiao, Chemical Engineering Journal 370 (2019) 1128-1153.

[3] L. Chen, J. Tang, L.-N. Song, P. Chen, J. He, C.-T. Au, S.-F. Yin, Applied Catalysis B: Environmental 242 (2019) 379-388.

[4] C. He, Y. Yu, L. Yue, N. Qiao, J. Li, Q. Shen, W. Yu, J. Chen, Z. Hao, Applied Catalysis B: Environmental 147 (2014) 156-166.

[5] H. Sui, P. An, X. Li, S. Cong, L. He, Chemical Engineering Journal 316 (2017) 232-242.

[6] C.J. Hennigan, M.M.H. El-Sayed, A. Hodzic, Atmospheric Environment 188 (2018) 12-17.

[7] P. Wang, J. Wang, J. Shi, X. Du, X. Hao, B. Tang, A. Abudula, G. Guan, Molecular Catalysis 492 (2020) 111027.

[8] J. Fu, N. Dong, Q. Ye, S. Cheng, T. Kang, H. Dai, New Journal of Chemistry 42 (2018) 18117-18127.

[9] L. Torrente-Murciano, B. Solsona, S. Agouram, R. Sanchis, J.M. López, T. García, R. Zanella, Catalysis Science & Technology 7 (2017) 2886-2896.

[10] S. Zhao, K. Li, S. Jiang, J. Li, Applied Catalysis B: Environmental 181 (2016) 236-248.

[11] R. Peng, S. Li, X. Sun, Q. Ren, L. Chen, M. Fu, J. Wu, D. Ye, Applied Catalysis B: Environmental 220 (2018) 462-470.

[12] H.C. Genuino, S. Dharmarathna, E.C. Njagi, M.C. Mei, S.L. Suib, The Journal

of Physical Chemistry C 116 (2012) 12066-12078.

[13]   L.F. Liotta, H. Wu, G. Pantaleo, A.M. Venezia, Catalysis Science & Technology 3 (2013) 3085.

[14]   Y.-s. Ding, X.-f. Shen, S. Sithambaram, S. Gomez, R. Kumar, V.M.B. Crisostomo, S.L. Suib, M. Aindow, Chemistry of materials 17 (2005) 5382-5389.

[15]   X. Chen, Y.-F. Shen, S.L. Suib, C. O'Young, Chemistry of materials 14 (2002) 940-948.

[16]   C. Lahousse, A. Bernier, P. Grange, B. Delmon, P. Papaefthimiou, T. Ioannides, X. Verykios, Journal of Catalysis 178 (1998) 214-225.

[17]   S.L. Suib, Journal of Materials Chemistry 18 (2008) 1623.

[18]   S. Luo, L. Duan, B. Sun, M. Wei, X. Li, A. Xu, Applied Catalysis B: Environmental 164 (2015) 92-99.

[19]   S. Ming, P. Wang, P. Liu, J. Duan, F. Mei, L. Pang, Z. Chen, T. Li, Chemical Engineering Journal 379 (2020) 122287.

[20]   L. Lamaita, M.A. Peluso, J.E. Sambeth, H.J. Thomas, Applied Catalysis B: Environmental 61 (2005) 114-119.

[21]   S. Mo, Q. Zhang, J. Li, Y. Sun, Q. Ren, S. Zou, Q. Zhang, J. Lu, M. Fu, D. Mo, J. Wu, H. Huang, D. Ye, Applied Catalysis B: Environmental 264 (2020) 118464.

[22]   P. Wang, J. Wang, X. An, J. Shi, W. Shangguan, X. Hao, G. Xu, B. Tang, A. Abudula, G. Guan, Applied Catalysis B: Environmental 282 (2021) 119560.

[23]   H. Sun, Z. Liu, S. Chen, X. Quan, Chemical Engineering Journal 270 (2015) 58-65.

[24]   J. Hou, Y. Li, L. Liu, L. Ren, X. Zhao, Journal of Materials Chemistry A 1 (2013) 6736.

[25]   M. Sun, W. Li, B. Zhang, G. Cheng, B. Lan, F. Ye, Y. Zheng, X. Cheng, L. Yu, Chemical Engineering Journal 331 (2018) 626-635.

[26]   V.P. Santos, O.S.G.P. Soares, J.J.W. Bakker, M.F.R. Pereira, J.J.M. Órfão, J. Gascon, F. Kapteijn, J.L. Figueiredo, Journal of Catalysis 293 (2012) 165-174.

[27]   M. Luo, Y. Cheng, X. Peng, W. Pan, Chemical Engineering Journal 369 (2019) 758-765.

[28]   S. Yang, H. Zhao, F. Dong, Z. Tang, F. Zha, Catalysis Science & Technology 9 (2019) 6503-6516.

[29]   A. Iyer, J. Del-Pilar, C.K. King'ondu, E. Kissel, H.F. Garces, H. Huang, A.M. El-Sawy, P.K. Dutta, S.L. Suib, The Journal of Physical Chemistry C 116 (2012) 6474-6483.

[30]   Y. Yu, S. Liu, J. Ji, H. Huang, Catalysis Science & Technology 9 (2019) 5090-5099.

[31]   W.N. Li, J. Yuan, X.F. Shen, S. Gomez-Mower, L.P. Xu, S. Sithambaram, M. Aindow, S.L. Suib, Advanced Functional Materials 16 (2006) 1247-1253.

[32]   X. Liu, Q. Zhang, P. Ning, Q. Liu, Z. Song, Y. Duan, RSC Advances 7 (2017) 41936-41944.

[33]   L. Zhao, Z. Zhang, Y. Li, X. Leng, T. Zhang, F. Yuan, X. Niu, Y. Zhu, Applied Catalysis B: Environmental 245 (2019) 502-512.

[34]   X. Yu, Z. Zhao, Y. Wei, J. Liu, Scientific reports 7 (2017) 43894.

[35]   H. Huang, S. Sithambaram, C.-H. Chen, C. King'ondu Kithongo, L. Xu, A. Iyer, H.F. Garces, S.L. Suib, Chemistry of Materials 22 (2010) 3664-3669.

[36]   K.S. Lohar, A.M. Pachpinde, M.M. Langade, R.H. Kadam, S.E. Shirsath, Journal of Alloys and Compounds 604 (2014) 204-210.

[37]   W.-H. Ryu, J.-Y. Eom, R.-Z. Yin, D.-W. Han, W.-K. Kim, H.-S. Kwon, Journal of Materials Chemistry 21 (2011) 15337.

[38]   Z. Liu, R. Ma, Y. Ebina, K. Takada, T. Sasaki, Chemistry of Materials 19 (2007) 6504-6512.

[39]   Q. Kang, L. Vernisse, R.C. Remsing, A.C. Thenuwara, S.L. Shumlas, I.G. McKendry, M.L. Klein, E. Borguet, M.J. Zdilla, D.R. Strongin, Journal of the American Chemical Society 139 (2017) 1863-1870.

[40]   J. Huang, J.-Q. Wu, B. Shao, B.-L. Lan, F.-J. Yang, Y. Sun, X.-Q. Tan, C.-T. He, Z. Zhang, ACS Sustainable Chemistry & Engineering 8 (2020) 10554-10563.

[41]   M.A. Rahman, J.P. Thomas, K.T. Leung, Advanced Energy Materials 8 (2018) 1701234.

[42]   L. Zhang, J. Tu, L. Lyu, C. Hu, Applied Catalysis B: Environmental 181 (2016) 561-569.

[43]   J. Liu, L. Ke, J. Liu, L. Sun, X. Yuan, Y. Li, D. Xia, Journal of hazardous materials 371 (2019) 42-52.

[44]   W. Song, A.S. Poyraz, Y. Meng, Z. Ren, S.-Y. Chen, S.L. Suib, Chemistry of Materials 26 (2014) 4629-4639.

[45]   F. Wang, H. Dai, J. Deng, G. Bai, K. Ji, Y. Liu, Environmental science & technology 46 (2012) 4034-4041.

[46]   V.P. Santos, M.F.R. Pereira, J.J.M. Órfão, J.L. Figueiredo, Applied Catalysis B: Environmental 99 (2010) 353-363.

[47]   S. Mo, Q. Zhang, Y. Sun, M. Zhang, J. Li, Q. Ren, M. Fu, J. Wu, L. Chen, D. Ye, Journal of Materials Chemistry A 7 (2019) 16197-16210.

[48]   X. Yang, X. Yu, M. Lin, X. Ma, M. Ge, Catalysis Today 327 (2019) 254-261.

[49]　Y. Wang, H. Arandiyan, Y. Liu, Y. Liang, Y. Peng, S. Bartlett, H. Dai, S. Rostamnia, J. Li, ChemCatChem 10 (2018) 3429-3434.

[50]　S.B.T. Tran, H. Choi, S. Oh, J.Y. Park, Journal of Catalysis 375 (2019) 124-134.

[51]　Y. Huang, Y. Liu, W. Wang, M. Chen, H. Li, S.-c. Lee, W. Ho, T. Huang, J. Cao, Applied Catalysis B: Environmental 278 (2020) 119294.

[52]　C. Dong, Z. Qu, X. Jiang, Y. Ren, Journal of hazardous materials 391 (2020) 122181.

[53]　X. Zhang, H. Zhao, Z. Song, W. Liu, J. Zhao, Z.a. Ma, M. Zhao, Y. Xing, Applied Surface Science 493 (2019) 9-17.

[54]　Y. Luo, Y. Zheng, J. Zuo, X. Feng, X. Wang, T. Zhang, K. Zhang, L. Jiang, Journal of hazardous materials 349 (2018) 119-127.

[55]　Q. Zhang, S. Mo, J. Li, Y. Sun, M. Zhang, P. Chen, M. Fu, J. Wu, L. Chen, D. Ye, Catalysis Science & Technology 9 (2019) 4538-4551.

[56]　J.-J. Li, E.-Q. Yu, S.-C. Cai, X. Chen, J. Chen, H.-P. Jia, Y.-J. Xu, Applied Catalysis B: Environmental 240 (2019) 141-152.

[57]　J. Li, H. Na, X. Zeng, T. Zhu, Z. Liu, Applied Surface Science 311 (2014) 690-696.

[58]　C. Zhang, C. Wang, H. Huang, K. Zeng, Z. Wang, H.-p. Jia, X. Li, Applied Surface Science 486 (2019) 108-120.

[59]　M.D. Hernández-Alonso, I. Tejedor-Tejedor, J.M. Coronado, M.A. Anderson, Applied Catalysis B: Environmental 101 (2011) 283-293.

[60]　A. Lu, H. Sun, N. Zhang, L. Che, S. Shan, J. Luo, J. Zheng, L. Yang, D.-L. Peng, C.-J. Zhong, B. Chen, ACS Catalysis 9 (2019) 7431-7442.

152

Chapter 4 Low content of samarium doped CeO$_2$ oxide catalysts derived from metal organic framework precursor for toluene oxidation

4.1 Introduction

Volatile organic compounds (VOCs) including aldehydes, benzene series and polynuclear aromatic hydrocarbons are enormously emitted from industrial and residential activities. They can participate in a series of atmospheric chemical reactions [1-4], and become the primary threat to both the environment and human health [5, 6]. Catalytic oxidation is an economic and efficient way to reduce VOC emission without the secondary pollution [7, 8]. Owing to the high-stability, low-cost and high oxidation activity at low temperatures, transition metal oxide based catalysts are attracting more and more attentions [9-11].

In recent years, various transition metal oxides catalysts were successfully prepared for the oxidation of VOCs. Especially, Mn-based [12-15], Co-based [16, 17], and Ce-based [18-20] metal oxide catalysts exhibited excellent performances. Since CeO$_2$ has high oxygen storage capacity and excellent redox behavior, it always exhibits good performance for the oxidation of VOCs [21]. However, a broad conversion temperature region until the complete oxidation usually appears for the oxidation of toluene over the pure CeO$_2$ catalyst [22]. Thus, it is necessary to modify it for improving its performance. It is well known that the catalytic activity could be tuned by adjusting morphology, specific surface area, surface oxygen vacancy and so on. For instance, Feng *et al.* [23] synthesized three-dimensional hierarchical CeO$_2$ nanospheres with a relatively large specific surface area for the oxidation of toluene, and found that the catalyst had rich

surface oxygen vacancies, resulting in the excellent catalytic performance. To date, various methods such as the co-precipitation method [24], template-assisted sol-gel method [25], and modified solution combustion method [26] have been applied to modify CeO_2-based catalysts to improve the catalytic performance.

As the emerging porous coordination materials, metal organic frameworks (MOFs) with inorganic secondary building units and organic linkers have attracted tremendous attentions due to their intriguing properties, such as high specific surface areas, highly porous structures, chemical tenacity, and multifunctional species [27-30]. They have been widely applied in adsorption [31, 32], hydrogen storage [33], catalysis [34-36], photochemistry [37], and electrochemistry [38]. In particular, they can be used as the sacrificial template to generate nano-oxide catalysts by *in-situ* pyrolysis [39, 40]. For instance, Chen *et al*.[22] prepared mesoporous CeO_2 catalysts by pyrolysis of Ce-based MOF (Ce-MOF) precursor, and found that the obtained CeO_2 catalyst had a larger specific surface area, a smaller average grain size, higher relative percentages of Ce^{3+}/Ce^{4+} and O_{Sur}/O_{Latt}, and exhibited excellent catalytic activity. Herein, it is important to adjust the ratio between oxygen vacancy and lattice oxygen in the catalyst preparation. Recently, it is found that doping of rare-earth metals like samarium (Sm), holmium (Ho), europium (Eu), praseodymium (Pr) and Lanthanum (La) into the CeO_2 lattice could generate unique catalytic properties [41-46]. For example, Jiang *et al.* [42] synthesized rare-earth element containing CeO_2-based oxides of $CuMCeO_x$ (M=Rare-earth element) with enhanced oxygen migration capability by a self-precipitation approach for the catalytic oxidation of toluene. It is proved that Ho atom could be coordinated to two oxygen atoms and occupy the site of a Ce atom, leading to the weakening of Ce-O bonds and the enhancement of oxygen storage capacity. Huang *et al*.[47] doped Eu into CeO_2

nanosheets for the oxidation of HCHO, and found that the Eu-doped CeO_2 nanosheets had abundance surface defects with high redox ability. Moreno *et al*. [48] also found the cooperative effect of Ce and Pr in the modification of mixed Cu-Co oxide catalysts. Therefore, it should be an effective way to enhance the catalytic performance of CeO_2-based catalysts by doping with the rare-earth elements.

Inspired by the above studies, in this study, samarium (Sm) doped cerium oxide (x% Sm/CeO_2) catalysts with different Sm doping amounts were prepared by pyrolysis of Sm/Ce-MOF precursor, and employed for the oxidation of toluene for the first time. The catalysts were characterized by SEM, EDS, TEM, N_2 adsorption-desorption, H_2-TPR, O_2-TPD, Raman, and XPS analyses. The effect of Sm doping on the oxygen vacancy formation and the reducibility of the catalysts were discussed. The performance for the oxidation of toluene at different environments were investigated. In addition, the stability and moisture endurability tests over the best Sm/CeO_2 catalyst was performed to evaluate its feasibility as a catalyst for the VOC oxidation in the practical process.

4.2 Experimental

4.2.1 Catalyst preparation

Firstly, a series of mesoporous Sm doped cerium oxide (x% Sm/CeO_2) catalysts with nanorod morphology were synthesized by pyrolysis of Sm/Ce-MOF precursors. Typically, 8.64 g $Ce(NO_3)_3 \cdot 6H_2O$ and a predetermined amount of $Sm(NO_3)_3 \cdot 4H_2O$ (i.e., 0.0432, 0.0864, or 0.259 g, corresponding to x% = 0.5, 1, or 3 wt%) were dissolved in 100 mL of deionized (DI) water to get a homogeneous solution (A solution). Meanwhile, 2.1 g of 1,3,5-benzenetricarboxylic acid (H_3BTC) was dissolved in 100 mL of DI water-ethanol mixing solution (v/v = 1:1) as B solution, which was heated to 60 °C. Subsequently, the A solution was added into the B solution by a liquid feeding pump with a feeding speed

of 10 mL/min under vigorous magnetic stirring at 60 °C. After aging for 3 h, the obtained white precipitate (i.e., Sm doping Ce-MOF) was collected by centrifugation and washed for several times with ethanol and DI water successively to remove the impurities and then dried at 60 °C for 12 h. Finally, the Sm doping Ce-MOF precursor was annealed in air at 350 °C for 3 h with a heating rate of 5 °C/min. As such, the x% Sm/CeO_2 catalysts were obtained. Hereafter, the catalysts with different Sm doping contents are named as 0.5% Sm/CeO_2, 1% Sm/CeO_2, and 3% Sm/CeO_2. For comparison, the single cerium element contained catalyst (referred as pure CeO_2) was also obtained via the same process without the addition of Sm species.

4.2.2 Catalyst characterizations

Morphologies and nanostructures of the as-obtained x% Sm/CeO_2 catalysts were examined by a scanning electron microscopy (SEM, SU8010, Japan) with an energy dispersive X-ray detector (EDS, Horiba Scientific) at 15 kV and a transmission electron microscopy (TEM, JEM-2100, Japan) operating at a voltage of 200 kV, respectively. The crystalline structure was obtained by an X-ray diffraction system (XRD, Rigaku Smartlab, Japan) equipped with a Cu-Kα radiation (λ = 1.5418 Å) in 2θ range of 10º-90º at a scanning rate of 10 º/min. Raman spectrum was measured using a JASCO NRS-5100 Raman spectrometer at 532 nm. The Brunauer-Emmett-Teller (BET) surface area was conducted on a Micromeritics TriStar II (TriStar II 3020 V1.03, USA) using N_2 gas as the adsorbate at 77.3 K. The pore size distributions were generated by nonlocal (NL) DFT calculations on the desorption branch of the isotherms. The compositions and valence states of the elements were analyzed on an X-ray photoelectron spectrometer (XPS, ESCALab220i-XL, UK) with an Al Kα (hν = 1486.6 eV) radiation source. After the collection of the spectra, the corrective action of the samples was carried out by setting

the binding energy of adventitious carbon (C 1s) at 284.8 eV. The data were processed with CasaXPS software for Shirley background subtraction, fitting, deconvolution of the peaks and determination of the relative atomic concentrations. The evaluation of the spectra was performed using the binding energies found in the earlier investigations. The weight composition of the Sm/Ce-MOF precursor was characterized via Thermogravimetric analyser (TGA, Shimadzu DTG60, Japan).

H_2 temperature-programmed reduction (H_2-TPR) and O_2 temperature-programmed desorption (O_2-TPD) analyses were performed using an a BELCAT catalyst analyzer (Microtrac, Japan). In the H_2-TPR analysis, about 50 mg of catalyst was pretreated at 300 °C in helium (He) gas flow with a flow rate of 50 cm^3/min for 60 min. After cooling to 30 °C at the same gas flow condition, the reduction process was carried out under a flow of 5 vol% H_2/Ar gas mixture (50 cm^3/min) at a temperature range of 30-900 °C with a heating rate of 10 °C/min. For O_2-TPD analysis, about 100 mg of catalyst was pretreated at 110 °C in He gas flow with a flow rate of 50 cm^3/min for 60 min in order to remove out the physically adsorbed oxygen on the surface before O_2-TPD analysis. After cooling to 30 °C, the gas flow was changed to O_2 gas (>99.999 %) flow with a flow rate of 50 cm^3/min and kept for 60 min. After being purged under He with a flow rate of 50 cm^3/min for 60 min, the desorption was carried out in a temperature range from 30 to 900 °C with a heating rate of 10 °C/min.

4.2.3 Catalyst evaluation

Catalytic oxidations of toluene over the as-prepared x% Sm/CeO$_2$ catalysts (ca. 50 mg, 40-60 mesh) were performed in a fixed bed reactor (inner diameter = 8 mm) with a weight hourly space velocity (WHSV) of 60,000 mL/(g h). The toluene vapor was generated from a bubbler filled with liquid toluene in a thermostatic bath at 0 °C, and introduced

into the reactor with carrier gas, in which the gas mixture consisted of 1000 ppm toluene, 20 vol.% O_2, and N_2 as balance gas with a total flow of 50 cm^3/min. Before the activity test, the reactor system was pretreated in a N_2 gas flow at 100 ºC for 60 min in order to avoid the possibility of over-estimation of toluene conversion. The reaction temperature was measured using a thermocouple in the centre of catalyst layer and it is found that the actual measured temperature was about 12 °C higher than the setting temperature. For comparison, the activity tests were also performed under other two WHSVs of 30,000 and 100,000 mL/(g h) with 0.1 g and 0.03 g of catalysts, respectively. Moreover, water resistance performance of the most promising 1% Sm/CeO_2 catalyst was investigated under introductions of 5 vol.% and 10 vol.% H_2O vapors through a water saturator, respectively. The concentrations of inlet and outlet gases during the catalytic oxidation were monitored by an on-line gas chromatograph (GC) equipped with the double flame ionization detectors (FID, GC-2014, Shimadzu) and the thermal conductivity detector (TCD, GC-8A, Shimadzu). The concentration of CO_2 was in-situ detected by FT-IR gas analyzer (Horiba, FG-120).

Toluene conversion ($X_{toluene}$) and CO_2 selectivity (Y_{CO_2}) were calculated respectively by the following two equations:

$$X_{toluene} = \frac{C_{Inlet} - C_{Outlet}}{C_{Inlet}} \times 100\%$$

$$Y_{CO_2} = \frac{C_{CO_2}}{7(C_{Inlet} - C_{Outlet})} \times 100\%$$

where, C_{Outlet} and C_{Inlet} represent the outlet and inlet concentrations of toluene, respectively, and C_{CO_2} represents the outlet CO_2 concentration.

4.3 Results and discussion

4.3.1 SEM and TEM images

As shown in Fig. 4.1, the obtained x% Sm/CeO$_2$ catalysts were composed of particles with nanorod morphology. For the 1% Sm/Ce-MOF precusor, the particle sizes with a diameter range of 0.3-0.8 nm and a length range of 3-10 μm were observed (Fig. 4.1a). After calcination, as shown in Fig. 4.1b, the 1% Sm/CeO$_2$ catalyst maintained the rod morphology of MOF but displayed a rough surface and shrinking rod morphology. The nanostructure of Ce-based catalyst was further examined by TEM. As shown in Fig. 4.2, abundant well-resolved lattice fringes were observed. In the TEM image of the pure CeO$_2$ (Fig. 4.2a), the lattice fringe spacings of 0.19, 0.27, and 0.31 nm corresponded to the (220), (200) and (111) planes of CeO$_2$, respectively [22, 26]. After doping 1% of Sm species into CeO$_2$, as shown in Fig. 4.2b, the lattice fringe spacings of 0.27 nm and 0.31 nm corresponding to the crystal plane (200) and (111) of CeO$_2$ were still observed. Herein, it is worth noting that the edge dislocations and defects also appeared on the exposed crystal plane (200) of CeO$_2$ crystallites (Fig. 4.2b), which could provide abundant defects as active sites for the oxidation of toluene.

4.3.2 XRD characterization

Fig. 4.3 shows XRD patterns of the catalyst precursors and related final catalysts after calcination. As shown in Fig. 4.3a, the main diffraction peaks of the Ce-MOF were located in the range of 10-30° with a high degree of crystallinity, which is well agreement with the reported Ce-MOF crystalline structures [49, 50]. Comparing with the XRD pattern of pure Ce-MOF crystal, the peaks at around $2\theta = 17°$ of Sm-doped ones showed an obvious left-shift, indicating that the Sm species should be incorporated into the Ce-MOF crystal structure to affect the structure of Ce-MOF due to the strong interaction between Ce and Sm species. In addition, the thermal stability of the MOF structure was investigated by TGA analysis. As shown in Fig. 4.4, the total weight losses for the Ce-

MOF, 0.5% Sm/Ce-MOF and 3% Sm/Ce-MOF in the temperature range of 170-640 °C were almost the same, i.e., ca. 34 wt% but that for the 1% Sm/Ce-MOF was 38.5 wt%. It indicated that more organic components existed in 1% Sm/Ce-MOF, which could generate more porosity after the calcination. As shown in Fig. 4.3b, compared with a standard XRD pattern of CeO_2 (JCPDS 34-0394) [22, 26], the main peaks corresponding to the CeO_2 in 0.5% Sm/CeO_2, 1% Sm/CeO_2 and 3% Sm/CeO_2 catalysts obtained by calcination of MOF precursors were well matched with the fluorite structure of CeO_2 and without any left-shifts of peak. Meanwhile, it can be found that no new diffraction peaks assigned to Sm oxide and $SmCeO_x$ perovskite-like structure appeared in x% Sm/CeO_2 catalysts, which should be attributed to the low content of Sm species.
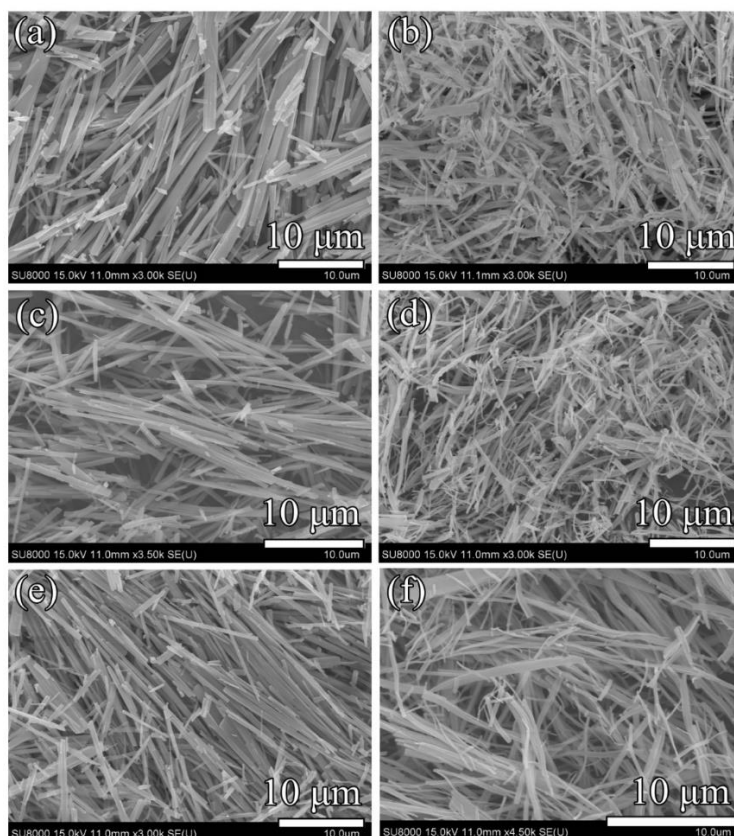
Fig 4.1. SEM images of Ce-MOF (a), pure CeO_2 (b), 0.5% Sm/Ce-MOF (c), 0.5% Sm/CeO_2 (d); and 3% Sm/Ce-MOF (e) and 3% Sm/CeO_2 (f).

160
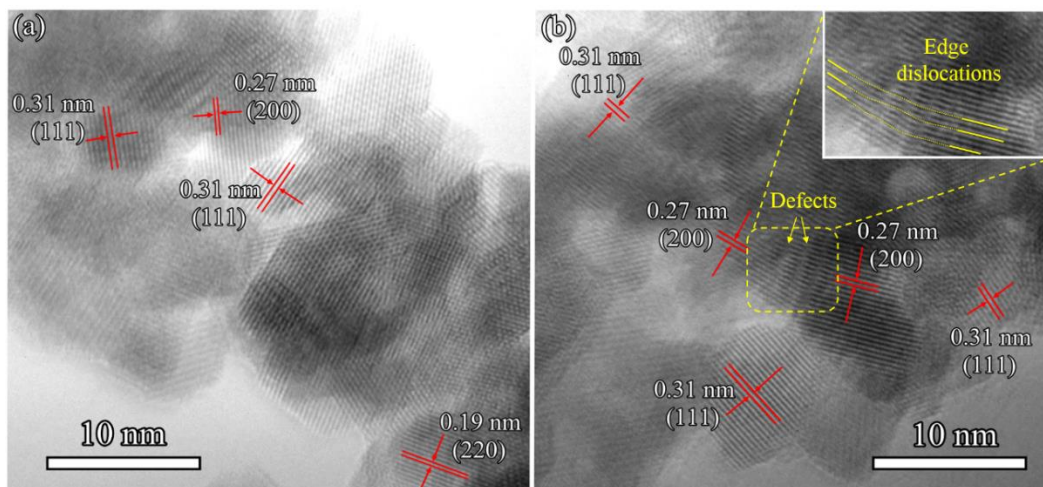
Fig 4.2. TEM images of pure CeO₂ (a) and 1% Sm/CeO₂ (b).
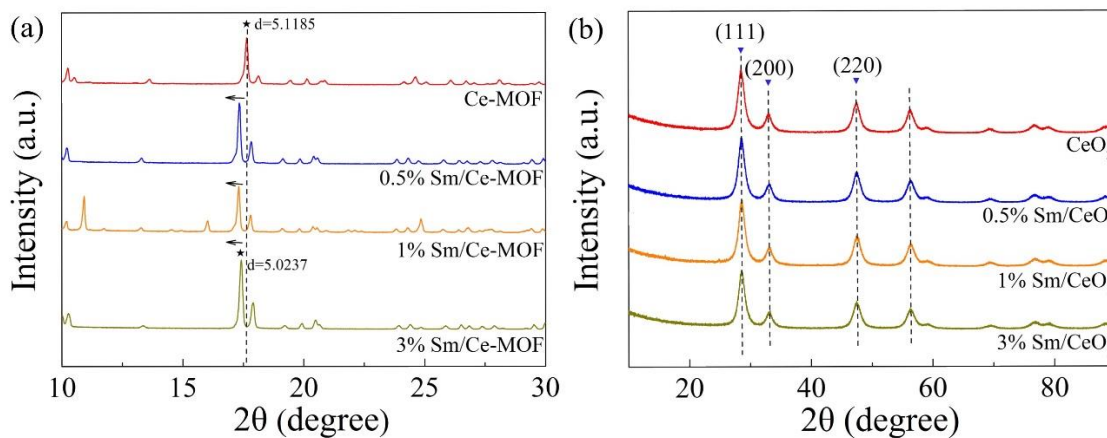
Fig 4.3. XRD patterns of x% Sm/Ce-MOF precursors before calcination (a), and x% Sm/CeO₂ catalysts after calcination.
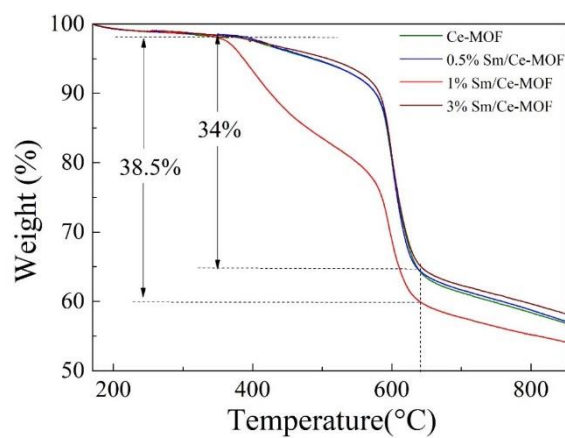
Fig 4.4. TGA results for Ce-MOF and x% Sm/Ce-MOF.

4.3.3 Temperature-programmed studies

To determine the reducibility of the x% Sm/CeO$_2$ catalysts, H$_2$-TPR profiles were measured within a temperature range of 300-900 °C and the results are displayed in Fig. 4.5. In general, during the reducing of CeO$_2$, three reducing temperature ranges of 100-400 °C, 400-600 °C, and 600-900 °C corresponding to the reductions of oxygen on the surface, on the subsurface and in the bulk respectively can be observed [51, 52]. Herein, the three reduction peaks at 370, 569.9, and 654.8 °C for the pure CeO$_2$ should be attributed to the surface, subsurface and bulk oxygen reductions, respectively [12]. However, for the Sm doped CeO$_2$ catalysts, only a broad peak was clearly observed in the reducing temperature range of 400-600 °C with a minimum reduction temperature at 561.6 °C (1% Sm/CeO$_2$) as shown in Table 4.1. The obvious shape changes reflected that the Sm doping had significant influence on the states of oxygen species for x% Sm/CeO$_2$. It is observed an imperceptible reduction peak below 400 °C and a peak coming to an end beyond 600 °C, which represented that a small amount of oxygen species on the surface and in the bulk could be reduced in the three x% Sm/CeO$_2$ catalysts. In other words, appropriate amount of Sm doping was conductive to promoting the evolution to the abundance subsurface oxygen species from the surface or in the bulk, which contributed to the deep oxidation of toluene due to the easy utilization of oxygen by comparison of the catalytic performance. Moreover, based on the total H$_2$ consumption during H$_2$-TPR measurements in Table 4.1, the order of the reducibility at low-temperature for the Sm doped CeO$_2$ catalysts was found to be 0.5% Sm/CeO$_2$ < 3% Sm/CeO$_2$ < 1% Sm/CeO$_2$, indicating that 1% Sm/CeO$_2$ should have the highest activity among these three x% Sm/CeO$_2$ catalysts. In addition, the total H$_2$ consumption of pure CeO$_2$ was higher than those of 0.5% Sm/CeO$_2$ and 3% Sm/CeO$_2$ catalysts, but its catalytic activity was limited

due to the low utilization efficiency of oxygen species in the bulk. The elemental contents on the surfaces of x% Sm/CeO$_2$ catalysts were also confirmed by EDS analysis. As shown in Table 4.1, the elemental content of Sm species was consistent with the corresponding theoretical doping amount on the surface. It is noteworthy that the content of oxygen on the surface of 1% Sm/CeO$_2$ was higher than the those of 0.5% Sm/CeO$_2$ and 3% Sm/CeO$_2$ catalysts, indicating that the optimal doping amount of Sm existed in the x% Sm/CeO$_2$ catalysts.
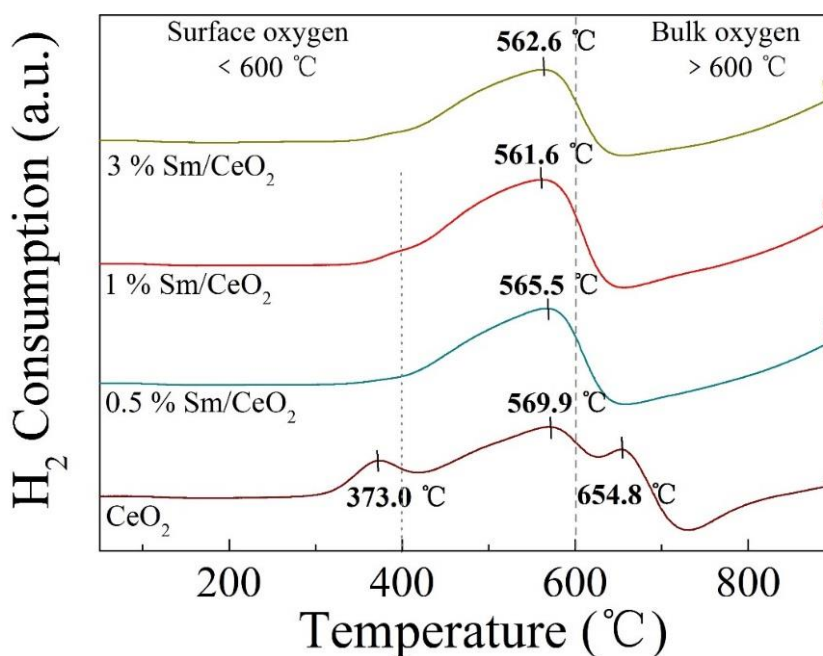
Fig 4.5. H$_2$-TPR profiles of pure CeO$_2$ and Sm doped CeO$_2$ catalysts.

O$_2$-TPD analysis was conducted to further determine the type and mobility of oxygen species in Fig. 4.6. For the CeO$_2$-based catalysts, the desorption of oxygen species can be proceed as follows: O$_2$ (ad) → O$_2^-$ (ad) → O$^-$ (ad) (100-500 °C) → O^{2-} (lattice) (> 500 °C), where O$_2$ (ad) means physically adsorbed oxygen; O^{2-} (ad) and O$^-$ (ad) refer to chemically adsorbed oxygen; O^{2-} (lattice) indicates lattice oxygen [53-56]. As shown in Fig. 4.6 and summarized in Table 4.1, the peaks on the O$_2$-TPD profile of 1% Sm/CeO$_2$ catalyst centered at 153.8, 233.1, 305.5 °C and a broad peak at the region from 400-800 °C

should correspond to O_2 (ad), O_2^- (ad), O^- (ad), and O^{2-} (lattice), respectively. Furthermore, the peak positions of these oxygen species (O_2 (ad), O_2^- (ad), and O^- (ad) oxygen species) were obviously shifted to low temperatures after Sm doping, indicating that the oxygen mobility was significantly enhanced by the doping of a little amount of Sm into CeO_2. Taking O_2 consumption into consideration (Table 4.1), the order of the amounts of O_2 consumption for the prepared catalysts was: $CeO_2 < 0.5\%$ $Sm/CeO_2 < 3\%$ $Sm/CeO_2 < 1\%$ Sm/CeO_2, also indicating that 1% Sm/CeO_2 should have the highest activity among these three Sm/CeO_2 catalysts.
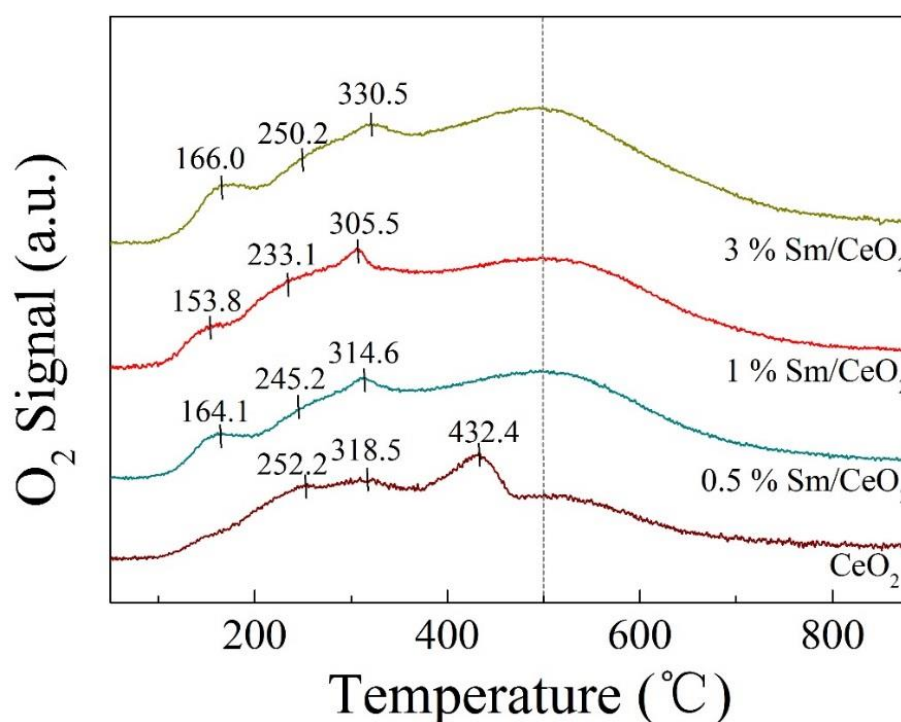
Fig 4.6. O_2-TPD profiles of pure CeO_2 and Sm doped CeO_2 catalysts.

Table 4.1 Element contents, peak positions, H_2 and O_2 consumptions of H_2-TPR and O_2-TPD for x% Sm/CeO_2 catalysts.

Catalyst	Element contents (wt. %) [a]				H_2-TPR (mmol/g)		O_2-TPD (mmol/g)	
	Ce	O	Sm	Sm/Ce	T (°C)	H_2-uptake	T (°C)	O_2-uptake

3% Sm/CeO$_2$	73.5	23.6	2.9	0.04	562.6	11.598	166, 250.2, 330.5	0.648
1% Sm/CeO$_2$	67.2	31.75	1.05	0.02	561.6	14.225	153.8, 233.1, 305.5	0.738
0.5% Sm/CeO$_2$	69	30.6	0.4	0.006	565.5	11.276	164.1, 245.2, 314.6	0.503
CeO$_2$	72.95	27.05	/	/	373, 569.9, 654.8	12.153	252.2, 318.5, 432.4	0.373

[a]Element contents were determined by the EDS analysis.

4.3.4 Raman spectral analysis

As observed in Fig. 4.7a, the most intense peak at 467 cm^{-1} was distinguished as the symmetric stretching vibrations (IF$_{2g}$) mode in the CeO$_2$ lattice. Meanwhile, the second intense peak at 587 cm^{-1} was related to the band of defect-induced (I$_D$) mode, which corresponded to the oxygen vacancies caused by the existence of Ce^{3+} [22, 57, 58]. It is reported that the concentration of oxygen vacancies can be closely reflected by the relatively intensity ratio of I$_D$/IF$_{2g}$ [59]. As summarized in Table 4.2, the concentration of oxygen vacancies increased with an order of CeO$_2$ < 0.5% Sm/CeO$_2$ < 3% Sm/CeO$_2$ < 1% Sm/CeO$_2$, suggesting more oxygen vacancies and defects were generated on the catalyst surface by the Sm doping. As illustrated in Fig. 4.7(b), the other two bands centered at ca. 835 and 1067 cm^{-1} were assigned to peroxide species (O$^-$) on the catalysts. Moreover, the second-order vibration (IIF$_{2g}$) was clearly observed at ca. 1178 cm^{-1} [22, 60, 61]. In addition, the peak located at 1375 cm^{-1} was ascribed to the effect of Sm species, which may represent the vibration of Sm-O bonds. In general, higher concentration of oxygen vacancies and defects were believed to be more beneficial to the catalytic activity of toluene combustion. Thus, 1% Sm/CeO$_2$ should have the best performance among these catalysts.
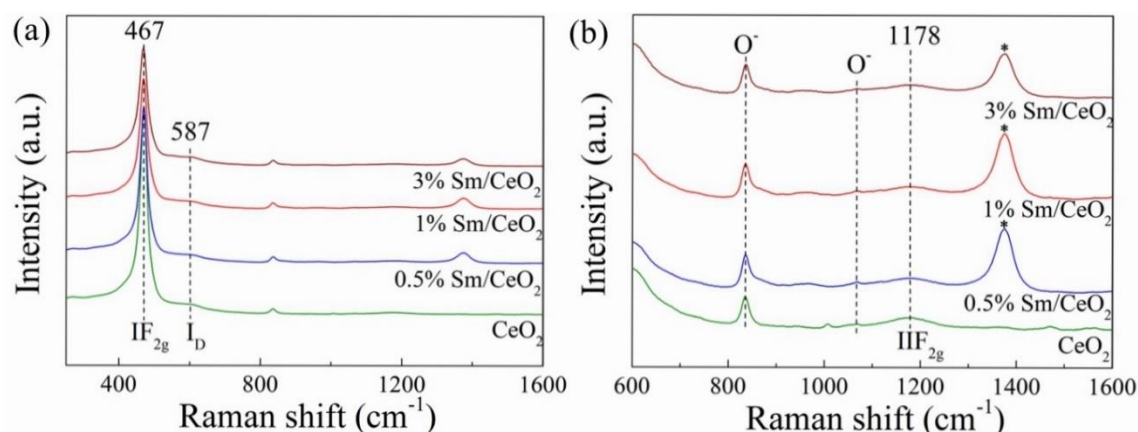
Fig 4.7. Raman spectra (a) and partial enlarged images (b) of pure CeO_2 and Sm doped CeO_2 catalysts.

Table 4.2 Oxygen vacancy concentrations (I_D/IF_{2g}) and pore structures of catalysts.

Catalyst	I_D/IF_{2g} (%)	BET [a] (m²/g)	D [b] (nm)	V [c] (cm³/g)
3% Sm/CeO₂	16.98	94	2.3-6.6	0.13
1% Sm/CeO₂	15.64	129	2.3-7	0.12
0.5% Sm/CeO₂	12.66	117	2.3-6.7	0.17
CeO₂	11.17	110	2.3-7.4	0.10

[a] BET specific surface area.

[b] Pore diameter calculated from the desorption branch of the isotherm using the DFT method.

[c] Total pore volume measured at $P/P_0=0.99$.

4.3.5 N_2 adsorption-desorption isotherm measurements

N_2 adsorption-desorption isotherms and the DFT pore size distribution curves of pure CeO_2 and 1% Sm/CeO₂ are shown in Fig. 4.8, and the pore structures of samples are summarized in Table 4.2. As shown in Fig. 4.8a, obviously, the classical type-IV isotherms were obtained for all the catalysts, indicating the presence of the similar

mesoporous architecture in them [62]. As observed in Fig. 4.8b, the incorporation of Sm

species seemed to have no significant influence on the pore size distribution. However,

the incorporation of a low content of Sm resulted in an increase in the surface area from

110 m^2/g (pure CeO_2) to 129 m^2/g (1% Sm/CeO_2), which should improve the catalytic

performance [63]. Conversely, the incorporation of more Sm (e.g., 3% Sm/CeO_2 catalyst)

resulted in the decrease in the surface area (94 m^2/g). It is possible that more Sm-doping

led to some structural collapses, which also resulted in the decrease of the catalytic

performance (as indicated in section 4.3.7).
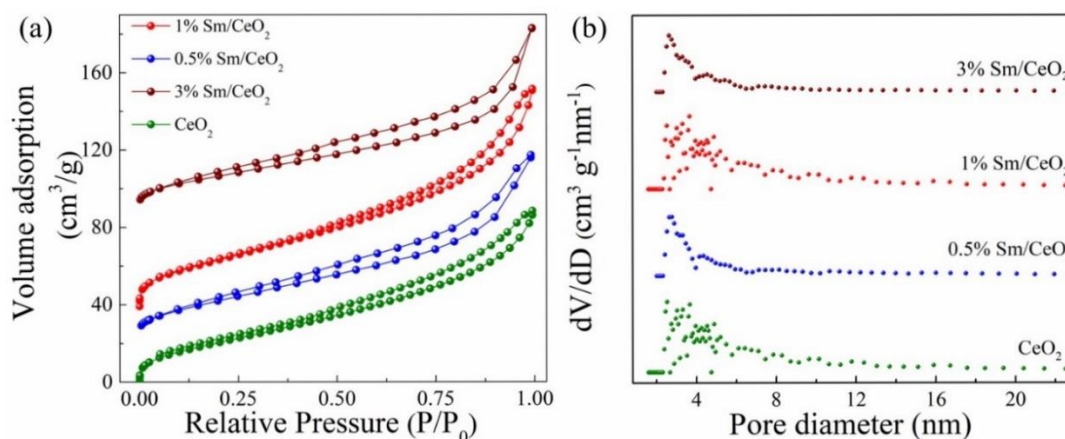
Fig 4.8. N_2 adsorption-desorption isotherms (a) and pore size distributions calculated

using the DFT method (b).

4.3.6 XPS study

The surface oxidation states of the pure CeO_2 and 1% Sm/CeO_2 catalysts, and the spent

1% Sm/CeO_2 catalyst after 10 and 30 h stability tests were estimated using the XPS

analysis (Fig. 4.9) and the quantitative analysis results are summarized in Table 4.3. For

Ce 3d XPS spectra, ten peaks corresponding to five pairs of spin-orbit states were

carefully distinguished due to the overlap among a series of peaks arising by the mixing

of O 2p and Ce 4f levels in the range of 870-920 eV, where the peaks denoted as V and

U were attributed to Ce $3d_{3/2}$ and Ce $3d_{5/2}$, respectively [64, 65]. As shown in Fig. 4.9a, the peaks labelled by V_0, V', U_0, U' represented the Ce^{3+} species whereas the peaks labeled V, V″, V‴, U, U″, U‴ were ascribed to Ce^{4+} species [66-68]. Distinction of ten peaks verified that the samples of CeO_2, 1% Sm/CeO_2, and the spent 1% Sm/CeO_2 after 10 h stability test contained both Ce^{3+} species and Ce^{4+} species, confirming the redox nature of the Ce-based catalysts [60]. Meanwhile, Ce^{3+} species is often used as an indicator for the existence of oxygen vacancies on the Ce-based catalyst surface, which is also related to the catalytic activity for the oxidation of VOCs [60, 69, 70]. Table 4.3 lists the contents of Ce^{3+} species in different catalysts. One can see that the amount of Ce^{3+} species in 1% Sm/CeO_2 was 51.76%, which was more than that of the pure CeO_2 (50.26%). Moreover, the amount of Ce^{3+} species of the spent 1% Sm/CeO_2 catalyst after 10 h stability test decreased to 44.22% and further decreased to 42.43% after 30 h stability test. In addition, it should be noted that the peak position U_0 of Ce^{3+} species was hard to be observed for the spent 1% Sm/CeO_2 after 30 h stability test, Tao *et al.* [70] reported that the change of Ce^{3+} fraction could largely influence the shape of the Ce 3d spectrum since the Ce 3d spectrum was typically deconvoluted into six peaks of Ce^{4+} and four peaks of Ce^{3+}, also evidencing that the amount of Ce^{3+} species declined obviously after 30 h stability test.

Additionally, Fig. 4.9b shows O1s XPS spectra, in which the adsorption oxygen (O_{ads}), surface active oxygen (O_{sur}), and lattice oxygen (O_{latt}) located at binding energies of 531.9-533.1, 530.1-531.3 and 528.5-529.8 eV, respectively, coexisted [12]. It is recognized that the higher the relative surface oxygen composition amount is, the easier the activation of adsorbed O_2 from gas environment into the electrophilic reactive oxygen (O_{ads}) species. As such, the surface-adsorbed oxygen species could play an important role in the deep oxidation of toluene [71]. As shown in Table 3, the ratios of O_{sur}/O_{latt} were

168

35.9 % and 40 % for the pure CeO_2 and 1% Sm/CeO_2 catalysts, respectively, suggesting that the O_{sur} concentration was greatly increased after Sm doping, which could apparently influence the catalytic oxidation of toluene. Moreover, for the 1% Sm/CeO_2 catalysts, with the increase in the stability test time, the content of the O_{latt} decreased gradually from 62.5% to ca. 58%, confirming the lattice oxygen transferred from the bulk structure to the surface of catalysts [72, 73]. Besides, for the spent catalyst after the stability test, the change of total value of O_{ads} and O_{sur} ($O_{ads} + O_{sur}$) was not so obvious, demonstrating the presence of oxidation/reduction cycle between $O_{latt} \to O_{ads} \leftrightarrow O_{sur}$. Thus, the Sm-doping could result in abundant oxygen vacancies due to the generation of more Ce^{3+} species, thereby promote the catalytic performance.
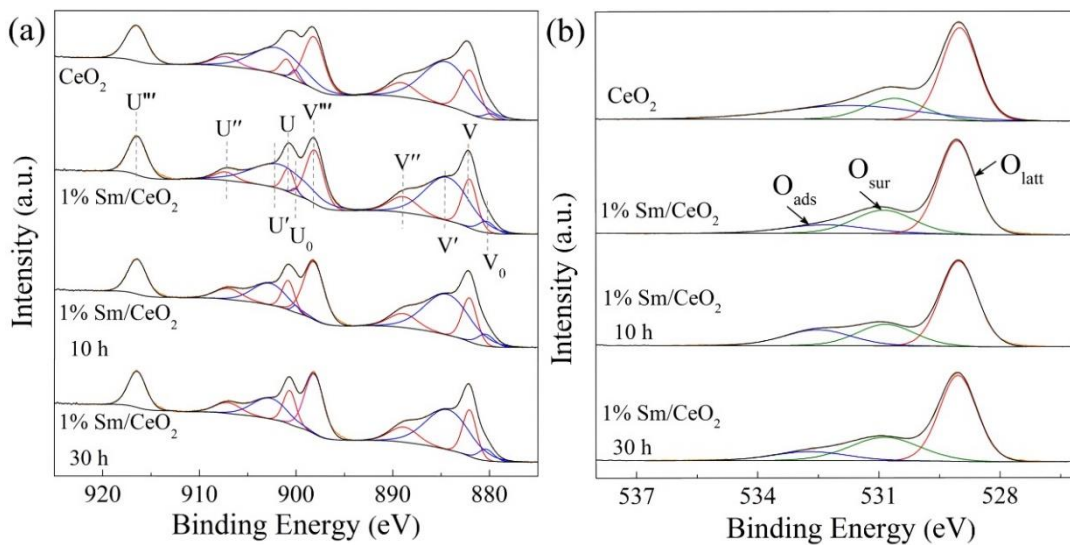
Fig 4.9. XPS spectra of Ce 3d (a), O 1s (b) in pure CeO_2, fresh and spent 1% Sm/CeO_2 catalysts after 10 and 30 h stability tests in section 4.3.8.

Table 4.3 Surface elemental compositions by XPS data.

Sample	$Ce^{3+}/Ce^{4+}+Ce^{3+}$ (%) [a]	$O_{ads}/(O_{ads}+O_{sur}+O_{latt})$ (%) [b]	$O_{sur}/(O_{ads}+O_{sur}+O_{latt})$ (%) [b]	$O_{latt}/(O_{ads}+O_{sur}+O_{latt})$ (%) [b]
CeO_2	50.26	28.89	18.79	52.32
1% Sm/CeO_2	51.76	12.48	25.02	62.50

Spent 1% Sm/CeO$_2$-10 h	44.22	19.43	22.50	58.07
Spent 1% Sm/CeO$_2$-30 h	42.43	11.82	29.65	58.53

[a]The ratio of surface Ce^{3+} to (Ce^{4+}+Ce^{3+}) based on XPS spectra, where Ce^{3+} = v$_0$ + v′ + u$_0$ + u′ and Ce^{4+} = v + v″ + v‴ + u + u″ + u‴.

[b]The ratio of surface O$_{ads}$ to (O$_{ads}$ + O$_{sur}$ + O$_{latt}$), O$_{sur}$ to (O$_{ads}$ + O$_{sur}$ + O$_{latt}$), and O$_{latt}$ to (O$_{ads}$ + O$_{sur}$ + O$_{latt}$) based on XPS spectra.

4.3.7 Catalytic performances

Catalytic activities of the x% Sm/CeO$_2$ catalysts were studied by oxidation of toluene in a temperature range of ca.130-330 °C (Fig. 4.10), and the temperatures for achieving 10 %, 50 %, 90 %, and 100 % of toluene conversions were summarized in Table 4.4. All catalysts evaluation experiments were repeated at least three times to ensure the accuracy of the results. One can see that the toluene conversion (Fig. 4.10a) and CO$_2$ yield (Fig. 4.10b) increased with the increase in temperature, and the toluene was completely decomposed at a temperature below 235 °C for the Sm-doped CeO$_2$ catalysts. Among all the Ce-based catalysts, the 1% Sm/CeO$_2$ catalyst exhibited the best catalytic activity and the order of complete toluene conversion temperature was 1% Sm/CeO$_2$ < 3% Sm/CeO$_2$ < 0.5% Sm/CeO$_2$ < pure CeO$_2$, suggesting that the catalytic performance was effectively improved by the Sm doping. The results of toluene combustion for three runs over 1% Sm/CeO$_2$ catalyst are displayed in Fig. 4.11. Compared with the previously reported Ce-based oxide catalysts (Table. 4.4), the as-obtained x% Sm/CeO$_2$ catalysts also showed a better catalytic performance. Moreover, the complete toluene mineralization temperatures also followed the similar sequence of 1% Sm/CeO$_2$ (237 °C) < 3% Sm/CeO$_2$ (238 °C) = 0.5% Sm/CeO$_2$ (238 °C) < pure CeO$_2$ (281 °C), indicating that the 1% Sm/CeO$_2$ catalyst had the lowest light-off temperature. Considering the characterization results together, it can be concluded that low content Sm-doping into the CeO$_2$ lattice framework by

170

pyrolysis of Sm incorporated Ce-MOF precursor effectively improved the catalytic activity. For the Ce-based catalysts, it is confirmed that the oxidation of toluene over it proceeded as follows: toluene should be rapidly transformed to aldehydic at first and then to benzoate species and finally to CO_2 and H_2O [22].
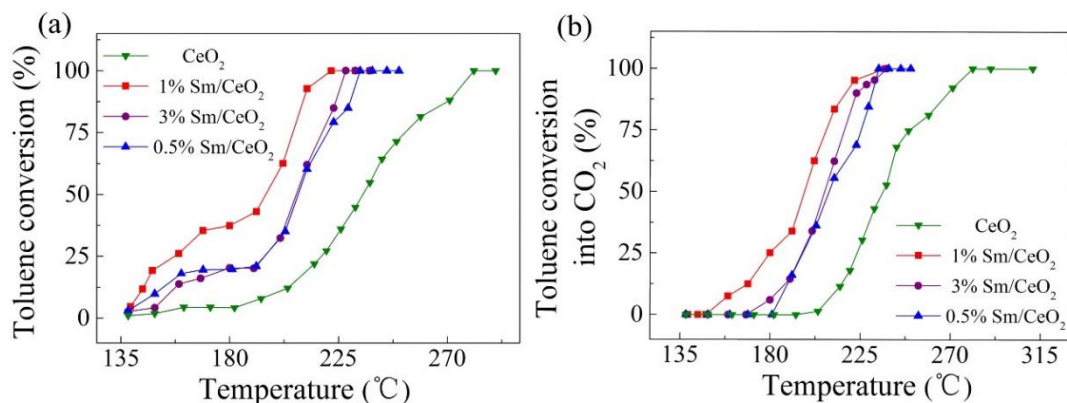
Fig 4.10. (a) Toluene conversions as a function of reaction temperature over the prepared catalysts; (b) CO_2 selectivity during the catalytic oxidation of toluene over the prepared catalysts.
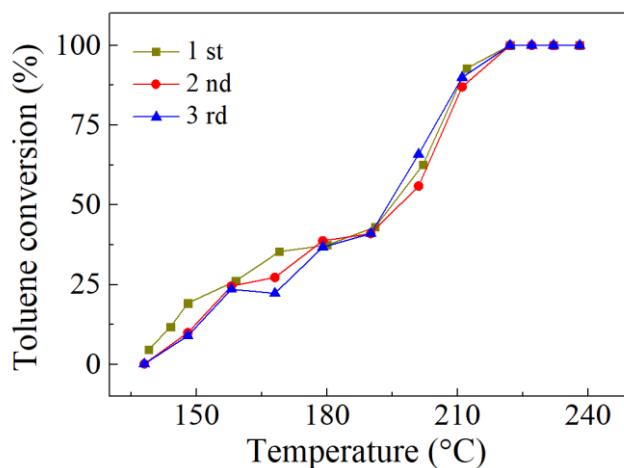
Fig 4.11. Catalytic performance of 1% Sm/CeO2 catalyst in the repeated runs.

Table 4.4 Catalytic toluene conversions over Ce-based catalysts reported in the literature and catalytic performances over the pure CeO_2 and Sm doped CeO_2 catalysts with different WHSVs.

Catalyst	WHSV	Toluene conversion temperature	Stability	Reference

171

	mL/(g h)	(°C)				time/h	
		$T_{10\%}$	$T_{50\%}$	$T_{90\%}$	$T_{100\%}$		
CuCeZr700	/	250	277	310	340	/	[35]
CeO$_2$-MOF/350	20,000	180	211	223	260	24	[22]
CuSmCeO$_x$	50,000	180	225	246	258	20	[42]
CeO$_2$-precipitation	60,000	185	232	280	320	/	[6]
CeO$_2$-particle	60,000	196	223	265	340	/	[74]
CeO$_2$	60,000	198	235	273	281	/	
3% Sm/CeO$_2$	60,000	155	208	225	228	/	
0.5% Sm/CeO$_2$	60,000	150	208	230	234	/	This
1% Sm/CeO$_2$	60,000	143	194	211	222	33	work
1% Sm/CeO$_2$	30,000	147	210	226	230	/	
1% Sm/CeO$_2$	100,000	204	240	285	296	/	

4.3.7 Effect of WHSV and stability test

The effect of WHSV on the toluene oxidation over 1% Sm/CeO$_2$ catalyst was investigated under different WHSVs of 30,000, 60,000 and 100,000 mL/(g h). As shown in Fig. 4.12 and Table 4.4, for 1% Sm/CeO$_2$ catalyst, when the WHSV was 60,000 mL/(g h), the $T_{50\%}$ and $T_{90\%}$ were 194 and 211 °C, respectively, which were drastically reduced from 239 and 283 °C with the WHSV of 100,000 mL/(g h). When the WHSV was further reduced to 30,000 mL/(g h), the $T_{50\%}$ and $T_{90\%}$ were also decreased, however, the temperature differences between 60,000 and 30,000 mL/(g h) for $T_{50\%}$ and $T_{90\%}$ were only 16 and 15 °C, respectively. Therefore, to reduce the cost and maintain efficiency for the catalytic oxidation, the WHSV of 60,000 mL/(g h) was selected as the optimum value in

the present study.
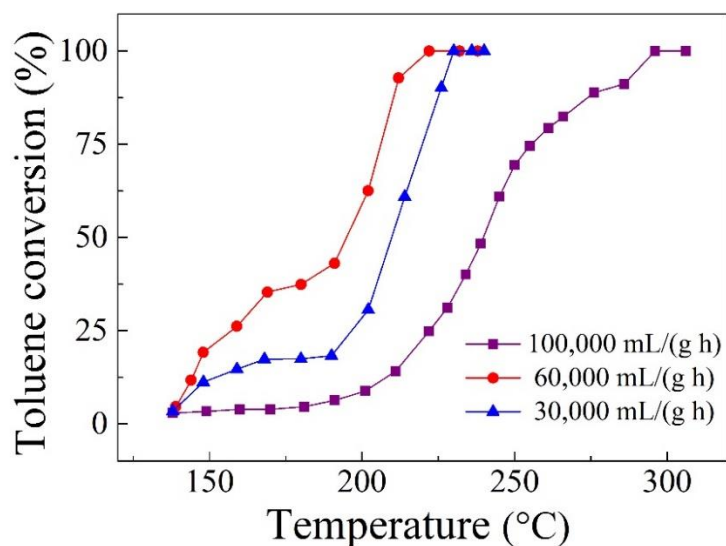
Fig 4.12. Effect of WHSV on toluene oxidation over 1% Sm/CeO$_2$ catalyst (Reaction conditions: [Toluene] = 1000 ppm, [O$_2$] =20%, and N$_2$ as balance).

4.3.8. Stability test

To investigate the catalytic stability and durability, the 1% Sm/CeO$_2$ catalyst with the best performance was tested on-stream for the oxidation of toluene in the absence of water vapor under different temperatures at first. As shown in Fig. 4.13a, the conversions of ca.75%, 62% and 35% had no obvious changes at least for lasting 32 h at 239.3 234.6, and 222.4°C, respectively. Obviously, the catalyst had an excellent catalytic stability at different levels of conversion for the oxidation of toluene, which is crucial for the practical application.
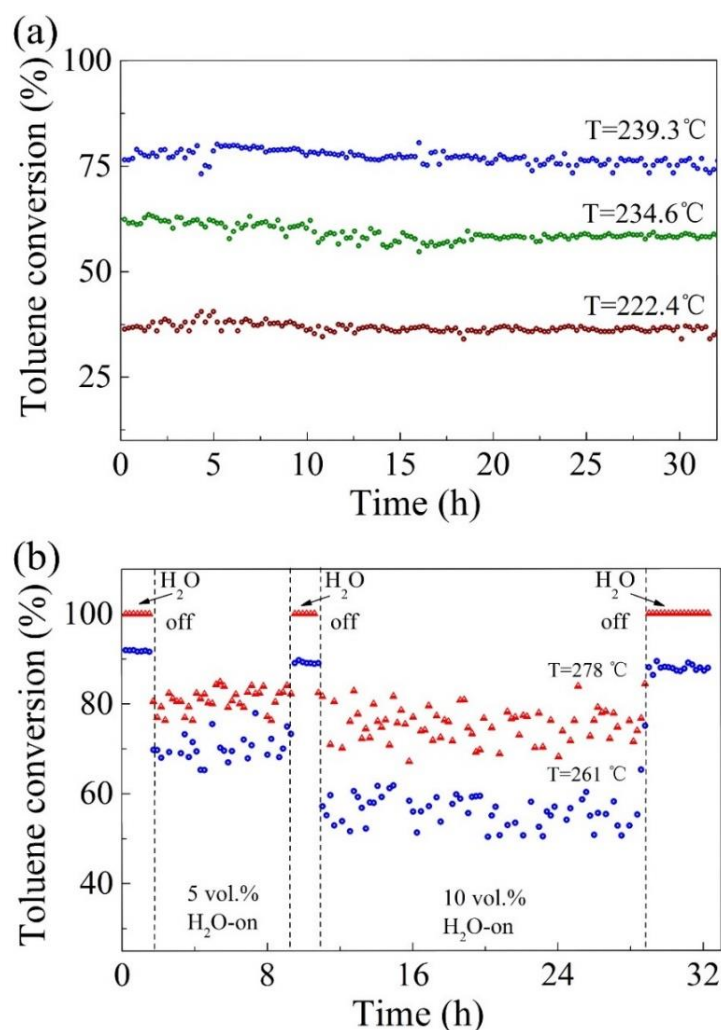
Fig 4.13. Catalytic stability test for the toluene oxidation at different temperatures in the absence of water vapor (a); and the effect of water vapor (5 and 10 vol%) on the catalytic activity of the 1% Sm/CeO$_2$ catalyst at different temperatures with a WHSV of 60,000 mL/(g h) (b).

Moisture tolerance is also important for the practical application [74]. Herein, the long-term catalytic performance of 1% Sm/CeO$_2$ catalyst under different water vapor concentrations were estimated. As shown in Fig. 4.13b, toluene conversion was attenuated to 80% and 75% of conversions from 100% of conversion in the absence of water vapor when 5 and 10 vol % water vapors were fed into the stream respectively at

278 °C during 32 h test. In addition, at a relatively low temperature of 261°C, 5 and 10 vol % water vapor additions resulted in more decrease on the toluene conversion from ca. 91% to 70 % and 55 % respectively over the following 32 h test. Importantly, as soon as H_2O was cut off, the catalytic conversions for the toluene oxidation at 261 or 278 °C were almost recovered to the initial level, indicating that this catalyst owned excellent water vapor tolerance. Fig. 4.14 shows the SEM images of all Ce-based catalysts after stability tests. Compared with fresh ones in Fig. 4.1, most of particles maintained the rod-shape morphology, also indicating that the x% Sm/CeO_2 catalysts had excellent stability during the reaction. Fig. 4.15 shows the related temperature change during the moisture tolerance test for the toluene oxidation. It indicated that the real oxidation temperature decreased to some extent during the introduction of water vapor, which also influenced the toluene conversion.
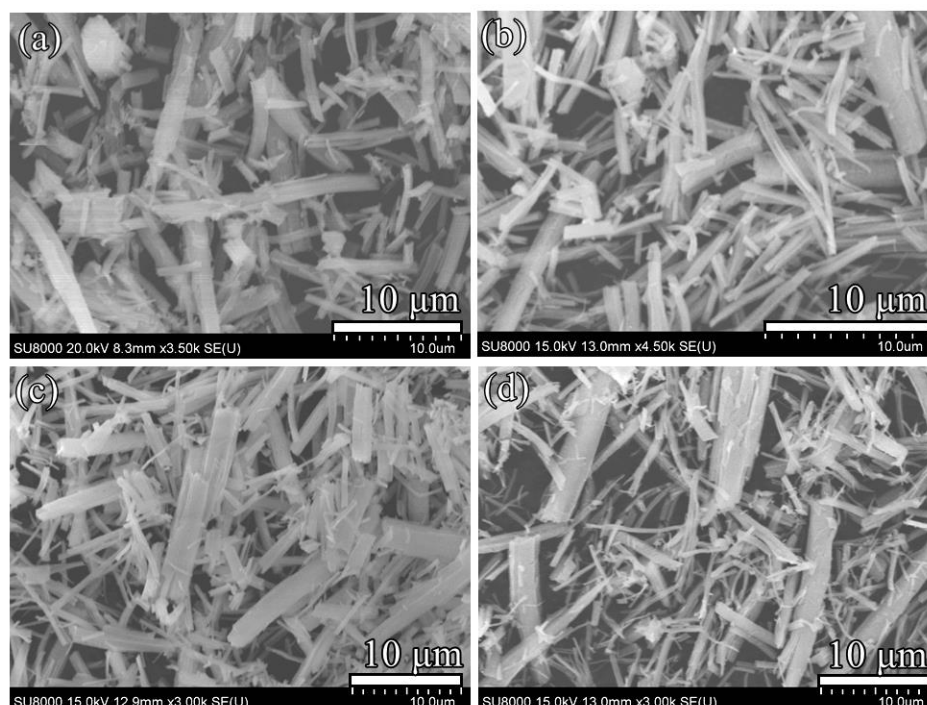
Fig 4.14. SEM images of Ce-based catalysts after stability tests (a) pure CeO_2 (b) 0.5% Sm/ CeO_2 (c) 1% Sm/CeO_2 (d) 3% Sm/CeO_2.
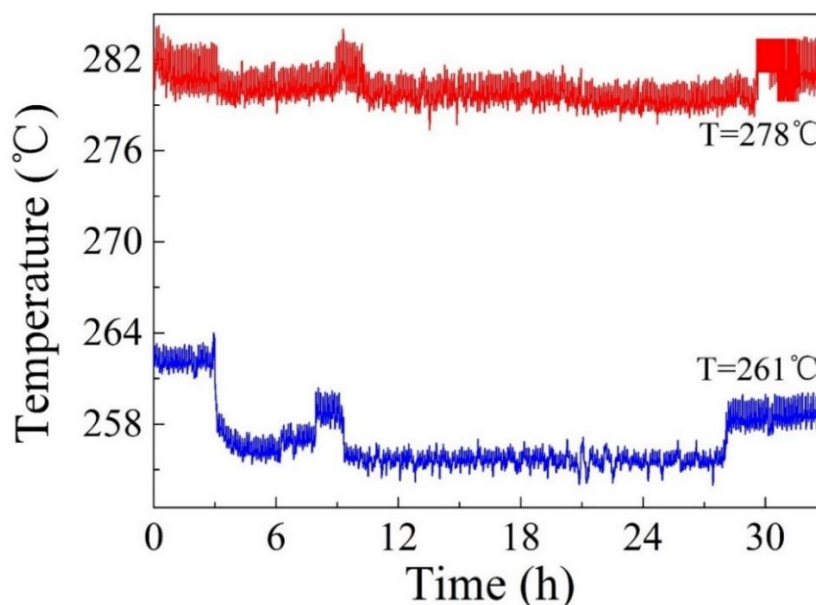
Fig 4.15. Temperature change during the moisture tolerance test for the toluene oxidation.

4.4 Conclusions

In this study, highly active x% Sm/CeO$_2$ catalysts were successfully synthesized by pyrolysis of Sm/Ce-MOF precursor, and applied for the oxidation of toluene. The characterizations confirmed that 1% Sm/CeO$_2$ catalyst had larger specific surface area, higher low-temperature reducibility, more surface oxygen vacancies and defects due to the higher concentration of Ce^{3+} species so that it had improved the redox properties. As a result, the 1% Sm/CeO$_2$ catalyst had the best performance for the oxidation of toluene with conversions of 50% and 100% at temperatures of 194 and 222 °C respectively under a WHSV of 60,000 mL/(g·h). Moreover, the 1% Sm/CeO$_2$ catalyst also exhibited excellent stability and high toleration to the moisture, indicating that it should be a promising catalyst for the VOC oxidation in the practical application.

176

References

[1] D. Gu, A.B. Guenther, J.E. Shilling, H. Yu, M. Huang, C. Zhao, Q. Yang, S.T. Martin, P. Artaxo, S. Kim, R. Seco, T. Stavrakou, K.M. Longo, J. Tota, R.A.F. de Souza, O. Vega, Y. Liu, M. Shrivastava, E.G. Alves, F.C. Santos, G. Leng, Z. Hu, Airborne observations reveal elevational gradient in tropical forest isoprene emissions, Nat Commun, 8 (2017) 15541.

[2] L.F. Liotta, Catalytic oxidation of volatile organic compounds on supported noble metals, Appl. Catal., B, 100 (2010) 403-412.

[3] K. Zeng, X. Li, C. Wang, Z. Wang, P. Guo, J. Yu, C. Zhang, X.S. Zhao, Three-dimensionally macroporous $MnZrO_x$ catalysts for propane combustion: Synergistic structure and doping effects on physicochemical and catalytic properties, J. Colloid Interface Sci., 572 (2020) 281-296.

[4] X. Zhang, X. Shi, J. Chen, Y. Yang, G. Lu, The preparation of defective UiO-66 metal organic framework using MOF-5 as structural modifier with high sorption capacity for gaseous toluene, Journal of Environmental Chemical Engineering, 7 (2019) 103405.

[5] M. Piumetti, D. Fino, N. Russo, Mesoporous manganese oxides prepared by solution combustion synthesis as catalysts for the total oxidation of VOCs, Appl. Catal., B, 163 (2015) 277-287.

[6] J. Chen, X. Chen, X. Chen, W. Xu, Z. Xu, H. Jia, J. Chen, Homogeneous introduction of CeO_y into MnO_x-based catalyst for oxidation of aromatic VOCs, Appl. Catal., B, 224 (2018) 825-835.

[7] M.S. Kamal, S.A. Razzak, M.M. Hossain, Catalytic oxidation of volatile organic compounds (VOCs)–A review, Atmos. Environ., 140 (2016) 117-134.

[8] M.L. Rodríguez, L.E. Cadús, D.O. Borio, VOCs abatement in adiabatic monolithic

177

reactors: Heat effects, transport limitations and design considerations, Chem. Eng. J., 306 (2016) 86-98.

[9] C. Zhang, C. Wang, W. Zhan, Y. Guo, Y. Guo, G. Lu, A. Baylet, A. Giroir-Fendler, Catalytic oxidation of vinyl chloride emission over $LaMnO_3$ and $LaB_{0.2}Mn_{0.8}O_3$ (B=Co, Ni, Fe) catalysts, Appl. Catal., B, 129 (2013) 509-516.

[10] A. Kołodziej, J. Łojewska, J. Tyczkowski, P. Jodłowski, W. Redzynia, M. Iwaniszyn, S. Zapotoczny, P. Kuśtrowski, Coupled engineering and chemical approach to the design of a catalytic structured reactor for combustion of VOCs: Cobalt oxide catalyst on knitted wire gauzes, Chem. Eng. J., 200-202 (2012) 329-337.

[11] S. Mo, S. Li, W. Li, J. Li, J. Chen, Y. Chen, Excellent low temperature performance for total benzene oxidation over mesoporous CoMnAl composited oxides from hydrotalcites, Journal of Materials Chemistry A, 4 (2016) 8113-8122.

[12] L. Zhao, Z. Zhang, Y. Li, X. Leng, T. Zhang, F. Yuan, X. Niu, Y. Zhu, Synthesis of Ce_aMnO_x hollow microsphere with hierarchical structure and its excellent catalytic performance for toluene combustion, Appl. Catal., B, 245 (2019) 502-512.

[13] Y.F. Chang, J.G. McCarty, Novel oxygen storage components for advanced catalysts for emission control in natural gas fueled vehicles, Catal. Today, 30 (1996) 163-170.

[14] C. Zhang, H. Huang, G. Li, L. Wang, L. Song, X. Li, Zeolitic acidity as a promoter for the catalytic oxidation of toluene over MnO/HZSM-5 catalysts, Catal. Today, 327 (2019) 374-381.

[15] X. Zhang, X. Lv, F. Bi, G. Lu, Y. Wang, Highly efficient Mn_2O_3 catalysts derived from Mn-MOFs for toluene oxidation: The influence of MOFs precursors, Molecular Catalysis, 482 (2020) 110701.

[16] G. Zhou, X. He, S. Liu, H. Xie, M. Fu, Phenyl VOCs catalytic combustion on

supported CoMn/AC oxide catalyst, Journal of Industrial and Engineering Chemistry, 21 (2015) 932-941.

[17] X. Xie, Y. Li, Z.Q. Liu, M. Haruta, W. Shen, Low-temperature oxidation of CO catalysed by Co_3O_4 nanorods, Nature, 458 (2009) 746-749.

[18] Y. Wang, Y. Yang, N. Liu, Y. Wang, X. Zhang, Sword-like CuO/CeO_2 composites derived from a Ce-BTC metal–organic framework with superior CO oxidation performance, RSC Advances, 8 (2018) 33096-33102.

[19] M.A.K.M. Hanafiah, Z.M. Hussin, N.F.M. Ariff, W.S.W. Ngah, S.C. Ibrahim, Monosodium glutamate functionalized chitosan beads for adsorption of precious cerium ion, Advanced Materials Research, 970 (2014) 198-203.

[20] Q. Dai, X. Wang, G. Lu, Low-temperature catalytic combustion of trichloroethylene over cerium oxide and catalyst deactivation, Appl. Catal., B, 81 (2008) 192-202.

[21] T. Montini, M. Melchionna, M. Monai, P. Fornasiero, Fundamentals and catalytic applications of CeO_2-based materials, Chem. Rev., 116 (2016) 5987-6041.

[22] X. Chen, X. Chen, E. Yu, S. Cai, H. Jia, J. Chen, P. Liang. In situ pyrolysis of Ce-MOF to prepare CeO_2 catalyst with obviously improved catalytic performance for toluene combustion, Chem. Eng. J., 344 (2018) 469-479.

[23] Z. Feng, M. Zhang, Q. Ren, S. Mo, R. Peng, D. Yan, M. Fu, L. Chen, J. Wu, D. Ye, Design of 3-dimensionally self-assembled CeO_2 hierarchical nanosphere as high efficiency catalysts for toluene oxidation, Chem. Eng. J., 369 (2019) 18-25.

[24] L.F. Liotta, M. Ousmane, G. Di Carlo, G. Pantaleo, G. Deganello, G. Marcì, L. Retailleau, A. Giroir-Fendler, Total oxidation of propene at low temperature over Co_3O_4-CeO_2 mixed oxides: Role of surface oxygen vacancies and bulk oxygen mobility in the catalytic activity, Appl. Catal., A, 347 (2008) 81-88.

[25] B. Solsona, R. Sanchis, A. Dejoz, T. García, L. Ruiz-Rodríguez, J. López Nieto, J. Cecilia, E. Rodríguez-Castellón, Total oxidation of propane using CeO_2 and $CuO-CeO_2$ catalysts prepared using templates of different nature, Catalysts, 7 (2017) 96.

[26] H. Wang, S. Liu, Z. Zhao, X. Zou, M. Liu, W. Liu, X. Wu, D. Weng, Activation and deactivation of Ag/CeO_2 during soot oxidation: influences of interfacial ceria reduction, Catalysis Science & Technology, 7 (2017) 2129-2139.

[27] X. Zhang, H. Li, X. Lv, J. Xu, Y. Wang, C. He, N. Liu, Y. Yang, Y. Wang, Facile synthesis of highly efficient amorphous Mn-MIL-100 catalysts: Formation mechanism and structure changes during application in CO oxidation, Chem. Eur. J, 24 (2018) 8822-8832.

[28] F. Bi, X. Zhang, S. Xiang, Y. Wang, Effect of Pd loading on ZrO_2 support resulting from pyrolysis of UiO-66: Application to CO oxidation, J. Colloid Interface Sci., 573 (2020) 11-20.

[29] F. Bi, X. Zhang, J. Chen, Y. Yang, Y. Wang, Excellent catalytic activity and water resistance of UiO-66-supported highly dispersed Pd nanoparticles for toluene catalytic oxidation, Appl. Catal., B, 269 (2020) 118767.

[30] X. Zhang, X. Lv, X. Shi, Y. Yang, Y. Yang, Enhanced hydrophobic UiO-66 (University of O_{slo} 66) metal-organic framework with high capacity and selectivity for toluene capture from high humid air, J. Colloid Interface Sci., 539 (2019) 152-160.

[31] X. Zhang, Y. Yang, X. Lv, Y. Wang, N. Liu, D. Chen, L. Cui, Adsorption/desorption kinetics and breakthrough of gaseous toluene for modified microporous-mesoporous UiO-66 metal organic framework, J. Hazard. Mater., 366 (2019) 140-150.

[32] X. Zhang, Y. Yang, L. Song, J. Chen, Y. Yang, Y. Wang, Enhanced adsorption performance of gaseous toluene on defective UiO-66 metal organic framework:

Equilibrium and kinetic studies, J. Hazard. Mater., 365 (2019) 597-605.

[33] D.A. Gómez-Gualdrón, Y.J. Colón, X. Zhang, T.C. Wang, Y.-S. Chen, J.T. Hupp, T. Yildirim, O.K. Farha, J. Zhang, R.Q. Snurr, Evaluating topologically diverse metal-organic frameworks for cryo-adsorbed hydrogen storage, Energy & Environmental Science, 9 (2016) 3279-3289.

[34] X. Zhang, L. Song, F. Bi, D. Zhang, Y. Wang, L. Cui, Catalytic oxidation of toluene using a facile synthesized Ag nanoparticle supported on UiO-66 derivative, J. Colloid Interface Sci., 571 (2020) 38-47.

[35] L. Wang, G. Yin, Y. Yang, X. Zhang, Enhanced CO oxidation and toluene oxidation on CuCeZr catalysts derived from UiO-66 metal organic frameworks, Reaction Kinetics, Mechanisms and Catalysis, 128 (2019) 193-204.

[36] X. Zhang, Y. Yang, L. Song, Y. Wang, C. He, Z. Wang, L. Cui, High and stable catalytic activity of Ag/Fe_2O_3 catalysts derived from MOFs for CO oxidation, Molecular Catalysis, 447 (2018) 80-89.

[37] X. Zhang, Y. Yang, W. Huang, Y. Yang, Y. Wang, C. He, N. Liu, M. Wu, L. Tang, g-C_3N_4/UiO-66 nanohybrids with enhanced photocatalytic activities for the oxidation of dye under visible light irradiation, Mater. Res. Bull., 99 (2018) 349-358.

[38] P. Wang, X. Du, T. Chen, X. Hao, A. Abudula, K. Tang, G. Guan, A novel electroactive PPy/HKUST-1 composite film-coated electrode for the selective recovery of lithium ions with low concentrations in aqueous solutions, Electrochim. Acta, 306 (2019) 35-44.

[39] X. Zhang, F. Hou, Y. Yang, Y. Wang, N. Liu, D. Chen, Y. Yang, A facile synthesis for cauliflower like CeO_2 catalysts from Ce-BTC precursor and their catalytic performance for CO oxidation, Appl. Surf. Sci., 423 (2017) 771-779.

[40] X. Zhang, X. Zhang, L. Song, F. Hou, Y. Yang, Y. Wang, N. Liu, Enhanced catalytic performance for CO oxidation and preferential CO oxidation over CuO/CeO_2 catalysts synthesized from metal organic framework: Effects of preparation methods, Int. J. Hydrogen Energy, 43 (2018) 18279-18288.

[41] C. Zhang, C. Wang, S. Gil, A. Boreave, L. Retailleau, Y. Guo, J.L. Valverde, A. Giroir-Fendler, Catalytic oxidation of 1,2-dichloropropane over supported LaMnO oxides catalysts, Appl. Catal., B, 201 (2017) 552-560.

[42] Z. Jiang, C. Chen, M. Ma, Z. Guo, Y. Yu, C. He, Rare-earth element doping-promoted toluene low-temperature combustion over mesostructured $CuMCeO_x$ (M=Y, Eu, Ho, and Sm) catalysts: the indispensable role of in situ generated oxygen vacancies, Catalysis Science & Technology, 8 (2018) 5933-5942.

[43] L. Liu, J. Li, H. Zhang, L. Li, P. Zhou, X. Meng, M. Guo, J. Jia, T. Sun, In situ fabrication of highly active γ-$MnO_2/SmMnO_3$ catalyst for deep catalytic oxidation of gaseous benzene, ethylbenzene, toluene, and o-xylene, J. Hazard. Mater., 362 (2019) 178-186.

[44] C. Zhang, Y. Guo, Y. Guo, G. Lu, A. Boreave, L. Retailleau, A. Baylet, A. Giroir-Fendler, $LaMnO_3$ perovskite oxides prepared by different methods for catalytic oxidation of toluene, Appl. Catal., B, 148-149 (2014) 490-498.

[45] J. Zhang, X. Weng, Z. Wu, Y. Liu, H. Wang, Facile synthesis of highly active $LaCoO_3/MgO$ composite perovskite via simultaneous co-precipitation in supercritical water, Appl. Catal., B, 126 (2012) 231-238.

[46] X. Wang, W. Zhao, T. Zhang, Y. Zhang, L. Jiang, S. Yin, Facile fabrication of shape-controlled $Co_xMn_yO_\beta$ nanocatalysts for benzene oxidation at low temperatures, Chem Commun (Camb), 54 (2018) 2154-2157.

[47] Y. Huang, B. Long, M. Tang, Z. Rui, M.-S. Balogun, Y. Tong, H. Ji, Bifunctional catalytic material: An ultrastable and high-performance surface defect CeO_2 nanosheets for formaldehyde thermal oxidation and photocatalytic oxidation, Appl. Catal., B, 181 (2016) 779-787.

[48] A. Pérez, M. Montes, R. Molina, S. Moreno, Cooperative effect of Ce and Pr in the catalytic combustion of ethanol in mixed Cu/CoMgAl oxides obtained from hydrotalcites, Appl. Catal. A, 408 (2011) 96-104.

[49] J. Ethiraj, F. Bonino, J.G. Vitillo, K.A. Lomachenko, S. Bordiga, Solvent driven gate opening in MOF-76-Ce: effect on CO_2 adsorption, Chemsuschem, 9 (2016) 713-719.

[50] A. Lin, A.A. Ibrahim, P. Arab, H.M. El-Kaderi, M.S. El-Shall, Palladium nanoparticles supported on Ce-metal organic framework for efficient CO oxidation and low temperature CO_2 capture, Acs Applied Materials & Interfaces, 9 (2017) 17961.

[51] W. Wang, Q. Zhu, Q. Dai, X. Wang, Fe doped CeO_2 nanosheets for catalytic oxidation of 1,2-dichloroethane: Effect of preparation method, Chem. Eng. J., 307 (2017) 1037-1046.

[52] X. Tang, Y. Xu, W. Shen, Promoting effect of copper on the catalytic activity of MnO_x-CeO_2 mixed oxide for complete oxidation of benzene, Chem. Eng. J., 144 (2008) 175-180.

[53] S. Li, X. Li, H. Wu, X. Sun, F. Gu, L. Zhang, H. He, L. Li, Mechanism of synergistic effect on electron transfer over Co-Ce/MCM-48 during ozonation of pharmaceuticals in water, ACS Appl Mater Interfaces, 11 (2019) 23957-23971.

[54] P. Li, C. He, J. Cheng, C.Y. Ma, B.J. Dou, Z.P. Hao, Catalytic oxidation of toluene over Pd/Co_3AlO catalysts derived from hydrotalcite-like compounds: Effects of preparation methods, Appl. Catal., B, 101 (2011) 570-579.

[55] C. He, Y. Yu, Q. Shen, J. Chen, N. Qiao, Catalytic behavior and synergistic effect of nanostructured mesoporous CuO-MnO_x-CeO_2 catalysts for chlorobenzene destruction, Appl. Surf. Sci., 297 (2014) 59-69.

[56] S.S. Lin, C.L. Chen, D.J. Chang, C.C. Chen, Catalytic wet air oxidation of phenol by various CeO_2 catalysts, Water Res., 36 (2002) 0-3014.

[57] Z. Wu, M. Li, J. Howe, H.M. Meyer, 3rd, S.H. Overbury, Probing defect sites on CeO_2 nanocrystals with well-defined surface planes by Raman spectroscopy and O_2 adsorption, Langmuir, 26 (2010) 16595-16606.

[58] I.D.C. Silva, F.A. Sigoli, I.O. Mazali, Reversible oxygen vacancy generation on pure CeO_2 nanorods evaluated by in situ Raman spectroscopy, Journal of Physical Chemistry C, 121.23 (2017) 12928-12935.

[59] B. Wang, C. Chi, M. Xu, C. Wang, D. Meng, Plasma-catalytic removal of toluene over CeO_2-MnO_x catalysts in an atmosphere dielectric barrier discharge, Chem. Eng. J., 322 (2017) 679-692.

[60] R. Peng, S. Li, X. Sun, Q. Ren, L. Chen, M. Fu, J. Wu, D. Ye, Size effect of Pt nanoparticles on the catalytic oxidation of toluene over Pt/CeO_2 catalysts, Appl. Catal., B, 220 (2018) 462-470.

[61] C. Hess, In situ Raman spectroscopy of catalysts: Examples from current research, Top. Catal., 56 (2013) 1593-1600.

[62] J. Du, Z. Qu, C. Dong, L. Song, Y. Qin, N. Huang, Low-temperature abatement of toluene over Mn-Ce oxides catalysts synthesized by a modified hydrothermal approach, Appl. Surf. Sci., 433 (2018) 1025-1035.

[63] L. Liu, H. Zhang, J. Jia, T. Sun, M. Sun, Direct molten polymerization synthesis of highly active samarium manganese perovskites with different morphologies for VOC

removal, Inorg. Chem., 57 (2018) 8451-8457.

[64] B. Govinda Rao, P. Sudarsanam, A. Rangaswamy, B.M. Reddy, Highly efficient CeO_2–MoO_3/SiO_2 catalyst for solvent-free oxidative coupling of benzylamines into N-benzylbenzaldimines with O_2 as the oxidant, Catal. Lett., 145 (2015) 1436-1445.

[65] W. Zhan, X. Zhang, Y. Guo, L. Wang, Y. Guo, G. Lu, Synthesis of mesoporous CeO_2-MnO_x binary oxides and their catalytic performances for CO oxidation, Journal of Rare Earths, 32 (2014) 146-152.

[66] F. Hu, J. Chen, Y. Peng, H. Song, K. Li, J. Li, Novel nanowire self-assembled hierarchical CeO_2 microspheres for low temperature toluene catalytic combustion, Chem. Eng. J., 331 (2018) 425-434.

[67] L. Wang, J. Zhang, Q. Zhang, N. Xu, J. Song, XAFS and XPS studies on site occupation of Sm^{3+} ions in Sm doped M-type $BaFe_{12}O_{19}$, J. Magn. Magn. Mater., 377 (2015) 362-367.

[68] A. Rangaswamy, P. Sudarsanam, B.M. Reddy, Rare earth metal doped CeO_2-based catalytic materials for diesel soot oxidation at lower temperatures, Journal of Rare Earths, 33 (2015) 1162-1169.

[69] R. Peng, X. Sun, S. Li, L. Chen, M. Fu, J. Wu, D. Ye, Shape effect of Pt/CeO_2 catalysts on the catalytic oxidation of toluene, Chem. Eng. J., 306 (2016) 1234-1246.

[70] Y. Zhu, S. Zhang, J.-j. Shan, L. Nguyen, S. Zhan, X. Gu, F. Tao, In situ surface chemistries and catalytic performances of ceria doped with palladium, platinum, and rhodium in methane partial oxidation for the production of syngas, ACS Catalysis, 3 (2013) 2627-2639.

[71] S. Mo, Q. Zhang, J. Li, Y. Sun, Q. Ren, S. Zou, Q. Zhang, J. Lu, M. Fu, D. Mo, J. Wu, H. Huang, D. Ye, Highly efficient mesoporous MnO_2 catalysts for the total toluene

oxidation: Oxygen-Vacancy defect engineering and involved intermediates using in situ DRIFTS, Appl. Catal., B, 264 (2020) 118464.

[72] C.-H. Chen, E.C. Njagi, S.-P. Sun, H. Genuino, B. Hu, S.L. Suib, Hydrophobic Polymer-Coated Metal Oxide Catalysts for Effective Low-Temperature Oxidation of CO under Moisture-Rich Conditions, Chem. Mater., 22 (2010) 3313-3315.

[73] S.R. Segal, S.L. Suib, X. Tang, S. Satyapal, Photoassisted Decomposition of Dimethyl Methylphosphonate over Amorphous Manganese Oxide Catalysts, Chem. Mater., 11.7 (1999) 1687-1695.

[74] F. Hu, Y. Peng, J. Chen, S. Liu, H. Song, J. Li, Low content of CoO_x supported on nanocrystalline CeO_2 for toluene combustion: The importance of interfaces between active sites and supports, Appl. Catal., B, 240 (2019) 329-336.

Chapter 5 Conclusions and Prospect

5.1 Conclusions

Catalytic oxidation to VOC elimination at low temperature is considered as the most effective way with less energy consumption and low cost. To promote the efficiency of catalytic oxidation, the key is development of high-performance catalysts with abundant oxygen vacancies, active oxygen species, large surface area, excellent reducibility. Herein, a series of transition metal oxide catalysts were developed to decrease the total toluene oxidation temperature. Furthermore, the toluene oxidation mechanism over each catalyst was proposed based on *in situ* DRIFTS analyses. The following results were obtained:

In chapter 1: Comprehensive introduction for oxygen vacancy defect (OVD) engineering of various catalysts. The relationship between OVD and catalytic activity for gaseous VOCs oxidation, the latest technologies for the increasing OVDs on the catalysts were introduced and discussed. Furthermore, novel and advanced characterization ways including HRTEM, STM, XPS, Raman, EPR, PALS, EELS and XAFS to understand the existence of OVDs in the catalysts were summarized.

In chapter 2: The Mn_xCo_y mixed oxide catalysts with defect-rich structures were successfully synthesized using the agar-gel method. It is demonstrated that the molar ratio of Mn/Co greatly affected the phase structure and textural properties of the as-prepared catalysts. Among the Mn_xCo_y mixed oxide catalysts, the Mn2Co1 mixed oxide catalyst exhibited a highest catalytic performance with $T_{50\%}$ of 228 °C and $T_{100\%}$ of 238 °C for the toluene oxidation. According to the characterizations of the Mn2Co1 mixed oxide catalyst,

it is considered that the enhanced catalytic performance was contributed to the higher surface area, higher contents of Mn^{4+}, Mn^{3+} and Co^{3+} species with more oxygen vacancies and better reducibility. The high stability and renewability of Mn2Co1 mixed oxide catalyst were also confirmed by the activity and endurability tests with 5, 10, and 20 vol% of water vapors. Furthermore, *in situ* DRIFTS analysis revealed that both adsorbed oxygen and lattice oxygen species could simultaneously participate in the toluene adsorption-oxidation process, especially the rate-controlling step should be the C = C breakage of aromatic ring. It is expected that the present agar-gel method with low cost and convenient operation can be widely applied for the designing of novel mixed metal oxides catalysts for VOCs oxidation.

In chapter 3: A novel Ho-doped OMS-2 catalyst with abundant active oxygen species was successfully prepared via a facile redox co-precipitation route. It is found that the addition of Ho species in the OMS-2 catalyst preparation stage can effectively tune the oxygen vacancy defects on the final Ho-doped OMS-2 catalyst via adjusting the Ho doping amount, and the trace Ho doping not only regulated the surface oxygen species, but also changed the textural properties of OMS-2 including crystal structure, specific surface area, low-temperature reducibility, oxygen storage capacity and surface elemental composition. As a result, the 0.5% Ho-OMS-2 exhibited the highest molar ratio of O_{ads}/O_{latt} with the highest performance for toluene oxidation among the prepared x% Ho-OMS-2, and its $T_{50\%}$, $T_{90\%}$ and $T_{100\%}$ values in the case with H_2O vapor (5 vol%) achieved at 217, 226, 228 °C, respectively. Comparing with the OMS-2, the active oxygen species on the Ho-doped OMS-2 were more easily released for promoting the adsorption and oxidation of toluene as well as intermediates. *In situ* DRIFTS study confirmed that either

the adsorbed oxygen species on the surface or lattice oxygen in the bulk of catalysts could take part in the adsorption and oxidation reaction simultaneously, where the benzyl, benzyl alcohol, benzaldehyde, benzoate, maleic anhydride, and carbonates should be the main intermediates during toluene adsorption-oxidation process at relatively low temperatures. Furthermore, since the difference of catalytic activity between OMS-2 and 0.5% Ho-OMS-2 under H_2O, two toluene oxidation mechanism were proposed based on the acidity.

In chapter 4: In this study, highly active x% Sm/CeO_2 catalysts were successfully synthesized by pyrolysis of Sm/Ce-MOF precursor, and applied for the oxidation of toluene. The characterizations confirmed that 1% Sm/CeO_2 catalyst had larger specific surface area, higher low-temperature reducibility, more surface oxygen vacancies and defects due to the higher concentration of Ce^{3+} species so that it had improved the redox properties. As a result, the 1% Sm/CeO_2 catalyst had the best performance for the oxidation of toluene with conversions of 50% and 100% at temperatures of 194 and 222 °C respectively under a WHSV of 60,000 mL/(g·h). Moreover, the 1% Sm/CeO_2 catalyst also exhibited excellent stability and high toleration to the moisture, indicating that it should be a promising catalyst for the VOC oxidation in the practical application.

5.2 Prospects

In this study, transition metal oxides were investigated as the catalysts for VOC oxidation. The latest strategies for the increasing oxygen vacancies among metal oxides include: (i) synthesis and/or calcination temperature controlling; (ii) atom substitution (isovalent-substitution and aliovalent-substitution); (iii) surface modification (noble

metal doping and transition metal doping); and (iv) *in-situ* surface treatment (chemical etching and surface reduction). However, the following key issues should be addressed for the easier generation of OVDs on the high-performance catalysts:

- The relationship between the amorphous phase sites and the OVDs should be clarified, how the OVDs to participate in the VOCs oxidation and affect the catalytic activity should be investigated in more details.

- The kinds of VOC molecules which can be effectively oxidated by tuning the concentration of OVDs should be classified.

- How to use the obtained signals to faithfully reflect the evolution of OVDs during the oxidation processes should be confirmed by various advanced analysis techniques. The thorough characterizations of OVDs should include advanced quantitative and qualitative methods to identify its role during the catalysis process.

- Sometimes, oxygen defective metal oxides fabricated by some strategies show poor stability. In this case, the relationship between the catalysis performance and OVDs should be analyzed in more details. It is very important for the development of novel VOCs oxidation catalysts with more excellent performance.

Although the reaction mechanism of the reduction-oxidation route with the OVDs is still ambiguous, the engineering of OVDs could strongly boost the performance of the designed catalysts for VOCs oxidation. Further exploration of effective strategies for tuning/introducing of OVDs should be considered, and its compatibility with the industrial VOCs emission system is worthy of further investigated.

List of publications and presentations

Publications

(1). **Peifen Wang,** Jing Wang, Xiaowei An, Jin Shi, Wenfeng Shangguan, Xiaogang Hao, Guangwen Xu, Bing Tang, Abuliti Abudula, and Guoqing Guan, "Generation of abundant defects in Mn-Co mixed oxides by a facile agar-gel method for highly efficient catalysis of total toluene oxidation" Applied Catalysis B: Environmental, 282 (2021) 119560.

(2). **Peifen Wang,** Jing Wang, Jin Shi, Xiao Du, Xiaogang Hao, Bing Tang, Abuliti Abudula, Guoqing Guan, "Low content of samarium doped CeO_2 oxide catalysts derived from metal organic framework precursor for toluene oxidation," Molecular Catalysis, 492 (2020) 111027.

(3). **Peifen Wang,** Junlan Zheng, Xuli Ma, Xiao Du, Fengfeng Gao, Xiaogang Hao, Bing Tang, Abuliti Abudula, Guoqing Guan, "Electroactive magnetic microparticles for the selective elimination of cesium ions in the wastewater," Environmental Research, 185 (2020) 109474.

(4). Jing Wang, Akihiro Yoshida, **Peifen Wang,** Tao Yu, Zhongde Wang, Xiaogang Hao, Abuliti Abudula, Guoqing Guan, "Catalytic oxidation of volatile organic compound over Cerium modified Cobalt-based mixed oxide catalysts synthesized by electrodeposition method," Applied Catalysis B: Environmental, 271 (2020) 118941.

(5). Jing Wang, **Peifen Wang,** Qiang Zhao, Tao Yu, Xiao Du, Xiaogang Hao, Abuliti Abudula, Guoqing Guan, "Highly dispersed Ag nanoparticles embedded on the surface of CeO_2/CF nanowires derived from three-dimensional structured Cu foam for toluene catalytic oxidation," Molecular Catalysis, 486 (2020) 110879.

(6). Jing Wang, **Peifen Wang,** Qiang Zhao, Jin Shi, Tao Yu, Xiao Du, Xiaogang Hao, Abuliti Abudula, Guoqing Guan "Stable hetero-metal doped Co-based catalysts prepared by electrodeposition method for low temperature combustion of toluene" Carbon Resources

Conversions, 3 (2020) 95-103.

(7). Jing Wang, **Peifen Wang**, Akihiro Yoshida, Qiang Zhao, Shasha Li, Xiaogang Hao, Abuliti Abudula, Guangwen Xu, Guoqing Guan, "Mn-Co oxide decorated on Cu nanowires as efficient catalysts for catalytic oxidation of toluene," Carbon Resources Conversions, 3 (2020) 36-45.

(8). Xiaoqiong Hao, Xiaowei An, Amar M. Patil, **Peifen Wang**, Xuli Ma, Xiao Du, Xiaogang Hao, Abuliti Abudula, and Guoqing Guan, "Biomass Derived N-doped Carbon for Efficient Electrocatalytic CO_2 Reduction to CO and Zn-CO_2 Batteries," ACS Applied Materials & Interfaces, 13 (2021) 3738-3747.

(9). Pattreeya Panpian, Thi Tuong Vi Tran, Suwadee Kongparakul; Lalita Attanatho, Yoothana Thanmongkhon, **Peifen Wang**, Guoqing Guan, Narong Chanlek; Yingyot Poo-arporn, and Chanatip Samart, "Production of bio-jet fuel through ethylene oligomerization using NiAlKIT-6 as a highly efficient catalyst," Fuel, 287 (2021) 119831.

(10). Jiajia Wang, Xiyan Yue, Yanyan Yang, Suchada Sirisomboonchai, **Peifen Wang**, Xuli Ma, Abuliti Abudula, Guoqing Guan, "Earth-abundant transition-metal-based bifunctional catalysts for overall electrochemical water splitting: A review," Journal of Alloys and Compounds, 819 (2020) 153346.

International presentations

(1). **Peifen Wang**, "Generation of abundant defects in metal-mixed-oxides by a facile agar-gel method for highly-efficient combustion of VOCs," Excellent PhD Students Forum, 12th Global Chinese Chemical Engineers Symposium (GCCES2020), Nanjing, China, Oct.30-Nov. 2, 2020 (on line).

(2). **Peifen Wang,** Jing Wang, Akihiro Yoshida, Suwadee Kongparakul, Chanatip Samart, Katsuki Kusakabe, Abuliti Abudula, and Guoqing Guan, "Enhanced toluene combustion

performance over Pt loaded Sm doping CeO$_2$ catalysts," The 32nd International Symposium on Chemical Engineering (ISChE2019), at Chungnam National University, Daejeon, Korea, December 6-8, 2019.

(3). Guoqing Guan, Xiao Du, **Peifen Wang**, Xiaogang Hao, Akihiro Yoshida, Abuliti Abudula, "Selective electrochemical extraction of low concentration of Li$^+$ ions from aqueous solution," 18th Asian Pacific Confederation of Chemical Engineering Congress (APCChE 2019), Sapporo, Hokkaido, Japan, September 23-27, 2019.

Domestic presentations

(1). 王佩芬, 王ジン, 趙 強, 于涛, 吉田曉弘, 阿布里提, 官国清, "Promotion effect of Ho doping on OMS-2 catalysts for toluene combustion at low temperatures," 化学工学会第51回秋季大会、岩手大学、2020年9月24-26日(On line).

(2). **Peifen Wang,** Jiajia Wang, Xiao Du, Xiaogang Hao, Akihiro Yoshida, Abuliti Abudula, and Guoqing Guan, "A novel electroactive PPy/HKUST-1 composite film-coated electrode for the selective recovery of lithium ions with low concentrations in aqueous solutions," 令和2年度化学系学協会東北大会, 八戸, 2020年9月26-27日（On-line）.

(3). **Peifen Wang**, Jing Wang, Qiang Zhao, Tao Yu, Akihiro Yoshida, Abuliti Abudula, Guoqing Guan, "Low-temperature catalytic combustion of toluene over Mn-Co oxides prepared by one-step agar-gel method," 4校交流会 in 一関工業高等専門学校, 2019年10月29日.

(4). 王佩芬、王ジン、吉田曉弘 、阿布里提、官国清、"A facile method to synthesize high performance Mn-Co oxides towards the oxidation of volatile organic compounds," 化学工学会横浜大会、横浜国立大学、2019年8月8日-9日.

(5). 王ジン, 王佩芬, 趙強, 張夢娟, 吉田曉弘, 阿布里提, 官国清, "Synthesis of MnO$_x$ dominated catalysts with cubic structure and its application in the catalytic combustion of volatile

organic compounds," 化学工学会第 51 回秋季大会、岩手大学、2020 年 9 月 24-26 日(On line).

(6). Jing Wang, **Peifen Wang**, Qiang Zhao, Jin Shi, Akihiro Yoshida, Tao Yu, Abuliti Abudula, and Guoqing Guan, "Cubic structured MnOx incorporated by Co-Fe nanowires for the low temperature catalytic oxidation of toluene," 令和 2 年度化学系学協会東北大会, 八戸, 2020 年 9 月 26-27 日（On-line）.

(7). Jing Wang, **Peifen Wang**, Akihiro Yoshida, Tao Yu, Abuliti Abudula, Guoqing Guan, "Low temperature catalytic oxidation of toluene over Ag-CeO2/CF catalysts synthesized by novel electrodeposition method," 化学工学会第 85 年会, 関西大学　千里山キャンパス 、 2020 年 3 月 15-17 日.

(8). 王ジン、**王佩芬**、吉田曉弘、阿布里提、官国清、"Mn-Co oxides supported on the nanowires of Cu foam for toluene catalytic combustion," 化学工学会横浜大会、横浜国立大学、2019 年 8 月 8 日-9 日.

List of patents

1. 王佩芬, 官国清, 関和治, 阿布里提, "VOC 除去触媒及びその製造方法並びに VOC の除去方法、"出願番号：特願 2021-005209、出願日：2021 年 1 月 15 日.

2. 王佩芬、王ジン、官国清、関和治、阿布里提、"VOC 除去触媒及びその製造方法"、日本特許、出願番号：特願 2020-021327、出願日：2020 年 2 月 12 日.

3. 王佩芬、官国清、王ジン、吉田曉弘、関和志、阿布里提、"VOC 除去触媒製造用前駆体、VOC 除去触媒及びその製造方法、" 出願番号：2019-154653、出願日：2019 年 8 月 27 日.

4. 王佩芬、王ジン、官国清、吉田曉弘、関和志、阿布里提、"金属酸化物触媒の製造方法及び VOC 除去方法"、日本特許、出願番号：特願 2019-081959、出願日：2019 年 4 月 23 日.

5. 王ジン、王佩芬、官国清、吉田曉弘、関和志、阿布里提、"VOC 除去用触媒の製造方法、ＶＯＣ除去用触媒及びＶＯＣ除去方法"、日本特許、出願番号：特願 2019-082755、出願日：2019 年 4 月 24 日.

6. 王ジン、官国清、王佩芬、吉田曉弘、関和志、阿布里提、"VOC 除去用触媒の製造方法及び VOC 除去用触媒並びに VOC 除去方法、" 特願 2019-155551、出願日：2019 年 8 月 28 日.

List of awards

(1). **Excellent Student Award**, Hirosaki University, Japan, March 5, 2021.

(2). "**優秀発表賞**", "**最優秀発表賞**", "**英語発表優秀賞**", 4 校交流会in一関工業高等専門学校, Japan, October, 29, 2019.

(3). **Student Encouragement Award** (学生奨励賞）, 化学工学会横浜大会、横浜国立大学, Japan, August, 8-9, 2019.

(4). **Chinese Government Scholarship**, China, May 14, 2019.

Curriculum Vitae

Name: Wang Peifen; **Sex:** Female; **Date of birth:** *February 13, 1991*; **Place of birth:** Taiyuan, *Shanxi, CHINA.* **Address:** Graduate School of Science and Technology, Hirosaki University, 1-Bunkyocho, Hirosaki, 036-8560, Japan; **Tel:** +86-18634356909; **e-mail:** h18ds252@hirosaki-u.ac.jp

EDUCATION

10/2018 Hirosaki University, Aomori, Japan, Chemical Engineering; **Ph.D**

9/2015 Taiyuan University of Technology, Taiyuan,China, Department of Chemical Engineering; **Master**

9/2011 Northeast Agricultural University, Harbin, China, Department of Applied Chemistry; **Bachelor**

HONORS and AWARDS

2021.3   **Excellent Student Award,** Hirosaki University, Japan.

2019.10 **"優秀発表賞", "最優秀発表賞", "英語発表優秀賞"**, 4校交流会 in 一関工業高等専門学校, Japan.

2019.8   **Student Encouragement Award,** 化学工学会横浜大会、横浜国立大学, Japan.

2019.5   **Chinese Government Scholarship,** China.

Pulications (First author):

(1) **Peifen Wang**, Jing Wang, Xiaowei An, Jin Shi, Wenfeng Shangguan, Xiaogang Hao, Guangwen Xu, Bing Tang, Abuliti Abudula, and Guoqing Guan, "Generation of abundant defects in Mn-Co mixed oxides by a facile agar-gel method for highly efficient catalysis of total toluene oxidation" Applied Catalysis B: Environmental, 282 (2021) 119560.

(2) **Peifen Wang**, Jing Wang, Jin Shi, Xiao Du, Xiaogang Hao, Bing Tang, Abuliti Abudula, Guoqing Guan, "Low content of samarium doped CeO_2 oxide catalysts derived from metal organic framework precursor for toluene oxidation," Molecular Catalysis, 492 (2020) 111027.

(3) **Peifen Wang**, Junlan Zheng, Xuli Ma, Xiao Du, Fengfeng Gao, Xiaogang Hao, Bing Tang, Abuliti Abudula, Guoqing Guan, "Electroactive magnetic microparticles for the selective elimination of cesium ions in the wastewater," Environmental Research, 185 (2020) 109474.

(4) **Peifen Wang,** Xiao Du, Tian Chen, Xiaogang Hao, Abuliti Abudula, Keyong Tang, Guoqing Guan, "A novel electroactive PPy/HKUST-1 composite film coated electrode for selective recovery of lithium ions with low concentrations in aqueous solutions," Electrochimica Acta, 306 (2019) 35-44.

(5) **Peifen Wang,** Xiao Du, Xiaowei An, Shasha Li, Fengfeng Gao, Xiaogang Hao, Guoqing Guan, "Synthesis of oriented coral-like polyaniline nano-arrays for flexible all-solid-state supercapacitor," Synthetic Metals, 232 (2017) 87-95.

(6) Tian Chen, **Peifen Wang** (equally as the co-first author), Xiao Du, Fengfeng Gao, Xuli Ma, Feifan Liu, Ayman Alameen, Keyong Tang, Xiaogang Hao. "A novel hexagonal prism Cu-BTC by unipolar pulse electropolymerization," Materials Letters, 254 (2019) 137-140.

Patents:

(1). 王佩芬, 官国清, 関和治, 阿布里提, 出願番号: 特願 2021-005209、出願日:2021.1.15

(2). 王佩芬、王ジン、官国清、関和治、阿布里提、出願番号：特願 2020-021327、出願日：2020.2.12

(3). 王佩芬、官国清、王ジン、吉田曉弘、関和志、阿布里提、出願番号：2019-154653、出願日:2019.8.17

(4). 王佩芬、王ジン、官国清、吉田曉弘、関和志、阿布里提、出願番号：特願 2019-081959、出願日：2019.4.13

(5) 王ジン、王佩芬、官国清、吉田曉弘、関和志、阿布里提、出願番号：特願 2019-082755、出願日：2019.4.24.

(6) 王ジン、官国清、王佩芬、吉田曉弘、関和志、阿布里提、特願 2019-155551、出願日：2019.8.28

I hereby certify that the matters noted above are all true.